High-Brightness Electron-Beam Production at the Brookhaven Accelerator Test Facility

Donald Patrick Russell III

A DISSERTATION
PRESENTED TO THE FACULTY
OF PRINCETON UNIVERSITY
IN CANDIDACY FOR THE DEGREE
OF DOCTOR OF PHILOSOPHY

RECOMMENDED FOR ACCEPTANCE
BY THE DEPARTMENT OF
PHYSICS

January, 1992

Abstract

The Accelerator Test Facility (ATF), under construction at Brookhaven National Laboratory, will consist of a high-brightness 50-MeV electron beam and a synchronizable 100-GW-peak-power CO_2 laser. It is designed to be a user facility for experiments that require a high-quality electron beam and that probe the interaction of electrons with strong electromagnetic fields.

The electron source is a radio-frequency (rf) gun incorporating a metal photocathode driven by a few-picosecond frequency-quadrupled Nd:YAG laser. The gun produces high-brightness pulses of few-picosecond duration and energy of up to 4.5 MeV. Upon exiting the gun the beam enters a low-energy transport line that allows for momentum selection, pulse compression, and diagnosis. The beam will be injected into a 50-MeV linear accelerator and transported to one of several experimental beamlines, where it will be brought into collision with the few-picosecond CO_2-laser pulse.

We have commissioned the rf gun and low-energy beamline and have found all operational characteristics to be as designed. For this we have constructed an electron-beam diagnostic system consisting of a series of phosphor-screen beam-profile monitors and an rf-deflection cavity that provides spatial profiles of the electron beam with 45-μm resolution and pulse-length measurements with picosecond resolution. In the course of this work we have had a unique opportunity to study in detail the physical mechanisms of electron-beam production and preservation.

The electron beam was measured to have a normalized transverse emittance of 4 mm-mrad and an rms pulse length of 6 picoseconds with a bunch charge of up to 2 nanocoulombs. From this we infer a peak current of 130 A and a normalized brightness of 10^{11} A/m^2, making the ATF the highest-brightness electron-beam user facility in the world. A previously unobserved rf-gun excitation mode has been identified in which a sufficiently intense laser pulse creates a plasma on the photocathode surface. The result is a train of micropulses over many rf cycles containing a total charge at least two orders of magnitude higher than that of the normal photoemissive mode.

We have also constructed an x-ray-backscattering diagnostic that will allow the synchronized interaction of the 50-MeV-electron and CO_2-laser beams to be established. Augmented by an x-ray spectrometer, this apparatus will be used to study nonlinear Compton scattering in the strong fields present at the CO_2-laser focus. This experiment has been approved for the ATF and is in the design phase.

Art is I; science is we.

—Claude Bernard

Never learn to do anything: if you don't learn, you'll always find someone else to do it for you.

—Mark Twain

Acknowledgements

An oft-conjured image of a difficult undertaking is that of climbing a mountain. I look back on the labors of the past few years more as a long trek over land of rapidly varying terrain and climate. The challenge was more one of navigation than locomotion. I would have lost the way on many (more) occasions had it not been for all those who placed trail markers and acted as guides. I offer them my heartfelt thanks.

At Brookhaven National Lab, I have valued the leadership and friendship of Harold Kirk, our project manager. He has given countless hours of his time to keep the ATF running, and was always available for discussion, assistance in beamline operation and data collection, and the occasional tennis match. Since the project inception he has coordinated the social as well as technical aspects of the project.

The engineering expertise of Stan Ulc is thoroughly interwoven with the work described herein. He provided the engineering design of the beam-profile monitors and constant assistance in making the system functional. Many thanks for the patient advice without which the Compton-scattering apparatus would have suffered considerably. By way of example he taught me the meaning of professionalism. I'm grateful to Rick Fernow for his helpful comments on drafts of this document. Working with someone of his acumen and patience has been an education and a pleasure. Marty Woodle kindly provided the beamline drawings in Chapter 2 and much assistance with AutoCad and vacuum design. The quick-mindedness and good humor of X. J. Wang have made for many fun and stimulating discussions. I was fortunate to have so lively a fellow crew member in the same boat.

At Princeton, I'm indebted to Sol Gruner for generously sharing his considerable experience with x-ray-imaging components. His willingness to provide phosphor samples and framegrabber software gave me a substantial shortcut in developing the profile-monitor system. What I learned from him will continue to prove useful in the future. The computer assistance of Joel Heinrich was invaluable, particularly in learning how to integrate Postscript drawings directly into a TEX document. I have also been fortunate to have the assistance and friendship of Mehran Ardebili, Brek Miller, and Michael Wall, each of whom brought a fresh perspective to this work.

In the process of building a diagnostic system and commissioning a beamline we have been dependent at every step on the effort of many individuals. At Princeton, the construction of the profile monitors and the Compton-scattering chamber have been in the skillful hands of Bill Groom, Bill Sands, Bob Klemmer, and the entire Elementary Particle Lab staff, with whom it's been enjoyable to work. Carl Bopp was always ready

to give electronics advice or to work a quick miracle on an ailing gizmo. Joe Horvath is lending his experience with vacuum systems to the never-trivial job of making nothing from something in the Compton chamber.

The Accelerator Test Facility exists because of the dedication, talent, and long hours of its technical staff: Cyrus Biscardi, Lenny DeSanto, Terry Monahan, Bob Harrington, and many others who have made sizeable contributions. Their unending work made our studies possible; their unfailing wit made it fun.

I would like to thank Laurel Lerner for her friendship and for smoothing the passage through the Princeton graduate program. The efficiency and cheerful countenance and Kathy Tuohy made life at Brookhaven much easier.

Each member of the Accelerator Test Facility has brought his or her unique abilities to the project, often working late into the night to maintain beam time. I have enjoyed and learned from working with every one of these talented individuals: Ken Batchelor, Ilan Ben-Zvi, Joe Fischer, Alan Fisher, Juan Gallardo, Ming Hung, Gerhart Ingold, Xie Jialin, King Leung, Bob Malone, Robert Palmer, Zohreh Parsa, Claudio Pellegrini, Igor Pogorelsky, Joe Rogers, Joe Sheehan, Triveni Srinivasan-Rao, Tom Tsang, Arie Van Steenbergen, and R.S. Zhang. The international character of this group was a delight.

Of my advisor, I must echo the sentiment of Alfred North Whitehead: "It requires a very unusual mind to make an analysis of the obvious." Kirk McDonald has the uncanny ability to penetrate to the heart of a problem, taking nothing for granted (the "obvious"), and produce an analysis that indeed makes the solution seem self-evident. My primary aim throughout this work has been to approach his crystal-clear style of thinking and his energetic and unflappable approach to experimental research. I have grown immensely as a physicist in pursuing this goal, but am yet a good distance from it. I hold him in the highest regard as a scientist and have treasured our professional relationship.

I also thank the entire faculty of the Princeton University Physics Department for making the education of a physicist a time not only of intense learning but also of great joy. It has been a privilege to sojourn among such unbounded intellect.

Finally, for the constant support of a host of family and friends, I owe a debt that cannot be repaid any more than it can be forgotten. My loving gratitude to you all.

This work was completed with the support of the United States Department of Energy.

Contents

List of Figures

List of Tables

Chapter 1

Introduction

The quest for higher luminosities in particle colliders and the production of shorter-wavelength free-electron lasers are two examples of the need for higher-quality electron beams. Two important measures of intrinsic beam quality are the *emittance* and *brightness*; improvements in beam quality should result in lower emittance and higher brightness.

The emittance expresses the volume occupied by a beam in phase space and is invariant under certain conditions. The transverse emittance is the area of the two-dimensional subspaces of the spatial and momentum coordinates transverse to the beam direction, (x, p_x) or (y, p_y). It carries such information as how far a beam can be transported within a given aperture and how small a focus can be produced. For example, the minimum output wavelength of a free-electron laser (FEL) is limited by the emittance of the driver beam.

The brightness of a particle beam, defined as the peak current divided by the transverse emittances, is identical to the brightness or *luminance* of an optical beam, namely the particle flux crossing a unit area into a unit solid angle. The luminosity of a collider is related to the brightness of the component beams, as is the power output of a free-electron laser (FEL). Among the many other applications that depend critically on beam brightness and emittance are electron-beam lithography, electron microscopy, and electron-beam welding.

Increasing beam brightness has long been the goal of accelerator facilities. For many years advances were achieved by improvements to a few existing beam-source technologies such as the dc thermionic gun and the field emitter. The emergence of accelerator physics as an independent discipline coupled with technological innovations of the past decade have resulted in rapidly growing efforts to create new and better particle sources. Such work is assuming a central role in several beamline facilities around the world.

One of these new technologies is the photocathode radio-frequency (rf) gun, developed by Los Alamos as an FEL driver [1]. A photoemitter is incorporated into a standing-wave radio-frequency cavity and stimulated by a short laser pulse. This design was shown to have several advantages over conventional electron sources. The beam can be rapidly accelerated to relativistic energies in the rf field, minimizing the emittance growth caused by mutual electrostatic repulsion, or "space charge," which is most prominent when the beam is nonrelativistic. The properties of the electron bunch are easily varied by altering the laser-pulse parameters. The intrinsically high brightness possible with an rf gun avoids the need for a beam buncher. The Los Alamos effort achieved a

higher brightness at the beam currents needed for accelerator and FEL applications than had been possible with conventional sources. This new technique is now being utilized and extended by several new accelerator facilities.

One of these, the Accelerator Test Facility (ATF), is being constructed by the Center for Accelerator Physics at Brookhaven National Laboratory. It consists of a 4.5-MeV photocathode rf gun driven by a Nd:YAG laser, a 50-MeV linear accelerator, and a synchronizable high-peak-power CO_2 laser with which the electron beam can be collided in one of several experimental beamlines. Experiments planned for the ATF will explore such phenomena as FEL's, laser-based particle acceleration, and nonlinear quantum electrodynamics. The underlying theme of the experimental program is the interaction of charged particles with strong electromagnetic fields, particularly in configurations that require a very high-quality electron beam.

The commissioning of this facility itself serves as an experiment in high-brightness beam production and the preservation of this brightness through the complex beam optics required to support a multi-user facility. The challenge is to incorporate the rf gun into a beamline that has the flexibility to meet the various beam requirements of different experiments while preserving the diagnostic capabilities needed to explore the beam properties in detail. The goal is to understand beam production and transport and the physical processes that limit beam quality. In the spirit of particle-beam physics this effort plays the dual role of optimizing the performance of the present facility and gaining experience that will allow improved designs in the future.

We report here on the commissioning of the ATF rf gun and low-energy beam transport, which serves simultaneously as the vehicle for experimentation on the electron beam and as the injector for the 50-MeV linac. Though beamline commissioning presents an interesting engineering challenge, the emphasis here is on the physical processes of beam production and transport as elucidated in studies of the injection line. The measured beam-performance parameters will also be compared to design specifications as an indicator of the progress of the ATF.

Specifically, we have constructed a beam-profile-monitor system that serves as the backbone of the ATF diagnostic capability. The system provides detailed spatial information about the low-energy electron beam. In combination with other beamline elements this allows us to measure such beam properties as spot size, momentum, momentum spread, transverse emittance, and pulse length. From such measurements we are able to determine the beam brightness. The diagnostic system is incorporated into the low-energy injection beamline, which combines the additional functions of momentum selection, pulse compression, and transport to the linac.

Armed with these capabilities we have made detailed measurements of the low-energy electron beam under a variety of conditions. These results are compared with our theoretical understanding of beam production and transport, including models of the ATF gun and beamline, in an attempt to verify that the beamline has performed at the level expected as well as to validate the computational models used to design and understand the gun and beamline. A primary goal is to understand the intrinsic physical limits to the brightness achievable using the rf-gun technique and assess how closely we have come to attaining it. We also verify that we can produce the beam quality required for the ATF experimental program and control it with the desired flexibility.

A tangential but important part of this effort has been the study of the background processes to photoemission, such as field emission. In addition, we have observed for the first time a new mode of rf-gun excitation, characterized by charge output two orders of magnitude higher than nominal photoemission and spread over many rf-cycle microbunches. This represents a limit to the laser intensity with which we may drive the gun in normal photoemission mode. The relationship of several other laser parameters to the resulting photoelectron-beam characteristics were studied, and the requirements placed on the laser by the desired electron-beam quality noted.

The high-energy beamline and CO_2 laser are still under construction. When they are completed the task of achieving a synchronized collision between the electron and laser beams, each of few-picosecond duration and focused to spot sizes of 1-10 μm will remain. We have constructed an x-ray-backscattering diagnostic that will provide an easily interpretable signal proportional to the degree of overlap between the two beams. This may be used to achieve the initial electron-CO_2-laser interactions and verify that the necessary temporal and spatial stability of the component systems has been attained before initiating experiments.

Finally, we have proposed an experiment that utilizes the unique capabilities of the ATF to probe strong-field quantum electrodynamics through one of the simplest such processes: nonlinear Compton scattering. This experiment will utilize the x-ray diagnostic apparatus augmented by an x-ray spectrometer, presently in the design stage.

An overview of the Accelerator Test Facility emphasizing the design of the rf gun and low-energy transport is presented in Chapter 2. Chapter 3 provides an introduction to the characterization of particle beams, including precise definitions of emittance and brightness and a discussion of the conditions under which such quantities are conserved by beam transport. In Chapter 4 we consider the physics underlying electron emission from a photocathode and the intrinsic limits to the achievable beam brightness. The mechanisms that can decrease beam brightness during acceleration in the gun and transport through the beamline are the subject of Chapter 5. Chapter 6 is a brief introduction to beam-transport theory and the methods by which the phase-space properties of a beam are measured. The ATF beam-profile-monitor system is described in Chapter 7.

Chapter 8 is a summary of the beamline-commissioning experience, including data collected that are not directly related to the photoelectron beam, followed by a presentation of the photoelectron-beam data in Chapter 9. Chapter 10 describes some of the studies that would be a natural extension of the work we have done thus far, including a description of the x-ray-backscattering diagnostic. The ATF experimental program is outlined as well. The nonlinear Compton-scattering experiment is described in Chapter 11. A summary of the work presented here and the conclusions drawn from it are given in Chapter 12.

Chapter 2

The Accelerator Test Facility

2.1 Purpose

The Brookhaven Accelerator Test Facility was proposed in 1985 by Robert Palmer for the exploration of novel laser-based particle-acceleration techniques. This requires an electron beam of very low emittance and a laser with high peak power to produce the accelerating fields. The ATF was conceived as a dedicated accelerator facility for achieving the needed beam quality and synchronization with a short laser pulse.

This evolved into the concept of a user facility for experiments that require a high-brightness electron beam and/or a high-peak-power laser. The general theme is to probe the interaction of electrons with strong electromagnetic fields, particularly the coherent transfer of energy from the laser beam to the electron beam or *vice versa*. Some of the experiments planned for the ATF are described briefly in Sec. 10.3.

2.2 Structure

The Accelerator Test Facility consists of a 50-MeV electron beam and a synchronizable 100-GW-peak-power CO_2 laser system. The electron source is a photocathode radio-frequency (rf) gun. A 2-GW-peak-power Nd:YAG laser drives the electron gun and switches the CO_2 laser, providing synchronization between the two systems. A master oscillator common to the laser and rf systems provides system timing. A block diagram of the ATF is shown in Fig. 2.1; the design parameters are listed in Table 2.1.

The Nd:YAG laser strikes the rf-gun photocathode and ejects an electron pulse, which is accelerated to an initial energy of up to 4.5 MeV. The bunch is transported to two SLAC-type linear-accelerator sections after momentum selection in the low-energy injection line. The beam is accelerated to an energy of 50 MeV and transported to the experimental area, where it can be brought into synchronized interaction with the CO_2 laser.

The electron-beam parameters shown in Table 2.1 are those of the "high-current" mode, in which all data reported here were collected. A low-current mode will be available in which the number of electrons per bunch will be reduced by a factor of around 10^{-4} by reducing the laser spot size and energy. This will lower the emittance by a factor of about 10^{-3}. This mode will be used for experiments that require an electron beam with extremely low emittance but that do not need as many electrons.

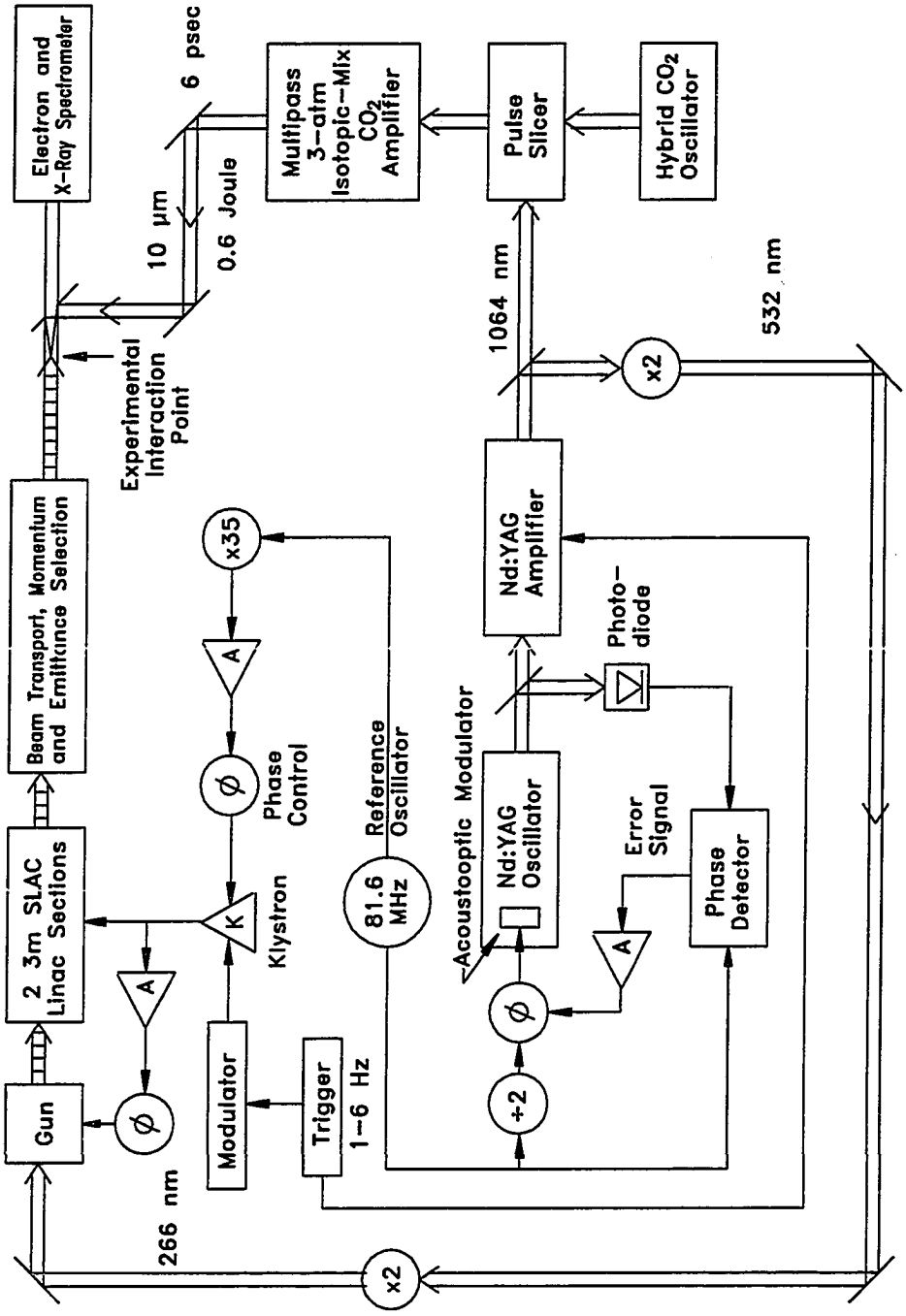

Figure 2.1: Block diagram of the Brookhaven Accelerator Test Facility

Table 2.1: Design parameters of the Accelerator Test Facility

Electron-beam parameters	
Momentum	50 MeV/c
Momentum spread $\Delta p/p$	0.1%
Electrons per bunch	10^{10}
Bunch length (FWHM)	6 psec
Normalized emittance ϵ_N	5 mm-mrad
Normalized brightness B_N	5×10^{10} A/m^2
Repetition rate	1-6 Hz
CO_2-laser-beam parameters	
Wavelength	10.4 μm
Pulse energy	0.6 J
Pulse length (FWHM)	6 psec
Peak power	100 GW
Nd:YAG-laser-beam parameters	
Wavelength	1.04 μm
Pulse energy	10 mJ
Peak power	2 GW
After frequency quadrupling:	
Wavelength	266 nm
Pulse length (FWHM)	6 psec
Pulse energy	100 μJ
Timing jitter	$<$ 3 psec

Each major component of the ATF will be described in more detail in the following sections, with the main emphasis on the rf gun and low-energy injection beamline. The other components utilized during commissioning are the Nd:YAG laser, the synchronization between rf and YAG-laser systems, and the control system. The high-energy transport and CO_2 laser, presently under construction, will be briefly described as well.

2.3 The rf Gun

The idea of the photocathode rf gun originated at Los Alamos [1]. A photocathode is incorporated into the end wall of a standing-wave rf cavity capable of supporting large accelerating electric fields. A laser with photon energy exceeding the work function of the photocathode material is used to eject electrons, which are accelerated to relativistic velocities in the gun cavity. This design offers several advantages over traditional dc sources with thermionic cathodes:

- Larger instantaneous electric fields can be sustained without breakdown at radio frequencies than is possible with static fields. Rapid acceleration of the beam reduces the effects of space charge, which are most severe the beam is nonrelativistic.
- The electron bunch is synchronized to the laser pulse to within a picosecond.
- The electron-bunch length is determined by the laser-pulse length, which may be as short as a few picoseconds. This allows the direct production of high peak currents, eliminating the need for a bunching mechanism. It also allows the electron bunch to have a rather narrow energy spread.
- The effective emitter area is determined by the spatial profile of the laser on the cathode. The transverse emittance of the electron beam can thus be made quite small by reducing the laser-spot size. The beam profiles need not be round.
- An intrinsically bright beam may be produced, limited only by the characteristics of the cathode and laser and by the dynamics of the electron pulse in the gun cavity.

The concepts of emittance and brightness, which express the quality of a beam, are defined in Chapter 3.

A cross section through the ATF rf gun is shown in Fig. 2.2, and the design parameters are summarized in Table 2.2. The gun is constructed primarily of copper and consists of two cells that support standing waves at 2856 MHz, the so-called "S-band" radio frequency. Radio-frequency power is coupled into the two cells from a rectangular waveguide via slots in the cell walls. The first cell is of only half length so that the longitudinal electric field is at a maximum at the half-cell wall, where the photocathode is located.

The photocathode is the polished surface of a copper plug, designed to be removable so that the photocathode can be periodically inspected and replaced. The cathode used for commissioning had a 1-mm-diameter hole in the center that was used for Nd:YAG-laser alignment.

The primary goals of the ATF gun design [2, 3] are as follows:

1. Maximize the accelerating electric field at the cathode in order to minimize the effects of space charge.
2. Maximize the charge ejected by a given laser-pulse energy.
3. Minimize the emittance increase in the gun cells due to time-dependent and nonlinear rf forces.
4. Make the design robust enough to run many hours under excitation by high rf fields and intense laser pulses.

The Los Alamos rf-gun design was based on similar constraints, but had a cavity shape based on static electric fields even though it was operated at 1300 MHz.

The major improvements introduced in the ATF design are optimization of the cavity shape for radio-frequency fields, operation at a higher frequency to achieve more rapid

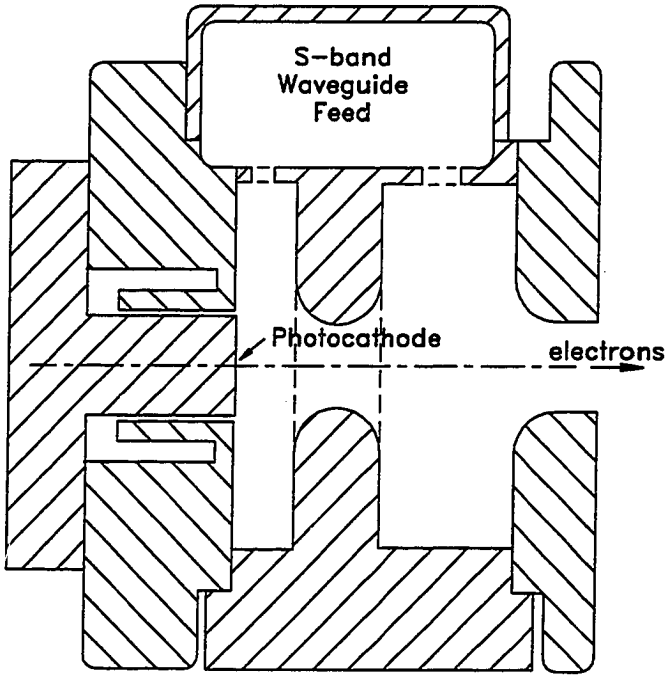

Figure 2.2: Cross section of the ATF rf gun. The gun is axially symmetric except for the waveguide feed. The cavity consists of $1\frac{1}{2}$ cells of a standing-wave rf resonator. The Nd:YAG laser enters through the end aperture and strikes the photocathode, ejecting an electron bunch that is accelerated to an energy of up to 4.5 MeV.

acceleration and higher output energy, and a more robust design appropriate for the rigorous requirements of a user facility. Below we will see how these considerations affect the gun design. We will defer calculations of the space-charge- and rf-induced emittance increase until Chapter 5.

Goal number one, maximization of the accelerating field, mandates the use of high-frequency rf fields, which can produce high peak electric fields in the gun cavity. As discussed in Sec. 5.1, almost all of the space-charge effects occur while the electrons are still nonrelativistic, within the first half-cell of the gun cavity. The more rapidly they are accelerated, the less time for electrostatic repulsion to act on the bunch.

The most common approach to rf-cavity design is to maximize the effective shunt impedance, a measure of the power required to sustain accelerating fields of a given strength (see Sec. 9.2). In such a design the maximum longitudinal field on the gun axis can be as much as a factor of six lower than the peak surface field. Here we are interested in achieving the largest possible longitudinal field without rf breakdown and would thus like the ratio of surface to longitudinal field to be small. From Table 2.2 we see that this is the case in the ATF design, which has a ratio of less than 1.2. Fortunately, this is an

Table 2.2: Design parameters of the ATF rf gun

Cell diameter	8.31 cm
Cell length	5.23 cm
Number of cells	1+1/2
Aperture diameter	2.0 cm
Radio frequency (wavelength)	2856 MHz (10.4 cm)
Effective shunt impedance Z_S	57 MΩ/m
Cavity Q	11,700
Cavity peak power	5.3 MW
Peak surface electric field	118 MV/m
Peak longitudinal field on cathode	100 MV/m
Peak output momentum	4.5 MeV/c

automatic consequence of another design consideration, discussed shortly.

An additional benefit derived from operating at high frequency is that the rf structures, which have dimensions on the order of the rf wavelength, are smaller and less expensive to manufacture. One drawback, however, is that the mechanical tolerances become more exacting with decreasing wavelength.

Goal number two, maximum charge output, is achieved by using a photocathode material with a large quantum efficiency at the driver-laser wavelength. Semiconductors, some of which have quantum efficiencies approaching 10%, are obvious candidates. For example, the Los Alamos rf gun employs Cs_3Sb. The problem with such materials is that they must be prepared, transferred to the gun cavity, and maintained under very good vacuum conditions to prevent contamination. Even so, they require frequent replacement.

Metals have quantum efficiencies three or four orders of magnitude lower but do not require extensive vacuum preparation. They are also robust to the intense rf fields in the gun and can sustain repeated rf breakdown without lowering the quantum yield, though other ill effects may be sustained. In order to make the rf gun easy to manufacture and maintain for long running periods (goal number four), copper was chosen as the best photocathode material. The metal yttrium, for example, has a quantum efficiency about ten times higher, but a copper cathode has the additional convenience of being the material from which the gun cavity is made. As such, the half-cell wall can simply be polished to give a good cathode surface. Another metal would require some method of being deposited or attached to a copper surface without introducing surface defects that would promote rf breakdown.

The primary factor dictating the shape and resonant mode of the gun cavity is goal number three, the minimization of beam deterioration by the rf fields in the gun. As will be discussed in Sec. 5.3, forces acting on the electron bunch that are nonlinear functions of the transverse coordinates lead to apparent transverse emittance growth (and hence a

decrease in brightness). An ideal cavity geometry would support standing-wave rf fields that exhibit at most a linear dependence on the radial distance from the cavity axis.

2.3.1 rf Fields in the Gun Cavity

A solution of Maxwell's equations for a cylindrically symmetric cavity supporting fields with the properties stated above is

$$\begin{aligned} E_z &= E_0 \cos kz \sin(\omega t + \phi_0) \\ E_r &= \frac{kr}{2} E_0 \sin kz \sin(\omega t + \phi_0) \\ B_\theta &= \frac{kr}{2} E_0 \cos kz \cos(\omega t + \phi_0). \end{aligned} \tag{2.1}$$

E_0 is the peak longitudinal field, the z (longitudinal) axis is coincident with the gun axis of symmetry with the origin at the center of the cathode, ω is the rf angular frequency, $k = 2\pi/\lambda$, where λ is the rf wavelength, and ϕ_0 is the rf phase at $t = 0$, defined so the longitudinal field is a maximum at $\phi_0 = 90°$.

Note that the longitudinal electric-field component may be considered as the superposition of two travelling waves, one of which is

$$\frac{E_0}{2} \sin(kz - \omega t - \phi_0).$$

This wave provides continuous energy transfer to a relativistic particle moving along the the $+z$ axis, so that any number of such cavities may be placed in series at the appropriate interval and still provide acceleration. This is the basis for rf linear accelerators, such as the ATF 50-MeV linac, patterned on the cavities composing the Stanford Linear Accelerator [4].

To support fields given by Eqs. 2.1 requires a unit cell equal in length to half the rf wavelength, so that the fields in each cell are at a phase advance of 180° (π radians) from those in the previous cell. This is the so-called "π-mode" of a multi-cavity structure. Such a cavity has a low ratio of peak surface to longitudinal electric field. Another resonant mode of the gun is the "0-mode," in which adjacent cells are at the same phase. It has a frequency in the ATF gun different from that of the π-mode by only 2 MHz [3], so care must be taken not to excite this unwanted mode. In the rf-power coupling shown in Fig. 2.2, the waveguide is operated in the TE_{01} mode, which is well-matched to the counter-circulating magnetic fields of the π-mode, but not to the 0-mode, for which the magnetic-field lines are in the same direction in each cell.

The shape of the unit cell that supports the fields given by Eqs. 2.1 is found from the boundary condition that the conducting inner surface of the cell be everywhere perpendicular to the electric field. If an aperture of radius a separates the cells, then the cell wall is described by

$$r^2 = a^2 - \frac{4}{k^2} \ln(\sin kz),$$

for which $r \to \infty$ as $z \to 0$. As no finite cavity can fulfill this condition, the "iris-loaded" design of the ATF gun (Fig. 2.2) was chosen as a reasonable approximation to

the ideal. An analysis of the gun cavity [2] using the rf-cavity-modelling code SUPERFISH indicates that all higher harmonics, which introduce nonlinear field components that lead to emittance growth, have Fourier coefficients less than 15% that of the fundamental, given by Eqs. 2.1.

Another effect that can lead to emittance growth is the time-dependent nature of the rf fields, an unavoidable consequence of the high radio frequency. The E_r and B_θ components of the rf field both contribute to the radial component of the Lorentz force, which at a fixed location in z depends on the rf phase $\phi = \omega t + \phi_0$. Due to the finite longitudinal length of the electron bunch, it requires a finite interval in time to cross a fixed location in z. Each section along the bunch receives a time-dependent radial kick as it traverses the gun. This results in a distortion of the transverse phase space occupied by the entire bunch.

An additional benefit of the π-mode design is that the fields described by Eqs. 2.1 automatically minimize the time-dependent rf forces. Assume that an electron is launched from the photocathode (located at $z = 0$) at $t = 0$ with an initial phase $\phi_0 = 90°$ and is immediately accelerated to a relativistic energy. At this phase the accelerating field is maximized, as we desire. (The situation for electrons initially at rest is only slightly different, as we will see below.) Notice that the longitudinal electric field E_z experienced by the electron is always the same sign; it is always accelerated in the cavity.

The E_r and B_θ components, on the other hand, are antisymmetric with respect to the boundary between cells. Hence the radial forces experienced by a relativistic electron launched at $\phi_0 = 90°$ in traversing the first half-cell are exactly cancelled as it traverses the first half of the next cell. This cell-by-cell cancellation of the time-dependent rf forces is a well-known advantage of the π-mode. The cancellation is less than exact for pulses of finite duration due to portions of the pulse that were launched at phases other than 90°.

There is no compensation, however, for the last half-cell of the gun. This is where almost all of the time-dependent-rf emittance growth occurs. A calculation of this effect is given in Sec. 5.2.

2.3.2 Longitudinal Momentum Gain

In order to understand the output characteristics of the gun, it is instructive to start by calculating the longitudinal momentum gain imparted to an electron in traversing the length of the rf gun as a function of launch phase. The gun is operated with peak accelerating fields in the range of 50-100 MV/m. An electron is relativistic after travelling about a centimeter in such fields, so we anticipate that the momentum gain in the gun and the cavity-by-cavity cancellation of transverse rf forces should be essentially the same as that for an initially relativistic electron. This is illustrated in Fig. 2.3 for a field of $E_0 = 75$ MV/m.

Figure 2.3(a) shows the momentum gain of an initially relativistic electron as a function of launch phase. This is obtained by integrating the equation $dp/dt = eE_z$ over the length of the gun. For an electron moving at the speed of light this integral can be

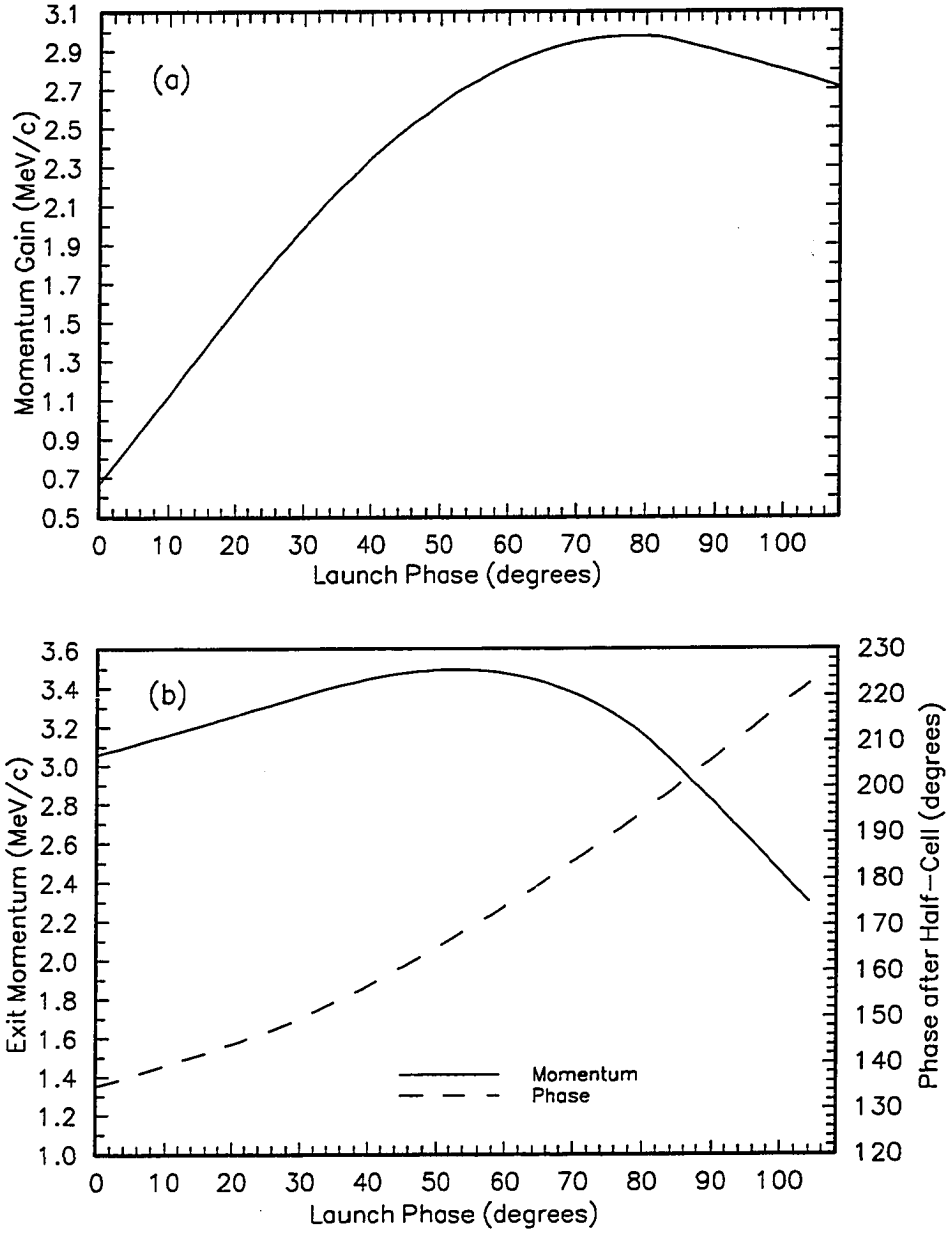

Figure 2.3: Properties of an electron in the rf gun as a function of launch phase at a peak accelerating field E_0 of 75 MV/m. Part (a) shows the momentum gain of an electron that is already relativistic at launch. In part (b) the electron is initially at rest. The solid line shows the momentum at the gun output; the dashed line shows the rf phase as the electron crosses the boundary between gun cells.

evaluated analytically and yields

$$\Delta p = \frac{eE_0\lambda}{4\pi c}\left(\cos\phi_0 + \frac{3\pi}{2}\sin\phi_0\right).$$

It is interesting to note that, as shown in the graph, the maximum momentum gain of 3.0 MeV/c is obtained by launching at $\phi_0 = 78°$ rather than $\phi_0 = 90°$, which maximizes the initial electric field.

At the optimum launch phase for momentum gain the average electric field experienced by the electron over the length of the gun is $0.511 \cdot E_0$. The total gun length is $3\lambda/4 = 0.078$ m, so the maximum obtainable momentum gain is

$$\Delta p_{\max} = (0.040\,\mathrm{m}) \cdot \frac{eE_0}{c}. \tag{2.2}$$

The assumption that the electron is immediately relativistic upon leaving the cathode means that it remains in phase with the accelerating rf wave. We consider now that the electron is actually nonrelativistic initially, emerging from the cathode with only a few eV of kinetic energy.

The momentum at the gun output of an initially nonrelativistic electron is shown in Fig. 2.3(b). The momentum gain was calculated by numerically integrating the equation of motion from the initial condition $v = 0$. The rf phase at which the electron crosses the boundary between cells is also plotted. Notice that the maximum energy gain (as opposed to momentum gain) is very nearly equal to that of the relativistic case. This confirms our intuition that the electron is accelerated rapidly to relativistic velocities. Note, however, that the launch phase at which the maximum momentum is obtained, around 54° is lower by some 24°. This is the phase lag that occurs while the electron "catches up" to the accelerating field. Hence the electron must be launched ahead of the maximum field.

More important than obtaining the maximum possible output momentum is the requirement that the electron cross the first half-cell boundary at an rf phase of 180° (corresponding to launching an initially relativistic electron at $\phi_0 = 90°$) in order to achieve the cell-by-cell cancellation of the transverse rf forces, as discussed above. From Fig. 2.3(b) we see that this occurs for a launch phase of around 67°. As the momentum gain at this phase is only slightly lower than the maximum, this is the optimal phase at which the laser should strike the photocathode for the assumed accelerating field of 75 MV/m.

The momentum spread $\Delta p/p$ of the beam is due to the extent of the beam in time, corresponding to an extent in launch phase. From Fig. 2.3(b) we would estimate, for example, that a laser pulse with an rms length of 6 psec would produce an rms output momentum spread of 1.8% at a central launch phase of 67°, with higher-momentum particles occupying the earlier portion of the beam pulse. This spread can be reduced to a minimum of around 0.3% by operating at 54°, the phase corresponding to the peak momentum.

2.3.3 Transverse Momentum Kick

We now calculate the radial component of the Lorentz force $\boldsymbol{F} = e(\boldsymbol{E} + \boldsymbol{v} \times \boldsymbol{B}/c)$, assuming that the electrons are relativistic in the last half cell. As they reach an energy of up to 4.5 MeV by the gun exit, this is a valid assumption. The sign convention is chosen so that the product eE_0 is positive and hence gives acceleration along the positive z axis at an initial phase of $\phi_0 = 90°$. The electron velocity $\boldsymbol{v}$ is taken to be in the positive z direction and equal in magnitude to c. The radial force component is then

$$\begin{aligned} F_r &= e(E_r - B_\theta) \\ &= \frac{kr}{2} eE_0[\sin kz \sin(\omega t + \phi_0) - \cos kz \cos(\omega t + \phi_0)] \\ &= -\frac{kr}{2} eE_0 \cos(2kz + \phi_0), \end{aligned}$$

since for relativistic velocities, $kz = \omega t$.

We now integrate the equation of motion $dp_r/dt = F_r$ over the last half-cell. To simplify the calculation we assume that r remains constant. The last half-cell of the gun occupies the region $\lambda/2 < z < 3\lambda/4$. Converting from a time integral to a spatial integral via $dt = dz/c$, we find

$$p_r = \frac{1}{c} \int_{\lambda/2}^{3\lambda/4} F_r \, dz = \frac{eE_0 r}{2c} \sin \phi_0.$$

From this we note three things. First, it is phase dependent, as anticipated. This is the cause of the apparent emittance increase. Furthermore, at the launch phase[1] that minimizes emittance growth, namely $\phi_0 = 90°$, the radial kick is at a maximum. Second, between 0 and 180° the radial-momentum kick is positive, or defocusing. Third, it depends linearly on r, which is not surprising since the fields producing the kick are linear in r.

Emittance growth aside, this radial kick acts as a defocusing lens at the gun output. For this reason we must place focusing optics as close to the gun as possible to control the diverging beam. We can calculate this effect for the ATF gun. What we are interested in is the angular divergence as a function of radius (in optical terms this is the inverse of the effective focal length). The angular kick r' is given to good approximation by $r' = p_r/p_z$.

At a peak accelerating field of $E_0 = 100$ MV/m the output momentum of the gun is $p_z = 4.5$ MeV/c. We thus find for a launch phase of 90°

$$\frac{r'}{r} = 11 \frac{\text{mrad}}{\text{mm}},$$

which is equivalent to a defocusing lens of focal length 90 mm. A detailed simulation of the gun output characteristics [2] yielded a result of $r'/r = 7$ mrad/mm. The above calculation based on a fixed radial position overestimates the effect. We see that the beam will emerge from the gun with a large divergence and a transverse phase space that is highly correlated, or elongated.

[1]Since we have assumed relativistic motion in our analysis, the phase ϕ_0 must again be taken to be the equivalent launch phase of an initially relativistic electron.

2.4 Electron Beamline

The beamline serves the primary functions of accelerating the beam produced in the rf gun to 50 MeV and transporting it to the experimental stations. It is divided into two sections: the low-energy injection line from the rf gun to the linac entrance, and the linac and high-energy transport to the experimental hall. Each section is described below, along with some of the additional functions provided.

2.4.1 Low-Energy Injection System

This section of beamline transports the low-energy electron beam issuing from the rf gun to the linear accelerator. Several other crucial roles are played by this section, which will be highlighted below. The low-energy transport is shown in Fig. 2.4.

Beam matching from the gun exit: The beam emerges from the rf gun with a large angular divergence, as was seen in Sec. 2.3.3. It must be focused immediately upon exiting the gun into a form more readily transported over several meters. This function is provided by the quadruple triplet Q1/Q2/Q3. A quadrupole magnet acts as a lens that is focusing in one transverse axis and defocusing in the other (see Sec. 6.1). The focal length is altered by varying the electric current through the magnet coils. A series of three such magnets of alternating focusing properties may be configured to provide net focusing in both axes. This first triplet grabs the diverging beam exiting the gun and focuses it so that it is converging at the triplet exit. The exact location of the focus is varied to suit the needs of a given beamline tune.

Momentum selection and recombination: Dipole D1 steers the beam by 90° and introduces a horizontal momentum dispersion similar to the effect of a prism on a light beam. The dipole is set to a strength that deflects electrons of a chosen momentum, the beam "central momentum," by 90°, while electrons with higher momentum are bent slightly less than 90° and those with lower momentum bent more. Quadrupole Q4 is horizontally focusing and is used to cancel the angular dispersion introduced by D1, resulting in a parallel beam. Downstream of Q4 is a variable-width horizontal aperture, called the momentum slit, centered on the beam optic axis. Since the beam has a horizontal position dispersion correlated with the momentum spread, the momentum bite of the beam allowed to pass through the slit is determined by the slit opening.

The transmitted beam still has horizontal momentum dispersion, however. This is removed by operating quadrupole Q5 (which is also horizontally focusing) and and dipole D2 in exact symmetry to Q4 and D1. As Q4 cancels the angular dispersion introduced by D1, operating Q5 at the same strength introduces an angular dispersion of the same magnitude and opposite sign as existed at the entrance of Q4. D2 introduces an identical angular dispersion to that of D1, so the net effect of Q5 and D2 is to reverse the effect of D1 and Q4. The beam is thus achromatic after passing through D2. This is referred to as "momentum selection/recombination." It provides momentum-selection capability between the dipoles, and an achromatic beam at the entrance to the linac.

Beam matching into the linac: After deflection by D2, a final quadrupole triplet, Q6/Q7/Q8, focuses the beam into the linac, where it is accelerated to 50 MeV. From there the beam enters the high-energy beamline, described in Sec. 2.4.2.

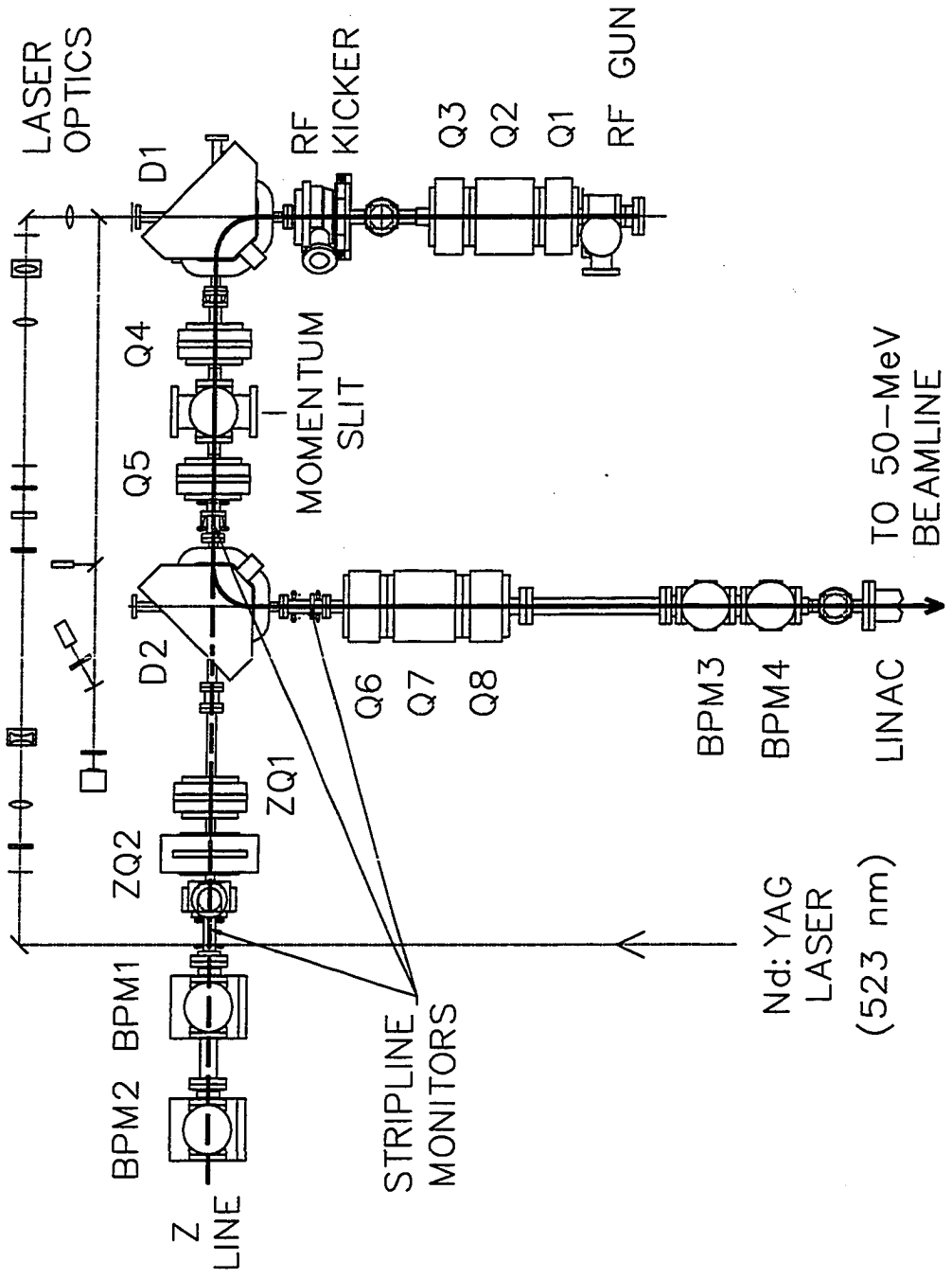

Figure 2.4: The ATF low-energy injection system. The path of the electron beam through the double bend is shown by the thick solid line; the path in the 'Z'-line is shown as a thick dashed line. The labelling scheme is: Q = quadrupole magnet, D = dipole magnet, BPM = beam-profile monitor. Also shown is the optical path of the Nd:YAG laser.

Optic-Axis Correction: One type of beamline element not shown in Fig. 2.4 is the "trim coil," a deflection magnet used to make small adjustments to the optic-axis direction. This is a Helmholtz-coil pair that can steer the beam by less than a degree. Trim coils are placed at several locations in the low- and high-energy beamlines to correct for such effects as small quadrupole displacements and stray magnetic fields from ion pumps and the earth.

Diagnostics: As a primary goal of the ATF is the production of high-brightness (low-emittance) electron beams, it is critical to have available the necessary diagnostics to measure these and other beam properties. The needed measurements include beam charge, momentum spread, and the profile and position of the beam in the spatial (transverse) and temporal (longitudinal) domains. From these we may derive quantities such as peak current, emittance, and brightness.

Spatial profiles are provided by the beam-profile-monitor (BPM) system, the subject of Chapter 7. The beam-profile monitors, the locations of which are shown in Fig. 2.4, consist of phosphor screens that intercept the beam and are viewed by video cameras. The momentum slit is also coated with phosphor and can be viewed by a camera, and so served as an additional profile monitor, though one with lower resolution. It is used to diagnose the beam's momentum properties since the momentum dispersion is maximum at the slit, and it is here that momentum selection occurs.

The momentum slit also serves as the charge-measurement device. The slit is thick enough to completely stop 5-MeV electrons, so that when closed to zero aperture it acts as a beam stop. The slit jaws are electrically isolated from their surroundings, so the slit serves as a "Faraday cup." A coaxial cable connects the slit to an oscilloscope,[2] on which the collected charge is measured.

Field emission from the rf-gun photocathode, or "dark current," occurs over the entire 3-μsec rf pulse, a time scale long enough to be resolved by the 400-MHz bandwidth of the oscilloscope. The photoelectron pulse lasts only a few picoseconds, but temporal resolution is limited to the characteristic time constant of the Faraday cup and coaxial cable, about 15 nsec. In each case, however, the total charge is obtained from the time-integrated current. Also, since the detected photocurrent pulse is about 100 times shorter than the dark current pulse, the photoelectron signal can be clearly distinguished above the dark current even when two orders of magnitude smaller in total charge. This is a useful signal for adjusting the beam optics and rf timing to optimize photocurrent when it is not visible on a profile monitor.

In addition to the "double-bend" beamline leading to the linac, there is another beamline reserved exclusively for measurements on and experiments with the low-energy beam. When dipole D2 is turned off, the beam passes into the 'Z' line, so named because of the possibility of measuring the longitudinal, or (z, p_z), phase space there. This beamline contains two profile monitors, preceeded by two quadrupole magnets. The presence of horizontal momentum dispersion renders the horizontal emittance a quantity of dubious interpretation; only the vertical emittance is measured in the 'Z' line.

As discussed in Sec. 6.2, emittance measurements can be made either by varying the

[2]Typically the Model 54502A 400-MHz digitizing oscilloscope from Hewlett-Packard, Santa Clara, CA; or the Model 2440 250-MHz digitizing oscilloscope from Tektronix, Inc., Beaverton, OR.

focus of the beam with a quadrupole and examining the changing profile on a single profile monitor or by focusing the beam onto one monitor and measuring the profile on it and one other monitor. As shown in Fig. 2.4, a pair of profile monitors was placed in the 'Z' line and just upstream of the linac, so that either measurement technique was available in both locations.

The temporal pulse length is measured with an rf-deflection cavity, just upstream of dipole D1. This device transforms the temporal profile of the beam into a vertical profile, which can measured on a profile monitor, as will be detailed in Sec. 6.4. With the addition of a vertical collimator in the 'Z' line and considerable care in beamline tuning, the possibility exists to measure simultaneously the momentum spread and the temporal profile in the 'Z' line, effectively mapping the longitudinal phase space. This would represent a rather unique capability among existing beamline facilities.

Also shown in the low- and high-energy beamlines are "stripline monitors" [5]. These are pairs of capacitive-pickup electrodes placed inside the beampipe on opposite sides of of the beam axis. The sum of the signal from the two electrodes is proportional to the total beam charge, while the difference signal is proportional to the beam position relative to the point midway between the electrodes, positioned so as to be coincident with the beamline. Since the beam is not intercepted by these monitors, they are nondestructive and hence can provide beam intensity and position data at the same time beam is delivered to experiments downstream. These were still in the development and construction phase during the commissioning studies presented here.

Pulse compression: The double bend was designed to perform magnetic pulse compression on the beam produced by the rf gun. As noted in Sec. 2.3.2, the gun is operated at an rf phase at which the electrons with higher momentum are located in the earlier portion of the pulse. Higher-momentum electrons follow a longer path length in the double bend than lower-momentum electrons, causing the former to be delayed with the respect to the latter. The net effect is a reduction of the bunch length. Beamline and rf-gun simulations indicate that a bunch-compression factor of 3-5 should be obtainable in the ATF beamline [6].

Nd:YAG-laser transport: Some of the Nd:YAG-laser optics are shown in Fig. 2.4. The YAG-laser beam is transported from the experimental hall into a laser "hutch" containing the optics shown in the figure. It enters the electron beamline through an optical vacuum window in a beampipe 'T' located in dipole D1, and from there passes to the photocathode in the rf gun. A small part of the laser beam is deflected 90° before entering the beamline and impinges on a video camera located at the same optical path length as the photocathode in the undeflected beam. The camera has no lens and so presents a profile of the laser beam on the photocathode with unity magnification. Part of this deflected beam is split off and transported to an energy meter[3] for on-line monitoring. The same meter is occasionally used to measure the energy of the full beam directed to the photocathode as a calibration of the fraction of the beam energy recorded in the on-line configuration.

Low-energy electron-beam experimentation: Experiments can be performed

[3]Model J3-09 Pyroelectric Joulemeter Probe and Model JD2000 Joulemeter Ratiometer, Molectron Detector, Inc., Campbell, CA.

with the low-energy electron beam in the 'Z' line. For much of the commissioning period the downstream beam-profile monitor (BPM2) was replaced by the Smith-Purcell experiment (described briefly in Sec. 10.3). BPM1 is available to assist the experimenter in focusing the electron beam into the experimental chamber.

2.4.2 Linac and High-Energy Transport

From the double-bend beamline, the electron beam is injected into the linear accelerator consisting of two linac sections of the type used in the Stanford Linear Accelerator. Like the rf gun, these are S-band structures, which operate at 2856 MHz. These accelerate the beam to an energy of up to 50 MeV, after which it enters the "high-energy" transport line. The section between the linac exit and experimental-hall entrance is depicted in Fig. 2.5.

Several important functions are provided by the high-energy beamline. Note the large number of diagnostic devices (labelled PM, SM, and BS). These provide information about the beam profile, position, and charge. After the beam is deflected by the dipole, its momentum spread can be measured at a profile monitor and reduced at a momentum slit. The dipole can be turned off, allowing the beam to pass into a straight-ahead section containing additional diagnostics. The high-energy beamline also provides the capability of "emittance selection," in which collimators (C) are used to "clean up" the beam by removing tails in the radial distribution, hence reducing the transverse emittance in both x and y.

Fig. 2.6 shows the experimental hall, including the experimental beamlines and the optical tables housing the Nd:YAG and CO_2 lasers. Note the large amount of shielding required to block the x- and gamma-ray radiation and neutrons produced by the electron beam. The beam enters the experimental hall and is deflected into one of three experimental beamlines by the associated dipole magnet, which also serves to remove the chromaticity induced by the dipole upstream in the high-energy line. The final quadrupoles in each line focus the beam to the size required at the experimental station. Each beamline ends with an electron-momentum spectrometer and beam dump. The CO_2-laser beam is transported to experiments by an optical system not shown in Fig. 2.6.

2.5 Laser System

The ATF laser system consists of two major components: the Nd:YAG laser and the CO_2 laser. As shown in Fig. 2.1, the YAG laser is used to drive the rf gun and switch the short CO_2-laser pulses, while the CO_2 laser is the high-power source of electromagnetic radiation at 10 μm for experimental interaction with the electron beam. Below are listed some of the required properties of the laser system in the context of ATF design specifications.

- The Nd:YAG laser must be synchronizable with the rf system driving the electron gun and linac.

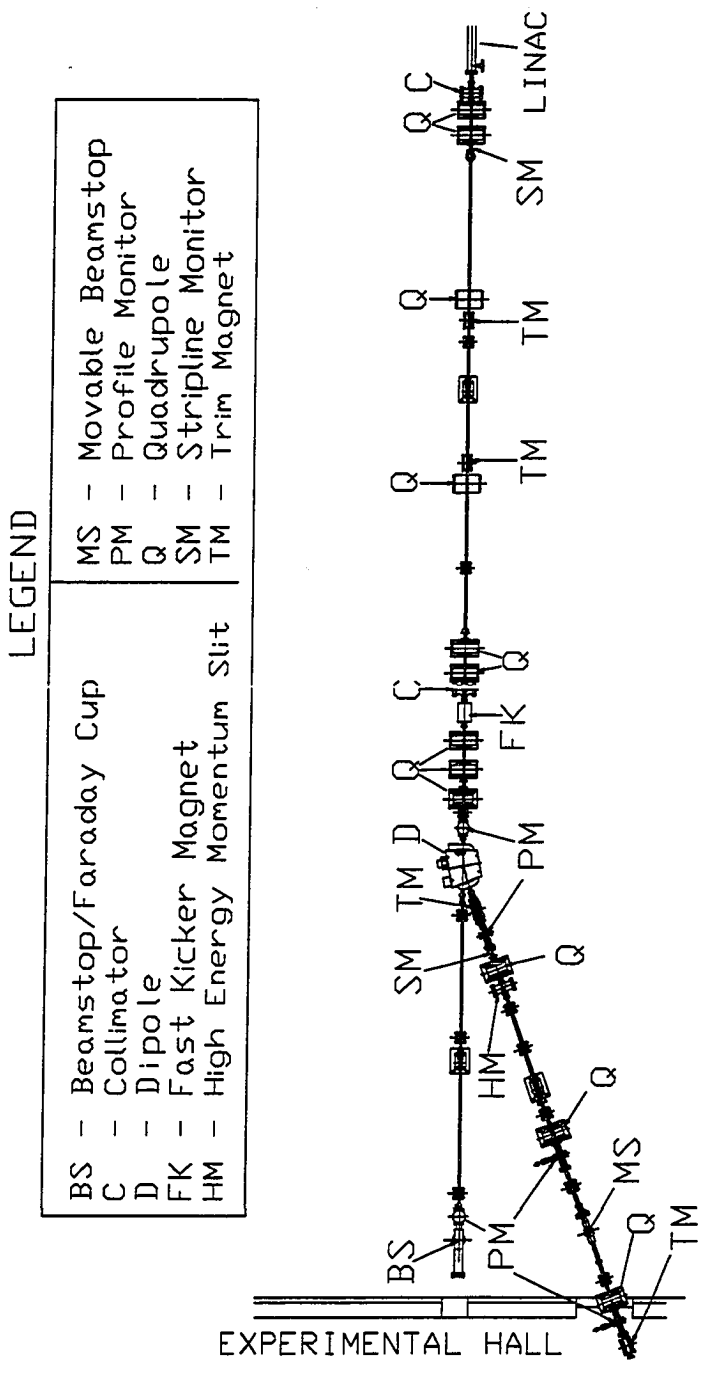

Figure 2.5: The ATF high-energy beamline. The beam exits the linac (at the top of the figure) with an energy of 50 MeV and is transported into the experimental hall.

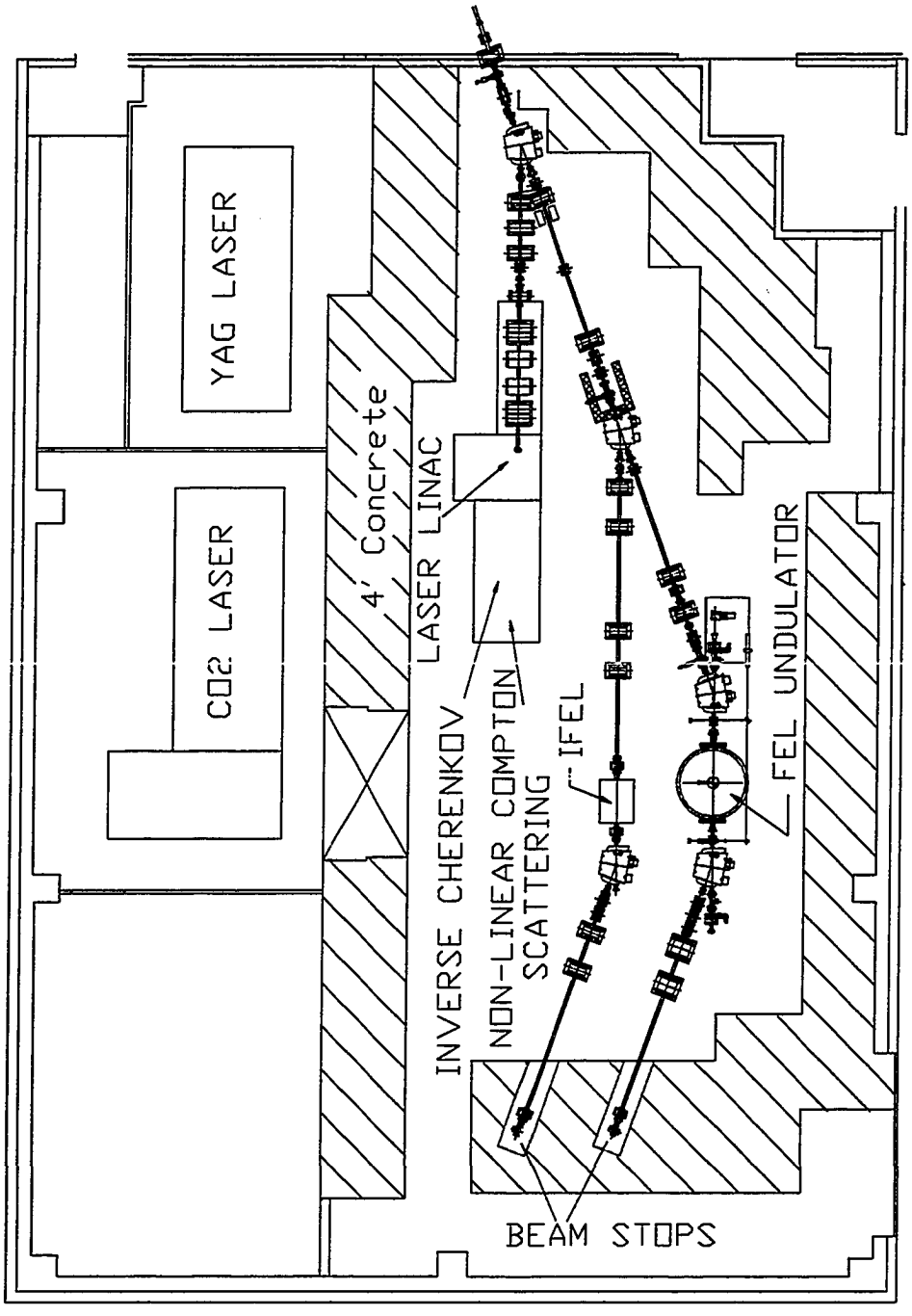

Figure 2.6: The ATF experimental hall. The beam enters at the top of the figure and is deflected into one of the three experimental beamlines. Also shown are the locations of the CO_2 and Nd:YAG lasers.

- The YAG-laser pulse must have sufficient energy, after being split and quadrupled in frequency, to eject the required number of electrons from the photocathode. Metal photocathodes have a quantum efficiency in the range of 10^{-5} to 10^{-4}. The photon energy of the quadrupled YAG laser is 4.65 eV. Hence a pulse of 10^{10} electrons requires a laser pulse of $10^{10} \cdot 4.65\ \text{eV}/10^{-5} \simeq 5\times10^{15}\text{eV} \simeq 100\ \mu\text{J}$. It should be possible to vary the pulse energy.
- The YAG-laser pulse must be quite stable in time and amplitude. Jitter in the time of arrival of the YAG-laser pulse at the gun translates into variation of the beam momentum. Amplitude jitter in the YAG oscillator will be magnified by the non-linearity of the frequency-doubling process and cause pulse-to-pulse fluctuations in the number of electrons.
- The pulse must be short enough to produce the required peak beam current and switch the CO_2-laser pulse sufficiently quickly.
- The optical system transporting the YAG-laser pulse to the rf gun should provide the capability of changing the laser-spot size on the photocathode.
- The CO_2 laser must give high enough peak power to yield the required field strengths in the focus region of an experiment.
- The CO_2 laser must preserve the timing stability of the output pulse with respect to the electron pulse.

2.5.1 Nd:YAG Laser

The Nd:YAG-laser system consists of an oscillator, an amplifier, and components to select and compress a single pulse for delivery to the rf gun. The continuous-wave (cw) Nd:YAG oscillator[4] produces a continuous beam with a wavelength in the infrared (ir) at 1064 nanometers. The output is mode locked to the master rf oscillator, a technique that employs an acousto-optic modulator as a rapid shutter to select a single longitudinal mode of the oscillator. It was the availability of radio-frequency acousto-optic modulators for Nd:YAG rods that drove the choice of a lasing medium. The result is a train of pulses 80 psec long separated by 12.25 nsec, the period of the master oscillator. (The oscillator frequency is actually stepped down by a factor of two before driving the mode locker to compensate for the fact that two output pulses are selected per oscillator period.) Each pulse has an energy of 10 nJ.

The laser pulses pass through a 200-meter-long optical fiber, the nonlinear properties of which introduce a time-dependent frequency spread or "chirp." A single pulse is selected for amplification via a Pockels cell,[5] an electro-optic device that can rapidly rotate the polarization of the laser pulse. The bandwidth of the Nd:YAG amplifier is narrower than the frequency spread introduced by the fiber. Since this is a time-correlated spread, only a limited part of the pulse length can be amplified. The pulse is simultaneously amplified to 10 mJ and compressed to a few picoseconds [7, 8].

[4]Model 3400, Spectra-Physics Lasers, Inc., Mountain View, CA.
[5]Model 6025 Electro-optic Shutter, Lasermetrics, Inc., Engelwood, NJ.

The output of the YAG amplifier is split, with part of the beam going to slice the short pulse from the output of the CO_2 oscillator. The short CO_2-laser pulse is then amplified and delivered to experiments. The rest of the YAG-laser beam is frequency doubled twice to a wavelength in the ultraviolet (uv) of 266 nm and delivered to the photocathode of the rf gun.

Frequency doubling, or second-harmonic generation, occurs first in a crystal[6] of deuterated KH_2PO_4 (KD*P), which converts the 1064-nm light to green light at 532 nm. It is this green light that is transported to the laser hutch near the low-energy beamline (Fig. 2.4). There the second frequency doubling occurs in a crystal[7] of β-BaB_2O_4 (BBO). The second-harmonic generation in these materials is due to a nonlinear response to the incident laser intensity. This does not occur with 100% efficiency and is proportional to the square of the incident intensity when not saturated. Hence each frequency doubling reduces the pulse length of a Gaussian profile by a factor of $\sqrt{2}$. The uv pulse has energy of around 100 μJ and is half as long as the initial ir pulse of 10 mJ.

2.5.2 CO_2 Laser

The CO_2 laser, like the Nd:YAG laser, consists of an oscillator, and amplifier, and system for producing few-psec pulses. The oscillator produces pulses of 10.4-μm radiation with an energy of around 50 mJ and a FWHM duration of 50 nsec. From this a 10-psec pulse is gated by a pair of semiconductor shutters that are controlled by the 1.06-μm YAG laser. The short CO_2-laser pulse of about 1 μJ energy enters the amplifier [9], a multipass gain cell that contains a mixture of CO_2 isotopes. The large bandwidth of this mixture allows the amplification of few-psec pulses [10]. The output pulse will initially have an energy of 100 mJ, for a peak power of around 10 GW. (The design specifications of 600 mJ and 100 GW could be achieved in a future upgrade.)

The fast semiconductor shutters are based on the principle of rapidly modulating the reflective and transmissive properties of the material by optically controlling the free-charge-carrier density [10, 11]. The shutters are made of intrinsic germanium. A picosecond laser pulse with photon energy above the bandgap of germanium (0.67 eV) creates a highly reflective plasma in the semiconductor, which is normally transparent to 10-micron radiation. The portion of the YAG-laser pulse that is not frequency doubled in the first crystal (about 60% of the 10-mJ YAG-amplifier output) is transported to the Ge shutters. A fluence of around 1 mJ/cm^2 is sufficient to "metallize" the semiconductor and switch it from a window to a reflector. This occurs on a subpicosecond time scale.

In the two-switch setup employed at the ATF, the CO_2 laser is polarized and is incident on a Ge plate at the Brewster angle and in the p-polarization state, so that the radiation is very nearly 100% transmitted. The first shutter, a reflection switch, defines the leading edge of the pulse. This reflected pulse is about 300 psec long, the time scale governing the loss of reflectivity being that of free-carrier diffusion. The second shutter, a transmission switch, defines the trailing edge of the transmitted pulse. The same YAG-laser pulse is used to operate both switches, with a few-psec time-of-flight

[6]Cleveland Crystal, Cleveland, OH.

[7]Quantum Technology, Inc., Lake Mary, FL.

delay introduced between. The resulting pulse has nearly the same peak power as the longer pulse from which it was sliced.

The CO_2 amplifier and pulse-slicing system are still under development at the time of writing. A series of experimental and semiempirical modelling studies [12] performed on the reflection switch showed that it performs in a manner consistent with theoretical expectation and with the requirements placed on the switching system by the ATF laser specifications.

2.6 Synchronization

The YAG laser determines the timing of both the electron and CO_2-laser beams. This has the advantage of making the location of the electron-CO_2-laser interaction point independent of small timing fluctuations in the YAG-laser beam for fixed path lengths. It is still necessary, however, to achieve picosecond synchronization between the YAG-laser pulse and the rf phase in order to produce electron pulses with stable momentum properties.

Both the rf system and the YAG laser derive their timing from a highly stable 81.6-MHz reference oscillator.[8] This oscillator is stepped up in frequency by a factor of 35 to provide the 2856 MHz (S-band) frequency for the rf system. The cw Nd:YAG oscillator is mode locked to the reference signal. Additional timing stability is obtained by phase locking via a feedback loop,[9] which synchronizes the YAG laser and the reference oscillator to about one picosecond [13]. This determines the timing of the mode-locked output with respect to the master oscillator (and rf frequency). Which pulse is amplified is determined by the few-Hertz system trigger, which operates the YAG-amplifier Pockels-cell switch and initiates the 3.5-μsec rf pulse. This system trigger is not referenced to the master oscillator as it need only be stable at the nanosecond level.

The system trigger was fanned out through a four-channel digital delay generator,[10] which provided variable delays stable to a few picoseconds. These units can be altered to improve the stability to about a picosecond. This is quite important as many triggers with different arrival times are required throughout the ATF in order to compensate for electron-beam or signal-travel times or the response time of system components.

2.7 Control System

Computer control of most ATF functions was based on a VAXStation-II/GPX.[11] A window-based user front-end program [14] provides control of magnet power supplies and stepper motors via an RS232 serial highway communicating with CAMAC modules.

Devices employing stepper motors include the beam-profile monitors, slits and collimators, and laser optics. Development and initial beamline operation of the profile-

[8] Built by Leonard DeSanto of the ATF technical staff.

[9] Series 1000 Timing Stabilizer, Lightwave Electronics, Mountain View, California.

[10] Model DG535, Stanford Research Systems, Inc., Sunnyvale, CA.

[11] Digital Equipment Corporation (DEC), Maynard, MA.

monitor motion-control system were based on an inexpensive system called the A-Bus,[12] which proved underdesigned for the rigorous environment of a multi-user beamline facility. Manual control of profile monitors was provided by a handheld stepper controller,[13] while manual control of other devices was based on a rack-mount device.[14] Motion control has since been upgraded.

Most ATF control functions are located in a control room adjacent to the high-energy beamline. In addition to the VAX control station, this room contains the beam-profile-monitor control system (see Chapter 7) and most system timing devices. The majority of rf control is located on a mezzanine located over the low-energy beamline.

[12]Alpha Products, Darien, CT.
[13]Model EPC-015 Stepping Motor Controller, Hurst MFG, Princeton, IN.
[14]Unidex 11 Motion Controller, Aerotech, Inc., Pittsburgh, PA.

Chapter 3

Characterization of Particle Beams

In this chapter some of the quantities used to characterize particle beams, primarily emittance and brightness, are defined and the conditions under which such quantities are useful are discussed. These parameters have a number of desirable properties: they are intrinsic beam qualities defined in a position-independent manner and applicable to any particle beam; they are measurable in the lab; and they are invariant under certain important conditions. They carry useful information about a beam such as how far it can be transported within a given transverse size, or how tightly it can be focused over how long a region and at what rate particles cross this region. (In fact as we will see, particle beam brightness is defined in analogy with the brightness or *luminance* of an optical beam.) These qualities are extremely important in determining a beam's usefulness in applications such as particle colliders and free-electron lasers. They allow beams at different facilities to be compared in a well-defined manner.

3.1 Emittance

The most general way to characterize a beam particle is by its position in the six-dimensional *phase space*, consisting of the three components each of the particle's position and canonical momentum, (x, p_x, y, p_y, z, p_z). A large collection of beam particles may be characterized by their density distribution in phase space. The invariant beam parameters are derived from the discovery of Liouville that the phase-space density of a system of noninteracting particles described by a Hamiltonian is constant in time. A charged-particle beam propagating through a beamline composed of magnetic elements is such a system, if the interaction among the beam particles is ignored.

The invariance of the phase-space density of a fixed number of particles implies that the volume occupied in phase space is constant. The concept of *emittance* is closely related to the phase space volume of a beam. There are a baffling number of variations in the definition of emittance. They do not all satisfy the same invariance criteria, so great care must be taken in using such quantities. A rather complete discussion of emittance and related quantities is given by LeJeune and Aubert [15], whose conventions we follow.

In practice the six-dimensional phase space is usually split into three two-dimensional subspaces, (x, p_x), (y, p_y), and (z, p_z), where z is taken to be the average direction, or *optic axis*, of the beam. This procedure is valid when the particle motion associated with each spatial coordinate is independent. The Hamiltonian then splits into the sum

of three terms, each containing only one coordinate pair, and the conservation of phase space is valid separately in each plane. The emittance is defined in terms of the area occupied by the beam in these two-dimensional spaces. In the discussion that follows we will confine ourselves to the (x, p_x) plane, but all statements are applicable to the (y, p_y) plane as well. These are the *transverse* phase spaces. The (z, p_z), or *longitudinal*, phase space is treated in a slightly different fashion.

If the area occupied by the beam in the (x, p_x) plane is Γ^x, then the *normalized* or *invariant emittance* is defined as

$$\epsilon_{N,x} \equiv \Gamma^x / \pi m_0 c,$$

where m_0 is the particle rest mass and c is the speed of light. In practice it is not the transverse momenta of beam particles that are usually measured, but rather the gradients of the trajectories in the x-z and y-z planes. Hence another frequently-used definition is obtained by replacing the variable p_x with $x' = dx/dz = p_x/p_z = p_x/(\gamma\beta_z m_0 c)$, where $\beta = v/c$ and $\gamma = 1/\sqrt{1-\beta^2}$. The space of (x, x') is called the *trace space*. If the area occupied by the beam in trace space is A^x, then the *geometric emittance* is defined as

$$\epsilon_x \equiv A^x / \pi.$$

It can be seen that for a beam in which all particles have the same longitudinal momentum, the two definitions are simply related by $\epsilon_{N,x} = \gamma\beta_z\epsilon_x$. The normalized and geometric emittance have units of distance-times-angle, such as m-rad or mm-mrad.

In fact, very often in characterizing a beam the slope x' is replaced by the angle θ_x. This is valid in the *paraxial*, or *Gaussian-optics*, approximation, for which $x' = \tan\theta_x \simeq \theta_x$. The paraxial-ray formalism is an analytical approach to beam optics that assumes that the particles travel near a central trajectory. The electric and magnetic fields of beamline elements can then be expanded as power series in the transverse coordinates. This approximation is usually valid and is extremely useful in simplifying the design of particle beamlines. In particular, often only linear terms are included, referred to as *first-order* optics. A brief introduction to first-order beam transport will be given in Chapter 6.

The longitudinal phase space is similarly redefined for convenience. Particle coordinates are referenced to the "central ray," which is the coordinate of a particle in the center of the particle bunch and with the central momentum of the beam. The $+z$ axis is always taken as the direction of the central ray's motion. The coordinate p_z is replaced by $\delta = \Delta p_z/p_z$, the fractional variation of a particle's momentum from the central momentum. The spatial coordinate, z, becomes $\ell = \Delta z$, the longitudinal distance between a particle and the central ray. Hence the central ray carries the information about the average beam trajectory, while the longitudinal trace space, (ℓ, δ), describes the extent of the beam around this central ray. The longitudinal emittance, ϵ_L is just $1/\pi$ times the area the beam occupies in this space, with normalized value also given by multiplying by $\gamma\beta_z$.

The emittance definitions given above, in referring to the trace-space area occupied by a beam, assume a hard-edged distribution. They are, however, easily generalized to more realistic trace-space density distributions $\rho(x, x')$ that are continuous in x and

x'. The density distribution of a beam is often taken to be constant along elliptical contours so that it may be fully characterized by its second moments. These contours are conveniently characterized by the quadratic form

$$x^T \sigma^{-1} x = k^2$$

where x is the trace-space vector (x, x') and σ is the symmetric matrix

$$\sigma = \begin{pmatrix} \sigma_{11} & \sigma_{12} \\ \sigma_{12} & \sigma_{22} \end{pmatrix}.$$

The expanded quadratic form is

$$\frac{1}{\det \sigma}(\sigma_{22}x^2 - 2\sigma_{12}xx' + \sigma_{11}x'^2) = k^2.$$

The contour with $k = 1$ defines an ellipse of area $\pi\sqrt{\det \sigma}$ and with orientation as shown in Fig. 3.1.

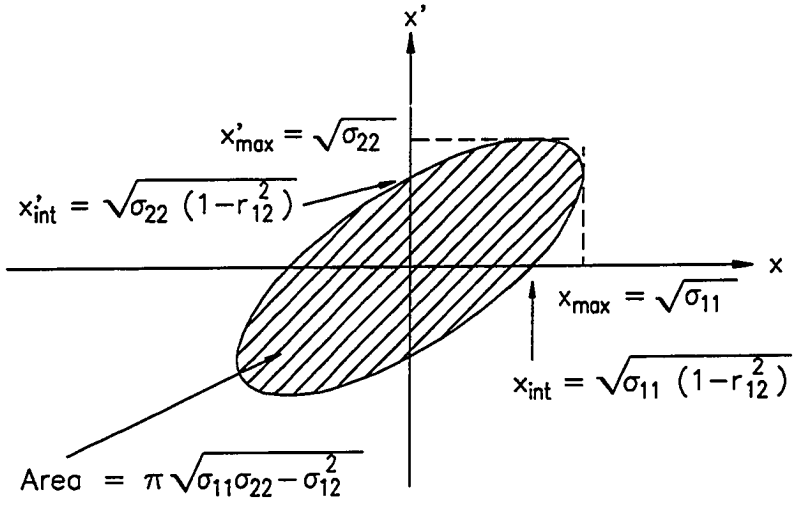

Figure 3.1: A trace-space beam ellipse. The correlation coefficient, r_{12}, is defined as $r_{12} \equiv \sigma_{12}/\sqrt{\sigma_{11}\sigma_{22}}$.

Often the density function ρ is Gaussian, and the convention is to choose σ such that with $k = 1$ the matrix elements are the second moments of the distribution, *i.e.*, $\langle x^2 \rangle = \sigma_{11}$, $\langle xx' \rangle = \sigma_{12}$, and $\langle x'^2 \rangle = \sigma_{22}$. The matrix so defined is called the *beam matrix*, and the density distribution is given by

$$\rho(x) = N \exp(-x^T \sigma^{-1} x/2). \tag{3.1}$$

In other words, $\sqrt{\sigma_{11}}$ is just the standard deviation of the distribution in x obtained by integrating ρ over x'. We then define the geometric emittance as

$$\epsilon_x \equiv \sqrt{\det \sigma} = \sqrt{\sigma_{11}\sigma_{22} - \sigma_{12}{}^2}. \tag{3.2}$$

This corresponds to $1/\pi$ times the area occupied by the $k = 1$ elliptical contour, which contains 39.3% of the beam. The normalized emittance is defined as $\epsilon_{N,x} = \gamma\beta_x\epsilon_x$.

It should be noted that in first-order optics, in which only linear transformations are applied to beam rays, a distribution that begins with an elliptical shape will always have an elliptical shape. The orientation changes under linear transformations, but the area remains constant. In such cases this description based on second moments is perfectly adequate for tracing beam evolution through an optical system.

The definition of emittance given by Eq. (3.2) may be generalized to any beam distribution, including those without an easily defined shape, by replacing the matrix elements with the second moments of the distribution referenced to the beam axis. The *rms emittance*, $\bar{\epsilon}$, so defined is

$$\bar{\epsilon} \equiv \left[\langle x^2\rangle\langle x'^2\rangle - \langle xx'\rangle^2\right]^{1/2}. \tag{3.3}$$

The normalized equivalent is again given by multiplying by $\gamma\beta_z$, which we may also write as

$$\bar{\epsilon}_N \equiv \frac{1}{mc}\left[\langle x^2\rangle\langle p_x{}^2\rangle - \langle xp_x\rangle^2\right]^{1/2}.$$

The emittances defined by Eqs. Eq. (3.2) and Eq. (3.3) (and the normalized versions) are used interchangeably throughout the main text. For a beam with Gaussian distributions in the phase-space variables the two are equivalent. For beams that exhibit noticeably non-Gaussian spatial profiles we use Eq. (3.3).

The rms emittance $\bar{\epsilon}$ is a good example of why it is always prudent to clearly define such quantities. A factor of four is frequently included in the definition Eq. (3.3). The rms emittance was originally defined by Lapostolle [16] based on the concept of the "equivalent perfect beam." This is an imaginary beam that has a uniform distribution within a hard-edged elliptical contour and that has the same second moments and total intensity as the real beam. The rms emittance was defined as $1/\pi$ times the area in trace space of the equivalent perfect beam, which is $4\bar{\epsilon}$ as we have defined $\bar{\epsilon}$. For a Gaussian distribution this corresponds to a contour containing 86.5% of the beam. It is becoming standard [17] to call this the "effective emittance," and to use Eq. (3.3) as the definition of the rms emittance.

3.2 Conditions for Emittance Invariance

At this point it is important to review the additional conditions assumed in deriving the invariance of the several definitions of emittance. To the extent that these conditions are violated in a given beamline, the emittance may no longer be a constant of motion.

1. Liouville's theorem applies only to systems of *noninteracting* particles. Charged particles interact via mutual Coulomb repulsion, the so-called *space-charge* force, which leads to emittance growth.

2. The beam transport does not couple the various two-dimensional projections of the six-dimensional phase space.

3. The slope of a particle ray x' can replace p_x as a variable canonically conjugate to x. Recall that for a particle of charge e in a vector potential $\boldsymbol{A}$, the canonical momentum is given by $\boldsymbol{p} = \gamma\beta m_0 c + e\boldsymbol{A}/c$. Hence x and x' are canonically conjugate (resulting in the invariance of the transverse geometric emittance) only if (a) the transverse components of the vector potential, A_x and A_y, are zero; and (b) the beam energy γ remains constant.

4. Beamline elements are accurately described by linear transformations.

Condition 1 is violated in any charged-particle beam. The effect of space charge is the subject of much study during the design and operation of high-brightness sources and beamlines. For sufficiently low charge density it can be neglected. Condition 2 is violated by certain beamline elements such as sextapoles, solenoids, rf kickers, and improperly oriented quadrupoles. Certain magnetic elements violate condition 3a. In simulating the passage of particles through the rf gun this is manifested as wild oscillations in the emittance if it is calculated using only the kinetic piece of the momentum. Care must then be taken to use the canonical value. Condition 3b is clearly invalid during acceleration. Hence the geometric emittance decreases as beam energy increases, while the normalized emittance remains invariant. It is for this reason that the geometric emittance, which is obtained from lab measurements, is converted to the more useful normalized emittance. Nonlinear elements, which violate condition 4, introduce distortions of the phase space volume that do not violate Liouville's theorem but render a second-moment description inadequate. In fact the increase of the rms emittance is often a good measure of the nonlinearity of a transport system.

3.3 Brightness

The emittance characterizes the extent in phase space a beam occupies, but conveys no information about the beam flux, or charged-particle current. The emittance and current may be combined into a single quantity, the *normalized brightness*, defined by

$$B_{\mathrm{N}} = \frac{2I}{\pi^2 \epsilon_{\mathrm{eff},x} \epsilon_{\mathrm{eff},y}},$$

where I is the beam current and ϵ_{eff} is the effective normalized emittance, equal to four times the rms normalized emittance ϵ_{N}. Most often what is of interest is the peak brightness, obtained by using the peak current of the beam. As with the emittance, a variety of conventions are used in the definition of brightness, with some authors using the rms rather than effective emittance, and others leaving out the factor of π^2 in the denominator or 2 in the numerator. Again, care must be taken in comparing results reported by different groups. The expression above may be rewritten

$$B_{\mathrm{N}} = \frac{I}{8\pi^2 \epsilon_{\mathrm{N},x} \epsilon_{\mathrm{N},y}}, \tag{3.4}$$

and we will use this definition throughout.

Since the dimensions of emittance are distance × angle, the dimensions of brightness are particles (or charge) per second per unit area per unit unit angle squared. For small angles, the angle squared is the same as the solid angle subtended. So this quantity expresses the particle flux that can be delivered to a given area with a given angular spread. This is what is of greatest interest to the designer of a particle collider, electron microscope, or free-electron laser. This is why the brightness is quoted as a performance specification for accelerators designed for a wide variety of applications. Commonly used units are $\mathrm{A/(m\text{-}rad)^2}$, which we abbreviate $\mathrm{A/m^2}$.

Brightness is conserved under beam transport if the transverse emittances and peak current are invariant. So in addition to emittance increase, brightness can be degraded by particle loss or bunch lengthening. Both of these are a concern in a high-brightness, high-peak-current beamline. Particle loss occurs if the beam is collimated by an aperture such as a beampipe or slit. A beamline with a given set of optics can only pass particles within a certain region of trace space. The area of this allowed space is called the *acceptance* or *admittance* of a beamline. If the beam occupies a region of trace space outside the beamline acceptance, part of the beam will be attenuated. Space charge can cause lengthening of the beam, but this effect tends to be less severe than the transverse component.

3.4 Correspondence to Other Common Beam Parameters

It is instructive to relate the emittance and brightness to other quantities commonly used to characterize a beam. Laser and particle beams are often characterized at a focus, where the beam size is at a minimum. Here σ_{12} is zero,[1] so only two parameters are required to characterize fully the trace space of a beam (assuming an elliptical contour in trace space is a reasonable representation). In beam-matrix argot these may be, say, the emittance and the spot size at the waist, from which one can find the angular divergence at the waist.

The quantity corresponding to emittance in describing optical beams is the *geometric entendue*. This seems to be rarely used in practice, but as we shall see shortly, there is a more familiar analog to the emittance of an ideal Gaussian optical beam of the lowest order. In describing such a beam, one often employs the minimum spot size w_0 and the *Rayleigh range* z_R. The optical convention is to define w_0 so that the intensity profile is a Gaussian with standard deviation $w_0/2$.

The Rayleigh range is the distance from the waist at which the laser area increases to twice what it was at the waist. This a convenient way of characterizing the length of the focus region, termed the *depth of focus* of an optical system. It is determined by the waist size and the wavelength of the light, λ:

$$z_\mathrm{R} = \frac{\pi w_0^2}{\lambda}.$$

[1]Strictly speaking, the focus, where the spot size is minimized, and the waist, where σ_{12} is zero, are not identical (see Sec. 6.2). But in most cases they may be considered so to good approximation.

This same quantity for a particle beam is called the β^* and may be calculated from the emittance ϵ and an elementary knowledge of beam transport (see Chapter 6):

$$\beta^* = \frac{\sigma_w^2}{\epsilon},$$

where σ_w is the standard-deviation spot size at the waist, also assuming a Gaussian distribution for the particle beam.

Comparing these two relations we find that the emittance of a perfect lowest-order Gaussian optical beam is just

$$\epsilon = \frac{\lambda}{4\pi}.$$

This is nothing more than an expression of the Heisenberg uncertainty principle relating the minimum uncertainty in the transverse position and transverse momentum:

$$\Delta x \, \Delta p_x \sim \hbar/2.$$

Dividing each side of this equation by the longitudinal momentum of a beam photon, $p_z = h/\lambda$, reproduces the above result.

In reality the beam will be diffracted by finite-sized lenses, mirrors, and apertures and may have contributions from higher modes. The value $\lambda/4\pi$ represents a lower limit to the achievable emittance. Hence the minimum possible emittance of a CO_2 laser, with $\lambda = 10$ μm is just under 1 μm-radian, or 1 mm-mrad. Significantly lower values are achieved with electron beams, which are not diffraction-limited (short of the de Broglie wavelength!). Instead, particle beams tend to be thermally limited, that is, the limiting factor is the spread in transverse velocities of the particles emitted by the source. Space charge can further increase the emittance, but nothing can lower it from the initial value without loss of particles.

Another quantity defined for light sources is the *luminance*, or brightness, which is the luminous flux emanating from a unit area into a unit solid angle. It is functionally identical to the brightness of a particle beam, differing only by a possible numerical factor.

An important particle-beam parameter called the *luminosity* is related to brightness. The luminosity $\mathcal{L}$ is defined for colliding beams or a beam on a fixed target as the number of collision events observed per second, N, divided by the event cross section σ, that is

$$\mathcal{L} = \frac{N}{\sigma}.$$

If we take the target to be a single particle, the luminosity of the incident beam is the same as the flux density, essentially the beam current divided by the area of the beam spot focused onto the target, or $\mathcal{L} = I/A \sim I/r^2$, where r is the radius of the focused spot.

We can relate the luminosity to the beam brightness B_N (an intrinsic quantity) and characteristics that are particular to the beam facility. We assume that the maximum beam radius is limited by the beam-pipe radius R, and that the last focusing element prior to the interaction point is at a distance D. Taking the focused spot size to be

much smaller than R, the beam convergence angle at the focus is just $\theta \sim R/D$. The emittance is then $\epsilon \sim r\theta \sim rR/D$. We may write the luminosity as

$$\mathcal{L} \sim \frac{I}{\epsilon^2 (D/R)^2} \sim B_{\mathrm{N}} \left(\frac{R}{D}\right)^2 .$$

In other words, the brightness of the beam determines the maximum luminosity that can be obtained with a given set of focusing conditions.

Chapter 4

Electron Emission

4.1 Introduction

The normalized transverse emittance ϵ_N of a beam is at best a constant of motion, as discussed in Chapter 3. Under nonideal conditions it can increase, but it cannot decrease without loss of particles. The normalized brightness is defined by

$$B_N = \frac{I_p}{8\pi^2 \epsilon_{N,x} \epsilon_{N,y}},$$

where I_p is the peak current. Emittance growth leads to a decrease in brightness, as does loss of beam current.

The only method available for increasing the brightness of a beam once produced is to increase the peak current by reducing the pulse length. This is accomplished by subharmonic rf bunching and magnetic compression. The peak current in the injector to the Stanford Linear Collider is increased by a factor of around 100 by a combination of these techniques [18]. The drawbacks of subharmonic bunching are that the beam suffers unavoidable emittance increase; the method works only for nonrelativistic particles, for which the space-charge forces are more severe; and it requires the use of lower frequencies for acceleration and hence lower gradients. The increase in brightness so obtained falls somewhat short of the increase in current. It is desirable to produce the beam directly with the required brightness.

Conventional electron sources usually consist of a thermionic cathode in a cavity across which is applied a static voltage. The maximum electric fields that can be supported by metal surfaces before a discharge occurs are insufficient to accelerate the electrons to relativistic velocities before exiting the cavity. As will be discussed in Sec. 5.1, emittance growth is caused by the mutual electrostatic repulsion of the electrons, which decreases rapidly with increasing energy. Hence to improve the brightness of high-current sources it is necessary to accelerate the electrons off the cathode more rapidly than is possible with dc fields. The maximum brightness that has been achieved with dc thermionic sources is around 10^{10} A/m^2.

Among the highest brightnesses reported (in excess of 10^{11} A/m^2) have come from field-emission guns, in which the cathode is a small, sharply pointed metal tip [19]. These were developed for scanning transmission electron microscopy and are also used in electron-beam lithography. The tip geometry enhances the electric field at the surface to values at which field emission results in an extremely high current density (up to

10^9 A/cm^2), but which is emitted from an effective surface area on the order of microns in diameter. The total current, around a milliampere, is small enough to avoid the effects of space charge, but is also too small to be useful in most accelerator and FEL applications.

Materials can support much higher instantaneous radio-frequency electric fields than static ones for reasons that will be discussed in Sec. 4.4.2. Such fields are used to produce accelerating gradients of up to 20 MV/m in linear accelerators. A fundamental improvement in electron sources occurred with the introduction of the "rf gun" [20]. A thermionic emitter was incorporated into a resonant rf cavity, resulting in a beam of up to 1 MeV in energy. The gun brightness is now primarily limited by the properties of the thermal cathode and the fact that the pulse length is determined entirely by the range of rf phase over which electrons are accelerated out of the gun.

The idea of using laser-driven photocathodes as high-current electron sources was first associated with the lasertron [21] (a source of microwave power) and the production of spin-polarized electrons [22]. The main advantages of such a system are that the spatial and temporal profile of the source can be varied to the extent that the driver laser can be controlled. In 1985 a program was begun at Los Alamos to study the use of photoemitters in a high-brightness source for use as an FEL driver [23, 24]. Semiconductors were chosen for the photocathode due to their high quantum efficiency (around 10%) and the fact that they could deliver high current densities [25]. A Cs_3Sb photocathode was found to yield a peak current of around 200 A/cm^2, as compared with the 20 A/cm^2 characteristic of thermal emitters. It was demonstrated that laser-driven photocathodes could produce intrinsically high-brightness beams [26].

The photocathode rf gun, pioneered at Los Alamos [1], incorporated a semiconductor photoemitter into the first cavity of a standing-wave rf structure. The photocathode was driven by a mode-locked laser. This first gun produced a peak current of over 100 A, a peak current density of 600 A/cm^2, and a brightness of 8×10^{10} A/m^2 at an energy of 1 MeV. This concept was clearly an improvement over the dc thermionic gun.

Semiconductor photocathodes have a short lifetime and must be made and transferred to the gun cavity under very high vacuum. Metals need no such vacuum apparatus and are very long lived even under the rigorous conditions prevailing in an rf cavity. For these reasons a metal photocathode was chosen for the ATF gun.

The main drawbacks to metals are their consistently high work functions (several eV) and much lower quantum efficiencies. Metal quantum efficiencies are around 10^{-4} or less in the ultraviolet. The difference between semiconductor and metal quantum efficiencies can be understood from a brief discussion of the mechanism by which an incident photon ejects an electron from the material [27]. The high reflectivity of metals ($\sim$ 90%) results in a factor of ten difference in the amount of light absorbed. The absorbed light penetrates the cathode to the characteristic absorption length for light in that material. Very nearly every photon produces an electron with energy somewhat above the thermal equilibrium value in the solid. This electron must reach the surface of the cathode with sufficient energy to escape from the surface.

The primary energy-loss mechanism in metals is electron scattering, which because of the abundance of free electrons results in an escape depth of just a few angstroms. In semiconductors phonon scattering is the dominant mechanism and allows electrons to

reach the surface from several hundred angstroms. The absorption length for visible light in semiconductors is on the order of hundreds of angstroms. A similar figure applies to metals [28]. Hence only a small fraction of the light absorbed by a metal ejects electrons that reach the surface with enough energy to overcome the work function.

Due to the reduced quantum efficiency of metals, a more powerful laser is required to eject a given amount of charge. Furthermore, the high work function requires a laser beam in the ultraviolet. Fortunately these requirements are met by the frequency-quadrupled high-power Nd:YAG laser. The photon energy of 4.66 eV is a good match for the work function of copper, around 4.4 eV.

The properties of the beam produced by the rf gun are determined by the properties of the cathode, the laser, the rf fields, and the space-charge force. In the remainder of this chapter we will consider the emission of electrons from the cathode surface under rf and uv excitation, followed by quantitative estimates of the limiting emittance and brightness produced at the cathode. In the next chapter, degradation of the beam as it travels from the cathode to the gun exit and through the transport optics will be discussed.

4.2 Mechanisms for Electron Emission from Metals

There are three sources of energy available in the rf gun to liberate electrons, each of which will be discussed and an estimate made of its contribution to the gun output. These sources are heat (thermal emission), rf fields (field emission), and uv laser light (photoemission).

4.2.1 Thermal Emission

The kinetic-energy of electrons within a solid at temperature T is governed by the Fermi-Dirac distribution, from which may be obtained a prediction for the current density J emitted by a metal with work function ϕ. This is called the *Richardson-Dushman equation*, which is expressed numerically as [29]:

$$J = (120\,\mathrm{A\,cm^{-2}\,K^{-2}})\,T^2 e^{-\phi/kT}, \tag{4.1}$$

where the Boltzmann constant $k = 1\,\mathrm{eV}/11{,}600^\circ$ K. This formula indicates that with a work function of a few eV there should be no appreciable thermal current until the cathode is heated to a few thousand degrees K, which is in fact the operating temperature range of thermal emitters. The maximum obtainable current density is limited by the metal's melting point.

4.2.2 Field Emission

The presence of an electric field at the surface of a metal changes the shape of the potential energy barrier seen by an electron within the metal. The form of the potential energy $V(z)$ as a function of the distance z from the surface is easy to calculate. One piece comes from the electric field E, which induces a repulsive force eE away from the

cathode. The other piece comes from the attractive force of the image charge, $e^2/(4z^2)$. Together these give a potential of the form

$$V(z) = -\frac{e^2}{4z} - eEz.$$

We see that for zero field and $z = \infty$ the potential is zero. The work function, then, is just the negative of this function evaluated at the distance at which the electron first feels the image charge, usually taken to be on the order of an atomic diameter in order to make this classical derivation agree with measured values. With nonzero field the potential energy has a maximum at $z_0 = \sqrt{e/4E}$, at which point the potential energy is $V(z_0) = -e\sqrt{eE}$. We see that the work function has been effectively lowered by

$$\Delta\phi = e^{3/2}E^{1/2} = (0.038\,\mathrm{eV})\,E^{1/2},$$

with E in MV/m. This is known as the *Schottky effect.*

The maximum electric field at the cathode of the ATF rf gun is 100 MV/m. This has the effect of lowering the work function by 0.38 eV. Even at fields ten times larger than this, which lower ϕ by 1 eV, the effect is insufficient to give thermal emission with the modified work function inserted into Eq. (4.1).

There is another mechanism by which the electric field allows electrons to escape the cathode surface. After reaching a maximum at z_0, the potential decreases linearly with increasing z and will at some point descend below the energy of free electrons within the metal. As is well known the electrons can tunnel through this potential barrier, which gets narrower with increasing field strength. The emission of electrons from a cold metal in the presence of a strong electric field was one of the earliest confirmations of tunneling as predicted by the new quantum theory [30]. The resulting current density was first worked out by Fowler and Nordheim in 1928 and modified by Nordheim the same year to include the correct image potential. The result [31] is known as the *Fowler-Nordheim equation*:

$$J = 154\frac{E^2}{\phi}\exp\left(-6830\,v(y)\frac{\phi^{3/2}}{E}\right), \tag{4.2}$$

where J is in A/cm^2, E is in MV/m, ϕ is in eV, and $v(y)$ is a correction term equal to 0.9 for $E = 100$ MV/m.

Current densities of at least 1 mA/cm^2 are observed in the ATF gun for cathode fields of around 75 MV/m and higher. This field emission is called *dark current.* But Eq. (4.2) predicts that a current density of this magnitude requires a field of at least 2200 MV/m, about 30 times the rf field in the gun.

Part of the discrepancy is removed by recalling that electric fields are enhanced near surface structures. Such microstructures were observed on a metal cathode that was exposed to laser pulses of the same wavelength and about the same intensity and pulse length as those used in the ATF gun [32]. By measuring the quantum efficiency as a function of applied electric field, the enhancement factor β, defined as the ratio of the apparent effective field at the cathode surface to the applied field, was measured for various microstructure sizes. Values ranged from four to eight, consistent with enhancement

calculations for the measured structure sizes. (As an example, recall from electrostatics that at the surface of a conducting sphere placed in a uniform electric field E_0, the perturbed field reaches a value of $3E_0$. On scales much smaller than the wavelength of an oscillating electromagnetic field, the electric field may be treated as in the static case.) Possible sources of this discrepancy will be discussed when we return to the issue of field enhancement in Sec. 4.4.2.

4.2.3 Photoelectric Emission

The photocathode rf gun is based on the photoelectric effect [33]. The discovery that metals emit electrons under the stimulus of ultraviolet radiation provided some of the first experimental evidence of the quantum nature of light. The energy of the photon must exceed the effective work function of the metal in order to eject an electron. The number of electrons ejected depends linearly on the number of incident photons with the quantum efficiency as the proportionality constant. The electrons leave the cathode with maximum kinetic energy given by the difference between the photon energy and the effective work function, $E = h\nu - \phi_e$. For small energy differences the quantum efficiency η depends on the photon energy as [34]

$$\eta \propto (h\nu - \phi_e)^2,$$

where ϕ_e includes any Schottky lowering of the work function by an applied electric field.

In the case of copper excited by a quadrupled YAG laser, $h\nu = 4.66$ eV, and $\phi = 4.4$ eV. With an electric field of 100 MV/m and an enhancement factor β of 10, the effective work function is 1 eV lower. The field-enhanced quantum efficiency is then predicted to be 24 times higher than the zero-field value. In general the quantum efficiency is a sensitive function of conditions at the cathode, including surface smoothness, purity, and field strength.

Photoelectric emission occurs on time scales much shorter than a picosecond, so that the temporal profile of the electron pulse exactly follows that of the laser. Studies have verified this down to time scales of 100 fsec [35]. We may estimate the minimum time required by noting that visible light, with a wavelength of around 500 nm, has an oscillatory period of 2 fsec. In order for an electron to "know" what frequency (energy) a photon has, it seems likely that it would have to interact with it for at least one full cycle.

4.3 Cathode Brightness

The brightness of a source is ultimately limited by the peak current density that can be drawn from the cathode material and by the characteristic transverse kinetic energy of the electrons upon emission. As a benchmark by which to gauge the performance of various electron sources, it is instructive to calculate these intrinsic limits for different cathode types.

4.3.1 Thermal Cathode

A thermal cathode is a metal that is heated to sufficient temperature to achieve thermal electron emission. The electrons are accelerated away from the cathode by an applied electric potential. As discussed previously, the temperatures needed are on the order of a few thousand degrees kelvin, for which the thermal kinetic energy of the electrons is a few tenths of an eV. Emission occurs from the entire surface of the cathode. If a static voltage is applied, the current is also dc. In an rf gun electrons are emitted during the portion of each rf cycle for which net acceleration occurs, approximately a $\pm 45°$ region centered on 90°.

The normalized rms emittance at the cathode is given by

$$\epsilon_N = \gamma\beta(\langle x^2\rangle\langle x'^2\rangle)^{1/2} \tag{4.3}$$

since $\langle xx'\rangle = 0$. The rms velocity in a given direction of a Maxwellian velocity distribution at temperature T is given by $v_x^2 = kT/m$, where m is the electron rest mass. Then note that $\beta x' = (v/c)(v_x/v) = v_x/c$, and that for thermal velocities, $\gamma \simeq 1$. For uniform emission from the entire cathode surface of radius r, $\langle x^2\rangle = r^2/4$. This gives

$$\epsilon_N = \frac{r}{2}\left(\frac{kT}{mc^2}\right)^{1/2}.$$

For uniform emission the current density J is just $J = I/(\pi r^2)$, so we can write

$$\epsilon_N = \frac{1}{2}\left(\frac{I}{\pi J}\right)^{1/2}\left(\frac{kT}{mc^2}\right)^{1/2}.$$

Then the brightness is just $B_N = I/8\pi^2\epsilon_N^2$, so we find

$$B_N = \frac{J}{2\pi}\frac{mc^2}{kT}$$

as the maximum brightness from a thermal emitter. Typically $kT \simeq 0.1\,\text{eV}$, and the intrinsic current density limit is about $J = 20\,\text{A/cm}^2$, as was noted in Sec. 4.1. This gives

$$\epsilon_N = 0.28\,\text{mm-mrad} \cdot I[\text{A}]^{1/2} \qquad \text{and} \qquad B_N = 1.6\times10^{11}\,\text{A/m}^2$$

as the minimum and maximum values, respectively.

4.3.2 Photocathode

Photocathodes offer much greater control of the output beam than is possible with thermal cathodes. The electron kinetic energy can in principle be varied independently of the number of the electrons by changing the wavelength of the laser. The number of electrons is strictly a function of the laser pulse energy. The electron pulse length can be controlled by varying the laser pulse length. The effective emitter area is identical to the laser spot size, which can easily be varied.

The ATF uses a copper cathode driven by a quadrupled Nd:YAG laser. The work function of copper is around 4.4 eV, and a laser photon has energy $h\nu = 4.66$ eV. In the presence of an accelerating field of 100 MV/m, the work function is lowered by around 0.4 eV by the Schottky effect, so the electrons are ejected with a kinetic energy of around 0.65 eV. Assuming the electrons are ejected isotropically, $m\langle v_x^2\rangle/2 = E/3$ or $\langle v_x^2\rangle = (2/3)(E/m)$. We assume a Gaussian laser-intensity distribution $G(r) = G_0 \exp(-r^2/2\sigma^2)$, giving $\langle x^2\rangle = \sigma^2$. Then from Eq. (4.3)

$$\epsilon_N = \sigma\left(\frac{2E}{3mc^2}\right)^{1/2}. \tag{4.4}$$

The integrated current I is $2\pi\sigma^2 J$, where J is the peak current density, so

$$\epsilon_N = \left(\frac{I}{2\pi J}\right)^{1/2}\left(\frac{2E}{3mc^2}\right)^{1/2} = \left(\frac{IE}{3\pi J mc^2}\right)^{1/2}$$

and

$$B_N = \frac{3J}{8\pi}\frac{mc^2}{E}.$$

We have already noted that current densities on the order of 1000 A/cm^2 have been achieved from photocathodes. Using this value for J we find

$$\epsilon_N = 0.11\,\text{mm-mrad}\cdot I[\text{A}]^{1/2} \qquad \text{and} \qquad B_N = 1.0\times10^{12}\,\text{A/m}^2$$

for the limiting values.

Several conclusions emerge from the preceeding analysis. First, the emittance of a cathode is limited primarily by its characteristic transverse energy and can be made arbitrarily small by decreasing the emitter area. The maximum brightness is determined solely by the transverse energy and by the peak current density, independent of cathode size. For example, a photocathode capable of producing 1000 A/cm^2 with electrons of kinetic energy 0.26 eV has an intrinsic brightness about 10 times that of the best thermionic cathode and a factor of four lower emittance for the same current.

There has been some investigation into enhancing the photoemission process by illuminating the cathode with p-polarized laser light at large angles of incidence. The enhancement results from the reduced reflectivity at large angles and from the component of the laser-beam electric field perpendicular to the cathode surface. This field might violate the above assumption of isotropic emission and favor the forward direction, reducing the transverse kinetic energy. In an intense enough laser the field could become sufficiently strong to produce field-assisted photoemission via the Schottky effect.

In such a configuration p-polarization has been shown to yield enhancement factors of a few over s-polarization [36]. The potential disadvantages are that the effective illumination area is increased and there is a time-of-arrival difference at various points on the cathode, both of which could conspire to reduce the current density. Experimentation with this effect has been proposed for the ATF gun.

4.4 Limits to Cathode Brightness

Having considered the relation between brightness and cathode characteristics such as current density and electron energy, we will now examine those factors that in turn affect these parameters.

4.4.1 Current-Density Limit

There is an intrinsic limit to the charge that can be extracted from a surface, which is simply a consequence of Gauss's law. An estimate of this limit, known as *Child's law*, may be obtained by considering a simplified model of an electron gun. First assume an infinite planar geometry with a parallel cathode and anode separated by gap distance d. An electric field E is applied between the electrodes, causing a surface charge density of $\sigma = E/4\pi$ to form on each surface. This surface charge terminates the electric field lines on each conductor, preventing further penetration into the electrode volume. If all of this charge is suddenly ejected from the cathode (by a laser pulse or by field emission), it will be accelerated towards the anode, continuing to terminate the electric field lines so that there is no field on the cathode until the charge reaches the anode, effectively recharging the cavity. We see that no more charge than is necessary to terminate the electric field lines can be accelerated at one time. Such a pulse is said to be *space-charge limited.*

The usual expression of Child's law is in the form of a maximum current, assuming continuous operation of the source, the time scale governing the conversion of charge into current being the transit time of the charge bunch to the anode. We are interested in pulsed operation, for which the maximum charge is of interest. Numerically this is

$$\sigma \simeq 100 \frac{\mathrm{nC}}{\mathrm{cm}^2} \cdot E \left[\frac{\mathrm{MV}}{\mathrm{cm}}\right]$$

The peak current density is then determined by the length of the laser pulse τ according to $J_{\max} \simeq \sigma/\tau$. Lasers pulses of a few picoseconds are common. Taking $\tau = 10$ psec gives

$$J_{\max} \simeq 10 \frac{\mathrm{kA}}{\mathrm{cm}^2} \cdot E \left[\frac{\mathrm{MV}}{\mathrm{cm}}\right].$$

The ATF gun operates at up to 1 MV/cm, which permits current densities of at least a factor ten higher than had previously been achieved from an rf-gun photocathode.

This value is not exact since the gun cavity geometry is more complicated than that assumed above, and an exact relation would be obtained by solving Poisson's equation. The form of Child's law usually quoted in the literature [37] expresses the maximum current of nonrelativistic electrons emitted in a planar-electrode geometry operated at dc as a function of the applied static voltage. It is interesting to note that this is reproduced by the above model to within a factor of 8/9.

4.4.2 Electric-Field Limit

It has been seen that high rf fields at the cathode have several beneficial effects: (a) rapid acceleration of electrons, (b) lowering of the work function with its attendant increase

in quantum efficiency, and (c) elevation of the maximum achievable current density. In general one would like the rf fields in the gun to be as high as possible. There are, however, a couple of limiting considerations.

A negative side effect of strong electric fields is the production of field emission, which acts as an unwanted background to the photoelectron pulse. This can be largely reduced by momentum selection and temporal gating since the photoelectron pulse can have a narrower time and momentum spread than the dark current.

The maximum electric field that can be sustained by metal structures is limited by rf breakdown. This is similar to the static breakdown limit, but may have somewhat different causes at higher frequencies. There is a routinely cited threshold above which "sparking" can be expected known as the *Kilpatrick limit* [38]. In the 1950's the measured breakdown limits at different rf frequencies were parameterized by a model of the breakdown process in which ion back-bombardment of the cathode creates a cascade of secondary electrons. At high radiofrequencies this limit is routinely exceeded by a factor of 6-7, a fact likely due in part to improvements in surface preparation and vacuum technique that have occurred in the last four decades. Also, the breakdown model was based on the assumption of planar electrodes, which does not well characterize many rf structures. The maximum electric field of 100 MV/m achieved in the ATF gun is twice the Kilpatrick limit for 2856 MHz.

Recent interest in increasing the maximum accelerating gradients in linac structures has motivated several research efforts aimed at understanding the rf-breakdown process. Although much has been learned as a result of these studies, many questions about the fundamental breakdown process remain unanswered. A group at SLAC has done much work in this area [39]. They measured the field-emission current from rf structures as a function of applied electric field in order to determine the breakdown threshold and, by fitting the data to the Fowler-Nordheim relation, Eq. (4.2), inferred the effective enhancement factor $\beta_{\rm eff}$. They found S-band (2856-MHz) copper structures capable of supporting over 300 MV/m with $\beta_{\rm eff} \simeq 60$. Optical observations of the metal surface revealed microstructures consistent with factors of no more than about ten. This is quite similar to the ATF experience, where a higher $\beta_{\rm eff}$ was inferred from gun field emission than was consistent with observed microstructures on laser-conditioned surfaces. The reason for this discrepancy is not entirely clear, but two dominant theories have emerged.

The SLAC group invokes a mechanism in which surface oxides, adsorbed organic residues, and dielectric inclusions on the surface form a dielectric layer. The electric field polarizes this layer and provides an acceleration region accessible to conduction electrons, which can then be ejected from the surface. This contributes an additional enhancement factor. If the effective factor is taken as the product of the two effects, field enhancement by microstructures, β_1, and a dielectric layer, β_2, then $\beta_{\rm eff} = \beta_1\beta_2$, with each factor around eight. This is consistent with a dielectric layer 2 or 3 nm thick with dielectric constant $\epsilon = 3$. The existence of such a layer, even after rf conditioning and laser "scrubbing," is not unreasonable.

The other theory is that the large enhancement is due solely to the presence of sharp peaks, cracks, or whiskers. While it is possible to have features of metal surfaces that would produce enhancement factors of over 100, few optical observations of cathode surfaces have supported this.

Independent of the enhancement mechanism, there seems to be a consensus as to the general nature of rf breakdown at high frequencies. This is called explosive-electron emission (EEE), a good summary of which is given in Ref. [39]:

> The general model for EEE is that the local effective electric field at a particular surface site reaches a level such that the [field emission] current raises its temperature to the melting point. Instantaneous melting and evaporation of metal and inclusions take place, the gas rapidly expands and gets ionized into a plasma, light is emitted, the surface is irreversibly deformed and the condition of the initial site is changed. The local field emitted current drops off and the breakdown stops. The entire phenomenon resembles a volcanic eruption.

This scenario is consistent with observations of the behavior of the ATF gun. The reason the breakdown limit increases with increasing frequency can be understood in either the EEE or ion back-bombardment model. The characteristic time for the initiating event, either local heating or ion acceleration, is the period of the oscillating fields, which is the inverse of the frequency.

4.4.3 Laser-Intensity Limit

The interest in metal cathodes for high-brightness electron sources has prompted a series of detailed investigations of the properties of metal cathodes. One group is in the Instrumentation Division of Brookhaven National Lab. Several of their findings have already been mentioned. In one study [40] the quantum efficiencies of several metals were measured along with the maximum attainable current densities and laser-induced damage limits. The driving laser pulse was almost identical to that used by the ATF: quadrupled YAG-laser pulses 10 psec long with a repetition rate of a few Hz. The quantum efficiency of copper was found to be 1.4×10^{-4}. The laser energy-density threshold for optical damage was measured to be 100 mJ/cm^2. Based on these figures, copper could yield photocurrent of up to 300 kA/cm^2. A yttrium cathode produced a space-charge-limited current density of 21 kA/cm^2, the highest reported to date for a "macroscopic photoemitter."

Perhaps a more relevant figure in the context of an rf gun is the laser intensity at which a surface plasma is formed. At this point the dynamic interaction of the electrons with the rf fields in the gun cavity become quite different from that of the strictly photoemissive regime. More will be said about this in Chapter 9 during the discussion of "enhanced emission." The plasma-formation threshold was found to be 10 mJ/cm^2, which would limit copper cathodes to 30 kA/cm^2.

4.4.4 Sources of Transverse Energy

In the discussion of intrinsic cathode brightness, we assumed that the electron transverse energy was due entirely to the thermal kinetic energy in the case of the thermionic cathode or the photon energy in the case of the photocathode. Kinetic energy is imparted

to the electrons through several other mechanisms operating in an rf gun. Each will be briefly summarized with an estimate of the transverse component.

Laser heating

As we have already seen, the majority of the absorbed laser-pulse energy in a metal is converted to electron thermal energy via electron scattering. For time scales smaller than some relaxation time τ_R, which depends on the electron-phonon coupling strength, this thermal energy will diffuse without being absorbed by the atomic lattice [41]. For longer time scales the lattice will be in equilibrium with the conduction electrons and hence will be at the same temperature. The value of τ_R is on the order of a picosecond. The 10-psec pulse length of the YAG laser is sufficiently close to this value to warrant a calculation of the temperature increase in both regimes.

In either case, we will assume that 90% of the 100-μJ laser pulse is reflected and the remaining 10% deposited in an area of 1 mm^2, characteristic of the YAG-laser-spot size on the photocathode, and in an optical skin depth of 20 nm, for a volume of 2×10^{-8} cm^3.

Assuming the lattice stays at equilibrium with the electrons, we are interested in the temperature increase of the bulk copper in this volume. Copper has a bulk heat coefficient of 0.39 J $\cdot$ g^{-1} $\cdot$ K^{-1} and a density of 9 g/cm^3. A deposited energy of 10 μJ in a volume of 2×10^{-8} cm^3 would raise the temperature by 130 K or about 0.01 eV.

If the energy is taken up only by the conduction electrons, then we need only divide the pulse energy by the number present in the absorption volume. In copper there are 8×10^{22} free electrons per cubic centimeter, resulting in an energy gain of 0.06 eV per electron. In either case, laser heating does not make a significant contribution to electron transverse energy.

Laser electric field

The laser is incident normally on the cathode, so that the electric field of the laser could provide transverse acceleration. A 100-μJ pulse lasting 10 psec and focused into an area of 1 mm^2 gives an intensity of 1 GW/cm^2, corresponding to a peak electric field of 60 MV/m. The 266-nm laser light has a frequency of around 10^{15} Hz, and so could apply an accelerating field for around 1 fsec. The electrons are ejected with a few tenths of an electron volt of kinetic energy and have $\beta = v/c = 10^{-3}$, so in a fsec they travel about 3 Å, during which they gain 0.02 eV in the laser field. This is again a negligible contribution.

rf electric field

The peak electric field of the rf is of the same order of magnitude as that of the laser. The differences are that the rf period is long compared to the laser pulse and that the rf electric field is nominally a longitudinal one. Cathode surface structures, in addition to enhancing the rf field, redirect the field lines and introduce a transverse component. This effect is difficult to model and requires a good knowledge of the cathode surface topography. An order-of-magnitude estimate may be obtained from a simplified calculation.

The microstructures observed on metal cathodes exposed to laser pulses similar to those at the ATF were on the order of a micron in size and were rather densely packed [32]. These may be modelled as hemispherical tips of radius r on columns of height h. The measured enhancement factors $\beta \leq 8$ were consistent with what would be expected from the observed ratios h/r (both on the order of microns). The electric-field lines are normal to the surface everywhere on the hemisphere. Hence around an isolated structure field lines are converging at all angles relative to the average cathode surface. In a dense collection of such structures the average transverse component will be reduced, as will be the distance an electron must travel before it experiences a strictly longitudinal field.

Assuming a transverse electric field near the microstructure of 10% of the (unenhanced) applied field of 100 MV/m and that the electron will travel one tenth of the microstructure radius along the transverse direction, we see that it would gain 1 eV from the rf field. A more precise calculation [42] for mirror-quality metal surfaces modelled the surface features as cones of opening angle 60° and radius 100 Å. In an applied field of 100 MV/m an electron travelling 10 Å near such a structure would acquire a transverse energy of 3.5 eV.

Clearly this effect could easily dominate the characteristic transverse energy of a photocathode and hence limit the intrinsic brightness. In the literature the limiting brightness of a cathode is almost always discussed in the context of laser-photon energy with no mention of rf-field contribution. For example, using a transverse energy of 3.5 eV and a laser-spot size of 1 mm in Eq. (4.4), we find a cathode emittance of 2 mm-mrad. This is not far from the design value that includes the effects of emittance growth in the gun. This effect will deserve some experimental and simulation studies if the full potential of the photocathode rf gun is to be realized.

Chapter 5

Mechanisms of Emittance Increase

We saw in the previous chapter that the minimum emittance we can obtain from the rf gun is a function of the photocathode and laser properties. In Chapter 2 we noted that the ATF rf gun was designed to minimize the emittance increase caused by various forces inside the gun cavity. We will now estimate the size of these effects, which conspire with the cathode emittance to limit the gun performance. Some additional sources of emittance increase that can occur in the electron beamline are also included. Finally, it seems relevant in this context to briefly summarize several issues regarding emittance measurement and calculation that can cause confusion.

5.1 Space Charge

The space-charge force is the mutual electrostatic repulsion of a collection of particles of like charge. For bunched beams the transverse component scales as $1/\gamma$ to $1/\gamma^2$, depending on the ratio of longitudinal to transverse bunch size [43]. Here γ is the usual relativistic factor given by the electron energy divided by the rest mass. This is why it is desirable to accelerate the electrons off the cathode as rapidly as possible. The space-charge effects are most severe near the cathode before the electrons are relativistic.

Consider a cylindrical beam of uniform charge density. Gauss's law tells us that the radial electric field E_r anywhere within the beam is linearly proportional to r. This is quite sensibly called the linear space-charge force. It acts as a defocusing lens that, since it is linear in r, introduces no transverse phase-space distortion and hence no emittance increase (see Chapter 3).

Any deviation from a uniform charge distribution introduces nonlinear transverse field components that can cause transverse emittance increase. Another view is that a uniform distribution minimizes the electrostatic-field energy of a collection of charges. The excess energy of any other distribution is "thermalized," or converted to electron kinetic energy, as the uniform state is approached. This addition of radial momentum results in a phase-space increase. Reference [43] presents an analytic calculation of the space-charge emittance increase in an rf gun based on the former view, obtained by integrating the electron equation of motion including space charge as a driving term. An analytic form for the emittance increase has also been obtained from the latter view and is summarized in Ref. [44]. Both forms are in agreement at the 30% level for the ATF gun and exhibit similar agreement with simulation studies using the code PARMELA [2].

As an example, consider an electron pulse that has an rms transverse size of $x_{rms} = y_{rms} = 1.5$ mm, an rms pulse length of 5 psec (corresponding to a longitudinal length of 1.5 mm), and a bunch charge of 1 nC. If we take the peak accelerating field to be 75 MV/m, the output momentum is 3.5 MeV, corresponding to a γ of 7. The final normalized emittance $\epsilon_{N,f}$ as a function of initial emittance $\epsilon_{N,i}$ is given by [44]

$$\epsilon_{N,f} = \left(\epsilon_{N,i}^2 + 524 \frac{Qa}{\gamma} \frac{U}{w_0} \right)^{1/2}, \tag{5.1}$$

where Q is the bunch charge in nanocoulombs, a is the rms beam size in millimeters assuming spherical symmetry, emittances are in mm-mrad, and U/w_0 is a geometric factor that depends only the form of charge distribution. For a Gaussian distribution $U/w_0 = 0.3$. To get a feel for the size of the space-charge contribution to the transverse emittance, we calculate the final emittance at the gun output for the above parameters, assuming zero input emittance. From this equation we find a space-charge emittance of 6 mm-mrad. This is larger than the intrinsic cathode emittance.

This emittance increase is predicted to occur within a quarter of the "plasma wavelength" of the electron bunch, given by

$$z_p = \frac{\lambda_p}{4} = \frac{\pi a}{\gamma \sqrt{\kappa}},$$

where κ is the "generalized perveance,"

$$\kappa = \frac{I}{17 \text{ kA}} \frac{2}{\beta^3 \gamma^3}$$

The beam current I in this case is about 100 A, and the relativistic β is nearly one. This predicts that the emittance increase occurs within around 11 cm. Since these calculations don't account for the region of lower γ near the cathode, they slightly underestimate the emittance growth and overestimate the distance scale. Reference [43] predicts a figure of 8 mm-mrad for the same input conditions. ATF simulations show that almost all of this occurs within the first half-cell.

5.2 Time-Dependent Forces

During the discussion of the rf-gun design in Chapter 2 we derived an estimate of the radial momentum kick given an electron as it exits the gun as a function of radial position. This was found to be (reverting from radius r to transverse coordinate x)

$$p_x = \frac{eE_0 x}{2c} \sin \phi_0,$$

where E_0 is the peak accelerating electric field and ϕ_0 is the launch phase of the electron. (It is actually the phase at which an already relativistic electron would have been launched to arrive at the exit at the time in question, but we may ignore the phase lag introduced by electrons starting from rest and consider them to have always been in

phase with the accelerating field. This will not affect our results.) It was noted that a finite bunch length, which has a range of phases, would exit the gun with a spread in the transverse momentum components, which would increase the phase space occupied by the entire beam. It is clear why an equivalent launch phase of 90° minimizes the this effect: the function $\sin\phi_0$ has zero slope at this phase.

Consider a beam with a Gaussian temporal profile of standard-deviation width $\sigma_\phi \ll 90°$ centered on $\phi_0 = 90°$. We may expand $\sin\phi_0$ as $1 - \phi_0^2/2$. The rms transverse emittance is then calculated from

$$\epsilon_N = \frac{1}{mc}[\langle x^2\rangle\langle p_x^2\rangle - \langle xp_x\rangle^2]^{1/2}, \tag{5.2}$$

where m is the rest mass of the electron. This yields [43]

$$\epsilon_N = \frac{eE_0}{2^{3/2}mc^2}\langle x^2\rangle\sigma_\phi^2.$$

For an average ATF case with $E_0 = 75$ MV/m, $\sigma_\phi = 5°$, and $x_{rms} = 4$ mm at the gun exit, we find an rf contribution to the emittance of 6.5 mm-mrad.

As long as there is not significant longitudinal mixing of the beam (as might be caused by space charge), the transverse phase space can be characterized as a single phase ellipse of a certain area modulated by a time-varying lens. The net area of the resulting beam is larger due to the superposition of these rotated ellipses. If they could be rotated back into the same orientation by a lens of time-dependent focal length the time-dependent-rf emittance growth could be reduced or removed. Such a technique employing radio-frequency quadrupoles has been proposed for the ATF gun [45].

To summarize the previous two sections we note two things. First, the space-charge effect is limited to the region near the photocathode while the time-dependent-rf forces are dominant at the gun exit. Second, the two effects introduce conflicting criteria for optimal gun operation in that space charge decreases with increasing rf fields while rf forces increase. Hence ideal operating conditions are achieved by striking a balance between the two. If the sample calculations given above represented a realistic set of input and output conditions, then they would represent such an optimum configuration as each predicted nearly equal emittance growth.

In practice, simulation codes such as PARMELA [46] and MAGIC [47] must be used to get more realistic results. These programs numerically simulate the passage of a group of "superparticles," each representing many electrons, through the gun cavity. They allow the effects of the space charge and rf forces to be explicitly calculated.

As an example, the following input conditions were modelled using both codes. The laser pulse had an rms radius of 1.25 mm, rms pulse length of 5 psec, and an rf phase of 52° (chosen to minimize output emittance). A nanocoulomb of charge was ejected into a peak accelerating field of 72 MV/m. The PARMELA [6] and MAGIC [48] results are compared in Table 5.1. The results are similar to the simplified analytic calculations presented above.

Unfortunately these simulations become increasingly difficult as the emittance becomes small. The results obtained for calculations of the ATF gun by these and other codes vary by as much as a factor of two depending on input conditions. There has

Table 5.1: PARMELA and MAGIC simulations of the ATF rf gun

Parameter	PARMELA	MAGIC
Momentum p (MeV/c)	3.5	3.5
$x_{\rm rms}$ (mm)	1.9	3.4
$x'_{\rm rms}$ (mrad)	14.8	14.8
$\epsilon_{\rm N}$(mm-mrad)	7.2	6.8
$z_{\rm rms}$ (mm)	1.25	1.25
$\Delta p/p$ (%)	0.4	0.7

been much more opportunity to compare codes amongst themselves than to experimental data. Experimental validation is strongly needed and fortunately is now becoming feasible.

5.3 Nonlinear Optics

In Chapter 3 it is noted that forces that depend linearly on the beam coordinates act effectively as lenses and only change the orientation of the phase space ellipse as defined by the second moments of the beam distribution. (For simplicity we confine our analysis to the two-dimensional space (x, p_x) or (y, p_y).) Forces that are nonlinear in the transverse coordinates do not change the true area of the phase-space distribution, but can introduce distortions that make the apparent emittance larger.

It was stated in Chapter 2 that the rf gun introduces nonlinear field components that have Fourier coefficients of less that 15% that of the fundamental. Design studies [2] verified that these fields contributed less emittance growth than the other effects discussed above.

The optical elements in the beamline also introduce nonlinear forces. This can be modelled with the help of beamline design codes such as TRANSPORT [49] and TURTLE [50], which use the matrix methods of paraxial optics but can include second-order effects. The design of the electron beamline relied heavily on such programs in order to minimize emittance increase. Among the elements that have to be considered are quadrupoles, dipole fringe fields, and chromatic-dispersion effects after the first dipole.

As an example of a higher-order effect, consider a quadrupole focusing a beam with a finite momentum spread $\Delta p/p$. The angular deflection imparted to an electron depends on the momentum; the focal length is momentum-dependent. This effect, like the optical analog in which the focal length of a lens depends slightly on the wavelength of the light, is called "chromatic aberration." The emittance growth produced in this manner is similar to that caused by time-dependent forces: a beam initially contained in a single transverse phase ellipse undergoes phase-ellipse rotations that vary with the particle momentum. The resulting whole-beam phase space is larger than before.

The emittance caused by chromatic aberration was calculated for a sample low-energy beamline tune using the program TURTLE. This is a ray-tracing code that simulates the passage of individual particles through the beamline using first- and second-order transfer matrices for each optical element. Even when performing only a first-order simulation the effect of a quadrupole on each electron is calculated explicitly in terms of its momentum. As such it simulates chromatic dispersion to all orders. For the tune simulated (which is described in more detail in Sec. 8.4) an initial normalized emittance of 4 mm-mrad increased by 22%, all of which occurred in the first quadrupole, Q1. This is understandable in that Q1 is operated at a strength of 2-4 times stronger than any other quadrupole in the beamline in order to focus rapidly the widely diverging beam issuing from the gun.

5.4 Issues Relating to Emittance Definition

We have seen how important the normalized emittance is as a beam characteristic. A great deal of attention is given to estimating either analytically or through simulations the effect of various forces on the emittance. In this context some care must be exercised in defining the emittance. A frequent choice is Eq. (5.2), the rms normalized emittance. As discussed in Chapter 3, the utility of this quantity derives from the conservation of phase-space area under certain conditions that we try to emulate in beam transport systems.

What is sometimes forgotten is that the momentum in the emittance definition is the *canonical* momentum, which in the presence of a vector potential $\boldsymbol{A}$ is given by

$$p = \gamma\beta mc + eA/c.$$

Reference is sometimes made to emittance "oscillations" occurring within an rf gun. This is usually just the effect of ignoring the oscillating vector potential of the rf fields when calculating the emittance; upon restoring this piece of the canonical momentum the effect disappears. This is only important within an rf structure. Within the field-free regions of the beamline, and even within the comparatively weak fields of magnetic optical elements, only the kinetic part of the momentum is relevant.

Another issue that has arisen in more than one context is the question of whether the emittance is defined with respect to a fixed time or fixed longitudinal position. For example, when we measure the emittance in the lab, we certainly measure it at a fixed location, so that each longitudinal section of the beam propagates to the same point, *i.e.*, the profile monitor, before it is integrated into the whole-beam profile. But when particle simulations are used to calculate the emittance at some point in the gun, the usual procedure is to step through a fixed time interval, stop the simulation, and calculate Eq. (5.2) for the beam ensemble, which is spread out over a finite length.

In order to get a feel for the order of magnitude of any potential discrepancy, a simple model was used to calculate both the "fixed time" emittance ϵ_t and "fixed position" emittance ϵ_z. The beam distribution in the transverse "trace space" (x, x') was taken to be a uniform, hard-edged ellipse of area $\pi\epsilon_0$ that was the same everywhere along the beam when measured at a fixed location $z = 0$. In other words, a geometric emittance

measurement performed with a profile monitor at $z = 0$ would measure $\epsilon_x = \epsilon_0$. Longitudinally the beam is also uniform and hard edged, of length τ. We now consider the beam to be longitudinally centered on $z = 0$ at time $t = 0$ and calculate the emittance at this fixed moment in time via the definition of geometric emittance

$$\epsilon = (\langle x^2 \rangle \langle x'^2 \rangle - \langle x x' \rangle^2)^{1/2}.$$

The trace-space ellipse at any point z along the beam is simply related to that at $z = 0$ by the transformation matrix for a drift of length z (see Chapter 6). From this simple model we find

$$\epsilon_t^2 = \epsilon_z^2 + \frac{\tau^2}{12} \langle x'^2 \rangle^2.$$

Applying this to the simulation of the gun exit in Ref. [2], with $\epsilon_t = 0.8$ mm-mrad, $\tau = 1.5$ mm (taken as the FWHM of output pulse), and $x'_{\rm rms} = 28$ mrad, we find ϵ_z is 10% smaller than ϵ_t. The model is an oversimplification, but it does indicate that the question of fixed time versus fixed position may not always be a trivial one.

One also needs to be careful to distinguish this trivial effect, that at fixed time each longitudinal section of the beam has undergone a slightly different spatial evolution, from the more serious effect of true *time*-dependent longitudinal evolution, such as inside the rf gun. I believe that on occasion they have been confused in the literature with the effect that so-called "emittance increases" have been claimed to be removed with a passive device such as a simple quadrupole magnet!

Chapter 6

Beam Transport and Phase-Space Measurement

Particle-beam propagation through a series of optical elements is called *beam transport.* Below we outline a mathematical description of beam transport. In this context the methods of measuring a beam's transverse and longitudinal phase-space properties are presented.

6.1 Beam Transport

It was noted in Sec. 3.1 that a particle beam that is characterized by elliptical contours in the two-dimensional trace space (x, x') retains the shape of an ellipse under linear transformations (first-order ray optics). This leads to a convenient approach, based on matrices, to tracing the evolution of a beam through an optical system [51, 52].

Each beam particle is represented by a ray $\boldsymbol{x}_0 = (x, x')$. A linear beamline element may be represented by a 2×2 matrix R,

$$R = \begin{pmatrix} R_{11} & R_{12} \\ R_{21} & R_{22} \end{pmatrix},$$

which represents the action of the element on the particle coordinates. This is referred to as the *transfer matrix.* The ray $\boldsymbol{x}_1$ resulting from the passage of $\boldsymbol{x}_0$ through R is just given by

$$\boldsymbol{x}_1 = R\boldsymbol{x}_0.$$

The action of R is the same for all rays; it does not depend on the particle coordinates.

Recall from Sec. 3.1 that a beam may be represented by an ellipse in trace space by the equation

$$\boldsymbol{x}_0^T \sigma_0^{-1} \boldsymbol{x}_0 = 1,$$

where the beam matrix σ_0 parameterizes the second moments of the beam distribution. We would like to know how σ_0 transforms through R. Applying the identity $RR^{-1} = I$,

$$\boldsymbol{x}_0^T R^T (R^T)^{-1} \sigma_0^{-1} R^{-1} R \boldsymbol{x}_0 = 1,$$

$$(R\boldsymbol{x}_0)^T (R\sigma_0 R^T)^{-1} (R\boldsymbol{x}_0) = 1.$$

We rewrite this as

$$\boldsymbol{x}_1^T \sigma_1^{-1} \boldsymbol{x}_1 = 1,$$

where

$$\sigma_1 = R\sigma_0 R^T. \tag{6.1}$$

This expresses the transformation of a beam σ_0 through a beamline element, R.

The mathematical statement of phase-space conservation is that the determinant of the beam matrix be unchanged by the transformation R. This places the requirement on the form of R that it have unit determinant. The transfer matrix R_T describing a series of elements, $R_1, R_2, R_3, \ldots$ is given simply by the product of the individual transfer matrices, $R_T = \ldots R_3 R_2 R_1$. It should be noted that the matrix method is applicable to the full 6-dimensional trace space $(x, x', y, y', \Delta z, \Delta p/p)$. The transformations are then represented by 6×6 matrices and the phase-space volume is a 6-dimensional hyperellipsoid. In the present discussion we continue to decouple the various two-dimensional subspaces for simplicity.

As an example, the transfer matrix of a simple drift length L is easy to derive. A particle that has initial coordinates (x_0, x_0') will have after drifting a distance L the coordinates $(x_1, x_1') = (x_0 + Lx_0', x_0')$. This is equivalent to the matrix equation

$$\begin{pmatrix} x_1 \\ x_1' \end{pmatrix} = \begin{pmatrix} 1 & L \\ 0 & 1 \end{pmatrix} \begin{pmatrix} x_0 \\ x_0' \end{pmatrix}. \tag{6.2}$$

As another example, the most common beamline element after the drift length is usually the quadrupole magnet. A quadrupole is the magnetic counterpart of a lens, except that it acts as a focusing lens in one transverse axis and a defocusing lens in the other. In the focusing plane the transfer matrix is

$$R_f = \begin{pmatrix} \cos kL & \frac{1}{k}\sin kL \\ -k\sin kL & \cos kL \end{pmatrix}, \tag{6.3}$$

where L is the effective length of the magnet, $k^2 = eg/p$, g is the magnetic-field gradient, e is the particle charge, and p is the beam momentum. In the defocusing plane the matrix is

$$R_d = \begin{pmatrix} \cosh kL & \frac{1}{k}\sinh kL \\ k\sinh kL & \cosh kL \end{pmatrix}. \tag{6.4}$$

Computer programs such as TRANSPORT [49] are available to perform these matrix manipulations for a user-defined optical system. In addition these programs are capable of carrying out second- and third-order ray-tracing calculations and varying system parameters to achieve a specified beam condition, such as a beam waist at a given location. These programs are extremely useful in designing and understanding a beamline.

6.2 Transverse Emittance Measurement

The measurement of a beam's transverse emittance consists of determining the three second moments in trace space (beam-matrix elements) at some location and calculating

the emittance from

$$\epsilon = \sqrt{\langle x^2\rangle\langle x'^2\rangle - \langle xx'\rangle^2} = \sqrt{\sigma_{11}\sigma_{22} - {\sigma_{12}}^2}.$$

The information available is in the form of transverse spatial profiles of the beam. From a single profile of the entire beam we can determine $x_{\rm rms} = \sqrt{\langle x^2\rangle} = \sqrt{\sigma_{11}}$. There are two rather different approaches we can take to obtain the other matrix elements.

In this section we address the technique of collecting several whole-beam profiles under varying transport conditions. This is how the photoelectron emittance was measured at the ATF. In Sec. 9.4 we will discuss another method, the "pepper pot," in which the beam is selectively masked upstream of a profile monitor in order to obtain all of the required information from a single beam profile. This was tested in the ATF beamline, but not utilized for photoelectron-beam data collection.

After passing through a series of beamline elements characterized by transfer matrix R the beam has matrix σ given by Eq. (6.1). It is instructive to the write out explicitly the expression for the element σ_{11}:

$$\sigma_{11} = R_{11}^2{\sigma_{11}}^0 + 2R_{11}R_{12}{\sigma_{12}}^0 + R_{12}^2{\sigma_{22}}^0. \tag{6.5}$$

This matrix element can be measured on a profile monitor. From at least three such measurements, each with a different known transfer matrix R_i applied to σ_0, we can determine the individual matrix elements of σ_0.

While in principle only three spot-size measurements are required, often in practice more than three are collected and the data subjected to a least-squares analysis. It is helpful to rewrite Eq. (6.5) with the following notational convention: s_i is defined to be the $i^{\rm th}$ measurement of σ_{11} and

$$\varsigma_1 \equiv {\sigma_{11}}^0 \qquad \varsigma_2 \equiv {\sigma_{12}}^0 \qquad \varsigma_3 \equiv {\sigma_{22}}^0$$

$$A_{i1} \equiv (R_{11}^2)_i \qquad A_{i2} \equiv (2R_{11}R_{12})_i \qquad A_{i3} \equiv (R_{12}^2)_i.$$

Eq. (6.5) can now be rewritten in matrix form:

$$\underline{s} = \underline{A}\underline{\varsigma}.$$

The chi-squared is defined as

$$\chi^2 = \sum_{ij} \frac{(s_i - A_{ij}\varsigma_j)^2}{\xi_i^2},$$

where ξ_i is the error in determining $s_i = \sigma_{11} = \langle x^2\rangle = x_{\rm rms}$. That is, $\xi = 2x_{\rm rms}\Delta x_{\rm rms}$, where $\Delta x_{\rm rms}$ is the error on the spot-size measurement. The χ^2 is minimized by setting the partial derivative with respect to each of the ς_k equal to zero:

$$\frac{\partial\chi^2}{\partial\varsigma_k} = 0.$$

This yields the solution

$$\underline{\varsigma} = (\underline{A}'^T\underline{A}')^{-1}\underline{A}'^T\underline{s}'$$

where $A'_{ij} \equiv A_{ij}/\xi_i$ and $s'_i \equiv s_i/\xi_i$. Further simplification of this expression is not possible since A is not in general a square matrix. The emittance is then given by

$$\epsilon = \sqrt{\varsigma_1\varsigma_3 - \varsigma_2^2}.$$

The error on the emittance is given by

$$(\Delta\epsilon)^2 = \sum_{ij}\left(\frac{\partial\epsilon}{\partial\varsigma_i}\right)\left(\frac{\partial\epsilon}{\partial\varsigma_j}\right)\varepsilon_{ij},$$

where ε is the error matrix:

$$\varepsilon = (A'^T A')^{-1}.$$

For completeness, this gives

$$(\Delta\epsilon)^2 = \left(\frac{1}{2\epsilon}\right)^2(\varsigma_3^2\varepsilon_{11} + \varsigma_1^2\varepsilon_{33} + 4\varsigma_2^2\varepsilon_{22} + 2\varsigma_1\varsigma_3\varepsilon_{13} - 4\varsigma_3\varsigma_2\varepsilon_{12} - 4\varsigma_1\varsigma_2\varepsilon_{23}).$$

There are two common methods of varying the transfer matrices R_i.

One is to vary the magnetic gradient g (focusing strength) of a quadrupole magnet at a point upstream of a profile monitor. This changes the transfer matrix via Equations 6.3 or 6.4. The spot size on the monitor as a function of the gradient (or the magnet-coil current), called the *emittance plot*, provides the information necessary to extract the beam matrix at the entrance to the quadrupole. Sample emittance plots can be found in Figures 9.6, 9.7, and 9.8. Any other elements, such as drift spaces and additional quadrupoles, may be between the varied quad and the monitor as long as they are included in the calculation of the matrices R_i.

This method offers the experimenter great flexibility in choosing the number of profiles to collect and the magnitude of gradient variation between successive measurements, and as such was the most often utilized during commissioning. The precision with which the emittance can be determined is in principle limited only by the monitor resolution, as discussed in the next section.

The second method is to collect beam profiles at several different locations in the beamline, equivalent to varying L in Eq. (6.2). The analysis is particularly straightforward if no other beamline elements affect the beam between monitor locations. The main drawback to this method is that it is limited by the number of profile monitors in the beamline. Further, by relying on beam measurements taken at different locations, the results cannot be decoupled from any perturbations to the beam occurring between profile locations. In particular, such measurements at the ATF had to rely on only two monitors. Clearly this is not enough to determine all three beam parameters unless additional information is supplied.

This information is in the form of a requirement placed on the beam at one of the monitor locations, namely that it be brought to a waist. A waist is the location at which the beam spot size is a local minimum (or maximum) with respect to longitudinal position. The beam ellipse is then upright in trace space, and the matrix element σ_{12} is zero. If the beam is known to be focused to a waist at one of the monitors, then only two beam-matrix elements remain to be determined from the two spot sizes. Of course

the waist condition at one monitor is found by varying a quadrupole upstream of the monitor until the minimum spot size is observed.

Hence the two-monitor method is something of a hybrid, making use of both varied quadrupole strengths and drift distances. It is also limited in information content to only two profiles. It's strength lies in the simplicity of the analysis, requiring only a knowledge of the distance between the two monitors. It is useful to make measurements using both methods as a consistency check.

In passing, one additional caveat should be noted. While a beam waist, where σ_{12} is zero, has the minimum spot size $\sqrt{\sigma_{11}{}^{\text{waist}}}$ with respect to distance along the beamline *for a given beam tune*, it is not identical to the minimum spot size achievable *at a fixed location*, $\sqrt{\sigma_{11}{}^{\text{min}}}$, termed the *focus*. It is actually a focus that is achieved by minimizing the spot size on a monitor. When the focus location is separated from the focusing lens by a drift length, L, the waist is located a distance l upstream with l given by [52]

$$l = \frac{L}{1 + \frac{\sigma_{11}{}^{\text{lens}}}{\sigma_{11}{}^{\text{min}}}},$$

and the spot sizes are related by

$$\frac{1}{\sigma_{11}{}^{\text{waist}}} = \frac{1}{\sigma_{11}{}^{\text{min}}} + \frac{1}{\sigma_{11}{}^{\text{lens}}}.$$

We see that when the beam size at the quadrupole lens, $\sqrt{\sigma_{11}{}^{\text{lens}}}$, is much larger than that of the focus, as is usually the case, the focus and waist conditions are at very nearly the same location and have nearly the same size.

6.3 Precision and Resolution

The formula for the error on the measured emittance given in the previous section is not very illuminating. It is more instructive to consider explicitly the case of the two-monitor method, for which the analysis is quite simple. From this we will gain a better sense of how the precision of an emittance measurement is related to the uncertainty on a spot-size determination. This intuition will be applicable to other methods as well. We will then relate the emittance resolution to the profile-monitor spatial resolution.

At one monitor the beam is brought to a waist and has rms spot size $x_w = \sqrt{\sigma_{11}{}^{w}}$. At another monitor a distance L downstream of the first monitor the beam has spot size x_L. Using the transform matrix for a drift space, Eq. (6.2), in Eq. (6.5) and making the identification $\sigma_{11} = \langle x^2 \rangle$, the emittance is found to be

$$\epsilon = \sqrt{\sigma_{11}{}^{w}\sigma_{22}{}^{w}} = \frac{x_w}{L}\sqrt{x_L^2 - x_w^2}. \tag{6.6}$$

The uncertainty on the emittance, $\Delta\epsilon$, is given by

$$(\Delta\epsilon)^2 = \left(\frac{\partial\epsilon}{\partial x_w}\right)^2 (\Delta x_w)^2 + \left(\frac{\partial\epsilon}{\partial x_L}\right)^2 (\Delta x_L)^2,$$

where Δx_i the uncertainty in the measurement of x_i, which we take to be Δx, independent of the spot size. The transport parameters (in this case the drift distance L) are assumed to be known with much higher precision than the measured spot sizes. We then find

$$\frac{\Delta\epsilon}{\epsilon} = \frac{\Delta x}{x_w}\left[\frac{x_L^4 - 3x_w^2x_L^2 + 4x_w^4}{(x_L^2 - x_w^2)^2}\right]^{1/2}.$$

Consider the limiting case of $x_L \gg x_w$, as is usually the case. We then find

$$\frac{\Delta\epsilon}{\epsilon} \simeq \frac{\Delta x}{x_w},$$

from which we learn that the precision on an emittance measurement is limited by the precision with which the smallest spot size can be determined. Now consider the other limiting case in which the two spot sizes differ by very little: $x_L = x_w + \delta$, where $\delta \ll x_w$. Then

$$\frac{\Delta\epsilon}{\epsilon} \simeq \frac{1}{\sqrt{2}}\frac{\Delta x}{\delta}.$$

In this case the precision is not limited by the ability to determine the smallest spot size, which is probably much larger than Δx, but by the ability to determine the angular divergence of the beam, δ/L, which is small.

An analysis of the emittance error in a three-monitor measurement [53], in which none of the profiles are assumed to be at a beam waist confirms these findings and provides further insight. The error increases with the distance between the beam waist and the nearest monitor. As expected, the minimum error occurs when the waist is located at one of the monitors, and this minimum is a function of the ratio of monitor resolution to minimum spot size. For given emittance and distance between monitors, this minimum is also a function of the minimum spot size (in other words, of the beam tune), indicating an optimum between a tiny waist size with large divergence and larger waist with small divergence. Finally, the smallest possible error for a fixed beam tune was found to decrease with increasing distance between monitors.

These results can be summarized so as to be applicable to a quadrupole-scan measurement as well. The following conditions should be met in order to make an emittance measurement as precise as the instrumentation will allow:

- The beam waist should be included within the measurement, with one of the spot sizes as close to a waist as possible.
- The region around the waist should be sampled in small enough steps to determine the curvature of the spot size as a function of transport condition as well as the location of the waist. (Roughly speaking, this corresponds to determining the beam-matrix elements σ_{11} and σ_{12}.)
- The region around the waist should be sampled far enough away from the waist to determine the asymptotic behaviour of the beam (determination of σ_{22}).
- The precision of the measurement is limited by ratio of the spot-size uncertainty to the smallest spot size measured.

Beamline experience and numerical simulations of emittance measurements both confirmed these general findings.

The uncertainty in a spot-size measurement may be due in part to beam fluctuations in time. The limiting precision is determined by the profile-monitor spatial resolution σ_x, the smallest spot size that can be measured. The emittance resolution is the error in the emittance measurement due to the monitor resolution.

The contribution of the monitor resolution to a two-monitor emittance measurement can be calculated by returning to Eq. (6.6), recalling that the resolution adds in quadrature to the measured spot sizes. If x_w is the true beam size at the waist and $x_{w,m}$ is the measured value, then $x_{w,m}^2 = x_w^2 + \sigma_x^2$. Rewriting Eq. (6.6) for the measured emittance ϵ_m we find

$$\epsilon_m^2 = \frac{x_w^2 + \sigma_x^2}{L^2}(x_L^2 - x_w^2) = \epsilon^2 + (\Delta\epsilon)^2 \simeq \epsilon^2 + \left(\frac{\sigma_x x_L}{L}\right)^2, \tag{6.7}$$

in the limit $x_L \gg x_w$.

A similar analysis for a quadrupole scan yields the formula:

$$\epsilon_m^2 \simeq \epsilon^2 + \left(\frac{\sigma_x x_Q}{R_{12}}\right)^2, \tag{6.8}$$

where x_Q is the spot size at the entrance to the quadrupole and R_{12} is an element of the transfer matrix between the quadrupole and the monitor. Hence the monitor resolution gives a contribution to the emittance which adds in quadrature with the intrinsic beam emittance and which determines the smallest emittance we can diagnose.

6.4 The rf Kicker Cavity

Temporal measurements of picosecond accuracy are difficult. With the development of ultrashort (few-picosecond and sub-picosecond) laser pulses, several techniques with the required temporal resolution have been developed, including nonlinear autocorrelation methods [54] and the picosecond streak camera [55]. Streak-camera measurements of the Nd:YAG-laser beam are discussed in Sec. 8.6. This section will describe a method of measuring the pulse length of the photoelectron beam using rf deflection. The pulse lengths so obtained were used in conjunction with transverse emittance to calculate the beam brightness. In the next section the use of this technique as part of a longitudinal emittance diagnostic will be discussed.

The primary temporal beam diagnostic consists of a resonant rf cavity placed in the beamline in conjunction with a profile monitor downstream. This "kicker" cavity introduces a time-correlated vertical deflection, thereby transforming the time profile of the beam into a vertical one, as illustrated in Fig. 6.1. The vertical profile is measured at the beam-profile monitor.

The ATF kicker cavity was designed and built by Varian during the 1960's for use as a beam chopper at the Frascati linac [56], based on an analysis of such cavities by Haimson [57]. It is designed to be operated in the TE_{102} mode at 2856 MHz. The electric- and magnetic-field lines for this mode are shown schematically in Fig. 6.1. Taking the

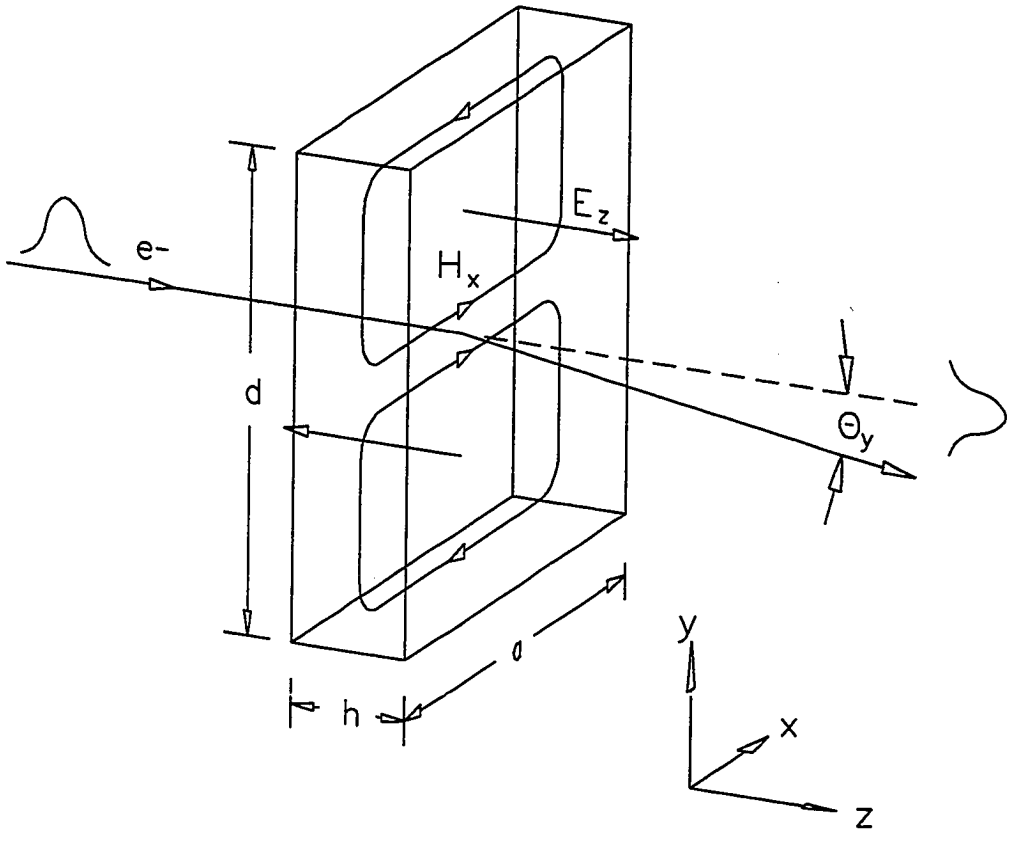

Figure 6.1: The rf kicker cavity. The radio-frequency magnetic field on the beam axis induces a time-correlated deflection.

coordinate origin to be center of the cavity, the fields are given by

$$\begin{aligned} E_z &= E_0 \cos\left(\frac{\pi x}{a}\right) \sin\left(\frac{2\pi y}{d}\right) \cos\omega t \\ H_x &= -\frac{\lambda}{d} E_0 \cos\left(\frac{\pi x}{a}\right) \cos\left(\frac{2\pi y}{d}\right) \sin\omega t \\ H_y &= -\frac{\lambda}{2a} E_0 \sin\left(\frac{\pi x}{a}\right) \sin\left(\frac{2\pi y}{d}\right) \sin\omega t, \end{aligned}$$

where E_0 is the peak electric field, and the transverse cavity dimensions d and a are as shown in the figure. In this mode the wavelength λ must satisfy the condition

$$\lambda = \frac{2ad}{\sqrt{4a^2 + d^2}}. \tag{6.9}$$

Now consider the effect of these fields on an electron traveling along the $+z$ axis with velocity $v \simeq c$ and transverse coordinates (x,y), where $x \ll a$ and $y \ll d$. The

components of the Lorentz force are given by

$$\begin{aligned} F_x = \quad -eH_y \quad &\simeq \frac{\lambda}{2a}\frac{\pi x}{a}\frac{2\pi y}{d} eE_0 \sin\omega t \\ F_y = \quad eH_x \quad &\simeq \frac{\lambda}{d} eE_0 \sin\omega t \\ F_z = \quad eE_z \quad &\simeq \frac{2\pi y}{d} eE_0 \cos\omega t. \end{aligned}$$

If the particle was at $z = 0$ at time t_0 then it entered the cavity, of longitudinal extent h, at time $t_{\rm in} = t_0 - h/2c$ and left the cavity at time $t_{\rm out} = t_0 + h/2c$. The momentum kick it received is

$$\Delta \boldsymbol{p} = \int_{t_{\rm in}}^{t_{\rm out}} \boldsymbol{F}\, dt.$$

The x component of this kick is negligible. The other two components relative to the longitudinal momentum $p_z \simeq \gamma mc$ are

$$\frac{\Delta p_y}{p_z} \simeq \frac{2\lambda}{d}\frac{\eta}{\gamma}\sin\left(\frac{\pi h}{\lambda}\right)\sin\phi_0 \tag{6.10}$$

$$\frac{\Delta p_z}{p_z} \simeq \frac{4\pi y}{d}\frac{\eta}{\gamma}\sin\left(\frac{\pi h}{\lambda}\right)\cos\phi_0, \tag{6.11}$$

where $\eta = eE_0/m\omega c$, $\phi_0 = \omega t_0$, and $\omega = 2\pi c/\lambda$.

As a pulse-length diagnostic, the kicker is operated such that the center of the bunch crosses the cavity at $t_0 = 0$, when there is no net y deflection. The position of electrons in the bunch are characterized by their distance from the center of the bunch, Δz, so that for pulse lengths much shorter than a single rf cycle,

$$\sin\phi_0 \simeq \phi_0 = -\frac{2\pi\Delta z}{\lambda}$$

$$\cos\phi_0 \simeq 1.$$

This gives for the relative momentum kick

$$\begin{aligned} \frac{\Delta p_y}{p_z} &\simeq -k\Delta z \\ \frac{\Delta p_z}{p_z} &\simeq ky, \end{aligned}$$

where

$$k = \frac{4\pi}{d}\frac{\eta}{\gamma}\sin\left(\frac{\pi h}{\lambda}\right).$$

Hence the cavity gives a transverse kick in y related to the longitudinal (temporal) position, but also a kick in longitudinal momentum related to the y position by the same factor. This complicates the simultaneous measurement of Δz and $\Delta p_z/p_z$ as will be discussed in the next section.

Table 6.1: rf kicker parameters

λ	10.4 cm
a	12.098 cm
d	10.586 cm
h	1.597 cm
Q	4500

The cavity dimensions were determined by the resonance condition, Eq. (6.9), and by certain optimization criteria. Chief among these was maximization of the peak magnetic-field component $H_x^{\max} = \lambda E_0/d$ obtained per unit input power. The parameters of the ATF kicker cavity, including the optimized dimensions, are shown in Table 6.1.

The kicker was calibrated for a given input rf power and beam energy by varying the input rf phase ϕ_0 through 360° and observing the vertical deflection of the beam position on a profile monitor a known distance downstream. For comparison with the above calculations, it is convenient to recast Eq. (6.10) in a more convenient form. For Δp_y kicks small compared to the beam momentum p_z we may write

$$\theta_y \simeq \frac{\Delta p_y}{p_z} \simeq \theta_y^{\max} \sin\phi_0$$

where

$$\theta_y^{\max} = \frac{2\lambda}{d}\frac{eE_0}{\gamma m\omega c}\sin\left(\frac{\pi h}{\lambda}\right). \tag{6.12}$$

We would like to know $\theta_y^{\max}$ in terms of quantities we can measure, namely the input power to the cavity. The total energy U stored in a TE_{102} cavity with peak field E_0 is (in rationalized MKSA units)

$$U = \frac{ahd}{8}\epsilon_0 E_0^2,$$

where ϵ_0 is the permittivity of free space. The quality factor Q is a measure of the power P required to maintain the cavity fields against the resistive losses in the cavity walls. It is defined as the stored energy divided by the energy lost per rf cycle, $Q = \omega U/P$. It depends solely on the cavity dimensions and the surface resistance of the material from which it is made. When the definition for Q and the expression for stored energy are inserted into Eq. (6.12) and the result numerically evaluated, we find

$$\theta_y^{\max} = \frac{1.30\times10^{-5}}{\gamma}\sqrt{PQ}, \tag{6.13}$$

where P is in watts. The kicker factor k defined above is just

$$k = \frac{2\pi}{\lambda}\theta_y^{\max}.$$

Fig. 6.2 shows a calibration performed using dark current. The momentum slit, serving as a profile monitor, was 800 mm downstream of the kicker. The data are fitted to a sine wave, shown as the smooth curve. The maximum centroid deflection is 9.35 mm, corresponding to $\theta_y^{\max} = 11.5$ mrad. The beam momentum was 3.3 MeV and the input power to the kicker was measured to be 13 kW. From Eq. (6.13) we would expect $\theta_y^{\max} = 15.1$ mrad. Given the difficulties associated with accurately measuring rf power, this is deemed reasonable agreement. The centroid shifts clearly exhibit the sinusoidal dependence on the rf phase. The error bars indicate the measured vertical spot size at each phase. Notice that the size varies from a minimum at maximum deflection to a maximum at the zero crossing, where the kicker is intended to operate as a pulse-length diagnostic. The slope at the zero crossing is proportional to the kicker factor k.

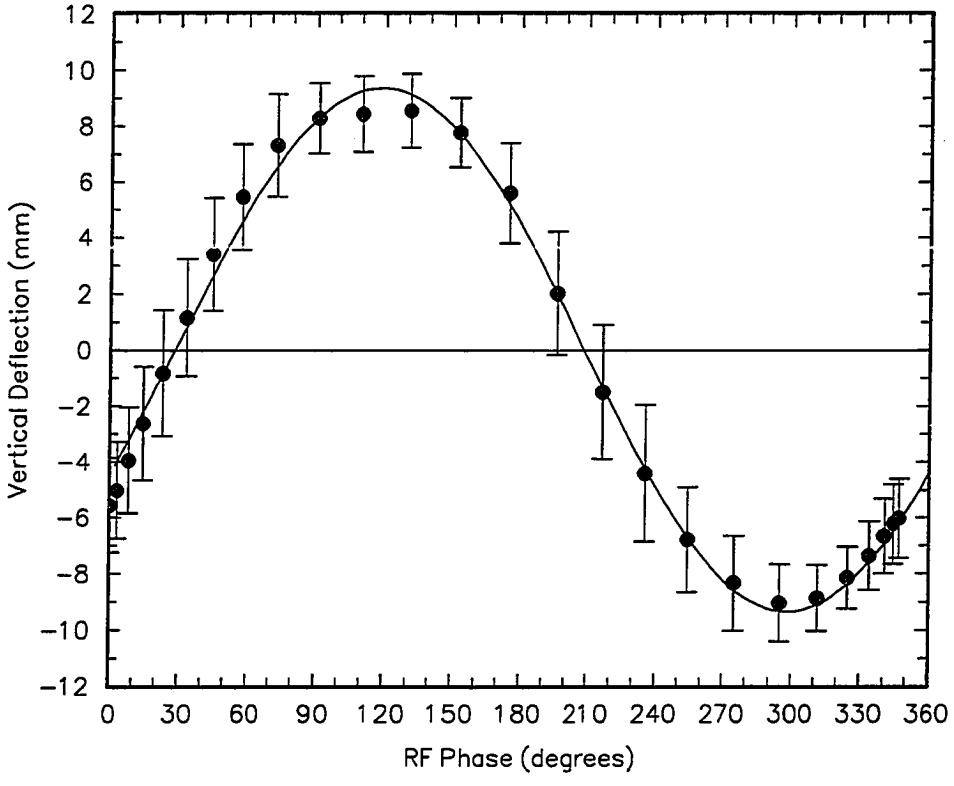

Figure 6.2: Calibration data for the rf-kicker cavity showing the vertical centroid deflection of the dark current pulse as a function of input phase. The error bars are actually the measured vertical spot size. Note the maximum size occurs at the minimum deflection and *vice versa*.

This is, in fact, how the kicker was calibrated for temporal measurements. The

position and spot size of the beam were measured with the kicker off. The kicker was turned on and the rf phase to the kicker varied until the beam centroid returned to the off position. This was defined as zero phase. The centroid shift was recorded for several phases within about 20° of the zero point. This slope was recorded as the kicker factor.

The spot size was again measured with the kicker on at zero phase. The kicker-off width was subtracted in quadrature from the kicker-on width and the pulse length extracted. The kicker factor determined from these data was 0.67 mrad/mm (0.21 mrad/ps). (We refer to beam-pulse lengths by either the spatial length Δz or the temporal length $\Delta t = \Delta z/c$ interchangeably.) This translated into a vertical deflection on the profile monitor of 0.165 mm/psec. From this calibration data the dark current was found to have an average rms width of 11 psec per rf cycle.

The rms spot size with the kicker off was 1.1 mm. The minimum quadrature contribution that can be resolved is about 0.5 mm, which would increase the spot size to 1.2 mm. This gives a resolution of about 3 psec. Sub-picosecond resolution should be possible by using profile monitor BPM1 or BPM2 in the 'Z'-line (Fig. 2.4), but such beamline tunes were not found during commissioning.

6.5 Longitudinal Emittance Measurement

The longitudinal emittance may be obtained from a simultaneous measurement of both longitudinal trace-space variables, momentum spread $\Delta p/p$ and pulse length Δz. This is done by examining the beam profile on a profile monitor in the 'Z'-line (Fig. 2.4) with the rf kicker on. The momentum spread is dispersed along the horizontal axis, and the time structure along the vertical, allowing the longitudinal phase ellipse and emittance to be measured in a single beam pulse.

A complication is introduced by the fact that the kicker has an unavoidable second effect on the beam. The kicker produces a vertical deflection given by

$$\theta_y = -k\Delta z,$$

where Δz is the longitudinal position relative to the center of the beam. In addition, a longitudinal momentum kick is given of the form

$$\frac{\Delta p}{p} = ky.$$

We can rearrange these two expressions as

$$\Delta z \frac{\Delta p}{p} = -y\theta_y,$$

independent of the kicker factor k.

What this tells us is that the resolution on the longitudinal emittance is limited by the vertical geometric emittance of the beam at the kicker. We would like 0.1% resolution in momentum spread and picosecond resolution in time, corresponding to 0.3 mm in Δz. This indicates we must have a geometric emittance of under 0.3 mm-mrad (which at 3.5 MeV is a normalized emittance of around 2 mm-mrad) before we can resolve the

longitudinal phase space. The electron beam is known to have a transverse emittance at least twice as large.

The solution is to collimate the beam vertically just before it enters the kicker. This decreases the vertical emittance at the cost of some beam loss. A slit just upstream of the kicker, however, would obstruct the Nd:YAG laser on its way to the photocathode (see Fig. 2.4). The way around this is to place a vertical collimator downstream of dipole D1 and arrange the beam optics to produce a point-to-point image of the kicker at the collimator. In this way the same particles that would have been collimated by a slit at the kicker are instead collimated at the image. The chosen location for the slit is between the second dipole (D2) and quadrupole ZQ1 (see Fig. 2.4). Beamline simulations using TRANSPORT indicate that a solution to the optical problem of simultaneously imaging the kicker onto the slit and producing an appropriate image on profile monitor BPM1 can be obtained with the present beamline.

Chapter 7

The Beam-Profile-Monitor System

One of the primary goals of the ATF is the production, preservation, and study of very high-quality electron beams. Hence we are interested in diagnosing the nature of the beam delivered by the rf gun and the effect of subsequent transport on that beam. The beam parameters of interest can be summarized as follows:

- Energy and momentum
- Bunch charge
- Transverse spatial information, including beam position, profile, and transverse emittance
- Longitudinal (temporal) information, including pulse length and longitudinal emittance
- Transverse profile of the laser driving the rf gun

Other quantities, such as brightness, can be derived from these. The beam-profile-monitor (BPM) system plays a key role in each of these measurements. It is the subject of this chapter.

7.1 Requirements

The purpose of the beam-profile-monitor system is to provide detailed spatial information about the electron beam. This information is used in a variety of ways. Several spatial profiles can be analyzed to yield the transverse emittance, as described in Chapter 6. When making beam-charge measurements it is useful to have direct visual verification that the beam spot is well contained on the charge-collection device. Similarly, proper momentum selection requires knowledge of the beam profile and position on the momentum-selection slit. Finally, the beam position and profile at certain locations afford direct information about the alignment and orientation of the magnetic elements and collimators upstream.

In brief, the beam-profile-monitor system consists of a number of fluorescent screens placed in the beam and viewed by video cameras, the output of which are coupled to a computer-based video-signal processing device. Below are listed the important characteristics of such a system with a brief assessment of the ATF requirements.

Spatial resolution: A profile monitor must be capable of resolving the smallest spatial profiles encountered. Simulations of the rf gun and low-energy transport indicated the smallest profiles would have rms sizes of around 100 μm.

Spatial linearity: The output intensity for a given incident beam flux should not be a function of position on the monitor.

Dynamic range: It should be possible to profile beams over several orders of magnitude in intensity in order to accommodate a wide variety of beam conditions. For the ATF high-current mode this should include beams with about 10^8 to 10^{11} electrons spread over areas of from 1 mm^2 to 1 cm^2.

Intensity linearity: The output intensity should vary linearly with incident beam intensity over the entire dynamic range.

Sensitivity: The profile-monitor components must be sensitive enough to measure beams at the low end of the dynamic range. A low-current mode of operation will produce beam intensities several orders of magnitude lower than the normal mode, for which the BPM system is designed. There must be provision for a high-gain device to raise the sensitivity to the proper level.

Low noise: The total system noise should be low enough so as not to seriously degrade the signal at low levels.

Convenient data access: The information collected by the profile-monitor system must be presented to the ATF operators and experimenters in the control area in a form that is easy to interpret and subject to further analysis. Some form of archiving all collected beam profiles is required.

Remote operation: The profile monitors must be operated remotely as they are in a radiation environment and under heavy shielding. This includes the ability to place them in or out of the beamline and change any sensitivity controls.

Radiation hardness: The parts of the profile monitors that are in or near the electron beamline must be resistant to damage caused by electron and x-ray bombardment. In particular the part that intercepts the beam must withstand pulses of up to 10^{11} electrons/mm^2 at a rate of 3 Herz for hundreds of hours.

Vacuum compatibility: The beamline is held under vacuum of around 10^{-9} torr. Those components in the beamline must outgas little enough to be compatible with this level.

Each of these qualities will be discussed below.

7.2 Hardware

The beam-profile monitor designed and built for the ATF is shown in Fig. 7.1. A phosphor screen intercepts the electron beam and emits light in proportion to the incident electron intensity. The light is deflected out of the beamline by a 45° mirror and is collected and focused into a CCD video camera by a pair of lenses. The mechanical-engineering design was provided by Stan Ulc of the Brookhaven Physics Department.

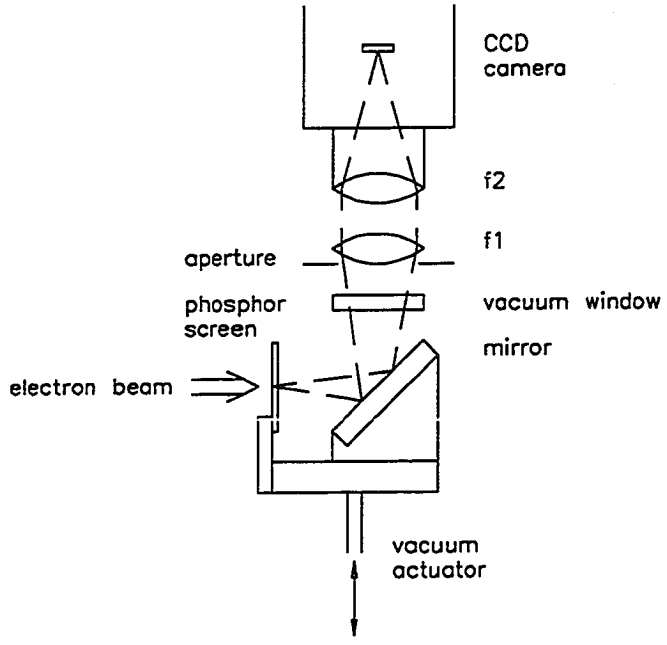

Figure 7.1: The beam-profile monitor

The phosphor[1] is terbium-activated gadolinium oxysulfide (Gd_2O_2S:Tb), designated type GY by the cathode-ray-tube industry. This phosphor was selected for its high conversion efficiency, its ability to form layers of uniform thickness, its linearity, and its ability to resist radiation damage. One photon is produced for approximately each 20 eV of deposited energy. The emission spectrum is sharply peaked in the green at 545 nanometers. The decay time to 10% of initial excitation is 1.2 milliseconds [58], as verified by photomultiplier-tube tests. It comes in powder form, with an average particle size of 10 μm, and a bulk density of 3 g/cm^3 [59]. It does not exhibit any degradation in performance until an integrated flux of about 10^{17} electrons/mm^2 and maintains linearity through charge densities of as high as 10^{12} electrons/mm^2 within a pulse much shorter than the 1.2-msec phosphor decay time [60]. This linearity limit

[1]Type 2611 x-ray intensifying phosphor, GTE/Sylvania Chemical and Metallurgical Division, Towanda, PA.

exceeds any beam observed or anticipated at the ATF. The damage limit corresponds to about 10^7 highly focused beam pulses.

A 30-μm-thick layer of phosphor was deposited on 25-μm-thick aluminum foil using the settling technique recommended by GTE/Sylvania [61]. The appropriate thickness was determined by the conflicting requirements of light output and resolution. As will be discussed below, a 30-μm thickness is adequate for ATF beams, while a thicker layer would only degrade the spatial resolution. Layers thinner than 30 μm suffer from serious nonuniformities caused by grain size. The uniformity of the 30-μm layer was observed under a microscope to be indeed limited only by the phosphor grain size.

The phosphor side of the screen faces the mirror, the thin foil allowing unattenuated passage of few-MeV electrons. A high-optical-quality mirror[2] oriented at 45° to the beamline deflects the phosphor light 90° out of the beamline. The half-inch-thick aluminum substrate of the mirror destroys the beam, so the screen-mirror assembly is mounted on an actuator that can move it out of the beamline when not in use. The actuator is a stepper-motor-driven motion feedthrough[3] with a vacuum bellows. The screen-mirror assembly employs a kinematic mount to assure reproducible placement in the beamline. All mechanical components are made of stainless steel to maintain good vacuum properties.

A vacuum window[4] separates the screen-mirror assembly from the light-collection optics and camera. The profile-monitor optics consist of a pair of commercial camera lenses configured to maximize light collection. The first lens has focal length f_1 and is mounted backwards just outside the vacuum window so that the phosphor screen is at the back focal plane when positioned in the beamline. The light rays originating from a point on the screen are imaged into parallel rays. These rays are collected by the second lens, of focal length f_2, which is a 'C'-mount video lens on the CCD camera. The phosphor screen is thus imaged onto the CCD with magnification f_2/f_1. The aperture of lens f_2 is motorized and computer controlled. This permits several orders of magnitude in beam intensity to be imaged without saturating the video signal.

The lenses chosen for the ATF profile monitor were a Nikkor SLR lens with f_1 = 35 mm and maximum aperture $f_1/1.4$, and a Schneider Xenar lens with $f_2 = 25$ mm and maximum aperture $f_2/0.95$. These lenses have well-matched maximum apertures, which avoids vignetting of the image. The Schneider lens, the aperture of which is motorized, can be closed completely. The beam profiles are demagnified by a factor of 25/35.

7.3 Electronics

The BPM image is converted by the camera to a signal conforming to the RS-170/330 video standard, which prescribes 30 frames per second, each frame containing 480 rows. Each frame consists of two video "fields," each of 240 lines, one field containing the odd-numbered lines and the other the even lines. Each field is updated every 33 msec (30

[2]Part number F-1.5-CAL, Diamond Electro-Optics, Wilmington, MA.

[3]Model VZSLMD50, Vacuum Generators, East Sussex, United Kingdom.

[4]Part number 44990, 2"-diameter etalon, coated both sides with #79730 antireflective coating for 0.55 μm, Oriel Corporation, Stratford, CT.

times a second), but offset from the other field by 16.5 msec. This is called "interleaving." The video signal is stored and processed by a framegrabber under computer control. The ATF video data analysis system is outlined in Fig. 7.2.

Video cameras based on the charge-coupled device (CCD) were chosen because of their good sensitivity and noise characteristics. Profile-monitor development was performed using a modification[5] of a Sony camera using the Sony ICX018CL interline-transfer CCD chip. The CCD sensing area is 8.8 mm wide × 6.6 mm high with a format of 510 horizontal × 492 vertical pixels, each of size 17 × 13 μm. It is sensitive to a minimum illumination of 3 lux, which corresponds to around 20,000 photons per pixel, and has a dynamic range of about 200. The amplifier was rebuilt to reduce electronic noise, and the ability to integrate an integral number of video frames under computer control was added. A Peltier cooler capable of lowering the CCD temperature to −30° C was incorporated into the CCD and readout electronics. This camera was used to study the noise, sensitivity, and resolution of the profile-monitor system and was installed in the first profile monitors. It has since been replaced by a different model[6] that uses an improved Sony CCD (ICX022) of the same size with a higher sensitivity and lower noise than the older chip, and a pixel format of 758 horizontal × 492 vertical.

Cooling was found to be unnecessary for ATF applications, as discussed below. Integration was likewise deemed unnecessary. A single video frame of 33 milliseconds is clearly sufficient to accept all of the light from a phosphor with a 1-msec decay time. For viewing events shorter than a video frame, an issue regarding CCD readout becomes significant. Due to the interleaving of the video signal, only every other row is read out during a given field. In some CCD's the accumulated charge in the rows not being read out are lost during the readout process. Hence each field contains charge collected for only 16.5 msec. In the Sony CCD's used in BPM cameras each field is collected for the full 33 msec before being read out. Otherwise a 1-msec event would only be captured on one field, effectively utilizing only half of the CCD's sensitive area.

The computer is an IBM PC-AT clone using an INTEL 80386 central processing unit with a clock speed of 16 MHz. An 80387 math coprocessor accelerates floating-point operations. The PC has two megabytes RAM memory and two hard disks, one with 80 megabytes storage and one with 40 megabytes. The 80-Mbyte disk is used to store system software, while the 40-Mbyte disk is dedicated to video-data storage.

The framegrabber serves the role of digitizing each video image and making the data available to the computer for analysis. Development work was done on the PCVISION*plus* Frame Grabber.[7] This has subsequently been upgraded to the VISION*plus*-AT Overlay Frame Grabber, a similar unit with additional features. These devices consist of two 512 × 480 × 8-bit video memories. A flash ADC digitizes each of the 480 horizontal rows into 512 pixels, each 8 bits deep. Hence a stored video image is an array of bytes 480 rows by 512 columns, or just under a quarter megabyte of data. The 8-bit pixel depth gives the framegrabber a dynamic range of 256:1. Two video images can be stored in framegrabber memory. The current video image, or "frame," is displayed on a standard video monitor. The framegrabbers are capable of simultaneously digitizing

[5]Model LPQ210, Patterson Electronics, Tustin, CA.
[6]Model TM-745E, PULNiX America, Inc., Sunnyvale, CA.
[7]Imaging Technology, Inc., Bedford, MA.

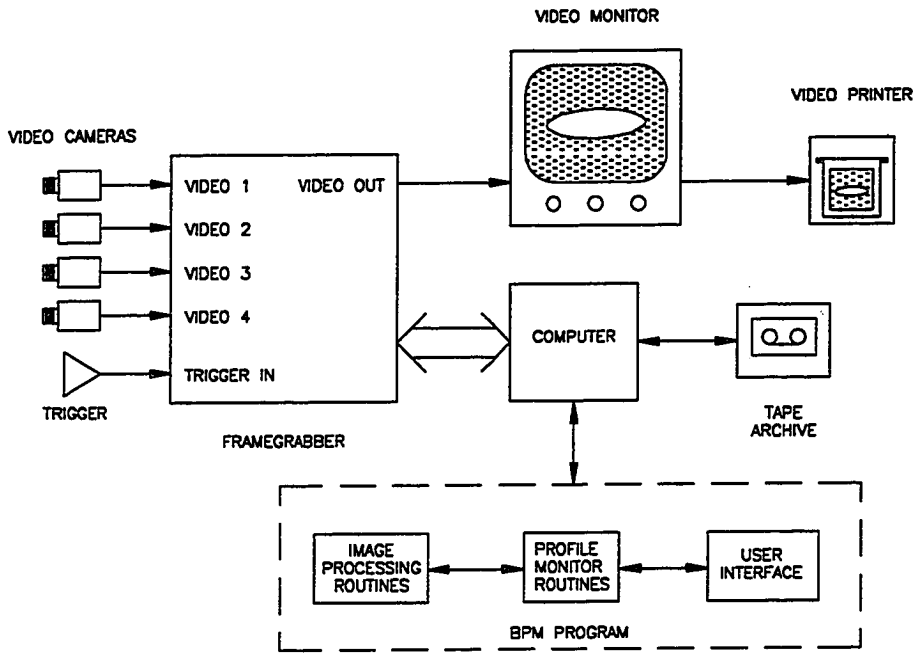

Figure 7.2: Block diagram of beam-profile-monitor electronics and video signal processing. One of four video-camera inputs is selected for digitization and display under computer control. The data is made available to the user for analysis. Images can be printed on a thermal printer and archived to tape.

and displaying the video signal in real time, but can be instructed to "freeze" a given image for analysis.

At this point a distinction needs to be drawn between a framegrabber pixel and a CCD pixel. While the RS-170/330 standard defines the timing structure of the 480 video rows, it does not define a pixel structure within each row. Unless a separate pixel-clock signal is provided by the camera and referenced by the framegrabber, there is not in general a one-to-one correspondence between the CCD pixels and digitized framegrabber pixels. Henceforth the term pixel will refer to framegrabber memory. From the known optical magnification and pixel timing, the effective size of each pixel at the profile monitor is easy to calculate. The size calibration was verified by placing fiducial marks on BPM screens.

The VISION*plus*-AT Overlay Frame Grabber can accept input from four cameras. A computer-controllable multiplexer selects one channel for digitization and display. An external trigger input is also available that allows the next video frame following the trigger to be frozen in memory until the next trigger. When given a suitable pretrigger related to ATF system timing, the video monitor displays a continuous beam profile without flicker which is updated on each beam pulse. This aids the operator in tuning

the beam, as incremental changes in profile are more easily perceived. Pulse-to-pulse variations are easier to detect as well. A chosen profile can be saved for analysis and/or archiving by pressing a key on the computer keyboard before the next pulse.

In addition to the 8 bits containing the stored intensity of each pixel, an additional 4 bits are available for "overlays." This provides the capability of nondestructively displaying auxiliary information such as text or a calibrated scale.

The processed video signal is also available to a video graphics printer,[8] which produces a small thermal print of the image. This was used primarily for logging purposes. Those images that were to be subjected to further off-line analysis or recalled at a later date for comparison were stored on the hard disk. At a quarter megabyte per image, it does not take long to fill the disk. Image files were permanently archived onto magnetic tape[9] automatically after each day's run. Each tape was formatted to contain 40 Megabytes of data and with compression could hold over 80 Megabytes, or about 350 image files.

7.4 Software and Data Analysis

The software for the profile-monitor system contains a hierarchy of routines as indicated in Fig. 7.2. At the highest level is the computer operating system. At the next level is the profile-monitor user interface, through which an operator requests and obtains data about the beam. This is constructed from high-level language routines for device control and data analysis. These routines in turn make use of lower-level routines that control the basic functions of key system components such as the framegrabber. The operating system[10] is DOS version 4.01. Programming was done using the Microsoft languages C version 5.1, FORTRAN version 5.00, and ASSEMBLER version 5.00. Many of the data-analysis routines were drawn from Ref. [62].

Access to data and control of the framegrabber is performed by programming a group of input/output registers. The software developed for the original framegrabber consisted of higher-level analysis routines written in C that called a group of low-level assembler routines [63]. When the framegrabber was upgraded, the opportunity was taken to replace the assembler routines with a library of C-callable framegrabber-control and video-analysis routines available from Imaging Technology [64]. This resulted in a more completely documented system which is better suited to future upgrade and alteration.

The beam-profile-monitor user-interface program, BPM, provides both on-line and off-line analysis capabilities. A sample of the main menu screen is shown in Fig. 7.3. The program provides the following control functions:

Triggered Video: freeze each frame following system trigger

Snap a Frame: freeze a single frame

[8]Model UP-811N, Sony Corporation, Paramus, NJ.

[9]JUMBO 120 Tape Backup System, Colorado Memory Systems, Inc., Loveland, CO.

[10]Microsoft Corporation, Redmond, WA.

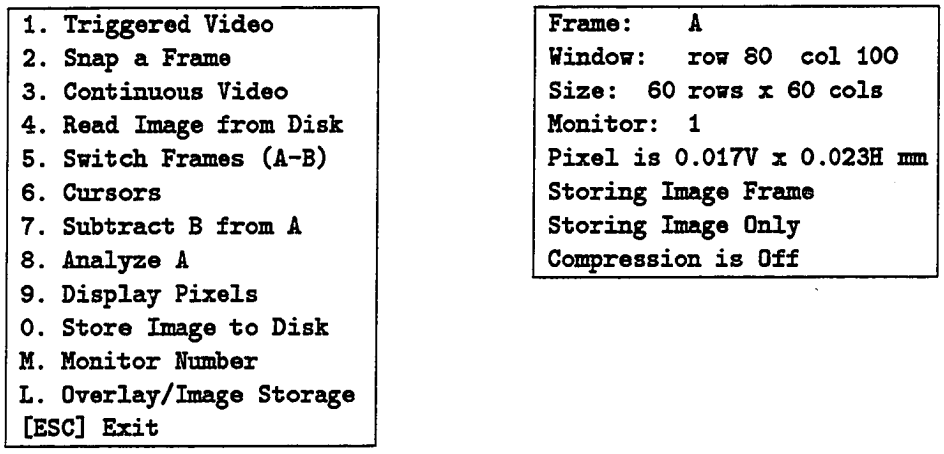

Figure 7.3: The main menu of the BPM program

Continuous Video: display real-time video signal

Switch Frames: toggle between the two frame memories

Read Image: read video image from disk into framegrabber memory

Store Image: store current video image to disk

Monitor Number: select which of the four camera inputs to process

Overlay/Image Storage: alter image display and storage parameters

The overlay/image storage submenu allows the user to choose the format for displaying and storing images. A calibrated scale or grid can display increments of a millimeter in x and y at the profile-monitor screen. A text field recording the time, date, and monitor number can be automatically stamped on each image. When storing the image to disk the user can choose to store only the 8 data bits or the data bits plus 4 overlay bits. One can also choose to store the entire video frame, or only the window of interest, discussed below.

The remaining functions are related to image analysis. They are

Cursors: select the window of interest

Subtract B from A: perform a pixel-by-pixel subtraction of one frame from the other

Analyze A: enter the profile-analysis environment

Display Pixels: display pixel values from the window of interest

All analysis is confined to a so-called "window of interest." This is a rectangular subregion of the video frame that the user selects using the mouse (Logitech serial mouse) and two cursors drawn on the video screen. There are several advantages to reducing the analysis area, particularly in the case of small beam profiles. First, computation time is greatly reduced due to the smaller number of pixels to be subtracted, added, *etc.*. Second, unwanted noise and signal components can be reduced or eliminated by a judicious choice of window. Finally, selected subregions of the beam can be isolated for analysis. This proved quite useful in a number of situations.

The two frame memories are called frames 'A' and 'B'. Frame A holds the primary image to be analyzed; frame B holds a "background" image. The image in frame B can then be subtracted pixel by pixel from frame A within the window of interest. This is used to eliminate or substantially reduce camera-related noise as well as to isolate a component of the beam pulse for analysis. For example, an image of the dark-current profile, that is, a beam pulse with no laser on the gun photocathode, can be stored in frame B and subtracted from an image in frame A of the full laser-induced beam. The dark current is an unavoidable component of the beam, but has the same spatial profile with or without photocurrent present. Hence subtracting frame B from A leaves an image containing only the photocurrent profile in frame A. (An example is shown in Fig. 9.2.) Sometimes this was the only way to discern the photocurrent against the dark-current background.

A status window displays such parameters of interest as the current frame, monitor number, window size and location, pixel-size calibration, and image-storage choices.

While using the original 8-bit framegrabber, which had no overlay bits, an undesirable artifact of image subtraction was discovered. With only 8 bits in which to represent a pixel, one can store values between 0 and 255. One component of the noise present in the video signal is the random shot noise associated with the readout of each pixel from the CCD chip. This results in small but finite signals present in each pixel even with no light impinging on the camera.[11] Hence in regions where the light level is identical in both frames, where pixel subtraction should result in a value of zero, the noise results in small positive and negative values. There was no way, however, to store the negative values in framegrabber memory, so these were clipped to zero. When the subtracted image was summed along one axis to give a profile along the other, the result was an unwanted nearly constant background on which the beam profile was superimposed. This complicates analysis as well as reduces the sensitivity of the system to low-intensity beams.

A way to avoid this was found with the overlay framegrabber. One of the overlay bits is used as a sign bit. Upon pixel subtraction the absolute value of the result is stored in the eight data bits and the sign is stored in the sign bit. This results in summed profiles with much smaller background levels.

The digitized values of the pixels within the window can be dumped to the computer screen. This allows the user to check for such effects as camera signal saturation or an invalid image subtraction, as evidenced by large regions of uniform or negative pixel

[11] A selectible offset voltage is added by the framegrabber to the video signal. This was chosen to just give nonzero pixel values in the absence of signal in order to insure all signal was above threshold.

values, respectively.

The window of interest in frame A can be subjected to detailed analysis using the analysis submenu. A sample of the analysis menu screen showing the results of a profile analysis is shown in Fig. 7.4. The analysis functions available are

```
1.  X/Y Analysis
2.  Statistical Analysis
3.  Gaussian Fit
4.  Define Background
5.  Width Percentage
6.  Generate Histogram File
```

```
                        x          y
Peak            :   4.370      3.712 mm
FWHM            :   3.577      0.294 mm
/2.35           :   1.522      0.125 mm
Mean            :   4.387      3.740 mm
RMS             :   1.306      0.140 mm
90.0% Width     :   5.849      0.499 mm
Gaussian Fit Parameters:
Amp             :   27366      90533
Center          :   4.410      3.705 mm
Sigma           :   1.227      0.129 mm
x analysis in progress
Window contains  12 saturated pixels
```

Figure 7.4: The analysis menu of the BPM program

X/Y Analysis select x or y axis for analysis

Statistical Analysis sum window data into profile along chosen axis and extract a series of statistical parameters

Gaussian Fit fit profile to a Gaussian

Define Background use cursor to define a fixed background level

Width Percentage choose fraction of total intensity for width characterization

Generate Histogram File write summed profile and fitted Gaussian to a disk file

The user selects either the x (horizontal) or y (vertical) axis to analyze. The pixel values within the window of interest are summed along the other axis to produce the

desired one-dimensional profile. This profile is then analyzed for the parameters of interest.

Let $p(x_i, y_j)$ be the two-dimensional beam profile stored in framegrabber memory, where x_i is the x coordinate of the ith column of the data array and y_j is the y coordinate of the jth row. The coordinates are in absolute units at the profile-monitor screen. Assume the profile along the x axis is being analyzed and that the window of interest is a subregion of the video frame n columns wide by m rows high. This one-dimensional profile is given by

$$P(x_i) = \sum_{j=1}^{m} p(x_i, y_j).$$

The total intensity is just $N = \sum_{i=1}^{n} P(x_i) = \sum_{i,j=1}^{n,m} p(x_i, y_j)$. The following statistical parameters are extracted for the profile:

- $\langle x \rangle = \frac{1}{N} \sum_{i=1}^{n} x_i P(x_i)$
- $x_{\rm rms} = [\frac{1}{N} \sum_{i=1}^{n} (x_i - \langle x \rangle)^2 P(x_i)]^{1/2}$
- $x_{\rm max}$ = coordinate of maximum value in profile
- full width at half-maximum, $x_{\rm FWHM} = x_l - x_k$, where $P(x_{k,l}) = P(x_{\rm max})/2$
- width containing f% of total intensity, where f can be selected by the user.

When the Gaussian fit is requested, a region of $\pm x_{\rm rms}$ around the mean is subjected to a linear-least-squares fit to the functional form

$$G(x) = Ae^{-(x-x_0)^2/2\sigma^2} \tag{7.1}$$

and the amplitude A, centroid x_0, and width σ determined.

This a nonlinear function of the parameters. Least-squares fitting of such functions involves parameter-space search algorithms [62] that are quite time-consuming and not guaranteed to converge on a solution. This is unacceptable for an on-line beam analysis. Eq. (7.1) can be converted into a linear equation by taking the natural logarithm of both sides. The log of the data is fitted as a second order polynomial:

$$\ln G(x) = a_0 + a_1 x + a_2 x^2.$$

The coefficients so obtained are related to the Gaussian parameters via

$$a_0 = \ln A - \frac{x_0}{2\sigma^2}, \qquad a_1 = \frac{x_0}{\sigma^2}, \qquad a_2 = -\frac{1}{2\sigma^2}.$$

One drawback to this approach is that it does not allow a background term to be added. The way around this is discussed shortly.

As shown in Fig. 7.4, the calculated parameters are displayed in a data window. The data histogram and fitted Gaussian (if requested) are displayed on the video screen (using an overlay plane). This allows the user to gauge the quality of the fit and the general shape of the beam profile. If the profile is nearly Gaussian, the fit closely coincides with

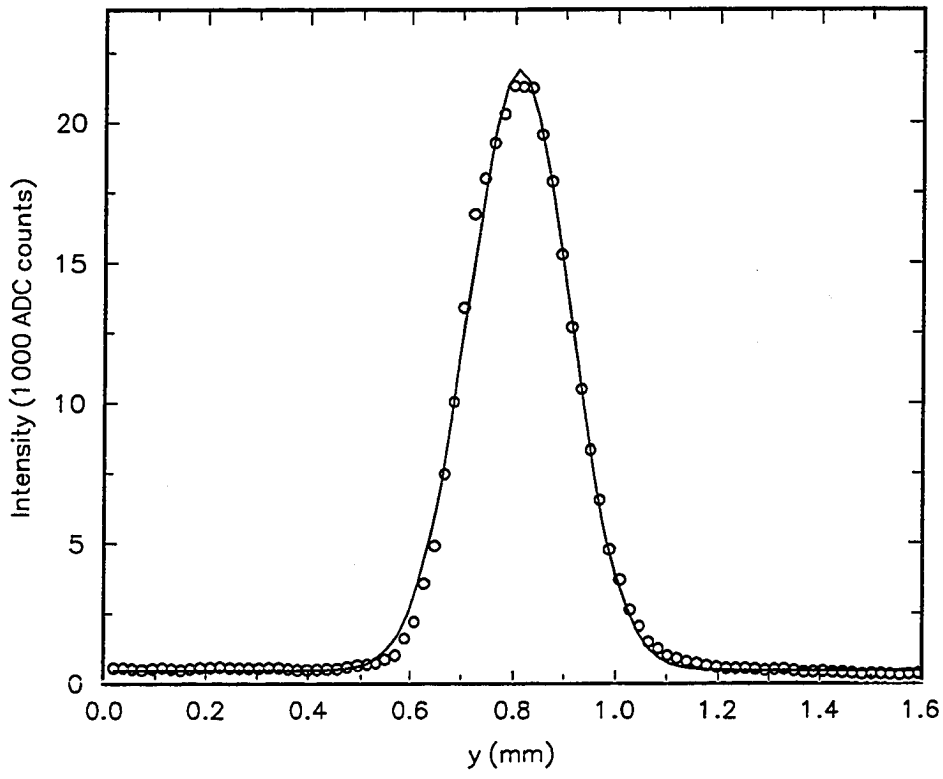

Figure 7.5: A sample beam profile

the data points and the rms width, FWHM/2.35, and Gaussian σ are nearly equal. If this is not the case, the rms width is usually taken as the best characterization of the beam size. A sample of a one-dimensional beam profile with a fitted Gaussian is shown in Fig. 7.5.

The presence of a constant or near-constant background level in the summed profile can bias the rms calculation and the Gaussian fit. The user can select a fixed background level by placing a cursor at the desired position relative to the displayed data profile. The analysis is repeated on the summed profile with the chosen background value subtracted. This is helpful in eliminating any remaining video noise or analyzing the central core of a beam with non-Gaussian tails.

During analysis the image is checked for saturation by counting the number of pixels within two counts of the maximum digitized value of 255. The number of such pixels is reported in the data window. When used with most cameras the framegrabber saturates before the camera. The TM745 camera, however, was observed to saturate at a pixel value of around 235. This was not deemed serious enough to fix during commissioning when the monitor system was being reconfigured frequently. It could be compensated for by setting the framegrabber offset voltage slightly higher when input channels connected

to this type of camera are selected. Saturated images are easily discernible by the presence of a uniform "washed out" area.

7.5 Performance

The various components of the BPM system were tested during development for compatibility with the ATF requirements as outlined above. The performance the entire system was verified during ATF commissioning. The results of these studies are presented in this section.

7.5.1 Hardware-Related Issues

The profile monitors were found to hold the vacuum levels required for the beamline, around 10^{-9} torr. After hundreds of hours of running, no radiation damage was detected in any BPM component. The remote control of the actuator and lens aperture was redesigned based on running experience, as previously discussed.

7.5.2 Linearity, Sensitivity, and Dynamic Range

The value of each of these parameters is affected by the phosphor, video camera, and framegrabber. Where possible, these characteristics were evaluated for each component separately and for the assembled system.

The phosphor has already been stated as having a dynamic range that exceeds the range of ATF beam intensities, with good linearity throughout. The framegrabber has a dynamic range of 256:1, as determined by the 8-bit pixel depth. It operates on a principle which ensures that the digitized value is linearly proportional to the input voltage.

The LPQ210 CCD camera was tested extensively for linearity, sensitivity, dynamic range, and noise characteristics. Linearity was tested by exposing the camera to a bright uniformly illuminated scene, interposing neutral density filters between the scene and camera lens, and recording the response with the framegrabber. The camera was found to be highly linear over the dynamic range of the framegrabber.

There are several sources of noise in a CCD. One random component is associated with fluctuations in resetting the readout capacitor on the CCD to zero voltage. The amplifier that processes this voltage also contributes random noise. These set a limit on the minimum signal that can be distinguished above the noise background. *Shot noise* is the $\sqrt{N}$ fluctuations in the number of electrons generated in a single pixel at a given incident-light level. Another noise source is *fixed-pattern noise.* This is the result of thermally-generated electron-hole pairs in the silicon substrate of the CCD. The nonuniformity of the pixel structures results in some pixels consistently collecting more charge than others. This is a sensitive function of temperature and can be all but eliminated by cooling the CCD, a capability of the LPQ210 camera.

These noise components were studied by collecting a statistical sample of images each under varying conditions of illumination, integration time, and temperature. The values of each pixel in a selected part of the CCD were averaged over the statistical set, yielding a mean and standard deviation. The set of these means and variations were

then averaged over all pixels. The mean pixel value at zero illumination reflects the level of total noise present, while the standard deviation of a given pixel indicates the random fluctuations. It is this value that sets the minimum signal, as any fixed-pattern noise can be removed by the technique of subtracting a background image pixel by pixel. When the mean pixel values are averaged over all pixels, the standard deviation so obtained is a measure of the fixed-pattern noise.

Under zero illumination the pixel values were found to have on average a random fluctuation of about one framegrabber ADC count. Hence the camera and framegrabber are well matched in terms of sensitivity. The noise contributed by the framegrabber was measure by collecting a set of data with no camera input. This contribution was found to be about 1/2 of an ADC count. The sensitivity of the camera, recall, was around 20,000 photons per pixel. With a CCD quantum efficiency of 20% (see below), this corresponds to 4000 electrons per pixel as the minimum signal. The maximum number of electrons that can be contained in the potential well of a pixel is called the pixel saturation value. These are typically a few hundred thousand. From these estimates the dynamic range is expected to be around 100 or 200. Manufacturer's specifications state 200. Again we see that the CCD camera operated at room temperature and the eight-bit framegrabber are well-matched.

When the video signal was integrated for more than a few frames under zero illumination, the fixed-pattern noise became noticeable at room temperature and was drastically reduced by cooling the CCD. Pixel-by-pixel subtraction can almost eliminate this effect, which turned out to be no larger a noise component for single-frame images (no integration) than the random components. Hence it was concluded that cooling was not an essential feature. Integration was also deemed unnecessary since one frame is sufficiently long to collect all the phosphor light from a beam pulse.

The total gain of the system, that is, the signal generated at the framegrabber per electron incident on the phosphor screen may be estimated. The quantum efficiency of the CCD used in the BPM cameras happens to peak very near 550 nm, where it is approximately 20%. (The silicon has an intrinsic efficiency of around 40%, but half of the CCD area is obscured by the buses used to transfer the pixel charges to the readout electrode.) The CCD is spectrally well-suited to the phosphor, with peak emission at 545 nm. About 3% of the light emitted by the phosphor is collected by the f1.4 lens at full aperture, with no more than about 25% of the collected light lost to reflection from the vacuum window and lenses.

A few-MeV electron loses about 17 keV in passing through 30 μm of phosphor. As the phosphor conversion efficiency is around 20 eV/photon, this electron yields about 850 photons. About 20 of these reach the CCD, where they liberate around four charges. A minimum signal of 4000 charges per pixel corresponds to 1000 beam electrons per pixel. The size of a framegrabber pixel at the CCD is 17 μm $\times$ 13 μm. Accounting for optical magnification, this corresponds to an area of 24 μm $\times$ 18 μm at the phosphor screen. So the minimum observable beam intensity is 2×10^6 electrons/mm^2, or about a nanocoulomb spread over an area of 10 $\times$ 10 cm^2. This is clearly adequate for any of the high-current beam conditions. A nanocoulomb in an area of 1 mm^2 would generate about 10,000 ADC counts per pixel, which is easily lowered to around 200 by using the motorized lens aperture.

7.5.3 Spatial Resolution

The spatial resolution determines the smallest beam that can be profiled. For the ATF beamline parameters, the smallest radially symmetric beam profiles are on the order of 1 mm rms, but the beam can be focused to about 100 μm in one axis at the expense of the focus along the other.

A number of factors conspire to degrade the spatial resolution, which if they are independent add in quadrature to the final value. Below are listed the main potential sources of image smearing. Numerical estimates of the effect of each are given where possible. The remaining sources were measured and will be discussed below.

Multiple scattering: The rms deflection $x_{\rm rms}$ suffered by a relativistic particle of unit charge and momentum p traversing a thickness t of a material of radiation length X_0 is given by [65] $x_{\rm rms} = (13.6\ {\rm MeV})\, t^{3/2}/(\sqrt{3X_0}p)$. The radiation length of the phosphor is 3 cm while that of aluminum is 9 cm. This gives a total deflection of 3 μm to a 3-MeV electron passing through 25 μm of aluminum and 30 μm of phosphor.

Phosphor grain size: The Gd_2O_2S:Tb powder has grains of around 10 μm.

Blooming: This is random scattering of light within the phosphor. This is the main resolution limitation and is discussed below.

Depth of focus: The transverse smearing of an image with depth $t = 30$ μm focused in the center by a lens with diameter $d = f/1.4$ is found from classical optics to be $(t/8)(d/f) = 3$ μm.

Camera/lens resolution: Today's commercially available camera optics are of excellent quality. In studies of the resolution of a CCD camera with a standard video lens, the limiting factor was found to be the pixel size of the CCD. In other words the smallest thing that can be resolved at a profile-monitor screen is just the size of a pixel projected onto the screen, here around 20 μm. In fact with the lens removed a laser could be focused through external optics into a spot on the CCD smaller than a pixel. As the camera was slowly translated transversely to the laser, the spot was seen to wink on and off as it moved from active pixel area to readout bus! A slight spillover of a single-pixel signal into adjacent pixels in the horizontal direction was observed, presumably due to the camera readout electronics.

Framegrabber: The effective pixel size of the framegrabber has already been seen to be similar to that of the CCD.

The quadrature sum of all the above effects except blooming amount to little more than an rms spread of 20 μm. Blooming is the most sizeable effect and is caused by the scattering of emitted light by phosphor grains. The literature on phosphors [66] contains discussions of this and other properties. Independent tests were done to make a quantitative assessment of the effect in the context of electron-beam use.

The parameter of interest is the phosphor response to a point-like excitation. The most relevant point excitation is obviously a single relativistic electron. The ATF electron beam was mimicked by a collimated strontium-90 source. ^{90}Sr decays via β emission in two steps yielding electrons with energy-spectrum endpoints of 2.28 MeV and 546 keV. The lower energy electrons suffer larger multiple-scattering deflections than the few-MeV electrons, but this effect can be estimated and accounted for.

Phosphor screens of thickness varying from 15 to 90 μm were tested in an optical configuration similar to that of a profile monitor, shown in Fig. 7.6. The electrons from the β emitter impinged normally on the screen, which was imaged by two back-to-back lenses (f_1 and f_2) and a 45° mirror. The intensity of the source was such that only a few electrons struck the screen during a video cycle. As discussed above, a single electron produces less than 1% of the light needed in this configuration to register a single ADC count in the framegrabber. Hence an additional gain mechanism was required.

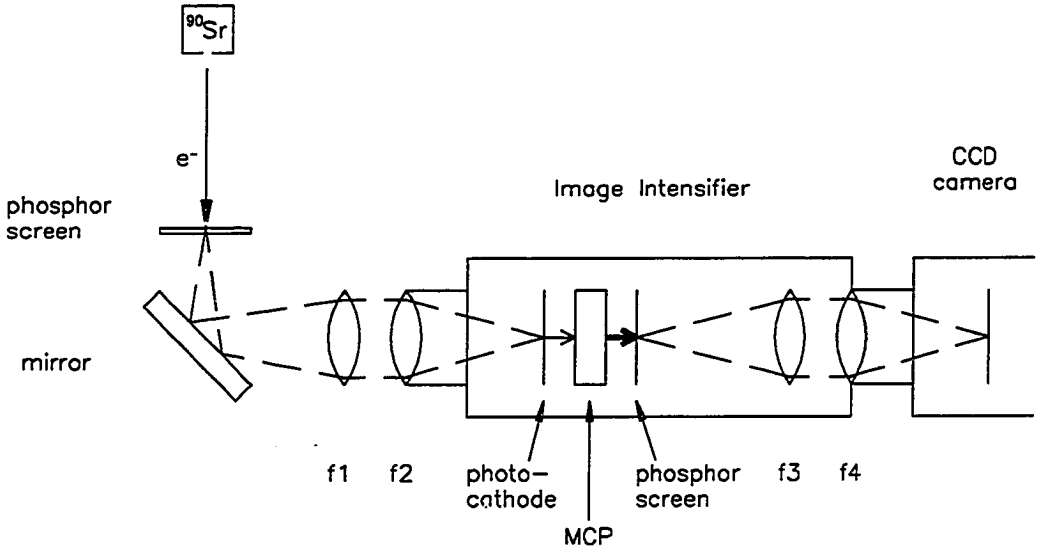

Figure 7.6: Apparatus for measuring phosphor-screen resolution. The image of a single electron from the ^{90}Sr source is amplified by an image intensifier and recorded by a CCD camera.

The needed gain was provided by an image intensifier,[12] a device that operates on the same principle as a photomultiplier tube but that maintains the spatial information of the input image. The input image is converted to an electron signal by a photocathode. The electron signal is amplified by a microchannel plate and converted back to a light

[12]Model LPQ50, Patterson Electronics, Tustin, CA; based on the Varo model 3603 25-mm microchannel plate.

signal by a phosphor screen within the image intensifier. This screen is imaged into a video camera by a pair of internal lenses (f_3 and f_4).

The model used for these studies had a variable gain of 10,000-50,000 and an rms spatial resolution of about 20 μm, which added in quadrature to the resolution of the optical system. This provided single-photon detection, and hence allowed individual electrons to be seen. In agreement with the estimate given above, each electron "hit" consisted of a few individual photons.

The CCD camera used in the phosphor-screen resolution studies was the Patterson camera that had been studied for camera resolution. The lenses used to image the phosphor screen onto the image intensifier had focal lengths of $f_1 = 35$ mm and $f_2 = 50$ mm, providing image magnification of 50/35. The image intensifier's internal lenses are of focal lengths $f_3 = 50$ mm and $f_4 = 35$ mm, so the input image is demagnified by a factor of 35/50. Hence the phosphor screen is imaged onto the CCD with unity magnification. The 20-μm resolution of the image intensifier is reduced to an effective contribution of $(35/50) \cdot 20$ μm$= 14$ μm at the phosphor screen.

The size of each electron image was analyzed by selecting a small region around it, subtracting a background image to remove video noise, summing into x (horizontal) and y (vertical) profiles, and calculating the rms width of each. The horizontal rms sizes for phosphor thicknesses of 15, 30, and 45 μm are plotted in Fig. 7.7. The total resolution of this system as a function of phosphor thickness was characterized by a baseline resolution of around 39 μm and a contribution in quadrature equal to the phosphor thickness. This is shown as the smooth curve in Fig. 7.7.

The baseline resolution represents the sum of the camera and image-intensifier resolutions and multiple scattering. The phosphor-thickness-dependent part is consistent with the limits to phosphor resolution caused by blooming as reported in the literature. Recent measurements from SLAC [67] on a phosphor (Al_2O_3S:Cr) with grain size similar to that of Gd_2O_2S:Tb indicate a thin-line resolution of 28 μm for a thickness of 120 μm.

From this study the total horizontal rms resolution of the beam-profile-monitor system constructed for the ATF, which uses a phosphor screen 30 μm thick, is measured to be 47 μm rms. This is value is arrived at by subtracting in quadrature the 14-μm contribution of the image intensifier from the data shown in Fig. 7.7. Vertical resolution is around 10 μm better, *i.e.*, 37 μm. The horizontal resolution is worse due to the slight horizontal smearing introduced by the CCD-camera readout electronics. This is adequate for the beam sizes expected and observed in the ATF low-energy injection line. Vertically focused beams of around 100-μm rms width are routinely observed.

The inclusion of the image intensifier in the profile-monitor optics increases the resolution to around 40 μm vertically and 50 μm horizontally, still adequate for diagnosing 100-μm beams. In some situations, such as low-current mode, the beam intensity will be reduced by a factor of 10^{-4} to 10^{-5}. At such times the intensifier will be needed.

7.6 Other Configurations

Since the framegrabber used in the BPM system can accept video from any camera conforming to the RS-170/330 standard, the analysis system can be used on other devices

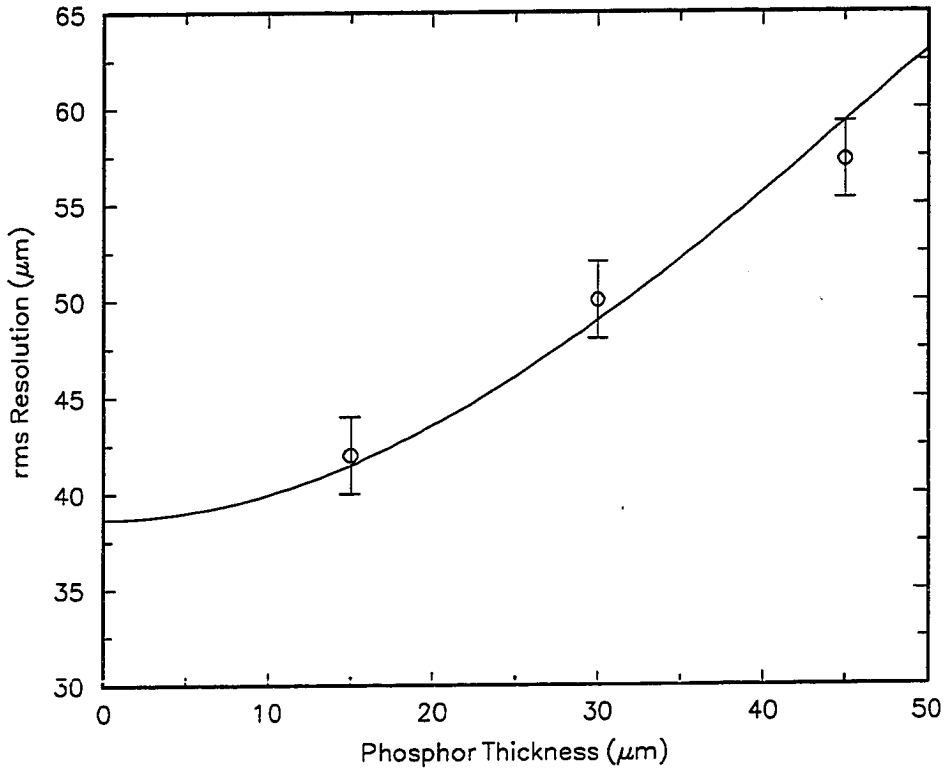

Figure 7.7: Single-electron horizontal spot size as a function of phosphor thickness. The smooth curve is a fit to the data interpreted as a constant baseline resolution and a contribution in quadrature equal to the phosphor thickness.

than beam-profile monitors. All that has to be provided is a separate pixel-size calibration for each different optical configuration. This is kept in a database so that when the user selects a given framegrabber input for processing, the corresponding calibration is automatically applied during data analysis.

For example, other beamline elements can be used to profile the electron beam. The momentum-selection slit was coated with the same phosphor as the standard BPM and viewed by a video camera. The optical arrangement is different from that of a BPM; the camera is 1.1 meters away and uses a single 200-mm lens.[13] The size calibration was performed by translating or opening the slit by a known amount and comparing images collected before and after the change. This was a valuable diagnostic for several reasons, as will be described in the next chapter. A sample beam video image on the slit is shown in Fig. 9.12.

Another use of the BPM analysis system is to measure the spot size of the Nd:YAG

[13]Zuiko Auto-T 200-mm *f*4 SLR lens with video-mount adapter, Olympus Corp., Woodbury, NY.

laser at the photocathode. The laser optics are arranged so that a small portion of the laser light is deflected 90° out of the nominal optical path and onto a CCD camera located such that the CCD is at the same path length as the photocathode in the undeflected beam. No lens is mounted on the camera so that the laser spot on the CCD is identical to that at the cathode. During each day's run a sample laser profile was collected and analyzed for spot size. This was important in determining the laser intensity at the cathode and for later comparison between experimentally observed beam conditions and rf-gun simulations which required the laser spot size as input. A sample Nd:YAG-laser profile is shown in Fig. 8.5.

The standard BPM can be used with auxiliary devices upstream to provide additional information about the beam. One such technique, which can provide single-shot emittance determination, is described in Sec. 9.4. The primary temporal pulse-length diagnostic, based on the use of rf deflection, is described in Sec. 6.4.

Chapter 8

Commissioning the rf Gun and Injection Line

In this and the next chapter we present the data collected during the commissioning of the ATF low-energy beamline. These results cover a time span of about three years, beginning with the initial construction of the ATF and ending with a major shutdown during which preparations were made for transporting beam into the linac and high-energy transport line, and thence into the experimental hall. A summary of the measured rf-gun properties is given in Table 8.1.

A great many technical challenges had to be met in order to reach the point of beam data collection; beamline commissioning is an engineering effort as well as a scientific one. During this time we achieved a number of the original design goals and found some elements of performance in excess of initial expectation. We have also identified aspects of the facility that need improvement or redesign.

In a document of this length it seems appropriate to chronicle some of the difficulties that had to be overcome in our efforts to bring the accelerator facility on-line and begin to understand and master it. I will only mention those issues that I had some part in addressing and that played a role in our efforts to become operational. Many other obstacles that required nothing short of heroic effort on the part of the technical and scientific staff to overcome must perforce be omitted. Those issues relating more to the functioning of the beamline itself will be discussed in this chapter, which will have a somewhat engineering character. In the next chapter we will turn to the properties of the photoelectron beam.

8.1 History

Some of the major operational milestones will be reviewed in order to convey a sense of the challenges and time scales involved in constructing a beamline facility "from scratch." Only approximate dates will be assigned to distinguish overlapping periods.

Conceptual design of the ATF occupied the years 1986-1988. During this time the rf gun and the transport from gun to experimental hall were designed, as outlined in Chapter 2. The next year and a half or so was spent constructing the rf system and initial components of the low-energy transport, including the gun.

The first laser-ejected electron beam was observed in July of 1989. In the same month the first emittance measurements were performed using the profile-monitor system. At

Table 8.1: Measured rf-gun parameters

Parameter	Design	Measured
Maximum beam momentum (MeV/c)	4.6	4.6
rms $\Delta p/p$ (%)	0.3	0.4
Repetition rate (Hz)	6	6
Cavity Q	11,800	10,000
Shunt Impedance (MΩ/m)	57	50
Bunch charge (nC)	1	2
Quantum efficiency	2×10^{-4}	6×10^{-5}
rms bunch length (psec)	2.5	5-6
Peak current (A)	160	133
Peak current density (A/m^2)	—	10^4
ϵ_N (mm-mrad)	7	4
Brightness (A/m^2)	4×10^{10}	$\geq 1\times10^{11}$

this time a yttrium photocathode was used, as had been the original design plan. The Nd:YAG-laser system was not yet available, so an excimer laser was substituted operating at a wavelength of 248 nm, close to that of the quadrupled YAG laser (266 nm). The length of the excimer-laser pulse was several nanoseconds, much longer than an rf cycle, so the properties of this early photoelectron beam were closer to those of the dark current than to the present few-picosecond photoelectron pulses. Nevertheless, it allowed us to acquire experience with gun operation, beam tuning, diagnostics, and synchronization. Most importantly, the gun was demonstrated to work. The electron pulses produced were of sufficient energy and intensity to necessitate the construction of an extensive shielding and interlock system, which halted operations in December, 1989.

Proposals for user experiments were first officially approved at the ATF user's meeting in November, 1989. At this time approval was given to the nonlinear-Compton-scattering experiment described in Chapter 11, along with the experiments mentioned in Chapter 10.

Operation of the rf gun resumed in November of 1990, this time with the Nd:YAG laser and copper photocathode. Slightly more than a week later, on November 28 at 10:30 p.m., the first YAG-laser-ejected photoelectrons were observed. This event is recorded in Fig. 8.1, which shows the first oscilloscope traces indicating the presence of photoelectrons. The traces show the "sum" signal from a stripline monitor, which is proportional to the beam current. The upper scope picture was taken at a time scale of 20 nsec/division and was triggered by the same signal that determines the firing of the laser. The upper trace is the signal from a fast photodiode monitoring the Nd:YAG-laser beam near the gun; the lower trace is the stripline signal (cable delays account for the

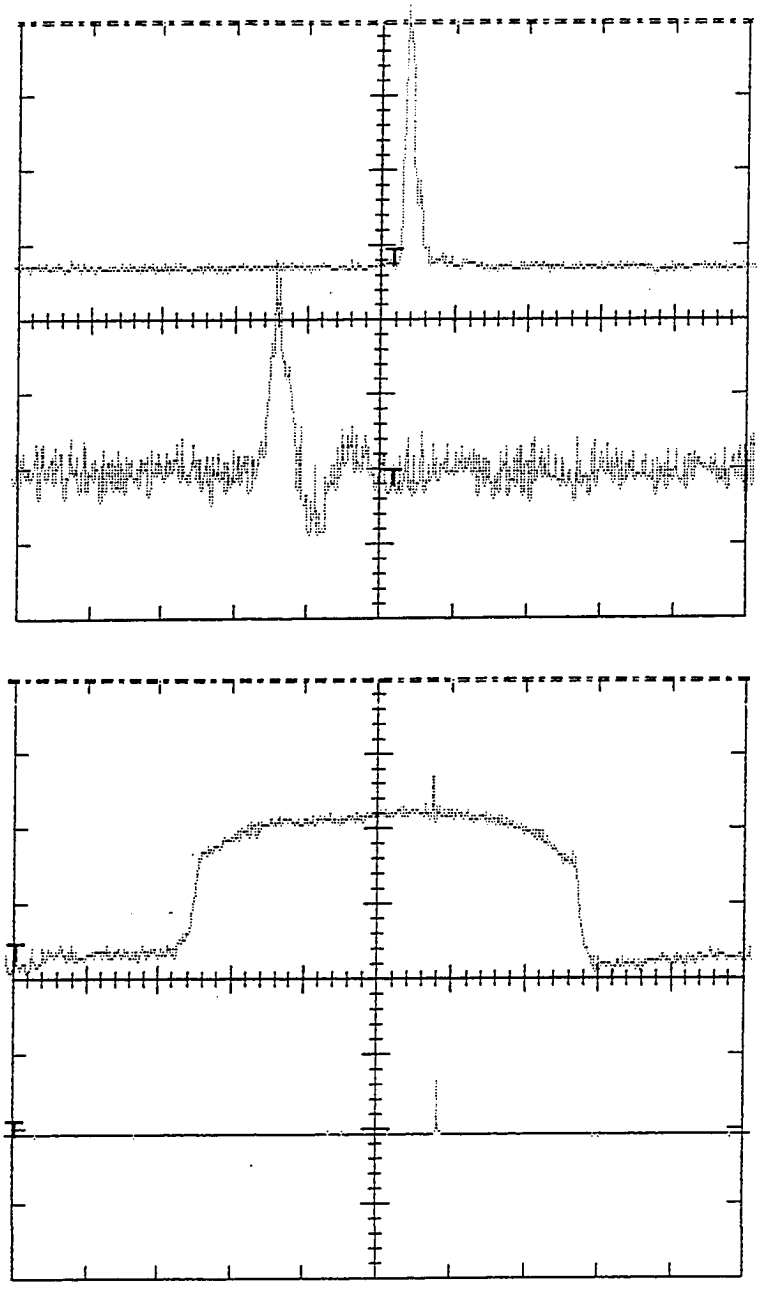

Figure 8.1: Oscilloscope traces of the first Nd:YAG-laser-ejected photoelectron beam. The top picture was taken at a time scale of 20 nsec/division; the bottom at 500 nsec/division. In each a fast photodiode signal is also present.

photodiode signal appearing after the photoelectron pulse). The measured photoelectron pulse width is limited by the bandwidth of the stripline electronics. The lower scope picture shows the signal on a longer time scale, 500 nsec/division. Now the dark-current signal is visible in the upper trace, occurring over about 3 μsec, on top of which can be seen the photoelectron pulse in coincidence with the photodiode in the lower trace.

This initiated the effort to achieve the high brightness for which the rf gun was designed. Achieving and documenting this was a primary objective of the period lasting until July 25, 1991. All photoelectron-beam data were collected from January to July, 1991. By this time sufficient information had been gathered about the gun and beamline to commence with acceleration to 50 MeV and transport to the experimental hall. The need for several significant improvements and additions to the beamline had been demonstrated, which would be implemented during this shutdown. While much further can still be learned about rf-gun dynamics and high-brightness-beam transport, the need to deliver high-energy beam for the experimental program will become the driving concern. This shutdown marks the transition from a time of dedicated beamline studies to one dominated by the need to push construction ahead and deliver 50-MeV beam to experiments with a minimum of delay.

Much progress was made in the laser system in parallel with the electron-beam efforts. While of a crucial nature to ATF operations, they were not the focus of the efforts recorded herein, and are given only cursory treatment.

8.2 Survey and Alignment of Electron-Beamline Optics

One of the initial challenges was the construction of a beamline that would preserve the high brightness of the rf gun but that had to be constructed from quadrupoles some of which were decades old and recycled from other projects. These magnets had no provision for accurately surveying their position in the beamline. Hence placement was a particularly challenging endeavor. One solution was to map the magnetic fields of some of these magnets individually and as part of a triplet and to mark magnetic centers with respect to the geometric center of the magnet bore. Such a program was begun using the magnet survey lab of the National Synchrotron Light Source. A Hall probe[1] mounted on a precision 2-dimensional translation table and shimmed to various heights was used to obtain 3-dimensional field maps for several magnets prior to placement in the beamline. The magnets were marked to visually indicate magnetic center, and the field-map data were made available on computer disk. Nevertheless, limited visual access by survey instruments made positioning and alignment of these magnets difficult at best.

Ideally a quadrupole should be placed in a beamline so that the magnetic center (the transverse location at which the magnetic field is always zero) coincides with the central axis of the beamline and so that focusing and defocusing gradients are aligned with the x (horizontal) and y (vertical) axes. A transverse offset results in steering of the beam, while a rotation about the central axis couples the x and y phase spaces.

An example of the latter was observed during the initial running with the yttrium-photocathode gun and excimer laser. The normalized vertical emittance was measured

[1]Model B-H15 Probe and Field Controller, Bruker Instruments, Karlsruhe, Germany

to be 8.5 mm-mrad, a figure four times higher than predicted by PARMELA simulations of the gun. This led to the discovery that the quadrupole used to make the emittance scan was rotated.

Such steering or rotation could be easily detected on a profile monitor located downstream of the magnet in question. On occasion we employed the technique of "electron-beam surveying," in which the beam image was recorded, the amount of steering or rotation measured, and the necessary correction to the quadrupole calculated. The beam would then be turned off, the magnet adjusted, and the process repeated until proper alignment was attained.

Such a tedious procedure is only a temporary solution however. Ground settling caused by the addition of heavy shielding, and perturbations resulting from work on the beamline created a continuing need to readjust optical elements. This experience indicated the need for a survey system that is accurate and relatively easy to repeat periodically. A laser-based survey program was initiated with the July, 1991 shutdown. Every element in the low-energy beamline was removed and fitted with precision targets for laser and optical surveying instruments.

Misalignments of apertures and collimating slits can cause beam clipping, resulting in a loss of acceptance through the beamline. This proved to be a source of constant concern. A study of the beamline acceptance based on emittance data coupled with ray-tracing simulations of the beamline is described in Sec. 8.4.

8.3 Beam Tuning

The functions for which the low-energy transport was designed were outlined in Sec. 2.4.1. The beam-profile-monitor system was used to verify that many of these features could be implemented. The profile monitors located at the momentum slit, in the 'Z' line, and in the double-bend section could provide beam information after every optical element in the low-energy transport. For a drawing of the beamline, see Fig. 2.4.

The important momentum-related functions of the beamline are momentum dispersion, analysis, selection, and recombination. Dipole D1 disperses the beam horizontally according to momentum. The horizontal dispersion at the momentum-selection slit (defined as the horizontal spread per unit momentum spread) is determined by the strength of D1 and of quadrupole Q4, which is horizontally focusing and cancels the angular dispersion introduced by D1. The horizontal dispersion was usually in the range of 4-6 mm/%. For a given strength of dipole D1, the trajectories of electrons with the beam central momentum are bent by 90° in D1 and intersect the horizontal center of the slit. The momentum spread of the beam out of the gun can be determined by viewing the phosphor-coated slit, which doubles as a profile monitor. The momentum bite of the beam presented to the 50-MeV linac is defined by the slit width.

Almost routinely a beam run begins by viewing the closed slit, selecting the central momentum via D1, and setting quadrupoles Q1-Q4 to produce the desired beam condition on the slit. When looking for photocurrent, the laser phase with respect to the rf system is varied until the photoelectron signal is observed on the slit. Several types of focus on the slit are common.

A momentum-spectrometer tune is used for momentum analysis and selection. This tune is achieved by minimizing the horizontal beam size at the slit. Beamline simulations with the program TRANSPORT indicate that in the absence of chromaticity an rms horizontal spot size of 0.5-1 mm can be achieved. Combined with a momentum dispersion of 5 mm/%, this yields a momentum spread resolution of 0.1-0.2%.

The beam can be focused simultaneously in x and y at the slit in order to maximize the beam current passing through the slit. (In some other tunes some of the beam is lost off the side of the slit assembly.) The beam can be focused vertically on the slit for use in a 2-monitor emittance measurement. In each case knowing the beam profile on the slit is crucial to the tuning process.

Having selected the momentum region of the beam, we would like to recombine this into an achromatic beam for injection into the high-energy beamline. This is accomplished with quad Q5, which is also horizontally focusing, and the second dipole, D2. In principle quads Q4 and Q5 are operated at the same strength, which is chosen so that Q4 cancels the angular dispersion introduced by D1, and Q5 introduces an angular dispersion of the opposite sign, which is in turn cancelled by operating dipole D2 at the same strength as D1.

In practice there is a small asymmetry between D1 and D2 and between Q4 and Q5 due to slight variations in the excitation constants. Any residual chromaticity in the beamline can have a large influence on the horizontal focusing properties of the beam, obscuring the horizontal emittance. Therefore this system must be tuned quite carefully when true achromatic beam operation is desired. As an example, the horizontal normalized emittance of the photocurrent was measured to be 23 mm-mrad before achromatic operation was achieved. This value was reduced to 4 mm-mrad with an achromatic tune.

This tune was found by setting D1 and Q4 to the appropriate strengths and starting with D2 and Q5 set symmetrically. The beam was focused horizontally on profile monitor BPM4, just upstream of the linac, using the quadrupole triplet Q6/Q7/Q8. Q5 was then varied slightly, and the horizontal spot size was minimized as a function of the strength of Q5. The minimum spot size indicates the correct choice for Q5 as the spot size increases much more rapidly as a result of increasing achromaticity than it does due to the small changes in focal length of Q5. Once this was chosen the strength of D2 was varied in small increments and same procedure repeated to find the minimum spot size as a function of the strengths of both Q5 and D2. This process yielded the proper achromatic tune for a given central momentum. The achromatic beam tune permitted the photoelectron beam to be focused to an rms spot radius of 150 μm at profile monitor BPM4.

Another tuning issue concerned the hysteresis of one type of quadrupole magnet used in the ATF. The quads recycled from SLAC were designed for much higher-energy beams than those at the ATF. Hence they were run at much lower currents than intended by design. At these low currents marked hysteresis was observed; a given excitation always had to be approached from the same direction. That the same excitation could thus be reproduced was verified from transverse profiles of the beam. These magnets, however, are quite sensitive to small changes in the current, so that beam tuning and diagnosis were complicated by the presence of a SLAC quad. This alerted us to the potential problems of using them in one of the experimental beamlines.

8.4 Beamline Acceptance

The beamline *acceptance* is defined as the area in trace space (see Sec. 3.1) that a given beamline will transport unattenuated. This is sometimes called the *admittance.* It is a function of the particular elements and magnetic fields comprising the beamline. If the beam ellipse is not contained within the acceptance region, then particle loss and apparent emittance reduction will result. An indicator of possible beam loss is provided by comparing the acceptance with measured beam ellipses.

The beamline acceptance was modelled by tracing individual particle trajectories through a simulation of the beamline that included collimating apertures and keeping track of which input rays are transported uncollimated to the end. A program called TURTLE [50] was used to do this. It makes use of the same matrix methods as TRANSPORT, but applies these matrices to individual rays rather than a collective beam matrix. This allows the inclusion of collimators in the beamline. Any ray with transverse position larger than a defined aperture is removed from the beam ensemble.

Only the first-order transport properties of the beamline were included in this acceptance calculation. Nonlinear optics will in general lead to larger beam sizes and hence greater particle loss than predicted in first order. These effects also increase the transverse emittance of the beam. The collimators in the high-energy beamline (Fig. 2.5) are in fact used to define the emittance of the beam by removing the unwanted tails in the transverse profile caused by nonlinear optics. The first-order acceptance, however, defines the beam that can be transported by the beamline even in the absence of any emittance increase.

The input beam is specified by providing a list of trace-space coordinates (x, x', y, y', z, $\Delta p/p$) that are used to generate particle rays within a Gaussian distribution. The initial rays are transported individually through the specified beamline. At any point along the beamline the surviving rays can be histogrammed in one or two trace-space coordinates and the second moments (corresponding to the beam-matrix elements) calculated.

The drift-space and magnetic beamline elements were simulated using input identical to that used in TRANSPORT calculations. The defining apertures in the ATF low-energy beamline are the beampipe, which has an inner radius of 12.5 mm, the rf-kicker cavity, which has a circular input aperture of 7.5 mm radius, and the momentum slit, which collimates only in the horizontal axis and is of variable width. All elements were assumed to be perfectly centered transverse to the beam axis. The beampipe and kicker were modelled as a square of side equal to the corresponding diameter.

Of particular interest was the question of whether the measured transverse emittance was being defined by beamline acceptance limits. A emittance measurement in the 'Z'-line (described in Sec. 9.6) was chosen as the basis for the study. This was a quadrupole scan of the vertical emittance using ZQ1 that yielded a value of 4 mm-mrad. The vertical beam matrix measured by the emittance scan at the entrance to ZQ1 was backprojected to the gun exit using the first-order matrices of the modelled beamline. The beam matrix

at the gun exit was thereby calculated to be

$$\sigma = \begin{pmatrix} \sigma_{11} & \sigma_{12} \\ \sigma_{12} & \sigma_{22} \end{pmatrix} = \begin{pmatrix} (1.329 \text{ mm})^2 & 17.54 \text{ mm-mrad} \\ 17.54 \text{ mm-mrad} & (13.223 \text{ mrad})^2 \end{pmatrix},$$

in qualitative agreement with gun simulations. This was used as input to the TURTLE simulation. The horizontal beam matrix at the gun exit was taken to be identical to the calculated vertical beam matrix there, as the gun is cylindrically symmetric.

As long as the emittance measurement was valid and the beamline modelled properly, we would expect no vertical collimation of this beam when it is ray-traced through the beamline to ZQ1. (Horizontal collimation occurs due to the momentum dispersion, but this does not affect the vertical emittance measurement. The effect was avoided by assigning the input beam zero momentum spread.) As expected, the TURTLE simulation showed 100% beam transmission.

The next step in the simulation was to increase the input emittance while maintaining similar elliptical contours. At twice the measured emittance there was no beam loss, while at four times the original value vertical collimation reduced the output emittance by 18%. This indicated that the emittance we had measured was a factor of at least 2 or 3 from being clipped by beamline elements in first order and assuming perfect alignment.

As a final step, the input trace-space was increased to a large enough area to saturate the beamline; only 1% of the input particles were transmitted uncollimated. The resulting beam ellipse backprojected to the gun exit might well be considered the acceptance for a Gaussian beam. This was

$$\sigma = \begin{pmatrix} (3.739 \text{ mm})^2 & 132.737 \text{ mm-mrad} \\ 132.737 \text{ mm-mrad} & (35.528 \text{ mrad})^2 \end{pmatrix},$$

which has a normalized emittance of 36 mm-mrad (the momentum of the beam was 3.5 MeV/c). This input beam was then TRANSPORTed through the beamline once again in order to obtain a plot of the vertical beam envelope. This is shown in Fig. 8.2 as the vertical rms beam size ($\sqrt{\sigma_{11}}$) as a function of position along the beamline. The beam scrapes the beampipe in the vicinity of Q3 and ZQ1, where the beam is seen to be the largest in Fig. 8.2. One interesting result of this study was that the rf kicker, located at $z = 0.91$ m, was not the limiting aperture, as had been suspected.

It is interesting that the beam scrapes at two places. This is consistent with the beampipe limiting the two-dimensional tranverse phase space. Indeed, the emittance is limited by scraping at Q3 and ZQ1 because the beam ellipse has rotated between these points: at Q3 the maximum along the y axis is determined; the particles that are along the y' axis at Q3 are transformed to lie along the y axis at ZQ1, where their extent is also limited by the beampipe. Hence the maximum area in (y, y') space is determined. This scheme of two collimators separated by a 90° beam-ellipse rotation is in fact how emittance selection is accomplished after the linac.

While these results are dependent on the exact excitations of each magnet in the beamline, most vertical emittance scans shared a qualitatively similar tune. From this study we can conclude that the emittance is not being defined by the beamline to first order. It should be remembered that this is based on the assumption that the

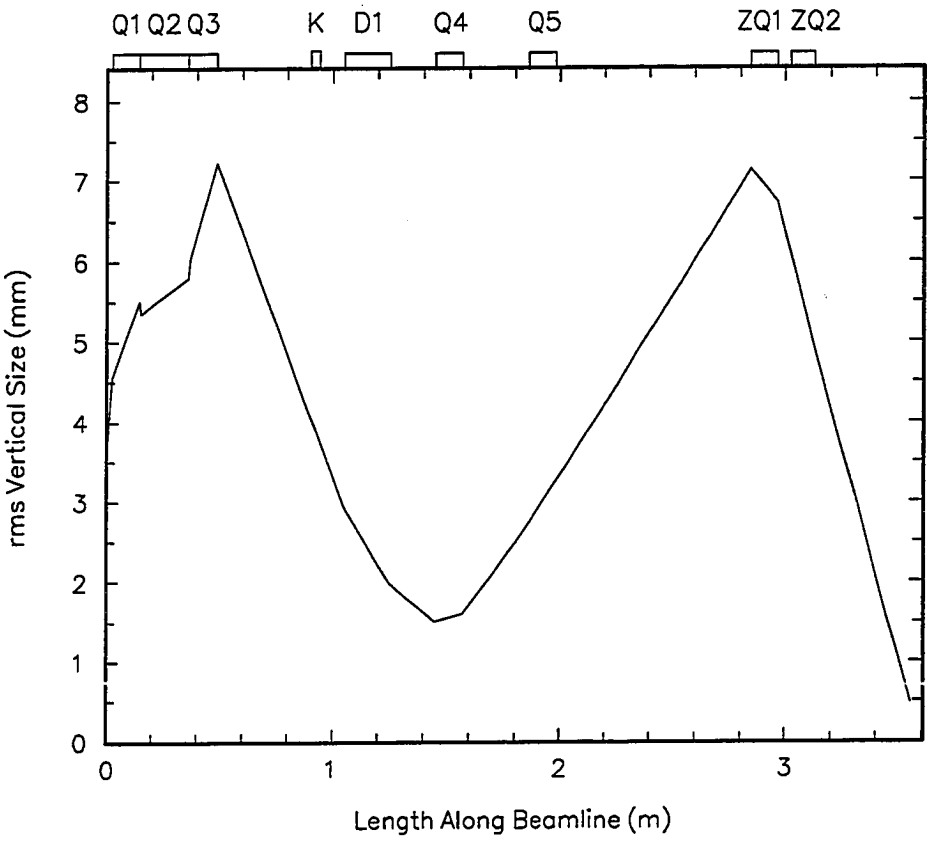

Figure 8.2: The rms vertical spot size along the beamline for an input beam with a phase ellipse equal to the acceptance calculated for a vertical emittance-measurement in the 'Z'-line. The positions of beamline optical elements are shown above the plot ('K' is the rf kicker).

beamline is exactly as modelled. The presence of stray magnetic fields to steer the beam or offset elements could result in additional collimation not included in this simulation. Furthermore, beamline elements were imprecisely surveyed and had shifted in some cases by as much as a couple of millimeters due to the addition of heavy concrete shielding.

Earlier studies [68] of the beamline including up to third-order effects indicated that with an initial normalized emittance of 8 mm-mrad, as much as 25% of the beam would be lost by the time it reached the momentum slit, accompanied by an emittance increase by a factor of six. A collimator consisting of the horizontal momentum slit and a vertical slit could reduce the emittance to 2 mm-mrad, which increases to 18 mm-mrad at the linac entrance, at the cost of collimating 80% of the beam.

It appears likely that some beam loss is inevitable. This cannot be ignored when considering the emittance results reported in Chapter 9.

8.5 Dark Current

With or without laser on the photocathode the gun produces field emission, or "dark current." As predicted by the Fowler-Nordheim relation (Eq. (4.2)), this is a very sensitive function of the rf power. The properties of the dark current are to be treated in detail elsewhere [69]. The dark current can serve as a probe of the properties of the photocathode and the electron-emission process. Here it will be considered only briefly as a background to the nominal photoemission.

Even taken as a background, the dark current is a useful signal from the point of view of beam tuning. The peak momentum of the dark current is a reliable indicator of the accelerating field at the cathode. This is because dark current is continuously emitted at all rf phases for which it will be accelerated out of the gun. The phase corresponding to maximum energy gain is close to 90°, when the electric field is strongest, as is field emission. The peak momentum is easy to measure by observing the cutoff of the dark-current momentum spectrum on the momentum slit.

The dark current provided a good signal on which to debug many of the measurements performed on the photoelectron beam. As its properties were fairly well understood, it served as a good crosscheck throughout the commissioning period. Of primary advantage was the pulse-to-pulse stability of the dark current. The framegrabber software allows each beam pulse to be displayed on the video monitor without flicker until the next pulse. It was not uncommon for people in the control room to stare intently at the updating dark current signal and refuse to believe that it was not a single frozen image! This was actually a very important result that informed us that the rf pulse and magnet power supplies were extremely stable on time scales of seconds to minutes. This made the dark current a stable signal on which to experiment.

Dark-current emission occurs every rf cycle (micropulse) during the 3-μsec macropulse when the gun is filled with rf power. The rms length of a micropulse averaged over the entire macropulse was measured to be 11 psec (see Sec. 6.4). At accelerating fields of around 75-80 MV/m, corresponding to an output momentum of about 3.5 MeV/c, the charge in a macropulse is 1-2 nC. This rapidly increases as the rf power is raised, but rf breakdown usually begins around 90 MV/m unless the gun is first conditioned at higher power levels. Below this range the dark current dwindles rapidly so that by about 65 MV/m (3.0 MeV/c) the dark current is no longer visible. For this reason photoelectron studies were often conducted at this lower momentum.

The transverse profile of the dark current was an interesting issue. The dark current tended to exhibit quite complicated structure as viewed on the profile monitors. It could appear to have several main components that were focused and defocused separately and moved relative to one another as the optics were changed. It sometimes had a rather filamentary appearance that was not conducive to obtaining quality focuses. Over periods of days the various profiles were reproducible, that is, one could duplicate a beam tune from a previous run and obtain the same beam profile. Over longer time periods, particularly after the discovery of the enhanced emission (see Sec. 9.6), the structure of the dark current was observed to change.

The existence of several distinct beam components is not inconsistent with the possibility that dark current is preferentially emitted from a small number of isolated struc-

tures on the cathode surface. Given the sensitivity of field emission to the (enhanced) electric field, this seems quite plausible. The slowly changing beam profile would be explained by alterations to the cathode surface by rf breakdown or laser damage. Also, it is not known precisely what effect the 1-mm hole has on the local electric fields.

Due to the complicated shape of the dark current, the normalized transverse emittance was often of dubious interpretation. Nevertheless, it was measured on a number of occasions and found to generally lie in the range of 4-20 mm-mrad (one of these measurements is described in Sec. 9.4). The range of values could be caused by several factors, including the choice of a beam-size parameter, the selected momentum spread, and real fluctuations of the emittance as the cathode surface changed. Measurements performed within a short time span under the same conditions tended to be reproducible. In such a comparison the x and y emittances were found to be similar in value, as would be expected.

8.6 Nd:YAG-Laser Performance

The properties of the photoelectron beam depend strongly on the operational characteristics of the Nd:YAG laser. We will report here some of the measured laser properties in the context of their effect on the electron beam, as well as certain laser parameters that are difficult to measure directly and that we can only infer from observations of the resulting electron beam.

The pulse length of the Nd:YAG laser was measured with a streak camera[2] having a resolution of under 2 psec. In a streak camera an incident light pulse is converted by a photocathode to an electron pulse, the length of which is measured using an rf-deflection technique similar to that described in Sec. 6.4. This camera could be positioned near the YAG-laser optical table for measurements of the ir and green Nd:YAG-laser beam. A sample streak-camera trace is shown in Fig. 8.3.

The 1064-nm pulse was found to have a FWHM length of between 18 and 24 psec; the 532-nm pulse a FWHM of around 14 psec [70]. As mentioned in Sec. 2.5.1, each frequency doubling has the effect of reducing the pulse duration by a factor of $\sqrt{2}$, so the 266-nm pulse should have a FWHM of 9-12 psec. Assuming a Gaussian temporal profile, this corresponds to an rms width of 4-5 psec.

A similar streak camera was also used to measure the length of the uv beam after frequency quadrupling. The second doubling occurs in the laser hutch in the double-bend area (Fig. 2.4). In this setting it was trickier to transport the laser out of the final optics leading to the rf gun and into an area in which the streak camera could be positioned. The difficulties in this configuration resulted in data of questionable interpretation.

The temporal stability of the laser at the picosecond level was not directly measurable. Instead the jitter of the electron beam was studied in two different ways. The more direct approach is to use the rf-deflection cavity as described in Sec. 6.4. The pulse-to-pulse variation of the beam vertical centroid when the kicker is on for a pulse-width determination provides a direct measure of the timing jitter of the laser pulse. This is a reasonably accurate prescription as the centroid of the beam can be determined even

[2]C1587 Universal Streak Camera, Hamamatsu Photonic Systems Corporation, Bridgewater, NJ

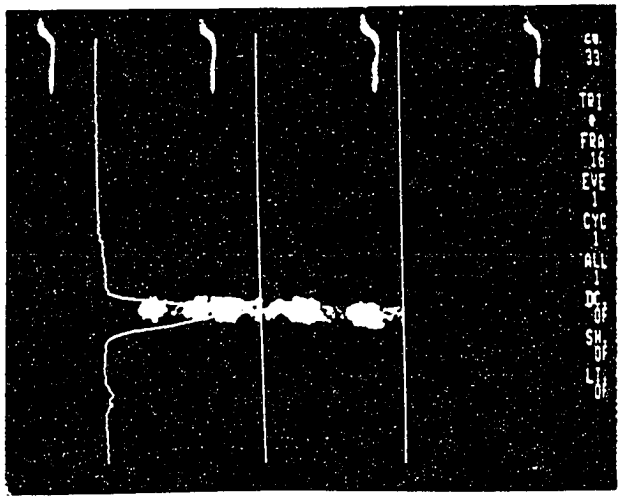

Figure 8.3: A sample streak-camera trace of the Nd:YAG laser at a wavelength of 532 nm, showing intensity versus time. The full vertical scale is around 650 psec, from which the FWHM of the pulse is estimated to be 30 psec. This trace was taken before the laser was fully optimized for producing short pulses.

more precisely than the width. When the laser beam was running stably the rms jitter was not more than a picosecond.

A more indirect method is to tune the beamline for momentum spectrometry and view the beam on the closed momentum slit. Shifts in the horizontal centroid are due to fluctuations in the beam central momentum, which in turn are the result of jitter in the laser with respect to the rf phase. (That variations in the gun power and accelerating electric field are not the cause is evident from the stability of the dark-current pulse.) From the momentum-dispersion constant on the slit, horizontal centroid shifts may be related to timing variations. These data confirmed a timing jitter of around a picosecond.

Before the rf cavity was installed in the beamline, such indirect information about the electron-beam temporal profile was extracted by examining the momentum structure of the beam on the momentum slit. Since the momentum of an electron is a function of the rf phase at which it leaves the photocathode (see Fig. 9.1), the momentum spectrum of the beam provides some information about the temporal length. While this wasn't an accurate temporal diagnostic, it provided some early clues about the temporal properties of the electron and Nd:YAG-laser beams.

An example is given in Fig. 8.4, which shows the horizontal profile of a photoelectron beam viewed on the phosphor-coated momentum slit with the beamline tuned in spectrometer mode. It shows clear evidence for at least two distinct peaks at different momenta, corresponding to two pulses in time. This is much more likely than such modulation occurring directly in the horizontal beam profile. This structure had been

hinted at by the observation of several rf phases at which the photoelectron beam was observed, but this was the first evidence showing the several features simultaneously. Early streak-camera measurements of the YAG-laser beam revealed such multiple pulsing on the few-picosecond scale, which have since been eliminated.

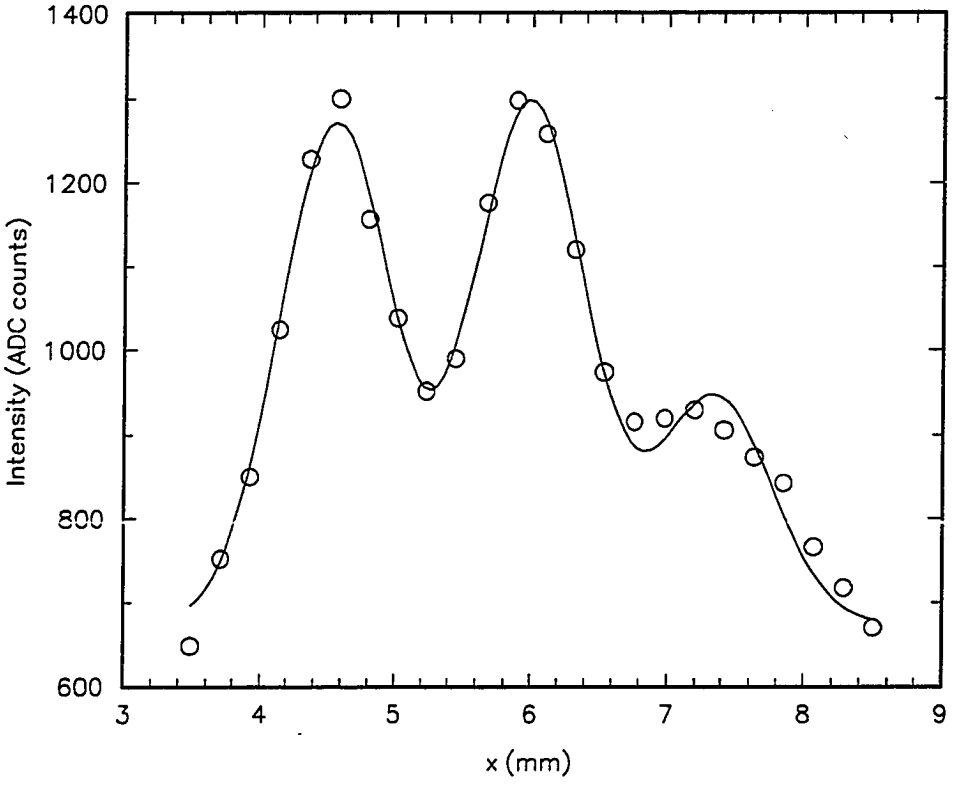

Figure 8.4: A horizontal beam profile on the momentum slit. The beam was tuned for momentum spectrometry at the slit. The horizontal profile is the momentum spectrum, which in turn is largely determined by the beam's time structure. The curve is a fit to three Gaussians, all of the same width. Obtaining a rough time calibration from the measured horizontal momentum dispersion and a PARMELA simulation relating momentum to rf phase, these data indicates at least 2 pulses of around 3-psec FWHM separated by about 5 psec. The temporal calibration is estimated to within a factor of two.

Although the Nd:YAG laser was shown to be stable at the picosecond level when operating properly, there are two types of instability exhibited by the laser. These occur frequently enough to make data collection an arduous process.

One of these is related to the mode locking of the YAG oscillator. The correct cavity length is maintained by adjusting a piezoelectric crystal housing the acousto-optic modulator. Such adjustments are necessary because temperature drifts or mechanical

vibration cause the cavity length to change. Small changes are compensated for by the phase-locked feedback device (see Sec. 2.6). Sufficiently large drifts (on the order of microns) can defeat the phase lock, at which point the picosecond synchronization to the rf system is lost. The resulting photoelectron beam is unstable in its momentum and spatial properties and was unsuited for study.

During most of the commissioning period the needed adjustment was performed manually by a laser operator, and could be required as often as several times in one day. Unfortunately such cavity adjustments had the attendant effect of resetting the relative phase between the mode locker and master oscillator. In other words the phase at which the modelocker was set to produce a given photoelectron-beam momentum jumped to a different value. This made studies of the electron beam as a function of rf phase challenging at best. Not long before the 1991-2 shutdown an automated adjustment mechanism was installed that utilizes an error signal from the phase-lock device to maintain the proper cavity length. This should eliminate, or at least greatly reduce, the number of manual adjustments necessary.

A second timing issue concerns the switching of the amplifier pulse via the Pockels cell. As the time between oscillator pulses is 12.25 nsec, and the round-trip time in the amplifier is 14 nsec, the Pockels cell must be switched within a nanosecond or so to avoid having two pulses in the amplifier cavity. Switching the Pockels cell entails applying a pulse on the order of 10 kV with a nanosecond rise time. A reliable high-voltage pulser was never found during commissioning and at the time of writing is still an open question.

In particular, the switching was incomplete so that there was often a second Nd:YAG-laser pulse separated from the first by 14 nsec. The result was a second rf phase at which photoelectron beam was observed. This was confusing, especially when the relative rf phase was reset by adjustments to the oscillator cavity length. Unfortunately, the relative intensity of the two pulses was not fixed, as the amplifier output is rather sensitive to the fraction of the second pulse allowed in the cavity. Great care had to be taken to insure that the "primary" pulse was always the one selected.

The spatial profile of the laser was stable on a pulse-to-pulse basis. The laser profile on the photocathode was monitored on-line (see Sec. 2.4.1) and was observed to have only small variations in shape and position (on the order of ten microns at most). A sample laser-spot profile is shown in Fig. 8.5.

One potential improvement to the laser optics was noted, however. The position of the photoelectron beam on a profile monitor was observed to be quite sensitive to the small variations in laser position on the cathode. The laser passes from the optic table in the experimental hall (Fig. 2.6) to the gun-injection optics through an air-filled tube some tens of meters in length and which is open at both ends. Covering the ends of the tube (allowing a small aperture for the laser beam) was observed to remove the large photoelectron beam fluctuations on one occasion. Presumably laser heating and movement of the air in the tube cause small but noticeable deflections of the laser. The solution is to evacuate the tube.

The relatively low robustness and reliability of the Nd:YAG laser represented one other obstacle to attaining an electron beam of the quality needed for systematic study and experimentation. The intensity of the amplified laser is such as to cause frequent

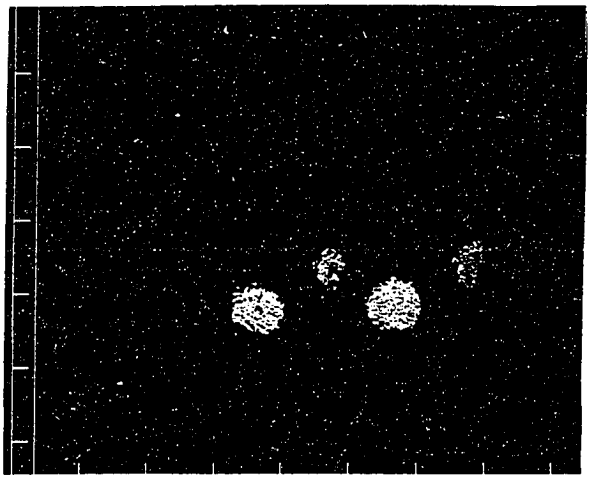

Figure 8.5: A sample video profile of the Nd:YAG laser on the photocathode. The larger spot on the right is the true image; the other spots result from reflections. Scale tickmarks are millimeters. The spot has an rms size in x of 0.22 mm and in y of 0.19 mm.

optic damage to certain key components such as the Nd:YAG amplifier rod or one of the doubling crystals. The result is a day or two during which the laser is unavailable while the component is replaced and the laser system realigned.

The down time due to optic damage, Pockels-cell problems, and various readjustments to the optical system was substantial. This rendered quality photoelectron beam time in shorter supply than was desired and made systematic studies requiring more than a couple of hours all but impossible. The experience gathered from the low-energy commissioning made it clear that some substantial redesign of the Nd:YAG laser will be required if a reliable electron beam is to made available for user experimentation at the ATF. These issues are being addressed during the 1991-2 shutdown.

Chapter 9

Studies of the Photoelectron Beam

In this chapter are presented the results of the photoelectron-beam studies, some of which are summarized in Table 8.1. Where possible the data are compared with the estimates and modelling results given in Chapters 2, 4, and 5. There are a number of beam studies that allow us to probe the physical mechanisms outlined in those chapters. We begin by listing those that were possible in the injection beamline as it existed during commissioning.

- Measure the pulse charge as a function of laser-pulse energy and determine the photocathode quantum efficiency (discussed in Sec. 4.2.3).
- Study the variation of the gun-output momentum with rf phase and rf-power input and measure the minimum momentum spread of the beam (Sec. 2.3).
- Measure the transverse emittance under a variety of gun-excitation conditions in order to minimize the emittance and identify the factor or factors barring further improvement (Sec. 4.3.2 and Chapter 5).
- Measure the photoelectron-beam pulse length, peak current, and peak current density (Sec. 4.4.1).
- From the measured transverse emittance and peak current calculate the normalized brightness (Sec. 4.3.2 and Chapter 5).

In the course of these studies we discovered an unexpected phenomena in the gun cavity. Above a threshold laser intensity the ejected charge jumped by two orders of magnitude. This prompted an interesting diversion:

- Characterize the "enhanced-emission" mode of rf-gun excitation.

9.1 Pulse Charge and Quantum Efficiency

The photoelectron bunch charge can be measured at the momentum slit, which doubles as a Faraday cup. Charge collection is performed under optimized beam-tune conditions that maximize the Faraday-cup signal. Acceptance studies of the beamline (see Sec. 8.4) indicate that the charge emitted can be transported to the slit with at least 70% efficiency.

From a simultaneous measurement of the beam charge and the laser-pulse energy the quantum efficiency (QE) of the cathode material can be calculated. The quantum efficiency η is defined as the number of photoelectrons liberated per incident photon, calculated from

$$\eta = \frac{Q\,h\nu}{U},$$

where Q is the number of electrons in a beam pulse, U is the energy in the laser pulse delivered to the photocathode, and $h\nu$ is the energy of a laser photon. For the quadrupled Nd:YAG laser with $\lambda = 266$ nm, $h\nu = 4.66$ eV. (What is measured is more properly called the "collection efficiency," which is the product of the quantum efficiency and the transport efficiency. It represents a lower limit on the quantum efficiency.)

The photoelectron charge recorded at the slit ranged from 0.3 to 2.0 nC, primarily influenced by the laser energy as expected. At the maximum charge of 2 nC the measured laser-pulse energy was 160 μJ. This gives a quantum efficiency of $\eta = 6\times10^{-5}$. Values no more than a factor of two smaller were found at other laser energies. In each case the cathode had been "conditioned," or driven at high rf power, for several hours to pull off as much accumulated surface contamination as possible.

This value is in reasonable agreement with Ref. [40], which reported a result two times larger. QE measurements are notoriously difficult to perform and exhibit great sensitivity to surface preparation. Recall also that the QE depends on the electric field applied to the cathode.

9.2 Momentum Properties

The momentum of the electron beam is measured by viewing the momentum slit as a profile monitor, centering the beam on the closed slit (which is horizontally centered on the beam axis), and noting the current applied to dipole D1. The magnetic field is a linear function of the coil current over the current range used to steer the low-energy beam. The measured field integral for the nominal path, a 90° bend, then defines a unique momentum. D1 has an excitation constant of 0.2579 MeV/Amp.

One of the first measurements performed on the photoelectron beam for comparison with rf-gun modelling studies was the gun output momentum as a function of the rf phase at which the laser strikes the cathode. The phase of the master oscillator signal to the Nd:YAG-laser modelocker was varied and the resulting photoelectron-beam momentum measured. A sample measurement is shown in Fig. 9.1. Shown for comparison is the curve predicted by the program PARMELA for a peak accelerating field of 86 MV/m. The peak field is calculated from Eq. (2.2) from our discussion of the maximum output momentum as a function of accelerating field in Sec. 2.3.2. Good agreement is seen.

The momentum spread of the beam is measured by configuring the beamline for the so-called "spectrometer tune," in which a monochromatic beam would be focused horizontally to a spot size on the slit that is small compared with the horizontal smear introduced by chromaticity (see Sec. 8.3). The momentum dispersion on the slit is calibrated by changing the dipole strength corresponding to a known change in momentum and measuring the horizontal deflection of the beam centroid. This yielded a measurement with a resolution of around 0.1-0.2% in $\Delta p/p$.

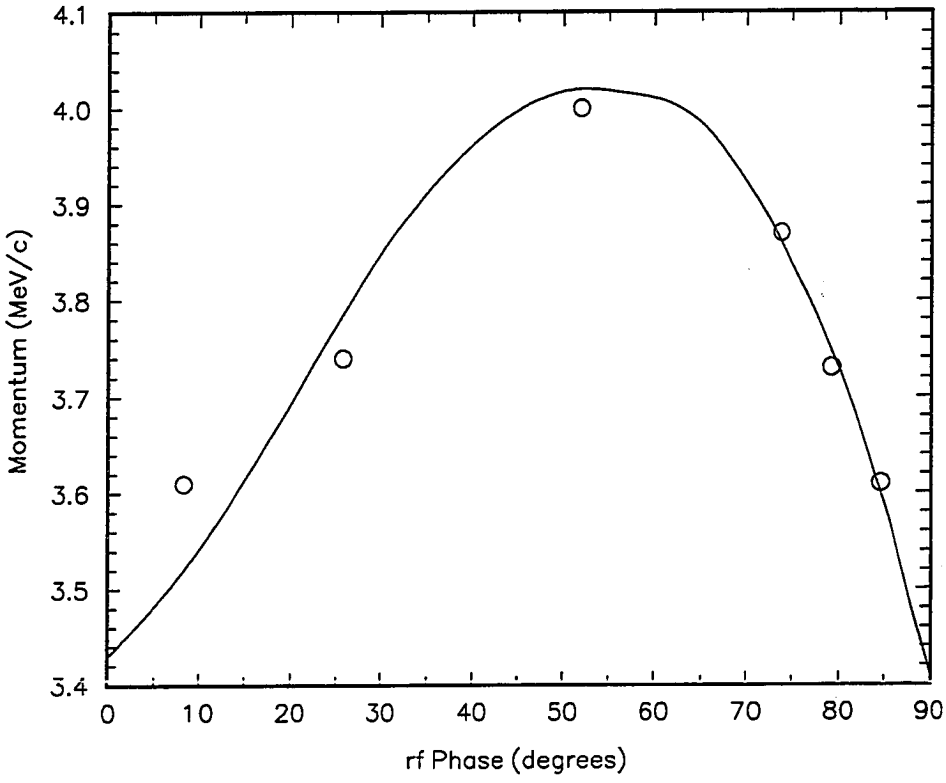

Figure 9.1: The photoelectron-beam momentum as a function of the rf phase into the gun. The data points are the momentum measured in the beamline. The curve is a PARMELA calculation with a peak axial field of 86 MV/m. (Compare with Fig. 2.3(b), calculated for a field of 75 MV/m.)

The minimum rms momentum spread observed for the photoelectron beam was 0.4%, at a peak momentum of 4.0 MeV/c. The momentum spread predicted for an rms pulse length of 6 psec from the PARMELA simulation at 86 MV/m shown in Fig. 9.1 is 0.3%, in agreement with the simple numerical study at an accelerating field of 75 MV/m presented earlier (Fig. 2.3(b)).

The shunt impedance Z_S of an rf structure expresses the power required to maintain accelerating fields of a given strength. It is defined by the expression

$$E^2 = Z_S \frac{dP}{dz}, \tag{9.1}$$

where E is the spatial average of the on-axis longitudinal electric field at the temporal maximum and dP/dz is the power drain per unit length. If E is in V/m and dP/dz is in W/m, then Z_S is in Ω/m.

The shunt impedance of the gun can be measured by recording the peak output momentum as a function of input rf power. To cast Eq. (9.1) into a form more amenable

to measurement we multiply each side by the gun length L squared and by a "transit-time factor" T squared. The transit-time factor relates the spatial-temporal average accelerating field experienced by an electron transitting the gun to the spatially averaged field in Eq. (9.1). We then obtain

$$E^2 \cdot L^2 \cdot T^2 = Z_S T^2 \cdot \frac{dP}{dz} \cdot L^2$$

or

$$\left(\frac{\Delta E}{e}\right)^2 = Z_S T^2 \cdot L \cdot P,$$

where ΔE is the electron energy gain (approximately equal to the output momentum) and P is the rf power input to the gun obtain the observed momentum.

For a peak accelerating field E_0, the spatial average of the sinusoidally varying field is $(2/\pi) \cdot E_0$. The spatial-temporal field average calculated in Sec. 2.3.2 is $0.511 \cdot E_0$, which makes the transit-time factor $T = 0.80$. From such measurements of $\Delta E \simeq p_z$ as a function of P the shunt impedance was found to be 50 MΩ/m. Simulations with the program SUPERFISH predicted 57 MΩ/m.

In principle the peak accelerating field could now be determined from the measured rf power into the gun and the shunt impedance. In practice, however, the rf-power measurements are of rather low precision (perhaps good to within 20%). A more accurate determination of the accelerating field is obtained from the peak output momentum and Eq. (2.2), as was done to calibrate the gun simulation to the data in Fig. 9.1.

The gun is designed for operation at accelerating fields of up to 100 MV/m, for which the output momentum is 4.5 MeV/c. We operated in the region of 58-88 MV/m (output momentum 2.8-4.0 MeV/c) as higher fields caused frequent rf breakdown unless extensive conditioning was done first.

9.3 Transverse Emittance

The transverse emittance was measured under widely varying conditions: rf phase in the range of 40-75°; laser rms spot size on the cathode varying from 0.2 to 1.2 mm; collected charge ranging from 0.3 to 2 nC; and beam momentum from 2.75 to 3.8 MeV/c. The emittance was measured in the 'Z' line and after the double bend. Most measurements were of the vertical emittance in the 'Z' line, where the momentum dispersion prevents determination of the horizontal emittance.

The emittance-measurement techniques are described in detail in Sec. 6.2. In brief, the photoelectron-beam video image is isolated by subtracting an image of the dark current (obtained with the laser blocked from the photocathode) from an image of the composite beam. The remaining image consists of only photoelectron signal. A series of such images collected at different monitors or at a single monitor at varied settings of an upstream quadrupole allows us to deduce the second moments of the beam distribution in trace space (corresponding to the spot size, angular divergence, and angular correlation) and the emittance.

The pulse-to-pulse stability of the dark-current profile allows it to be completely subtracted as a background, leaving an image that consists of only photoelectron beam

and video noise. This is illustrated in Fig. 9.2, which shows video images of the dark current, the composite beam consisting of dark current and photoelectron beam, and the subtracted image with only photoelectrons remaining. The photoelectron beam vertical profile so obtained is shown in Fig. 9.3.

Figures 9.4, 9.5, and 9.6 present a walk-through of the emittance-analysis procedure. This particular scan was taken in the 'Z' line on beam-profile monitor BPM1 by varying quadrupole ZQ2 (see Fig. 2.4). Fig. 9.4 shows the subtracted video images at three different settings of the quadrupole strength. Fig. 9.5 contains the vertical profiles of each of the corresponding video images. (The same data are plotted on the left side of each video image in Fig. 9.4.) The vertical spot size can be seen to pass through a minimum in image (b).

The vertical rms spot sizes are plotted as a function of the quadrupole current in Fig. 9.6. The beam matrix at the quadrupole is calculated from the data, and the predicted spot size as a continuous function of the quad current is plotted as a smooth curve. This is called an *emittance plot.* From these data the normalized emittance was found to be $\epsilon_N = 5.1 \pm 0.2$ mm-mrad. For this scan the beam charge was 0.3 nC and the momentum was 2.80 MeV/c. The rms laser spot size on the cathode was 0.4×0.2 mm^2.

The largest source of error in emittance measurements is the uncertainty in the beam size due to pulse-to-pulse variations in the beam spatial profile. (See Sec. 8.6.) This variation was much larger than the error in determining the width of a single pulse and had considerably greater effect on the emittance result than the uncertainties in the beam-transport parameters such as the drift distance and quadrupole excitation constant. As such it was usually the only factor included in the error analysis.

The only way to characterize the pulse-to-pulse spot-size variation is to collect and analyze multiple beam images at each transport condition and perform statistics on the sample of spot sizes. The error bars of the emittance scan shown in Fig. 9.6 were arrived at in this fashion. This was done only occasionally as it required large amounts of beam and analysis time. It was found that under good conditions, when the laser was reasonably stable, the electron-beam spot size exhibited rms fluctuations of around 10% on average. Hence for scans in which only one profile was collected per data point (as is the case for all remaining emittance measurements presented here), the spot-size error was chosen to be 10%. A rigorous error analysis of the emittance measurement tended to give a relative error close to that of the 10% spot-size uncertainty, as expected (see Sec. 6.2).

An emittance scan taken under rather different beam conditions is shown in Fig. 9.7. This is also a vertical emittance scan on profile monitor BPM1, but using quadrupole ZQ1 to vary the spot size. (ZQ2 is usually turned off during a scan using ZQ1, but does not have to be.) The beam charge is 2.0 nC, momentum is 3.80 MeV/c, and the laser-spot size is 0.14×0.35 mm^2. The measured emittance is $\epsilon_N = 3.8 \pm 0.3$ mm-mrad. Here only one beam profile was collected at each quadrupole strength, and the error bars assigned a value of 10%. The pulse-to-pulse variations of the photoelectron beam are more apparent than in Fig. 9.6, where several spot sizes are averaged to obtain each data point.

There were several experimental issues that had to be resolved before a clear interpretation of the emittance results emerged. Early measurements were plagued by

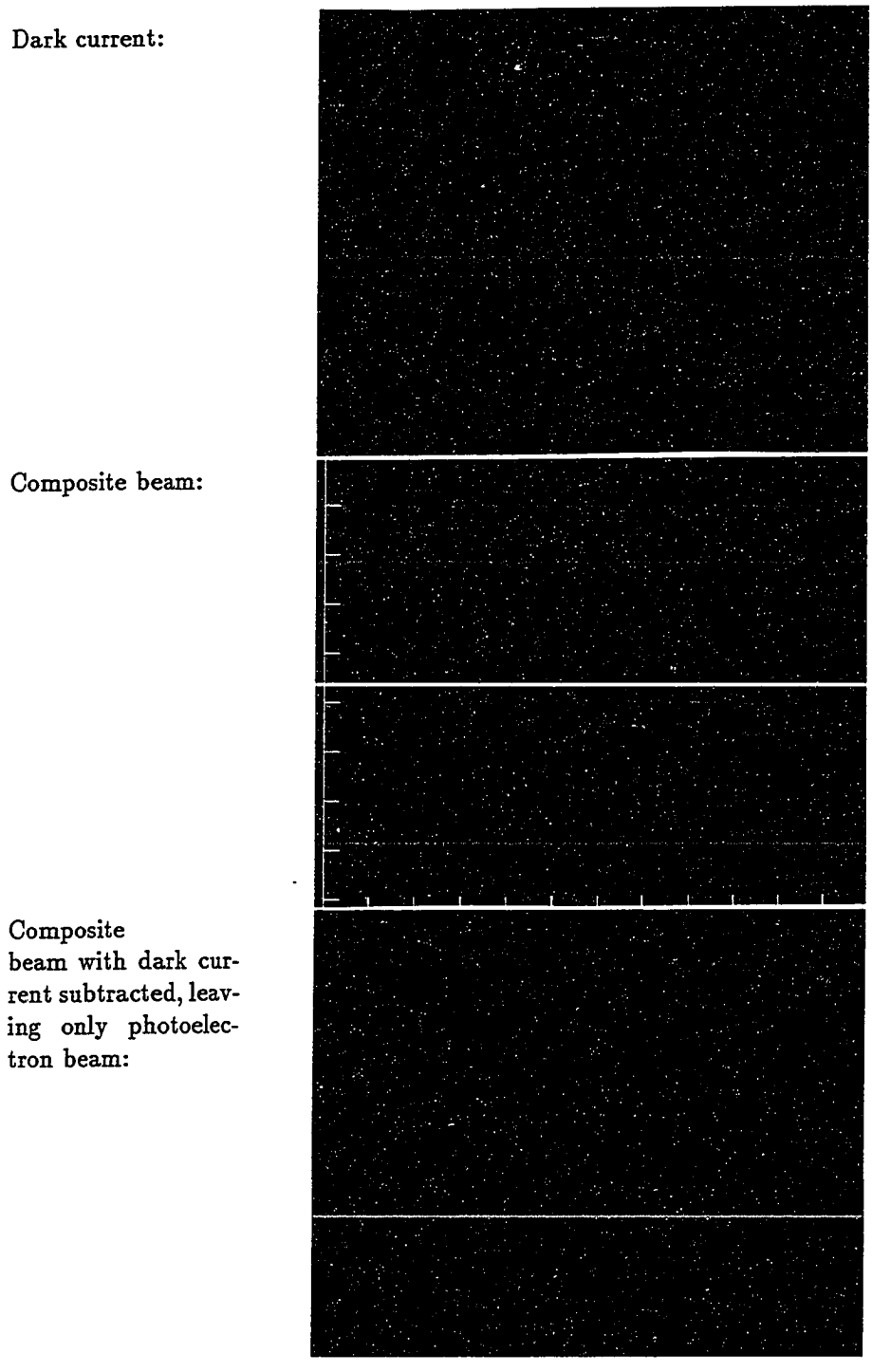

Figure 9.2: Video subtraction of the dark-current signal

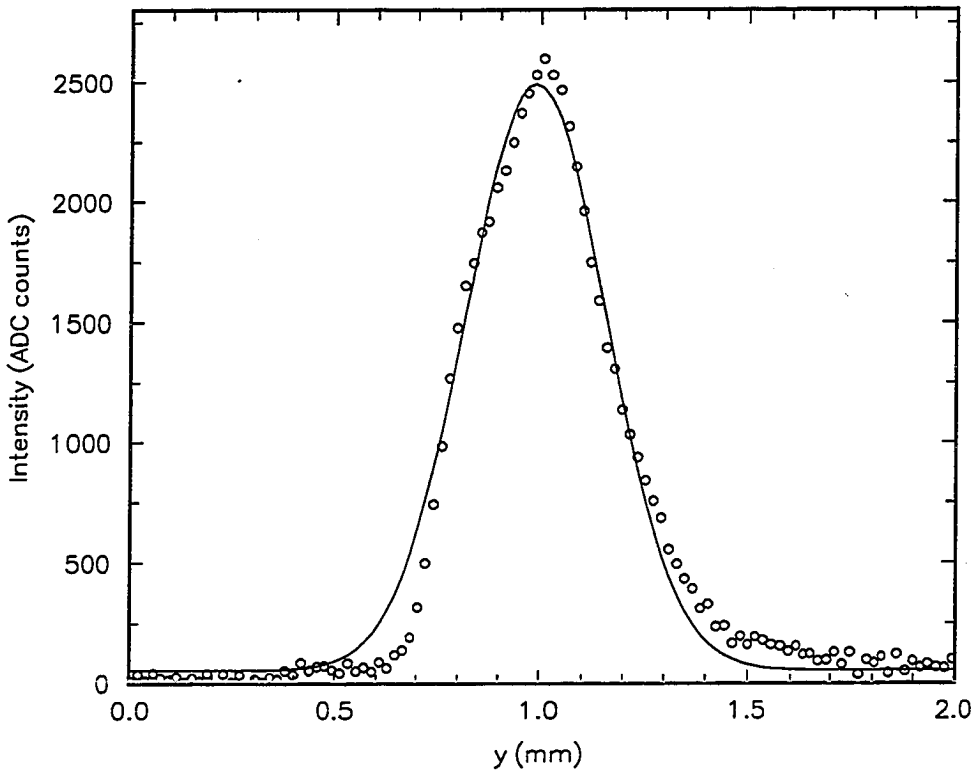

Figure 9.3: Vertical profile of the dark-current-subtracted beam, including fitted Gaussian; the width is $\sigma_x = 0.17$ mm.

irreproducible and nonphysical results. This was when the lessons outlined in Chapter 6 concerning the requisite number and spacing of beam-profile samples were learned "the hard way." It was also found that the analysis of certain data exhibited numerical instabilities in single-precision (four-byte) computation that were removed by performing calculations in double precision (eight bytes).

The contribution of the beam-profile-monitor spatial resolution to the measured emittance is calculated in Sec. 6.3. Applying Eqs. (6.7) and (6.8) to the ATF measurements, we find that the 37-μm vertical resolution (discussed in Sec. 7.5.3) contributes at most 10-15% of the measured emittance. This analysis was confirmed by subtracting the beam-profile-monitor resolution in quadrature from all spot sizes in sample emittance scans and repeating the analysis. The calculated emittance decreased by no more than 10-15%.

The question of beam-profile characterization is of great importance to a proper interpretation of the emittance measurements. In some situations the transverse profile of the beam was well characterized by a Gaussian, in which case the standard deviation was used in the emittance determination. Examples of such photoelectron-beam profiles

(a) ZQ2 = −0.330 A

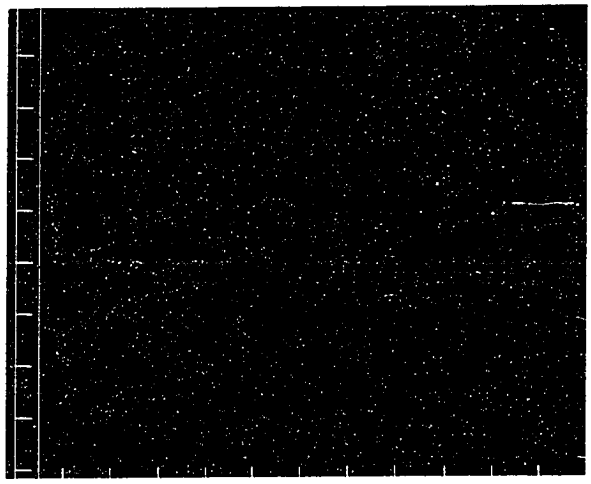

(b) ZQ2 = −0.320 A

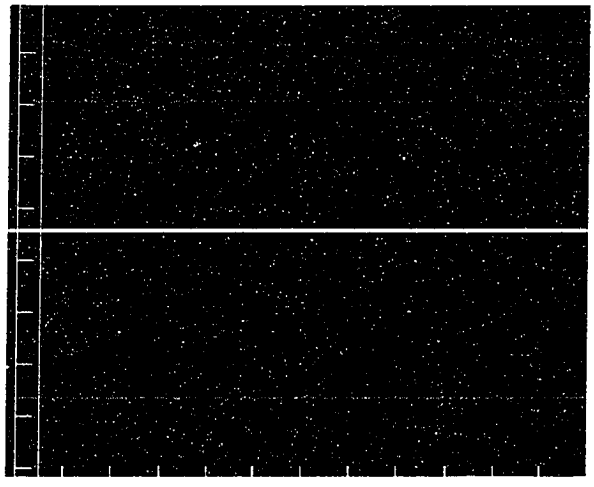

(c) ZQ2 = −0.309 A

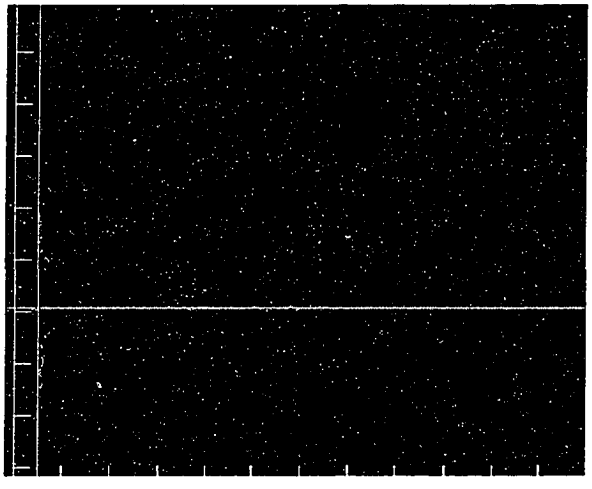

Figure 9.4: Video images from an emittance scan

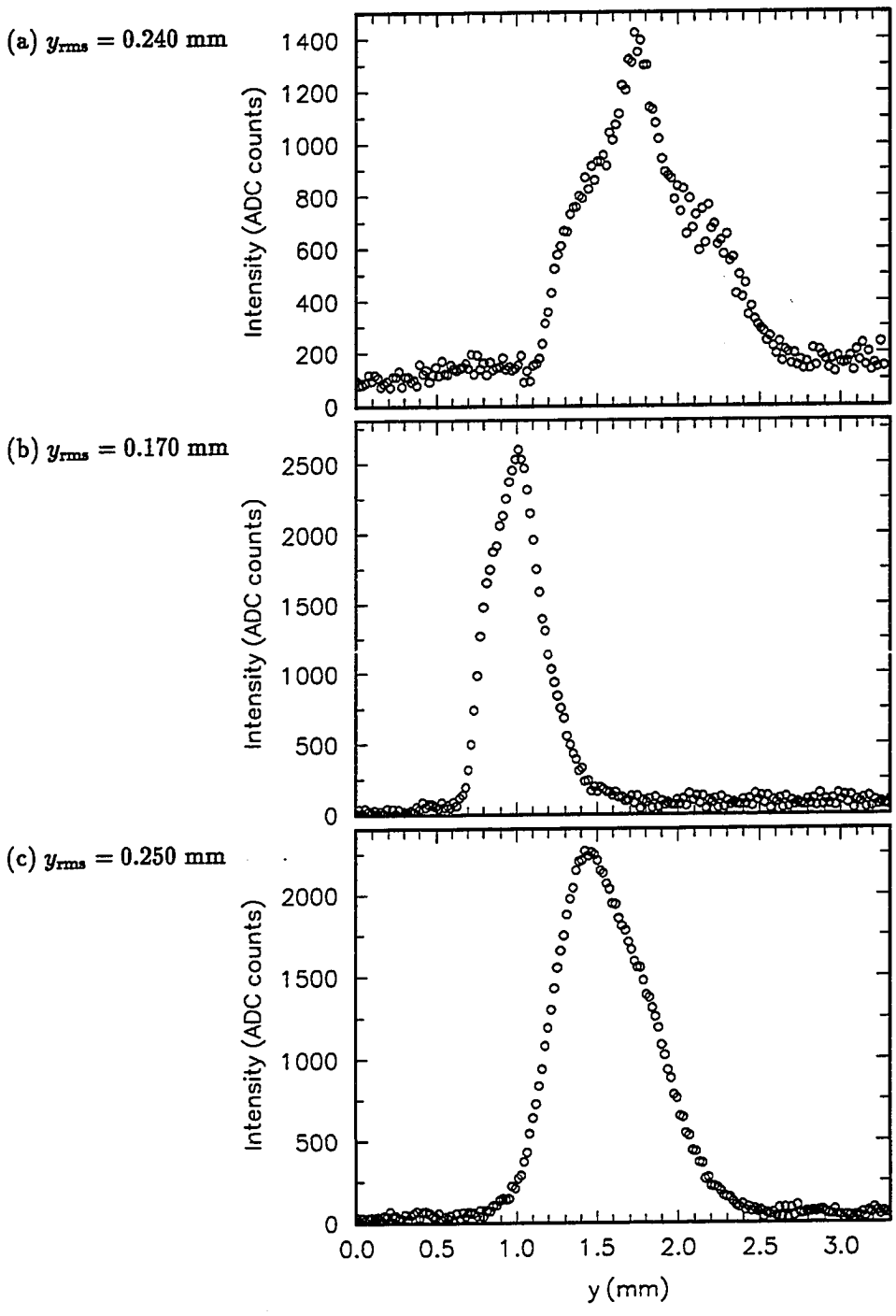

Figure 9.5: Vertical profiles of the beam images in Fig. 9.4

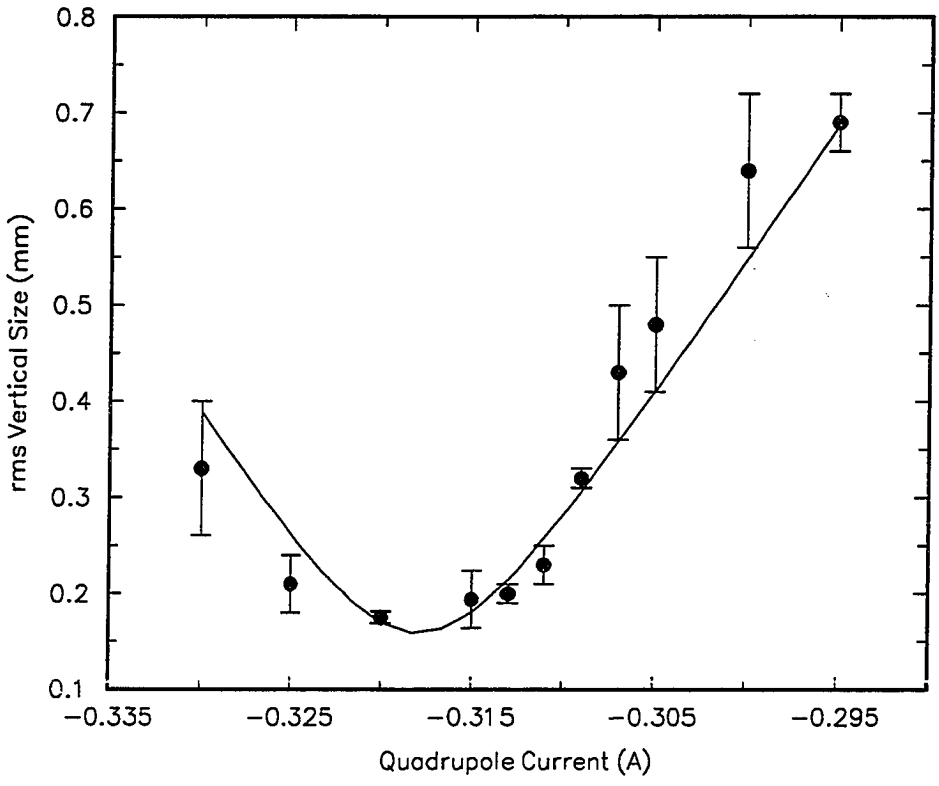

Figure 9.6: The emittance scan sampled in Figures 9.4 and 9.5. The rms vertical spot size of the photoelectron beam at profile monitor BPM1 is plotted as a function of current in the varied quadrupole (ZQ2). Error bars are statistically derived from repeated measurements at each quadrupole setting. The smooth curve shows the beam size predicted from the measured beam matrix, from which a normalized emittance of $\epsilon_N = 5.1 \pm 0.2$ mm-mrad was calculated. Beam charge is 0.3 nC; momentum is 2.80 MeV/c.

are shown in Figures 7.5 and 9.3, and an emittance scan in which the beam exhibited a Gaussian profile throughout is shown in Fig. 9.8. In this particular measurement the pulse-to-pulse beam variations were among the smallest observed, as evidenced by the internal consistency of the data, each point of which was collected in a single beam pulse. Sometimes the beam consisted of a clear Gaussian core surrounded by lower-level tails. The analysis was performed in such a manner as to exclude these tails. This was deemed appropriate, as one of the techniques implemented in the ATF beamline for preserving the small emittance is collimation of the beam to remove such tails.

In many other cases the beam had a more complex structure. Two commonly observed shapes were a flattop distribution and Gaussian-like main peak with one or more satellite peaks of varying relative height and position (see for example Fig. 9.5). Each of

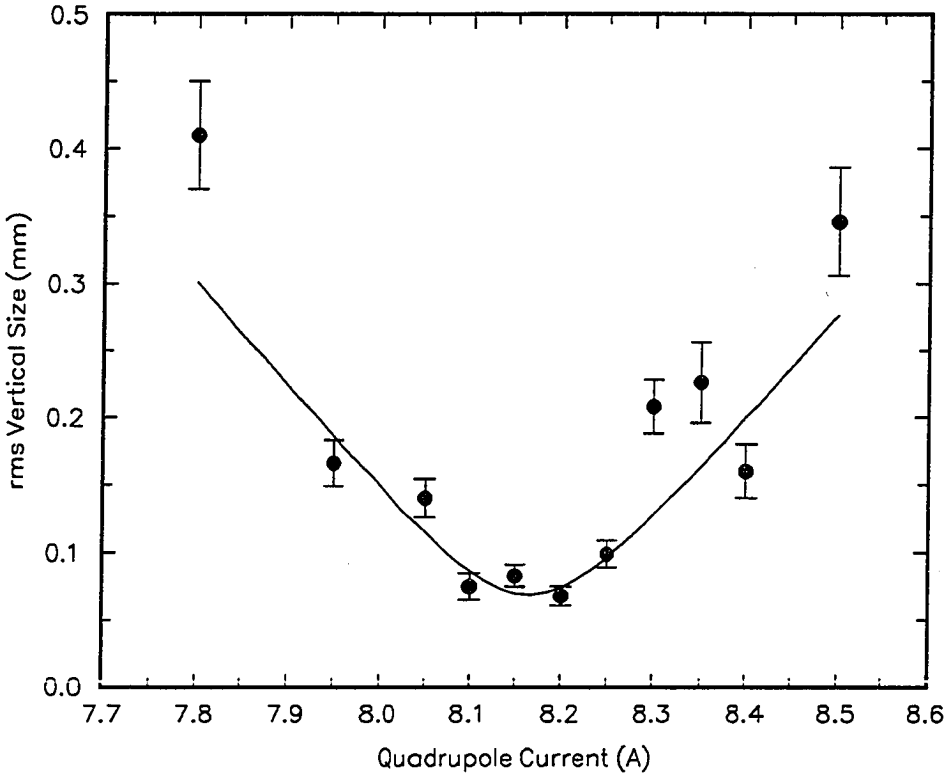

Figure 9.7: An emittance scan at a beam charge of 2.0 nC and momentum of 3.80 MeV/c. The normalized emittance is $\epsilon_N = 3.8 \pm 0.3$ mm-mrad.

these rendered a description of the beam based on a single Gaussian profile inadequate. In such cases the rms spot size was used in the emittance analysis. The difficulty of this approach is that it is sensitive to tails in the distribution. The approach usually adopted was to exclude any low-lying and nearly-constant tails as artifacts of the video signal and include any larger varying structures. The results obtained in this manner were consistent with analyses of Gaussian beams.

The cause of such beam structures is still an open question that will require further study. One possible cause of a flat profile is the homogenizing effects of space charge, which favors a uniform density profile as the lowest-energy configuration of a collection of charged particles (see Sec. 5.1). Another possibility is that the beam is collimated vertically. Acceptance studies of the ATF beamline, described in Sec. 8.4, did not reveal any obvious candidate for such collimation, but this explanation is hard to ignore given the strikingly hard edges sometimes observed. A multi-peak distribution could possibly be indicative of more than one region of the photocathode preferentially emitting electrons.

The most striking feature of the emittance results is their constancy. The normalized

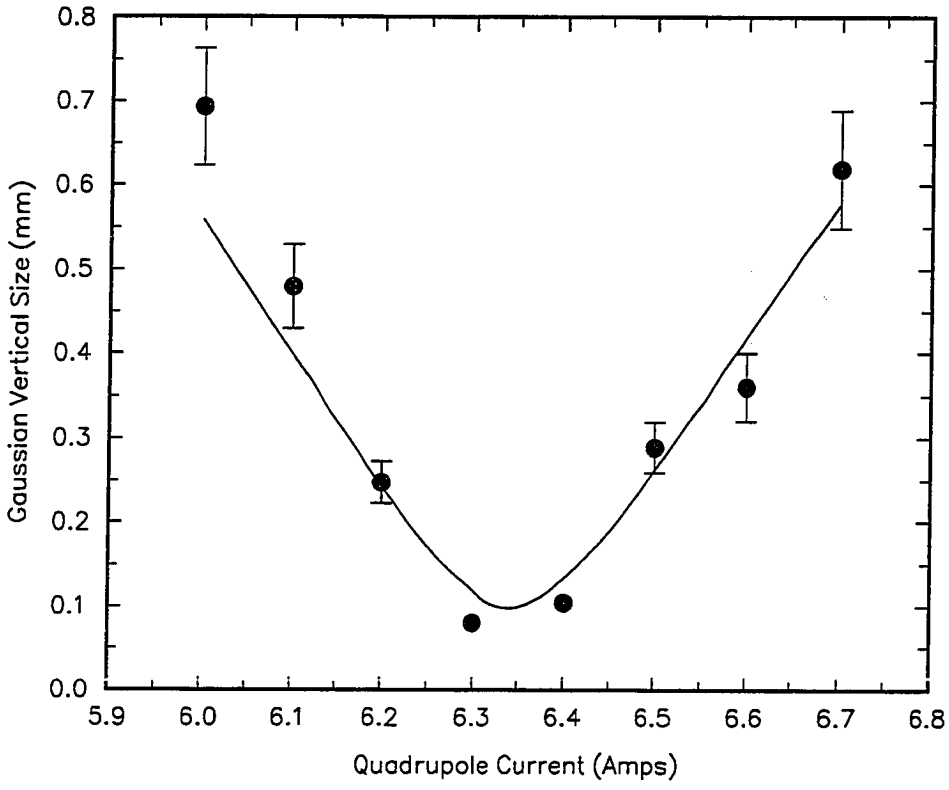

Figure 9.8: An emittance scan when the beam was particularly stable and exhibited Gaussian transverse profiles. The beam had momentum 2.95 MeV/c and normalized emittance $\epsilon_N = 4.0$ mm-mrad.

transverse emittance of the photoelectron beam was found to be surprisingly stable, maintaining a value in the range

$$3.8 < \epsilon_N < 5.0 \text{ mm-mrad.}$$

This is in marked contrast to the gun simulations, which predict more varied output emittances as a function of input conditions. The observed values are also consistently lower than the simulation predictions by as much as a factor of two or three. MAGIC tends to predict a smaller emittance than PARMELA for the same input, but neither indicates the emittance should be in the measured range for the measured gun conditions.

These observations could indicate a beam with a larger emittance is being collimated somewhere in the beamline. Although beamline acceptance studies failed to produce an obvious candidate region, this possibility cannot be dismissed since the position of beamline elements was not precisely surveyed. The results cited here are among the incentives for the precision laser-based alignment scheduled for the post-commissioning shutdown.

Another possibility is that the simulations are based on an only partially correct gun model that does not include all of the relevant effects. For example, the simulations are based on the assumption that the transverse energy of the electrons emitted from the cathode is either zero or given only by the difference between the laser-photon energy and the metal work function. The emittance variations thus found are due to the rf dynamics in the cavity and the effects of space charge, which are the primary contribution to the emittance. However, as was previously noted in Sec. 4.4.4, the contribution of the transverse energy imparted by the rf electric field alone could conceivably account for the magnitude of the observed emittance. The variation of this effect with the gun-excitation parameters would likely be different. Unfortunately the condition of the cathode at the time emittance data were being collected is not known, nor have simulations of the effect of cathode-surface morphology on electron transverse energy been performed. The effect of the 1-mm hole in the cathode was never simulated either. Some experimental studies that could help resolve this question are outlined in Chapter 10.

It should be noted that due to the sporadic availability of stable beam time and the ongoing construction of the beamline during commissioning, the beam emittance has not yet been studied under systematic variation of such variables as rf phase and power, laser spot size, and beam charge. Hopefully improvements in the Nd:YAG laser and additions to the laser optics will allow such studies in the future. The improvements to the laser optics necessary to allow systematic variation of spot size and pulse energy are being installed during the 1991-2 shutdown. The laser instabilities that hindered more systematic studies are described in Sec. 8.6.

Though not fully understood, the low emittance is good news whether it represents the true gun emittance or the beamline acceptance. It is the emittance and beam current passing through the beamline that determine the brightness of the beam to be accelerated and delivered to experiments (assuming no significant beam degradation occurs). The measured beam current and brightness are given in the next section.

9.4 The Pepper Pot

As outlined in Sec. 6.2, a transverse emittance measurement requires at least three transverse whole-beam profiles collected under varying transport conditions. This is because the information contained in a spatial profile effectively integrates out the angular divergence of the beam, yielding only one useful parameter: the transverse beam size. An emittance measurement thus involves collecting profiles of several pulses, separated by adjustments to the beamline optics. This takes valuable beam time and yields only a time-averaged value. Pulse-to-pulse variations in the emittance cannot be measured.

Additional information about the beam may be obtained by selectively masking off part of the beam upstream of the profile monitor. The known pattern of the mask combined with the resulting image at the profile monitor yield both spatial and angular information. A properly designed mask can allow emittance determination in a single beam pulse. The "pepper-pot" method has long been used to obtain single-shot emittance measurements. We tested this technique at the ATF as possible alternative or compiement to the whole-beam-profile methods. The pepper-pot method is illustrated

in Fig. 9.9.

The mask, or selection screen, consists of a plate thick enough to stop the beam, with a regular array of small holes allowing unattenuated passage of the beam. The individual "beamlets" defined by this selection screen impinge on a profile monitor downstream. The total intensity contained within each beamlet as a function of hole location provides a sampling of the beam spatial profile at the selection screen, akin to the profile obtained with no selection screen in place. The size of the individual beamlets at the monitor may be compared with the size of the defining holes and the spread of each beamlet thus determined. This is a sampling of the angular divergence of the beam at the selection screen. From these two types of information, we can find the emittance.

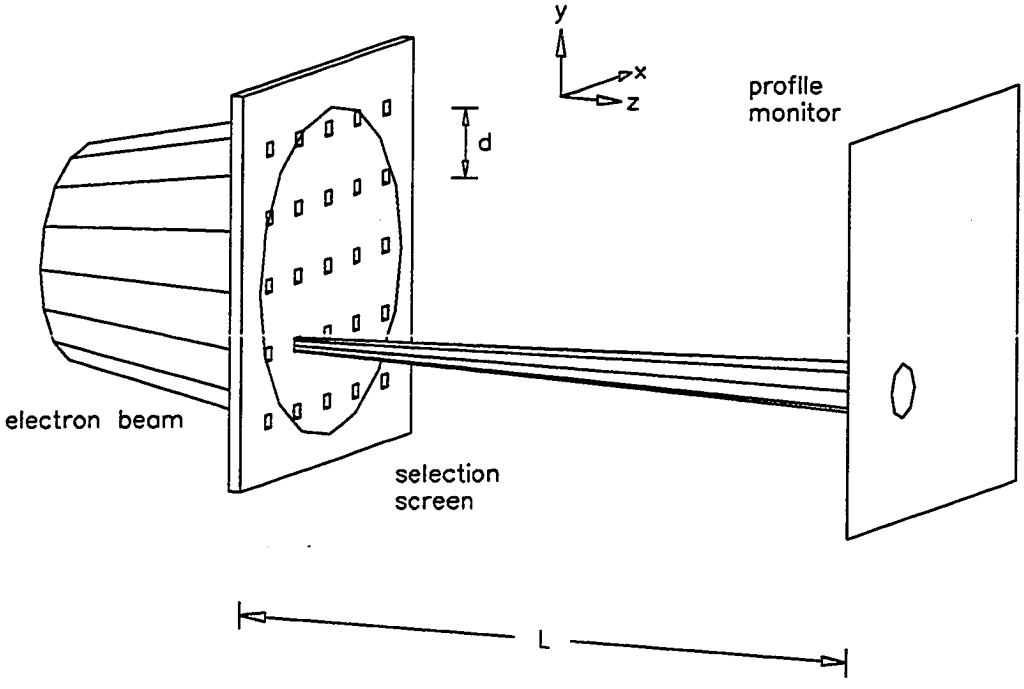

Figure 9.9: The pepper-pot technique. The electron beam impinges on a selection screen, which defines individual beamlets (only one of which is illustrated for clarity). These propagate to a beam-profile monitor. The resulting image reveals both the beam spot size and divergence at the selection screen, from which the emittance may be determined.

The size and spacing of the holes must be chosen appropriately for the parameters of the beam to be measured. For the ATF design the holes were chosen to be squares of side $s = 100$ μm on a square array of side $d = 1$ mm. The pepper-pot plate is made of 3-mm-thick lead, which completely stops 5-MeV electrons. The profile monitor was located a distance $L = 223$ mm downstream of the plate. This design was based on the

following considerations:

- The hole spacing d should be sufficiently small compared to the beam's spatial width at the selection screen to allow the spatial profile to be determined with reasonable resolution. On the other hand, it should be large enough that adjacent beamlet profiles at the monitor do not overlap.
- The hole size s should be sufficiently small compared to the beam width to insure that each beamlet represents to good approximation a sample of the beam intensity at a given point. But since the selection screen attenuates the beam by a factor of $(s/d)^2$, the holes should be large enough to pass a reasonable fraction of the beam.
- The plate should be thick enough to stop the vast majority of electrons, but no thicker, in order to minimize scattering from the inside surfaces of the holes, which have much longer dimensions along the beam axis than transverse to it.
- The distance to the profile monitor, L, should be large enough to allow the beamlets to spread to several times the size of the defining holes so that the hole-size contribution to the profile at the monitor is minimal.

The pepper-pot technique involves more data analysis because of the high information content of the image. This information can be used in several different ways to analyze the transverse trace space of the beam and calculate the emittance.

As one example, assume that the beam is characterized by a Gaussian distribution in the 2-dimensional trace space (x, x'). This is discussed in Sec. 3.1, where the trace-space distribution is written as

$$\rho(x,x') = \exp\left[\frac{-1}{2\det\sigma}(\sigma_{22}x^2 - 2\sigma_{12}xx' + \sigma_{11}x'^2)\right].$$

This can be written as

$$\rho(x,x') = \exp\left[\frac{-x^2}{2\sigma_{11}} - \frac{\sigma_{11}}{2\det\sigma}\left(x' - \frac{\sigma_{12}}{\sigma_{11}}x\right)^2\right].$$

In this form certain properties of the beam become more apparent.

First, we see that $\sigma_x = \sqrt{\sigma_{11}}$ is just the rms width of the beam in x integrated over x', in accordance with what is measured in a beam profile with no selection screen interposed. Second, the rms width of the beamlet angular profile is independent of x and is given by $\sigma_{x'} = \sqrt{\det\sigma/\sigma_{11}}$. The geometric emittance is then

$$\epsilon = \sqrt{\det\sigma} = \sigma_x\sigma_{x'}$$

and hence is just the product of the widths of beam spatial profile and the beamlet angular profile.

Finally, we see that the centroids of the beamlet angular distributions are a function of x with slope σ_{12}/σ_{11}. The angular centroid of a beamlet is the average angle it makes with respect to the beam axis (which has $x' = 0$ by definition). The matrix element σ_{12}

is the second moment $\langle xx' \rangle$, the beam angular correlation. The deviation of the hole pattern imaged onto the profile monitor from the regular array of side d gives a direct measure of σ_{12}. From ϵ, σ_{11}, and σ_{12} we may find σ_{22}. Hence a single pepper-pot image yields all three beam-matrix elements and the emittance.

To perform an analysis in the x plane as described above one may sum the pepper-pot data along the y axis as would be done for a whole-beam profile. Or individual rows can be analyzed and the results averaged. In either case the individual beamlet profiles are summed along the y axis to perform an analysis in x.

The beam distribution need not be assumed to be Gaussian, or even to have elliptical contours in trace space. The image can be analyzed in a general way that does not assume a particular beam distribution *a priori*. The width and centroid of the beamlet angular profiles as a function of x can be plotted to reveal the true trace-space distribution, Gaussian or otherwise.

The advantages of this technique are that the beam can be analyzed in a single pulse and the true phase space distribution can be measured. The disadvantage is that each profile must be subjected to a more extensive off-line analysis than would be required for simple whole-beam profiles.

In order to validate this method for future use, a brief test run was conducted with a pepper pot in the beamline. The selection screen was placed in profile monitor BPM3 located just upstream of BPM4 and the linac (Fig. 2.4), replacing the phosphor screen and mirror. As only dark current was available during the test run, it was used to find the beam tune most suitable for pepper-pot analysis.

Several configurations are possible: the beam can be focused upstream of the selection screen, at the selection screen, between selection screen and profile monitor, at the profile monitor, or downstream of the profile monitor. Having the focus at either the selection screen or profile monitor defeated the purpose of the selection screen by failing to provide a wide enough transverse sampling of the beam. Focusing upstream of the selection screen resulted in a few holes being magnified by a large factor at the profile monitor; this was not optimal. Focusing between the selection screen and profile monitor was similarly ineffective.

The best configuration was to focus downstream of the profile monitor. This resulted in many holes being demagnified by a factor of close to one at the profile monitor, so there was adequate sampling of the beam in both x and x'. Furthermore, this had the advantage of minimizing the correlation between x and x' (σ_{12}), which minimized the scattering of electrons from the hole walls and the effective narrowing of hole apertures by nonzero average angles of incidence. In this configuration, the diffuse background from scattering was quite small compared to the average beamlet intensity.

A sample pepper-pot analysis is depicted in Fig. 9.10. Part (a) is the x profile obtained by summing several rows together. From the widths of individual beamlets and the distance between selection screen and profile monitor, the rms angular divergence is measured to be $\sigma_{x'} = 0.67$ mrad. The whole-beam profile, obtained by plotting the integrated beamlet intensity as a function of horizontal position, is shown in Fig. 9.10(b). The fitted Gaussian has a width of $\sigma_x = 1.05$ mm. The geometric emittance is

$$\epsilon = \sigma_x \sigma_{x'} = 0.7\,\text{mm-mrad},$$

corresponding to a normalized emittance of 5.0 mm-mrad. This is consistent with values obtained for the dark current using the multiple-profile methods described in Chapter 6.

9.5 Pulse Length, Current, and Brightness

The temporal bunch length of the electron beam was measured using the rf-deflection technique described in Sec. 6.4. The rf kicker cavity introduces a time-correlated vertical deflection that is measured by viewing the phosphor-coated momentum slit. The beam is vertically focused onto the slit and the spot size measured. The kicker is turned on to zero phase, producing a time-correlated deflection, and the new width measured. The quadrature difference of the two, combined with the kicker calibration determine the pulse length.

This is illustrated in Fig. 9.11, which shows the vertical profile of the photoelectron beam before and after the kicker is turned on. The kicker-off profile has an rms size of 1.35 mm; the kicker-on profile 1.75 mm. The quadrature difference is 1.11 mm. The kicker produced a vertical deflection on the slit of 0.176 mm/psec, yielding an rms pulse length of 6.1 psec.

A beam of 1 nC was measured to have an rms length of 4.9 psec, and a beam of 2 nC a length of 6.0 psec. This in good agreement with the inferred Nd:YAG-laser pulse lengths in the uv of 4-5 psec from Sec. 8.6. While the profile of the pulse ejected from the cathode is expected to follow that of the laser at the subpicosecond level, two additional effects alter the photoelectron pulse length.

PARMELA simulations of the gun predict a 25% increase in the bunch length per nanocoulomb due to space charge [6]. Another prediction of PARMELA is an effect called "rf compression." This results from the fact that for launch phases between 0 and 90° the electrons ejected at the beginning of the laser pulse see a slightly smaller accelerating field than the electrons at the tail (see Eq. (2.1)). For launch phases of 40-50°, the compression factor is calculated to be 0.7-0.8 [6]. These simulations do not include possible bunch lengthening due to space charge between the gun exit and rf kicker.

The time profile of the beam current is assumed to be a Gaussian of the form $I(t) = I_p \exp(-t^2/2\sigma_t^2)$, where the peak current $I_p = Q/(\sqrt{2\pi}\sigma_t)$, and Q is the bunch charge. A bunch charge $Q = 2$ nC with $\sigma_t = 6$ psec gives a peak current $I_p = 133$ A.

We can also calculate the current density issuing from the cathode. The laser rms spot size at 133 A was 0.25 mm^2. Assuming the laser beam on the cathode has a Gaussian radial profile, the current density would have a profile given by $J(r) = J_{\max} \exp(-r^2/2\sigma_r^2)$, where the peak current density $J_{\max} = I_p/(2\pi\sigma_r^2)$. From this we infer a peak current density of 10 kA/cm^2, equal to the space-charge limit for an electric field of 100 MV/m, calculated in Sec. 4.4.1. This represents more than a factor of ten improvement in the current density previously achieved in electron sources.

The normalized emittance at this current was measured to be $\epsilon_N = 4.0$ mm-mrad. From this we find a peak normalized brightness of

$$B_N = \frac{I_p}{8\pi^2 {\epsilon_N}^2} = 1\times10^{11}\ \frac{\mathrm{A}}{\mathrm{m}^2}.$$

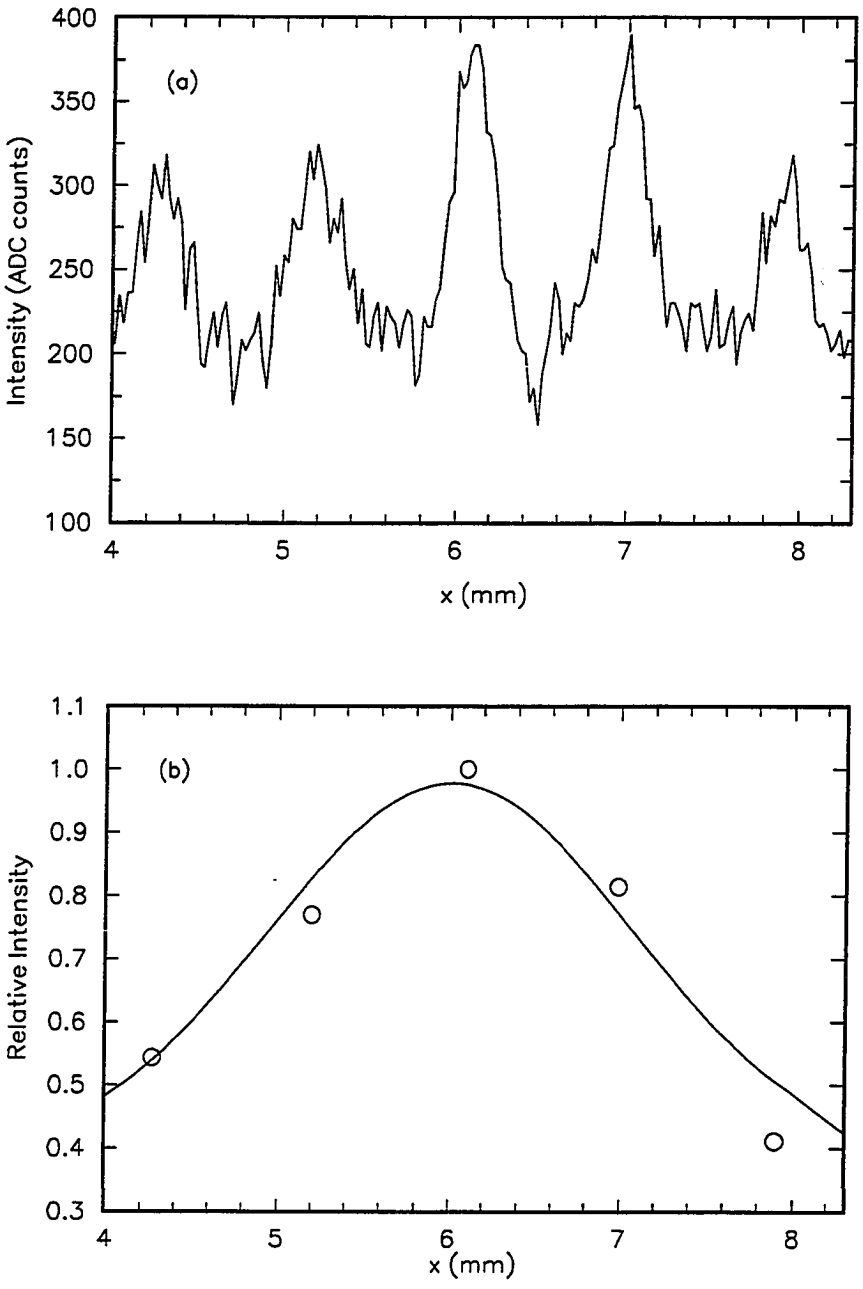

Figure 9.10: A transverse-emittance analysis using the pepper pot. Part (a) shows the beam profile along the x axis from which the angular divergence is determined. Part (b) shows the whole-beam profile. Results are given in the text.

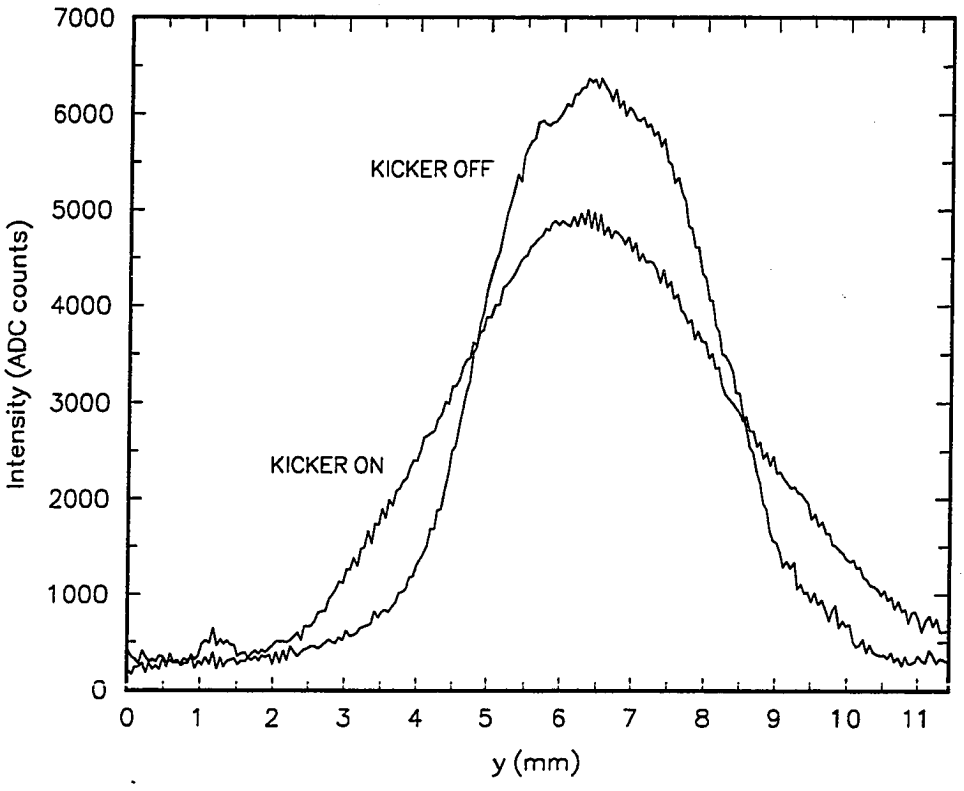

Figure 9.11: Sample pulse-length measurement using the rf kicker. The kicker-off vertical profile has rms width 1.35 mm, the kicker-on profile 1.75 mm. From the measured kicker deflection constant we measure the rms pulse length to be 6.1 psec.

This brightness is about the same as that achieved by the Los Alamos group that developed the photocathode rf gun and more than twice the design value of the ATF gun.

This value represents the brightness of the electron beam after it has passed through a portion of the low-energy beamline and may not be identical to the gun brightness, which cannot be measured directly. Three effects could conspire to lower the brightness between the gun exit and the diagnostics: charge could be lost, the pulse could be lengthened, and the emittance could grow. On the other hand, the measured emittance could be smaller than that at the gun exit due to beamline-acceptance limits (see Sec. 8.4), which would make the brightness measured in the beamline higher than at the gun exit.

Nevertheless, the brightness measured in the beamline represents what can be delivered to experiments (assuming no subsequent brightness loss). This was a primary design specification of the Accelerator Test Facility and has been exceeded by a factor of two. The ATF has the highest-brightness electron beam available for user experimentation in

the world.

9.6 Enhanced Emission

As improvements in the Nd:YAG-laser optics permitted more intense irradiation of the photocathode, a previously unobserved rf-gun excitation mechanism was discovered. Above a threshold laser intensity the charge issuing from the gun increased by two or three orders of magnitude and took the form of a series of short micropulses in a macropulse lasting up to 50 nsec. This is inconsistent with the nominal photoemission process.

We devoted several weeks to studying this mode as it represented both a limit to the current density achievable in the normal photoelectron pulse as well as an interesting high-charge mode of gun operation that we had not anticipated. Some of the basic properties of this "enhanced emission" that can be directly inferred from on-line diagnostics are presented here. A detailed study of the emission characteristics as a function of gun-excitation parameters and an off-line modelling study are presented elsewhere [75].

Previous to the discovery the laser had had an rms radius of greater than 1 mm and a pulse energy of around 100 μJ. The optical improvements resulted in spot sizes as small as 0.14×0.35 mm^2 and pulse energies of as high as 350 μJ. The estimated energy densities at which enhanced emission occurred were in the range of 12 to 54 mJ/cm^2, corresponding to intensities of 1.2 to 5.4 GW/cm^2.

As much as 30 nC of charge was measured on the momentum slit/Faraday cup. The momentum spread, however, was so large that the entire beam could not be focused on the slit simultaneously, even in momentum-spectrometer tune, in which the horizontal size of the beam is dominated by the momentum spread. This is illustrated in Fig. 9.12, which is a sample video profile of the enhanced current on the closed slit.

To measure the momentum spectrum the slit was opened to allow a momentum bite of 1% to pass through and downstream to a beam-profile monitor, where it was focused simultaneously in x and y. The total intensity of the digitized spot image was recorded at several settings of dipole D1 corresponding to different central momenta. (The linearity of the phosphor with electron intensity allows the profile monitor to serve as a relative beam-intensity meter).

The results are presented in Fig. 9.13 for a peak accelerating field of 62 MV/m corresponding to a peak momentum of 3.0 MeV/c. This procedure is somewhat crude as the beamline must be retuned at each momentum to produce the required focuses on the slit and profile monitor. Beam transmission to the monitor is not 100% and may vary with momentum to some extent. Nevertheless it is obvious that the enhanced emission occurs over a much greater range in momentum than the nominal photocurrent.

To study the enhanced emission in more detail, the unprocessed output of one electrode of a stripline monitor (located between quad Q3 and the rf kicker, as shown on Fig. 2.4) was recorded on a fast sampling oscilloscope[1] (200 gigasamples/second, 4.5-GHz bandwidth) capable of resolving individual rf cycles. This allowed the longer time

[1]SCD5000 Transient Digitizer, Tektronix, Inc., Beaverton, OR

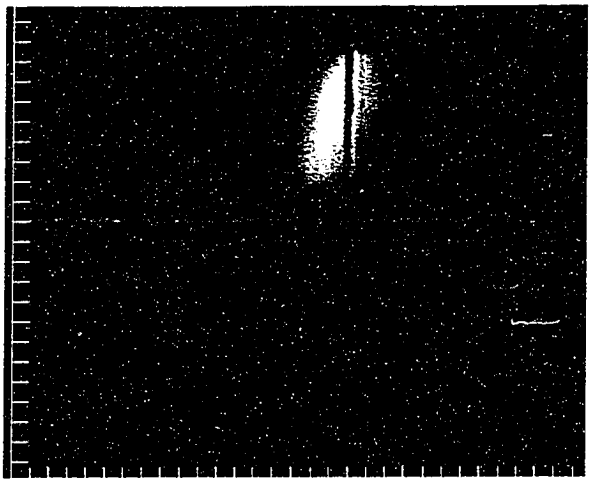

Figure 9.12: A video profile of the enhanced-emission beam on the momentum slit, with the beam tuned for momentum spectrometry. The dark vertical line is the closed momentum slit, and the circular halo is phosphor light reflecting off the inside of the beampipe. The axes are calibrated in millimeter tick marks.

evolution of the pulse to be traced. The stripline monitor located upstream of the first dipole allowed greater charge collection prior to momentum dispersion.

Like dark current, enhanced emission occurred over many rf cycles. Sample scope traces taken at two different times along the pulse evolution are shown in Fig. 9.14. The response of a stripline electrode to the passage of a short electron pulse is bipolar: the initial negative-going pulse has a bandwidth-limited risetime of 70 psec followed by a positive-going reflected pulse 540 psec ($1\frac{1}{2}$ rf cycles) later.

A fast photodiode monitoring the YAG laser provided the scope trigger. This is the first negative-going pulse at the beginning of the trace. First came the prompt photoemission, occurring during a single rf cycle, followed after a few rf cycles by the onset of enhanced emission. The current increased to a maximum after 15-25 nanoseconds and began a gradual decline to zero of about the same duration. The total charge is estimated by comparing the height of the nominal photoelectron pulse, which contained around 2 nC, with the height and number of the subsequent micropulses. An estimated maximum of 200 nC were measured on the stripline. Due to the large momentum spread of the beam, the collection efficiency was undoubtedly less than 100%.

An upper limit to the charge may be obtained by considering the stored energy of the gun cavity, which is around 2.6 J at a peak accelerating field of 75 MV/m, at which the above the charge estimate was made. This energy would be completely used in accelerating 500 nC of charge to a peak momentum of 4 MeV/c. In reality as the gun

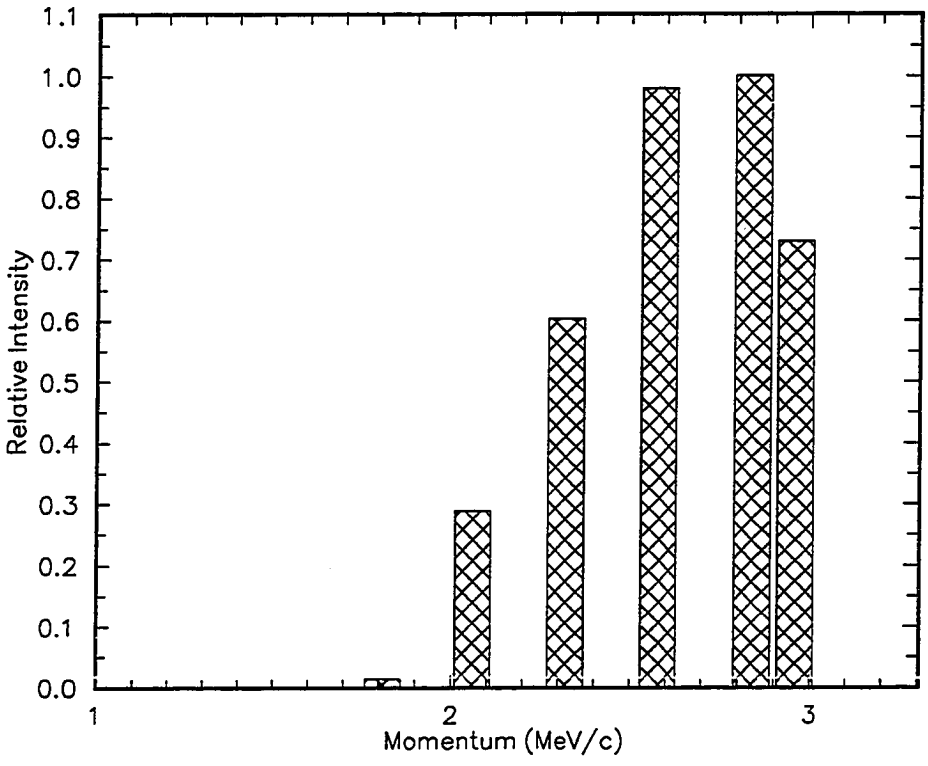

Figure 9.13: Momentum spectrum of the enhanced-emission beam, measured by using a beam-profile monitor in the 'Z'-line as a relative beam-intensity meter. The gun was operated at 62 MV/m, yielding a peak momentum of 3.0 MeV/c.

power is drained the accelerating field decreases, as does the peak momentum.

The effect of enhanced emission on the gun power is shown in Fig. 9.15. This is an oscilloscope trace of the rf power going into the gun (top trace) and the power reflected by the gun (bottom). The sudden energy drain caused by the large amount of charge being accelerated results in a mismatch between the gun and rf wave guide. The change in the gun's impedance is apparent. Apparently the cavity never recovers sufficiently to allow a good impedance match, and the gun power is perturbed for the remainder of the rf pulse.

The normalized transverse emittance of a 1% momentum bite of the enhanced beam was similar to that of the nominal photocurrent, around 4 mm-mrad. A sample emittance plot is shown in Fig. 9.16. Notice that the data is more internally consistent than that of normal photoemission, even though each data point was collected in a single beam pulse. In this sense the enhanced emission resembles the dark current. Each is stable pulse-to-pulse due to the longer emission time and momentum spread, which is

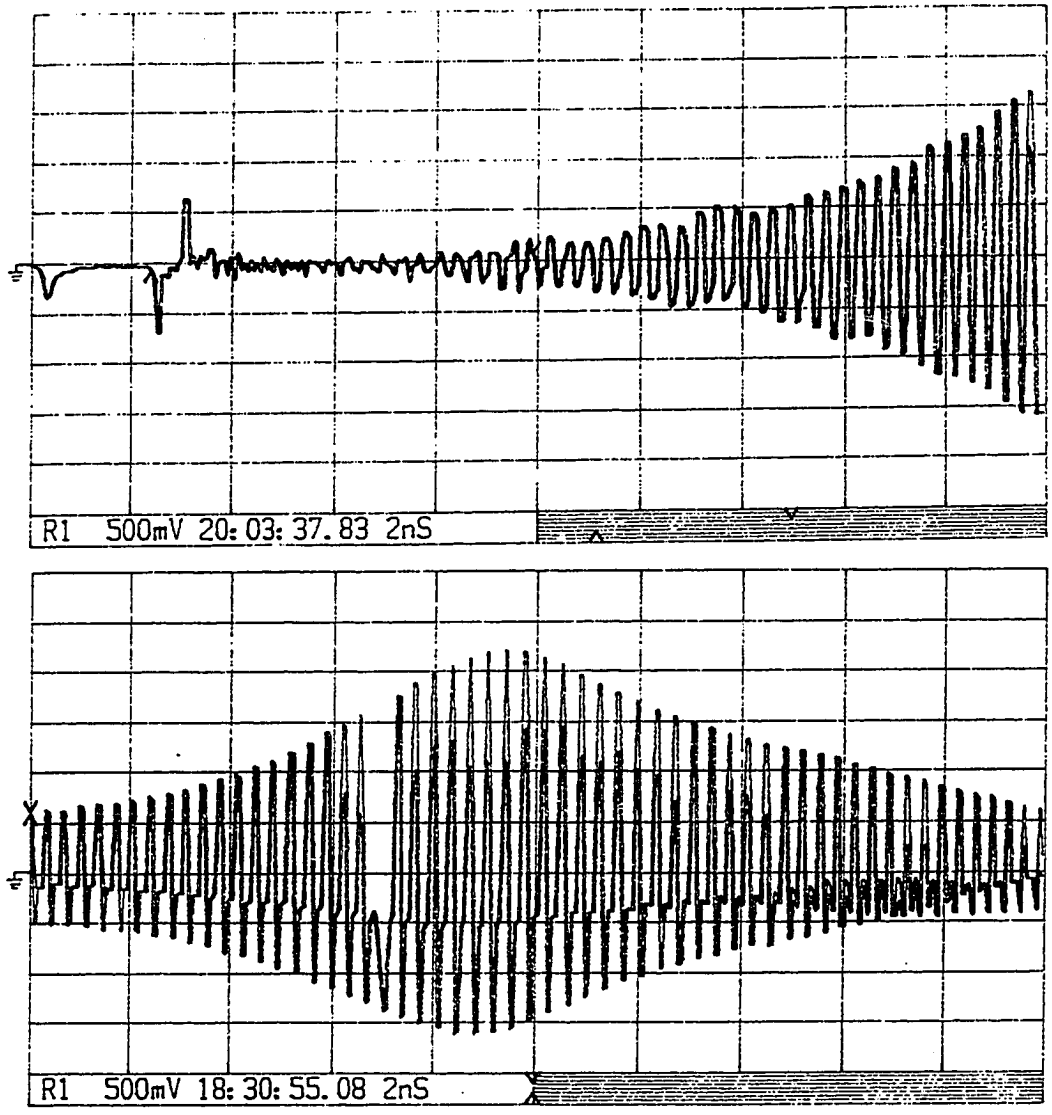

Figure 9.14: Fast oscilloscope traces of the enhanced emission signal on a stripline-monitor electrode. The top trace shows the onset of enhanced emission preceeded by the nominal photoemission pulse and a fast-photodiode trigger; the bottom trace shows a pulse of longer duration starting at a point in time approximately where the top trace ends. The scale is 2 nsec per horizontal division. The bipolar signal consists of an initial pulse with a risetime of 70 psec followed by the reflected pulse 540 psec ($1\frac{1}{2}$ rf cycles) later.

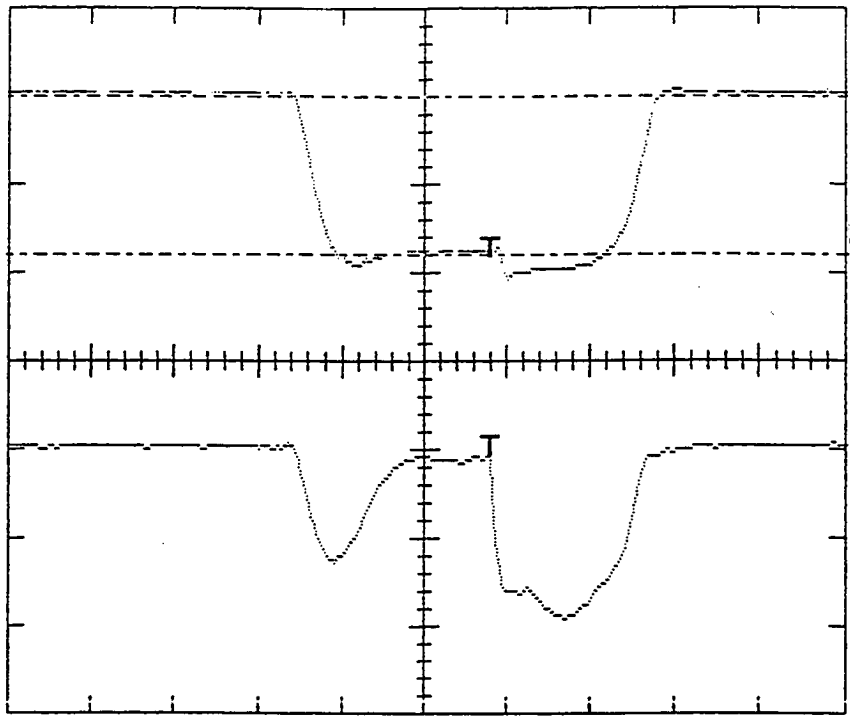

Figure 9.15: Oscilloscope traces of the rf-gun forward (top) and reflected (bottom) power during an enhanced-emission event. The 'T' marks the time at which the YAG laser is pulsed. The time scale is 1 μsec per division.

not dependent on the exact nature of the laser pulse. It is perhaps suspicious that the enhanced-emission beam exhibits such similar phase-space characteristics as the photoemission beam. The possibility that the emittance is defined by the beamline acceptance is considered in Sec. 8.4.

This type of rf-gun emission has not been observed before. An understanding of it involves the details of the interaction of high-power, short-pulse lasers with metal surfaces and the rf dynamics of the resulting charge distribution. Much work is being done on short-pulse laser interactions with metal surfaces; although many question remain unanswered, a remarkably consistent picture is beginning to emerge in the literature.

In the context of the effect on bulk matter, laser-pulse time scales may be divided into two categories, typically referred to as short (few picosecond to few nanosecond) and ultrashort (sub-picosecond). This distinction is due to the fact that the electrons in a metal require a characteristic time of 2-3 psec to come to thermal equilibrium with the lattice [71]. Laser pulses shorter than this produce a nonequilibrium temperature distribution in the electrons, which then cool to the lattice temperature. In this regime the laser pulse is best characterized by the *energy* density, as the bulk metal equilibrates

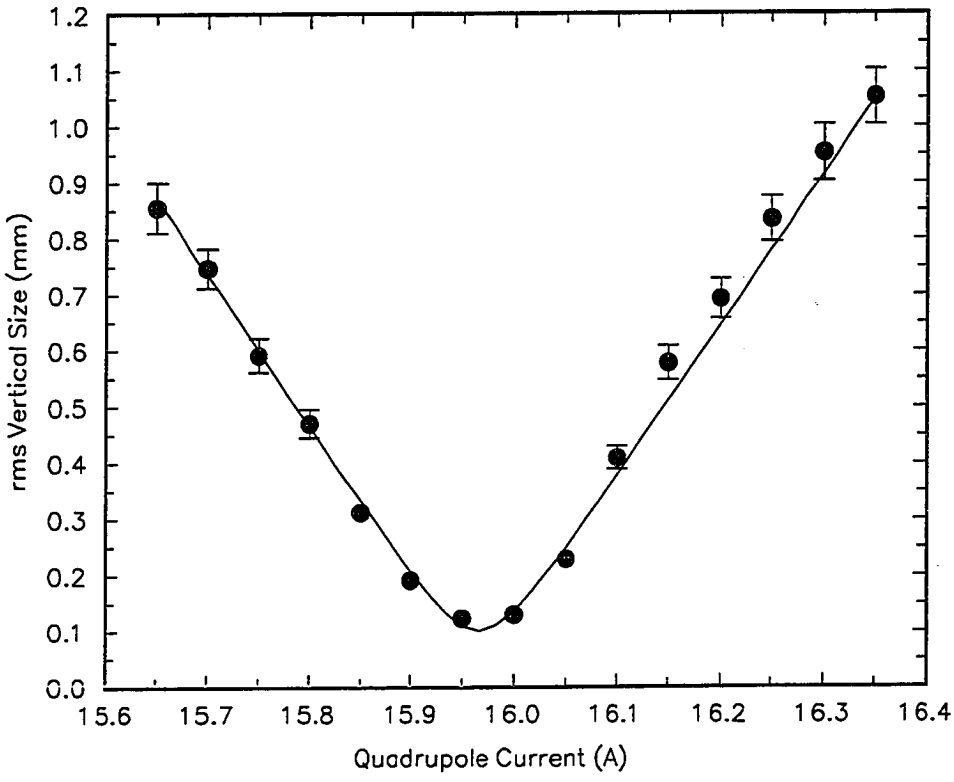

Figure 9.16: An emittance scan of the enhanced emission, showing the vertical rms spot size on profile monitor BPM1 as a function of the current in quadrupole ZQ1. The beam central momentum was 3.45 MeV/c. The normalized emittance is $\epsilon_N = 3.8$ mm-mrad.

with the energetic conduction electrons after the pulse and in a manner that is independent of the rate of energy deposition. Pulses longer than the thermalization time are best characterized by the *flux* density, or intensity. At 10 psec, we are on the boundary between these two regimes. Fortunately, they merge consistently at this time scale.

A clear scenario has emerged for the effect of high-intensity laser pulses on the nanosecond time scale [72]. Pulses of greater than 1 GW/cm^2 are sufficient to raise the temperature of some of the metal to the boiling point, which requires tens of picoseconds. This boiling results in the formation of a surface plasma. A precision study of 10-nsec pulses on copper showed that boiling sets in with a narrow threshold at 12 J/cm^2, corresponding to an intensity of 1.2 GW/cm^2 [73]. Microscopic examination of the surface following the laser pulse revealed the formation of craters and other structures due to the splattering of material upon boiling. These structures have the effect of reducing the various damage thresholds. This threshold is precisely the minimum laser intensity measured for the observation of enhanced current at the ATF.

A number of studies have been done on laser pulses of the intermediate time scale of 10 psec. A Brookhaven group found that the threshold for plasma formation was 10 mJ/cm^2, which also corresponds to an intensity of 1 GW/cm^2 [40]. This is consistent with the statement that for pulses of longer than 2-3 psec it is the intensity, not energy density, that is important. The threshold for optical damage was measured to be 100 mJ/cm^2.

Recent advances in the production of ultrashort laser pulses have allowed investigation of the interaction of laser light with metallic surfaces on the sub-picosecond time scale. One such study found that pulses of greater than 100 mJ/cm^2 caused the formation of a "solid-density" plasma, so named because the formation time is shorter than that needed for hydrodynamic expansion [74]. This threshold was independent of the laser-pulse length as long as it remained shorter than a picosecond. After formation the plasma undergoes rapid expansion. It appears that we are not in this regime.

It would seem, then, that enhanced emission is triggered by a laser pulse of sufficient intensity to form a surface plasma. The dynamics of this plasma with the rf extraction field result in a train of pulses each containing on the order of a nanocoulomb of charge. The details of the pulse time evolution are considered in another report [75]. The broad momentum distribution depicted in Fig. 9.13 is partially explained by the gradual depletion of the gun power, as well as by the fact that current is emitted over the entire accelerating portion of the rf cycle, as in the dark current. The difference in the enhanced emission is that the bulk of the charge is not liberated from the cathode by the laser; it is simply accelerated out of the plasma cloud formed by the laser.

After the enhanced-emission studies we returned to normal photoemission operation. The quantum efficiency was the same as before, around 6×10^{-5}. This confirms the robustness of metals as photocathodes. At the conclusion of the enhance-emission studies the cathode surface was examined under a microscope (see Fig. 9.17). This revealed a landscape that would make a planetary geologist giddy with delight. Structure of various shapes and sizes up to 0.1 mm had formed. Some of these could be the result of optical damage by the laser. Recall that intensities of up to 54 mJ/cm^2 had been recorded, and the threshold for clean, undamaged surfaces had been measured to be 100 mJ/cm^2. Other possible causes include rf breakdown and the back-bombardment. Clearly the possibility of substantial transverse fields on such a surface cannot be dismissed any easier than it could be precisely modelled (see Sec. 4.4).

Enhanced emission is obviously not good for cathodes that are intended for trouble-free use as normal photoemitters. As such it will probably not be of great interest to the ATF while the full electron-beam facility is being commissioned. Enhanced emission would perhaps be of interest as an FEL driver, where a regular series of microbunches, each with a nanocoulomb of charge, is desired. The advantage of this mode is that it makes considerably less demand of the driving laser than would be required to produce all of this charge via the normal photoemission mechanism. It may well prove worthy of further investigation.

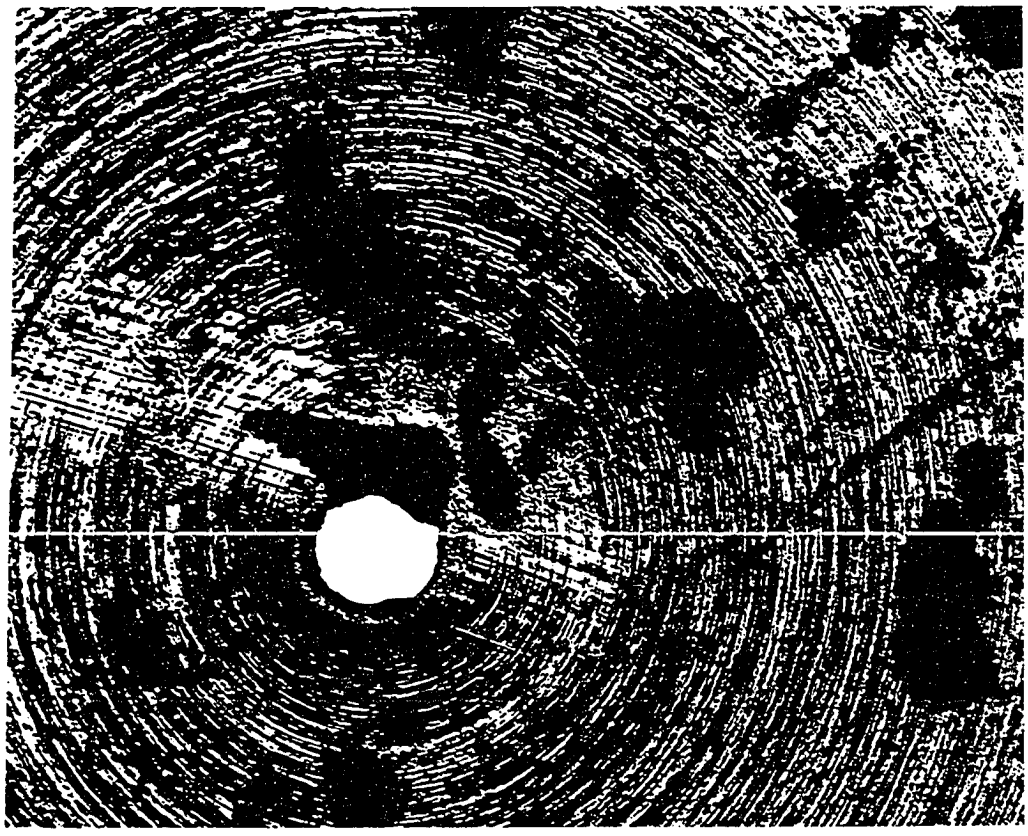

Figure 9.17: The copper photocathode after enhanced emission. The hole is 1 mm in diameter.

Chapter 10

Future Directions

In this chapter we outline some of the low-energy-beam studies that are a natural extension of those described in Chapters 8 and 9. We also describe a diagnostic we have constructed to study the interaction of the 50-MeV-electron and CO_2-laser beams, followed by a brief overview of the ATF experimental program.

10.1 Recommendations for Future Beamline Studies

The primary consideration driving the design of the ATF electron gun and beamline optics was the production of the highest possible brightness. The results of the commissioning studies presented in Chapters 8 and 9, together with the theoretical considerations given in Chapters 4 and 5, motivate several questions that could be addressed with the unique capabilities of the Accelerator Test Facility low-energy injection beamline.

What limits the brightness of the ATF beamline? Is it the rf gun or the transport optics? If it is the gun, is the exit emittance primarily determined by the cathode properties (including the transverse component of the rf electric field at the cathode), by space charge, or by rf dynamics?

A related question is: What is causing the apparent constancy of the transverse emittance (Sec. 9.3)? Is it the acceptance limits of the beamline, or is some other parameter that has not yet been varied significantly determining the emittance? Although most gun and beamline parameters measured during commissioning met or exceeded design specifications (the main exception being the Nd:YAG-laser pulse length, on which progress is being made), these questions are important for improving ATF performance and for future gun and beamline designs.

The improvements and new capabilities being introduced during the 1991-2 shutdown will provide the capability to perform some of the studies needed to address these questions. Following is a list of the beamline studies that have been previously inaccessible to us along with an assessment of what could be learned from them and is required to perform them.

- **Transverse emittance versus Nd:YAG-laser-pulse energy:** As the energy of the laser pulse determines the electron-beam charge, this study would allow the space-charge limit to be probed. If we are in the space-charge-limited regime, the emittance should be an increasing function of beam charge Q, with the scaling similar to that given by Eq. (5.1), which indicates that for small cathode emittance,

the final emittance scales as $Q^{1/2}$. Simulations of the gun using the program PARMELA indicate the scaling is closer to $Q^{0.9}$ [2]. The ability to vary consistently the laser energy is being installed during the 1991-2 shutdown.

- **Transverse emittance versus rf phase:** As predicted in Sec. 5.2, in the rf-dynamics-limited regime the gun-output emittance depends not only on the pulse length but also the rf phase at which the laser strikes the photocathode. The PARMELA simulations referenced above show that the dependence is quite sharp, with the emittance increasing by a factor of several within 10° of the minimum rf phase. Hence it should be a fairly simple matter to demonstrate this dependence if it plays a significant role in determining the emittance measured in the beamline. Although the ability to vary the rf phase of the laser pulse was in place during commissioning, such studies as this will require relatively long periods of running with good stability in the laser output and in the relative timing of the laser and rf systems. This combination of stability and long running periods has so far proven elusive. The upgrades to the laser and timing systems will hopefully change this situation for the better.

- **Transverse emittance versus rf power:** This study, while equally important as the previous two, will not yield as easily interpretable a result. We saw in Sections 5.1 and 5.2 that the choice of a peak accelerating field (and hence rf power) at which to operate the gun from the standpoint of minimizing emittance was a tradeoff between space-charge and rf-dynamics effects. Higher fields result in more rapid acceleration and hence smaller space-charge contribution, but increase the contribution of time-dependent rf forces. In addition, higher rf electric fields result in a larger transverse electric-field component at the cathode, which can also contribute to the emittance at the cathode. Clearly there is an optimum electric field that results in the lowest output emittance. The rf power is easily and consistently variable. The only requirement is again stable photoelectron beam.

- **Transverse emittance versus laser-spot size:** If the gun emittance is limited primarily by the cathode properties, this study should provide a clear signature. According to Eq. (4.4), the emittance at the cathode depends linearly on the laser-spot size for fixed characteristic transverse energy. In particular, we saw in Sec. 4.4.4 that the kinetic energy contributed by the transverse component of the rf electric field due to surface roughness could be much larger than the excess kinetic energy imparted by the laser. If the cathode emittance is substantial compared to the emittance measured in the beamline, which includes the contributions to the emittance from space-charge, rf forces, and nonlinear beamline optics, it would be evident as an increase in the emittance with increasing laser-spot size. This statement must be qualified by the fact that spot size also affects the space-charge and rf contributions to the gun-exit emittance. The new Nd:YAG-laser optics include the ability to vary the spot size at the photocathode.

The failure of the emittance to exhibit dependence on any gun-excitation parameter (as was hinted in the commissioning data presented in Sec. 9.3) would signify that the

beamline itself is the dominating factor. One possibility is that the emittance issuing from the gun is smaller but is being increased by nonlinear beamline optics. This seems less likely due to the fact that the measured emittance is already lower than simulations suggest would exist at the gun exit.

The other possibility is that the beamline is saturated, *i.e.*, that the input emittance is larger than the beamline acceptance and so is clipped to a constant value. This is more consistent with observations. To test this possibility it would be useful to have a second charge-collection device downstream of the profile monitors used to study the emittance. Charge loss between the momentum slit and the second Faraday cup would provide evidence of beamline-acceptance limitations. (Properly calibrated stripline monitors could provide the same information.) While if either proved to be true we would like to improve the situation, it is not critical as the measured emittance, beam charge, and brightness are already at the design values or better.

- **Longitudinal variation of the transverse phase ellipse:** As mentioned in Sec. 5.2 there is some interest in knowing the transverse phase ellipse as a function of longitudinal position within the electron-beam pulse. Such information is desired to assess the potential for reducing the emittance by application of a time-dependent phase-space rotation, such as could be supplied by a radio-frequency quadrupole. Such a measurement could in principle be carried out in two ways.

  In one the rf kicker is used to map the time structure onto the vertical axis. The horizontal phase-space ellipse (a byproduct of the emittance analysis) would then be measured after the second dipole as a function of vertical position on the profile monitor. (It must be after the second dipole so that the horizontal momentum dispersion introduced by the first dipole is cancelled.) This techniques is only valid in so far as there is no longitudinal mixing within the beam. Unfortunately the kicker also introduces additional longitudinal momentum smearing (see Sec. 6.4), which could result in sufficient path-length differences through the dipoles to cause significant mixing. This is the very basis for magnetic pulse compression.

  The other method exploits the correlation between electron gun-exit momentum and longitudinal position, caused by the varying accelerating field experienced by electrons as a function of rf phase. The first dipole disperses electrons of different momenta to different horizontal positions. The vertical phase ellipse as a function of horizontal position is thus akin to the sought-after time-resolved measurement to the extent that the momentum and longitudinal position are indeed correlated. This is not completely true even at the gun exit and could become less so in the beamline.

  This differential phase-ellipse rotation is most noticeable when the beam is at a waist, at which point the (central) ellipse is upright (see Chapter 3). Fortunately this is where emittance measurements are usually made. The difficulty is that the effect might well be smaller than the resolution of the beam-profile-monitor system for beam-matrix elements. This measurement in particular will require extreme stability from the electron beam in order to discern this possibly subtle effect.

- **Pulse compression:** A function for which the low-energy injection line was designed is magnetic compression of the electron pulse (see Sec. 2.4.1). To determine the pulse-compression factor requires measurements of the pulse length before dipole D1 and after dipole D2. The pulse length before D1 has been measured with the rf deflection cavity.

  Preliminary measurements of the electron pulse length after the second dipole were performed using the same streak camera used to study the uv laser pulse (see Sec. 8.6). Čerenkov light induced by the passage of the beam through a quartz crystal was collected by a mirror and lens assembly and transported to the streak camera. The relatively small amount of beam time allotted to these studies proved inadequate to optimize light-collection efficiency and temporal resolution sufficiently to obtain conclusive data. The proper electron-beam optics were achieved, however, and these initial studies could be continued at a future date.

  Another technique is available and will be tried after the linac has been commissioned. The electron pulse length can be determined by varying the rf phase in the linac and measuring the momentum spread out of the linac as a function of phase.

- **Longitudinal emittance:** An additional diagnostic capability for which the 'Z'-line was designed but which could not be implemented during commissioning is the longitudinal emittance measurement, described in Sec. 6.5. The vertical collimator required to simultaneously resolve the momentum spread and pulse length is slated for installation during a future maintenance shutdown. Such a measurement with the picosecond temporal resolution possible at the ATF would represent a rather unique capability among accelerator facilities. Los Alamos has achieved a longitudinal phase-space diagnostic with a temporal resolution of around 20 psec as part of its free-electron-laser program [76].

- **Acceleration to 50 MeV:** The studies outlined above would be quite useful in extending our understanding of rf-gun and transport dynamics. On the other hand, the rf gun and beamline have already been demonstrated to produce an electron beam with the properties required for the approved ATF experiments. The need to achieve acceleration to 50 MeV and transport to the experimental hall so that the experimental program can begin will likely assume a higher priority than time-consuming low-energy-beam studies in the near future.

After the 1991-2 shutdown, running will recommence with an extensively upgraded front end including a new rf gun with a flat photocathode, precisely aligned electron optics, and improved Nd:YAG-laser performance and optics. The first task will be to establish photoelectron beam again and measure its basic properties. Immediately thereafter should begin the commissioning of the linac and high-energy beamlines. There is no reason to expect this phase to offer any fewer challenges than awaited us in making the front end operational, but there is every reason to believe that the experience we gained will prove valuable.

10.2 The X-Ray Timing Diagnostic

Once the 50-MeV electron beam and CO_2 laser are available, it remains to bring them into collision in the experimental hall. There the electron beam will be focused to a spot size on the order of microns, while the CO_2 laser will be focused to a spot size of tens of microns. Each pulse will occupy a few picoseconds in time, corresponding to two or three millimeters longitudinally. Achieving this synchronized interaction consistently will be a nontrivial task. The path lengths and directions of the two beams will have to be quite stable against variations caused by temperature change, air movement, and mechanical vibration.

A diagnostic that gives a clear signal proportional to the degree of overlap and intensity of the two beams is needed. The experiments themselves obviously provide an indicator, but it would be preferable to have a signature that is independent of the physical processes being probed by the experiment, as these are often more subtle than simple scattering of the laser photons by the electron beam. We have designed and constructed the apparatus to provide the necessary signal based on x-ray backscattering.

The simplest interaction between a photon and an electron is Compton scattering. In the center-of-mass (CM) frame this is just the elastic scattering of a photon and an electron. The photon is scattered at angle θ^* with respect to the initial direction of the electron and has the same energy before and after scattering. In the lab frame, where the electron has beam energy γmc^2 and the photon has initial energy $\hbar\omega$, the scattered photon energy $\hbar\omega'$ is dependent on the lab scattering angle θ with respect to the initial electron direction:

$$\hbar\omega' = \frac{4\gamma^2\hbar\omega}{1 + 2\gamma^2(1-\cos\theta) + \frac{2\gamma\hbar\omega}{mc^2}(1+\cos\theta)}$$

for $\gamma \gg 1$.

The ratio $(2\gamma\hbar\omega/mc^2)$ is that of the photon energy in the CM frame to the electron rest-mass energy. The limiting case in which this ratio is much smaller than one is called Thomson scattering. In this case the CM frame and the rest frame of the electron are considered identical. With an electron-beam energy of $\gamma mc^2 = 50$ MeV and lab photon energy of $\hbar\omega = 0.12$ eV, the CM-frame photon energy is $2\gamma\hbar\omega = 24$ eV, so the scattering process is rather well approximated by Thomson scattering.

The Thomson-scattering differential cross section is the well-known formula

$$\frac{d\sigma}{d\Omega} = \frac{r_0^2}{2}(1+\cos^2\theta^*), \tag{10.1}$$

where $r_0 = e^2/mc^2 = 2.8\times10^{-15}$ m is the classical electron radius. As the differential cross section is symmetric around $\theta^* = 90°$, half of the scattered radiation in the CM frame is contained in the hemisphere centered on the initial electron direction. In the lab frame this hemisphere is compressed into a cone of opening angle $1/\gamma$ around the electron beam.

The total Thomson cross section, obtained by integrating the above equation over all solid angle Ω, is

$$\sigma = \frac{8\pi}{3}r_0^2 = 6.6\times10^{-29}\,\mathrm{m}^2.$$

We combine this cross section with the laser intensity to obtain an estimate of the total scattering rate.

At the focus of a diffraction-limited Gaussian laser beam the intensity is related to the power by $I \simeq \pi P/(2(f/d)^2\lambda^2)$, where f/d is the ratio of the focal length to the lens aperture, and λ is the wavelength of the laser [77]. A CO_2-laser beam with peak power 10 GW focused by a lens with $f/d = 2$ would have a peak intensity of around 4×10^{19} W/m^2 or 2×10^{39} photons $\cdot$ m^{-2} $\cdot$ sec^{-1}. This would produce a total Thomson-scattering rate of around 10^{11} per electron per second, so that in the picosecond around peak intensity there would be 0.1 scatters per electron.

The lab-frame scattered photon energies extends from the endpoint of $4\gamma^2\hbar\omega = 4.7$ keV at $\theta = 0$ down to zero (or to be rigorous, $\hbar\omega = 0.12$ eV) at $\theta = 180°$. The "Compton backscattering" of initially low-energy photons in this fashion is a useful source of collimated x-rays [78].

This x-ray beam is easily detected if the electron beam is deflected out of the way. Our diagnostic provides the means to produce the head-on collision of the electron and CO_2-laser beams and to detect the resulting x-rays. The number of scattered x-rays has the desired properties of being proportional to the strength of the electron and laser beams and on the degree of overlap between the two. This diagnostic could be placed in one of the experimental beamlines. Specifically, we plan to place it immediately downstream of the laser-linac experiment (Fig. 2.6).

A schematic diagram of the apparatus is shown is Fig. 10.1. The electron beam enters a vacuum chamber in which it collides head-on with the focused CO_2-laser beam. The laser enters the chamber through a 2.5″-diameter zinc-selenide vacuum window[1] and is simultaneously deflected 90° into the electron beam and focused by an off-axis paraboloidal mirror[2] with 2″ diameter and $f/d = 2$. It is then deflected back out of the chamber by an identical mirror and window and into a energy meter for on-line monitoring of the laser power. Transverse alignment is provided by dipole magnets in the electron beam and by translation stages in the laser optics. Longitudinal alignment is accomplished by varying the focal length of the quadrupole lenses in the electron beamline, not shown in Fig. 10.1. A variable optical delay line in the CO_2-laser path provides the synchronization adjustment.

The mirrors each have a 2-mm-diameter hole to allow the electron beam to pass through them. A beam with a normalized emittance of 1 mm-mrad has a geometric emittance of 0.01 mm-mrad. The final-focus electron optics permit such a beam to be focused into a spot with an rms size of around 5 μm. The rms angular divergence is 2 mrad. The mirrors are located 100 mm on either side of the focus, at which point the electron beam has an rms size of 200 μm, and so should pass cleanly through the holes once alignment has been achieved.

The x-rays that are backscattered to within 10 mrad of the electron-beam axis pass through the mirror hole and into an intrinsic germanium (HPGe) x-ray detector.[3] As the characteristic opening angle of the backscattered angular distribution is $1/\gamma \simeq 10$ mrad, a sizeable fraction of the x-rays are detected. The electron beam is deflected out of the

[1]Part no. 243559/CSM, II-VI, Inc., Saxonburg, PA.

[2]Part no. A8037-202, custom modified by manufacturer, Janos Technology, Inc., Townshend, VT.

[3]NIGP2010 detector with on-board RG11-B/C preamplifier, Princeton Gamma-Tech, Princeton, NJ.

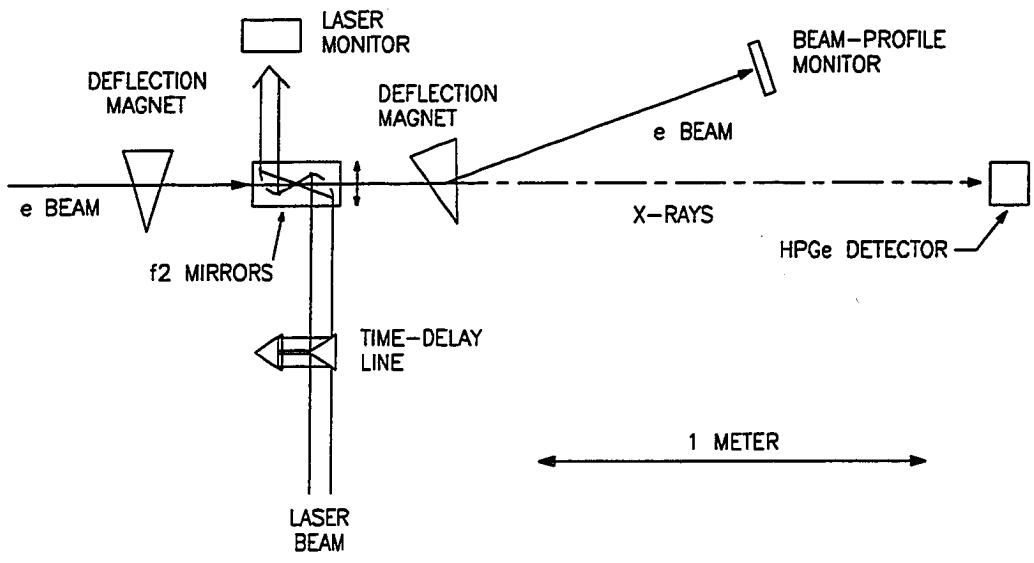

Figure 10.1: Schematic of the x-ray-backscattering diagnostic. The electron beam collides head-on with the focused CO_2-laser beam, yielding backscattered x-rays. The electron beam is deflected by a dipole magnet, allowing the x-rays to be analyzed in a high-purity germanium detector.

x-ray path and into a momentum-spectrometer beamline by a dipole magnet just after the scattering chamber. As the x-rays from the few-psec collision are not resolvable in time, the signal consists of a single pulse proportional to the total energy of the absorbed x-rays. This pulse is amplified[4] and recorded by a digital pulse-height analyzer[5] under PC control.

The Compton-scattering chamber is depicted in Fig. 10.2. The chamber is a 16″-diameter cylinder constructed from aluminum to minimize weight. A turbomolecular vacuum pump[6] will maintain the desired beamline vacuum of 10^{-6} torr. The CO_2-laser-mirror assembly is positioned by a computer-controllable stepper-motor-based x-y translation stage capable of 1-μm resolution.[7] The mirrors can be completely withdrawn from the beamline when not in use. Electrical multipin feedthroughs[8] pass the motor-control signals between the vacuum chamber and external environment. A sealable port provides access to the motors and laser optics from the top of the chamber without having to remove it from the beamline.

[4]Model 570 Spectroscopy Amplifier, EG&G ORTEC, Oak Ridge, TN.

[5]Spectrum ACE multichannel analyzer, EG&G ORTEC, Oak Ridge, TN.

[6]TSU 240 turbopump station, Balzers, Hopewell Junction, NY.

[7]ATS50-50 translation stage modified for vacuum compatibility under control of a UNIDEX 12 Motion Controller, Aerotech, Inc., Pittsburgh, PA.

[8]Catalog no. 809C10650-01-W, Ceramaseal, New Lebanon, NY.

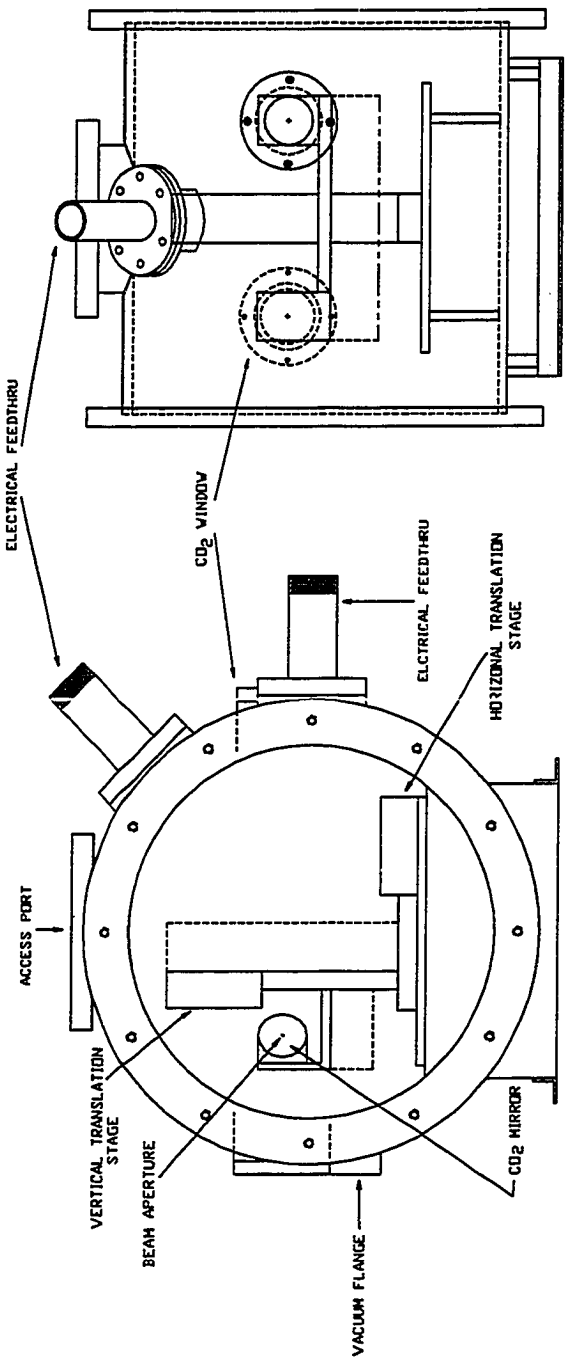

Figure 10.2: Design of the Compton interaction chamber. On the bottom is an end view looking along the electron-beam direction. On the top is a side view showing the two laser-window ports; the lower electrical feedthrough is not shown for clarity.

Five-keV x-rays have an attenuation length in air at atmospheric pressure of only 20 cm [79]. Hence the path length through air or any other material must be minimized. This is most easily done by extending the beampipe (held at 10^{-6} torr) to as close to the Ge detector as possible and terminating the pipe with a beryllium window of the minimum thickness necessary to hold one atmosphere. The Ge detector has a 0.5-mm-thick Be window that attenuates 30-50% of the x-rays (Be has an attenuation length for 5-keV x-rays of 1.3 mm [79]).

The Ge detector must be cooled to suppress thermal generation of electron-hole pairs, so it has a 5-liter liquid-nitrogen dewar that must be refilled every two or three days. It has a sensitive area of 2000 mm^2 and a FWHM energy resolution of 6% at 5.9 keV.[9]

Among the potential sources of background are synchrotron radiation from the electron beam traversing the dipoles and bremsstrahlung of the beam off of residual-gas molecules or collimating apertures. By far the most severe will be bremsstrahlung from apertures. It will be particularly important that the beam is "cleaned up" by the emittance selection apertures so that the beam passes through the mirror holes with no long tails in the transverse spatial distribution. All of the other candidates for such radiation are separated from the x-ray detector by at least one bend in the beamline. Lead shielding around the detector will undoubtedly be required.

The interaction chamber and x-ray detector, with the addition of a Bragg-scattering x-ray spectrometer, form the major components of the nonlinear Compton experiment described in Chapter 11.

10.3 Experimental Program

Once the high-energy beamlines have been commissioned and the synchronized interaction of the electron and CO_2-laser beams has been demonstrated the full experimental program of the ATF can commence. An experimental area for which the ATF is uniquely suited is laser-driven particle acceleration. Conventional rf-cavity techniques are approaching the technological upper limit to the achievable acceleration gradient. Gradients of around 20 MV/m are routinely achieved in linear accelerators such as the Stanford Linear Collider. It appears that rf breakdown will permit no more than a factor of ten improvement in this figure [39]. Beyond that higher center-of-mass energies in electron colliders will require the construction of longer machines. This trend is rapidly approaching the economical limit to growth. New approaches leading to higher gradients are needed.

One of the "novel accelerator" ideas being explored recently is that of replacing rf power with high-power lasers as the source of the accelerating electric field [80]. There are at least two advantages in going to shorter wavelengths (10 μm for the CO_2 laser versus 10 cm for S-band rf): the peak electric field that can be sustained without breakdown increases with increasing frequency, and it takes less energy to fill the accelerating

[9]This excellent resolution produced a surprising finding when the detector was tested. An americium-241 source was placed near the detector and the known x-ray lines used to calibrate the detector and check the resolution. The strongest line is at 59.5 keV. When the source was removed, the line at 59.5 keV persisted at a very weak level. The culprit was found to be the ^{241}Am source in the smoke detector some 8-10 feet distant!

structures, which have transverse sizes characterized by the wavelength of the accelerating field. Further, at 10 μm there is a well-established technology for producing high peak powers, the CO_2 laser. Because of the tighter tolerances imposed on accelerating structures by the much smaller wavelength, such techniques require very high-quality electron beams even for a proof-of-principle demonstration. Some of the experiments planned for the ATF [81] are briefly summarized below, with emphasis on the ATF beam parameters required for each. Another approved experiment, the nonlinear Compton-scattering experiment, is the subject of Chapter 11.

10.3.1 Laser Grating Accelerator

At the diffraction-limited focus of a 20-GW Gaussian CO_2-laser beam the electric field can reach over 10^5 MV/m, a factor of 1000 better than the best rf accelerating gradients. The dilemma imposed by Maxwell's equations is that a relativistic charged particle moving at constant velocity in vacuum far from any surfaces can receive no net acceleration from any arrangement of electromagnetic waves. All charged-particle-acceleration schemes involve circumventing one of the above constraints. In 1980 Robert Palmer proposed coupling the transverse electric field of a laser into an accelerating component through the use of grating-like structures [82].

The "laser linac" experiment is planned at the ATF to demonstrate laser-grating acceleration of electrons. The goal is to achieve an accelerating gradient of 1 GV/m over a region of 3 mm, leading to a net energy gain of 3 MeV, which will be measured in a momentum spectrometer after the interaction point. The required beam emittance can be deduced from a simple argument. The electron beam must be brought to a focus with a spot size of well under 10 μm and depth of focus of $\beta^* = \pm 1.5$ mm. This is to prevent electrons from striking and damaging the grating structure. Using a focused spot size of $w = 1$ μm we find (see Chapter 3)

$$\epsilon = \frac{w^2}{\beta^*} = 6\times10^{-4} \text{ mm-mrad}$$

or a normalized emittance of 0.06 mm-mrad. This will be achievable in the low-current mode of operation.

10.3.2 Smith-Purcell Radiation Experiment

The principle on which laser-grating accelerator is based is the 1953 discovery that an electron passing over a metallic grating emits visible radiation [83]. In this sense the laser linac could be called an "inverse Smith-Purcell accelerator." Hence the coupling of electrons to electromagnetic radiation via various surface structures can be studied without a light source. Such an experiment is presently underway using the low-energy electron beam.

10.3.3 Visible and UV FEL

In a free-electron laser (FEL) the reverse of acceleration occurs, namely the electrons emit coherent radiation via their interaction with a spatially periodic magnetic field, the

"wiggler" magnet. An FEL with wavelength tunable from 2000 to 500 nm is planned for the ATF with an electron-beam energy of up to 50 MeV. A planned upgrade raising the maximum electron-beam energy to 100 MeV would allow extension into the ultraviolet. This is the first planned experiment using the high-energy beam, as it does not require the CO_2 laser.

Certain constraints are placed on the electron beam by the requirement that the laser gain not suffer significant degradation due to the energy spread $\Delta p/p$ and finite emittance ϵ of the electron beam [84]. (For the definition of emittance, see Chapter 3.) These conditions are:

$$\frac{\Delta p}{p} \leq \frac{1}{4N},$$

where N is the number of the wiggler periods, and

$$\epsilon \leq \frac{\lambda}{2\pi},$$

where λ is the laser wavelength. For the ATF design $N = 70$, requiring an energy spread of less than 0.3%. At $\lambda = 500$ nm, the geometric emittance must be less than about $100\ \pi$ nm-rad $= 0.1$ mm-mrad, which at 50 MeV corresponds to a normalized emittance ϵ_N of 10 mm-mrad.

10.3.4 Inverse Čerenkov Accelerator

The passage of charged particles through a material with index of refraction n produces Čerenkov radiation when the particle velocity is greater than the speed of light in the material, c/n. The reverse of this process can be exploited to couple electromagnetic waves to a particle beam in such a way that the beam gains energy from the wave field. Inverse Čerenkov acceleration was first demonstrated by crossing an electron beam with a laser beam at the Čerenkov angle [85].

In the ATF experiment the electron beam will enter a hydrogen-gas cell at a pressure of 1.8 atmospheres. The CO_2 laser will interact with the electron beam in an axicon focusing scheme [86] that requires a radially polarized annular laser beam. The laser will be focused at the Čerenkov angle, 20 mrad. The goal is to obtain a maximum energy gain of 25 MeV over an interaction length of 25 cm, for a maximum accelerating field of 100 MV/m.

Chapter 11

The Nonlinear Compton-Scattering Experiment

The strong electromagnetic fields that will be present at the focus of the ATF CO_2 laser will provide access to a region of nonlinear quantum electrodynamics (QED). These scattering processes cannot be adequately characterized by the usual method of summing terms in a finite perturbative expansion represented by Feynman diagrams. Although the strong-field region of the laser focus has a volume on the order of only λ^3, where λ is the laser wavelength of 10 μm, the relativistic electron beam serves as a convenient probe, as the low emittance permits it to be focused well within this region.

The simplest manifestation of the interaction of electrons with strong fields is termed nonlinear Compton scattering in that the scattering rate is no longer linear in laser intensity. In this chapter we summarize the physics underlying the effect and describe an experiment that is being designed and built at Princeton to observe it.

11.1 Theory

As discussed in Sec. 10.2, the head-on collision of the CO_2-laser and electron beams results in Compton backscattered x-rays. The CO_2-laser photons have energy $\hbar\omega_0 = 0.12$ eV, and the electrons have energy $\gamma mc^2 = 50$ MeV. Photons that are scattered at angle θ with respect to the electron-beam axis have energy

$$\hbar\omega = \frac{4\gamma^2\hbar\omega_0}{1 + 2\gamma^2(1-\cos\theta) + \frac{2\gamma\hbar\omega_0}{mc^2}(1+\cos\theta)}. \tag{11.1}$$

The expression $(2\gamma\hbar\omega_0/mc^2)$ is the ratio of the photon energy in the center-of-mass frame to the electron rest-mass energy. It is sufficiently small in the present context (5×10^{-5}) that the last term in the denominator is negligible. This limit is sometimes referred to as Thomson scattering.

This energy spectrum extends from a maximum of $4\gamma^2\hbar\omega_0$ at $\theta = 0$ down to $\hbar\omega_0$ at $\theta = 180°$. Half of the scattered radiation is contained within a cone of angle $1/\gamma$ around the electron-beam axis ($\theta = 0$). The scattering process may be thought of as the dipole radiation of the electron oscillating in the electromagnetic field of the laser.

Consider an electron in a circularly polarized electromagnetic wave with electric field E and angular frequency ω_0. The motion of the electron is a circle [87] of radius r given by $\gamma m\omega_0^2 r = \gamma m\omega_0 v = eE$. This is just $F = ma$ with the centripetal force supplied by

the rotating electric field, and where we have used γm to allow for relativistic motion. From this we find

$$\gamma_\perp \beta_\perp = \frac{eE}{m\omega_0 c} \equiv \eta,$$

where $\gamma_\perp$ and $\beta_\perp$ refer to the electron motion transverse to the electromagnetic-wave propagation. We also note the relation $\gamma_\perp^2 = 1 + \eta^2$. Hence as the dimensionless parameter η approaches one, the electron motion induced by the wave fields becomes relativistic.[1] The radius of the circle is

$$r = \frac{eE}{\gamma m \omega_0^2} = \frac{\eta}{\sqrt{1+\eta^2}} \frac{\lambda}{2\pi} < \lambda.$$

As η approaches one there are two modifications to the normal Compton-scattering energy spectrum.

Since the radius of the electron motion is smaller than the wavelength of the electromagnetic field, the motion cannot be resolved by the wave, and the scattering process can be affected by this motion in only an average way. To the wave the electron appears to have a larger mass given by

$$\overline{m} = \gamma_\perp m = m\sqrt{1+\eta^2}.$$

We can then write

$$\gamma_{\text{eff}} = \frac{E}{\overline{m}} = \frac{E}{m\sqrt{1+\eta^2}} = \frac{\gamma}{\sqrt{1+\eta^2}}.$$

This has the effect of lowering the endpoint of the Compton-scattering energy spectrum in the lab frame to $4\gamma_{\text{eff}}^2 \hbar\omega_0 = 4\gamma^2 \hbar\omega_0/(1+\eta^2)$.

An electron moving in a circle radiates at all multipole orders, but the radiation due to the n^{th} order moment is smaller than dipole ($n = 1$) radiation by a factor of order $\beta_\perp^{2n-2}$ [88]. Hence as η nears one, higher order multipoles begin to contribute appreciably. The frequency of the n^{th} multipole radiation is at the n^{th} harmonic of the driving frequency. The usual Compton spectrum will be augmented by radiation beyond the nominal cutoff frequency $4\gamma^2\omega_0$. In the quantum-mechanical picture this corresponds to the absorption of n photons from the wave field followed by the reemission of one photon carrying away the total absorbed energy. This process is termed nonlinear Compton scattering.

It is useful to derive a numerical relation between the η of a wave field and the power and focusing properties of a laser beam.[2] The intensity as a function of electric field is $I = E^2/377$, where I is in W/cm^2 and E is in V/cm. At the focus of a diffraction-limited laser beam the intensity is related to the beam power P by $I \simeq \pi P/(2(f/d)^2\lambda^2)$, where f/d is the ratio of the focal length to the aperture of the focusing lens. We thus find

$$\eta^2 \simeq \frac{0.057 \cdot P[\text{GW}]}{(f/d)^2}.$$

[1] Our conclusions here are equally valid for a plane wave with other than circular polarization. We need only modify our definition of η to $eE_{\text{rms}}/m\omega c$ to account for the varying magnitude of the electromagnetic fields.

[2] It turns out that η is a relativistic invariant of the wave given by $(e/mc^2)\sqrt{-A_\mu A^\mu}$, where A_μ is the 4-vector potential of the field. This allows us to calculate η in the lab frame.

A 10-GW laser focused by an $f2$ lens produces a maximum η of 0.38. Such peak powers are now attainable in tabletop lasers such as the CO_2 laser at the ATF.

The exact cross section of nonlinear Compton scattering was worked out in the mid-1960's. The expression for a circularly polarized plane wave [89] is more compact than the case of linear polarization and is the situation we propose to study. The differential cross section of the n^{th} harmonic (absorption of n photons) is given by

$$\frac{d\sigma_n}{dy} = \frac{2\pi r_0^2}{x}\left\{-\frac{4}{\eta^2}J_n^2(z) + \left(2+\frac{u^2}{1+u}\right)\left[J_{n-1}^2(z)+J_{n+1}^2(z)-2J_n^2(z)\right]\right\}, \qquad (11.2)$$

where we have defined the dimensionless quantities

$$x \equiv \frac{4\gamma\hbar\omega_0}{mc^2}, \qquad y \equiv \frac{\hbar\omega}{\gamma mc^2} \le y_{\max} = \frac{nx}{1+\eta^2+nx},$$

$$u \simeq \frac{y}{1-y}, \qquad \text{and} \qquad z \equiv \eta\sqrt{1+\eta^2}\frac{2}{x}\sqrt{u\left(\frac{nx}{1+\eta^2}-u\right)}.$$

The total differential cross section is obtained by summing the contributions of all harmonics. This formula is quite general. In the limit of $\eta \ll 1$ it reduces to the Klein-Nishina formula for Compton scattering, which in the classical limit ($\gamma\hbar\omega_0 \ll mc^2$) in turn reduces to the Thomson cross section (Eq. (10.1) reformulated in terms of lab-frame photon energy). In the classical limit, but still allowing for large η, Eq. (11.2) reduces to a result first obtained by Schott in 1912 [90]. It is actually this limit we propose to explore, although we use Eq. (11.2) in all calculations to maintain generality.

The cross section for a circularly polarized plane wave of 10-μm wavelength and $\eta = 0.32$ in a head-on collision with a 50-MeV electron beam is shown in Fig. 11.1. Note the downward shift of the endpoint of the first-harmonic spectrum by 10%. The contribution of higher-order multipoles, corresponding to absorption of more than one photon, can be seen at energies higher than the cutoff for ordinary Compton scattering.

The experiment under construction at Princeton will observe both the mass-shift effect on the first-harmonic endpoint and the higher harmonics of the spectrum. The mass shift has not been experimentally observed to date. There has been only one previous experimental study of the higher harmonics [91]. The laser field had an η of 0.01, which permitted detection of a very weak second-harmonic component. Given sufficient laser intensity, the Princeton experiment should be able to detect a substantial second harmonic as well as the third and possibly fourth harmonics.

11.2 Overview of the Experiment

The experimental apparatus consists of the interaction chamber in which the electron and laser beams are brought into a head-on collision, an x-ray detector system, and an x-ray spectrometer. The interaction chamber and x-ray detector are those used in the x-ray timing diagnostic and were described in Sec. 10.2. The experiment would occur in the same location as the x-ray diagnostic, which will be located immediately downstream of the laser-linac experiment.

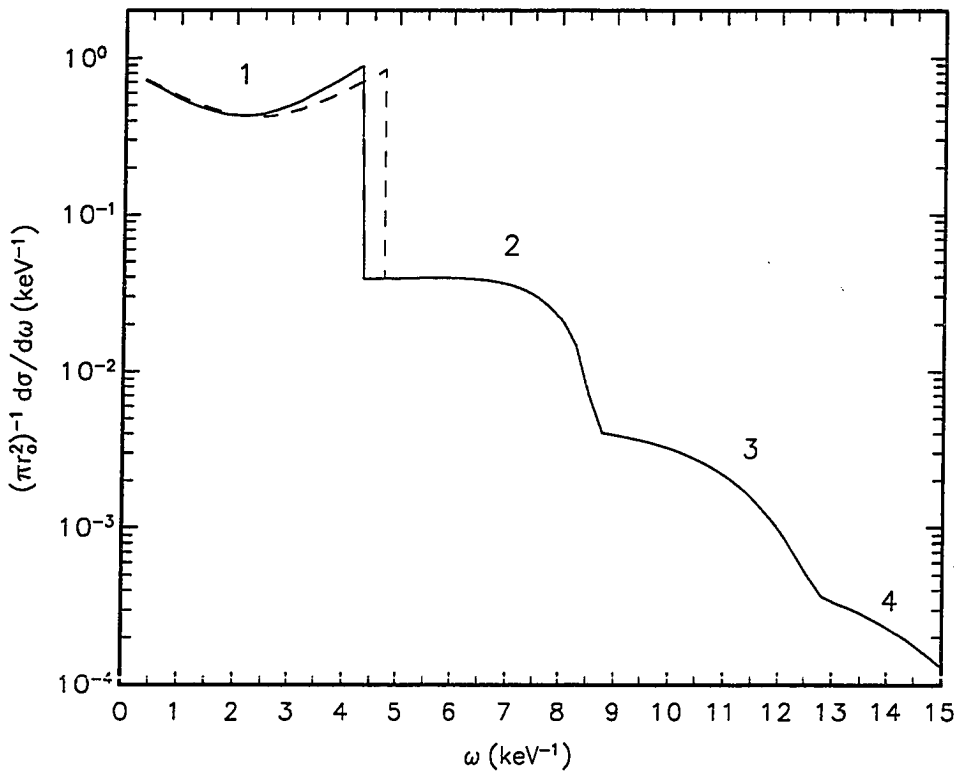

Figure 11.1: The differential cross section for nonlinear Compton scattering of a circularly polarized plane electromagnetic wave of 10-μm wavelength and $\eta = 0.32$ in a head-on collision with a 50-MeV electron beam as a function of the energy $\hbar\omega$ of the scattered photon. The contributions due to the absorption of 1 through 4 wave photons are labeled. The dashed curve is the ordinary Compton cross section.

The x-ray spectrometer is required to disperse x-rays of different energies to different locations for measurement of the differential cross section. This will be accomplished by placing a rotatable Bragg-scattering crystal in the path of the x-rays just downstream of the dipole magnet that deflects away the electron beam, and by placing the germanium detector on a rotatable stage allowing it to move along an arc centered on the Bragg-crystal axis. The modified experimental configuration is depicted in Fig. 11.2.

The backscattered x-rays will enter a vacuum chamber containing the Bragg crystal mounted on a rotary-motion feedthrough actuated by a stepper motor. When the crystal surface is oriented at the Bragg angle θ_B with respect to an incident x-ray of wavelength λ fulfilling the Bragg condition

$$\sin\theta_B = \frac{\lambda}{2d},$$

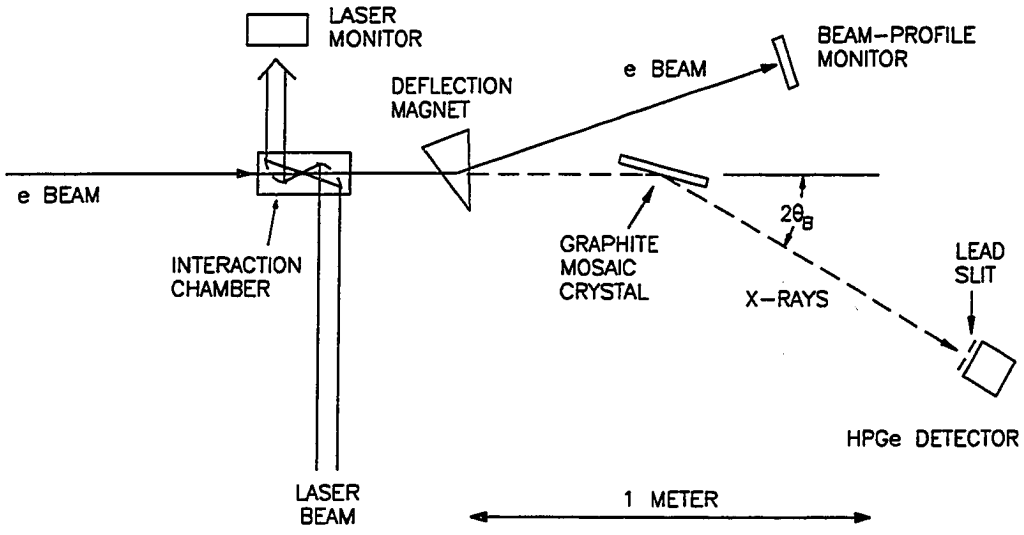

Figure 11.2: Layout of the nonlinear Compton experiment. Backscattered x-rays produced by the collision of the electron and CO_2-laser beams are analyzed in a Bragg-scattering x-ray spectrometer.

where d is the crystal-plane separation, the x-ray is scattered by angle $2\theta_B$, as shown in Fig. 11.2. The Ge-detector motion and crystal rotation will be linked by a 2:1 mechanism that assures that the detector is always at the correct position to intercept the Bragg-scattered x-rays. The x-ray energy to be analyzed is uniquely selected by the Bragg angle at which the spectrometer system is positioned.

The properties of the electron and CO_2-laser beams at the interaction region are summarized in Table 11.1. The electron beamline would be operated in a lower-current mode with approximately 10^7 electrons per pulse and a geometric emittance of around 1 mm-mrad. The final-focus optics then produce the properties listed in the table. The laser parameters are based on a diffraction-limited Gaussian beam focused by the $f2$ mirror in the interaction chamber.

The parameters β^* of the electron beam and the Rayleigh range z_R of the laser beam both express the same thing: the distances over which the beams increase in radius by a factor of two from the focus (see Sec. 3.4). The maximum η achieved at the laser focus is 0.32, smaller than the value of 0.38 calculated above for 10 GW because of the effects of finite-aperture transmission and reflective losses in the interaction chamber.

A longer laser pulse of 100 psec is assumed based on recent plans to abandon the isotopic mix in the CO_2 amplifier in favor of a simpler system based on ordinary CO_2 at a pressure of several atmospheres. The expectation is that the amplifier will be able to produce pulses no shorter than 100 psec but with enough energy in the pulse to yield the stated peak power. It is the power that determines the maximum η at the focus, and no ill effects are anticipated due to the laser pulse being significantly longer than

Table 11.1: Parameters of the nonlinear-Compton interaction region

Electron beam	
Pulse length (FWHM)	6 psec
r_{rms}	1 μm
θ_{rms}	1.5 mrad
β^*	0.67 mm
CO_2-laser-beam parameters	
Wavelength	10.4 μm
Pulse length (FWHM)	100 psec
Peak power	10 GW
r_{rms}	9 μm
θ_{rms}	180 mrad
z_R	50 μm
η_{max}	0.32

the electron pulse.[3] In fact this will simplify synchronization of the two pulses.

As the laser intensity is not constant in time and position, the electron beam will experience a continuum of η values from zero to the stated maximum. This will smear the mass-shift effect in the x-ray spectrum, resulting in the production of first-harmonic x-rays at energies up to the normal Compton endpoint. The above spatial and temporal variations in both beams are combined with the differential cross section for a plane wave of constant η to produce the photon scattering rate per electron shown in Fig. 11.3. The total scattering rate is 0.08 photons per electron. The mass-shift effect is still clearly visible. Only the first and second harmonic are shown. The spectrum at higher energies is similar to that of the plane-wave case shown in Fig. 11.1.

Also included in the scattering-rate calculation is the 2% FWHM spread in CO_2-laser photon energies as determined by the bandwidth of the amplifier. This introduces a simple smearing of the energy spectrum that is barely discernable on the scale of the figure (compare the unshifted Compton edges in Figs. 11.1 and 11.3). The energy spread of the electron beam will be reduced to well below 1% in the momentum-selection optics of the low-energy beamline.

The angular spreads of the electron and laser beams each introduce a different smearing effect. The 1.5-mrad spread of the electron beam will not affect the energy spectrum, but will introduce an angular spread of the same magnitude into the backscattered x-rays of a given energy. This is significantly less than the $\pm$10-mrad acceptance of the 2-mm hole in the $f2$ mirror located 100 mm from the interaction region. While this will not affect the collection of the x-rays by the Bragg crystal, it does influence the

[3] A possible exception is the greater chance of damaging CO_2-laser optical components due to the longer, higher-energy pulse.

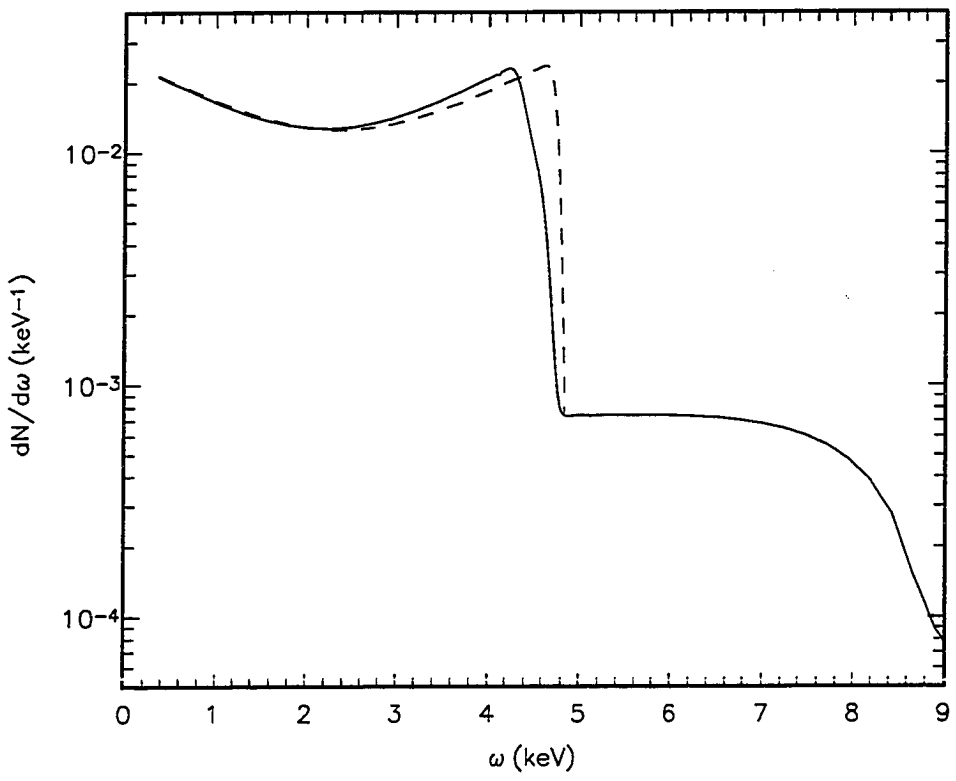

Figure 11.3: The scattering rate for a single 50-MeV electron beam in a head-on collision with a circularly polarized laser beam of 10-μm wavelength and a peak power of 10 GW focused by an $f2$ lens (maximum $\eta = 0.32$) as a function of the energy $\hbar\omega$ of the scattered photon. Only the first and second harmonics are shown; the spectrum at higher energies is similar to that in Fig. 11.1. The total scattering rate is 0.08 photons per electron. The dashed curve is the rate for ordinary Compton scattering.

scattering-angle acceptance, discussed below.

The angular spread of the laser photons due to focusing, on the other hand, alters the x-ray-energy spectrum rather than the angular spectrum. Consider a photon approaching the collision region at an angle θ to the nominal laser-beam axis. In the lab frame it has the 4-vector

$$(\omega_0,\ \omega_0 \sin\theta,\ 0,\ -\omega_0 \cos\theta),$$

where the $+z$ axis is taken along the electron-beam direction. In the center-of-mass (CM) frame this vector becomes

$$(\gamma\omega_0(1+\beta\cos\theta),\ \omega_0 \sin\theta,\ 0,\ -\gamma\omega_0(\beta+\cos\theta)).$$

In the CM frame the incident angle θ^* is given by $\tan\theta^* \simeq \sin\theta/\gamma(1+\cos\theta) \simeq \theta/2\gamma$ for

small θ. Hence the incident angle is close to zero and the CM-frame angular spectrum is nearly identical to that of a head-on collision ($\theta = 0$), as is the angular spectrum in the lab frame. The energy of the incident photon is shifted by a factor of $(1 + \cos\theta)/2$ from the head-on case, which for the 180 mrad characteristic of $f2$ focusing is less than 1%.

11.3 The X-Ray Spectrometer

As we are interested in detecting a 10% shift in the endpoint of the x-ray spectrum, energy bins of 1% would be quite suitable to analyze the effect. This is 10-100 times broader than the bandwidth of a typical x-ray monochromator using a perfect crystal. Our requirements are well matched by a pyrolitic graphite crystal, in which there is a spread (or mosaic) of 0.8°= 14 mrad in the orientations of individual microcrystals.[4] Such a crystal has the desirable properties of accepting a correspondingly larger angular spread (hence energy spread) while maintaining the same dispersive qualities of a single perfect crystal [92]. A monochromatic point source of x-rays a distance L from the crystal will be imaged in the scattering plane to a point an equal distance away.

This property is illustrated in Fig. 11.4. The mosaic spread of the microcrystals is denoted by Δ. An x-ray with energy $E = 2\pi\hbar/\lambda$ travelling along the central ray hits the crystal in the center and penetrates until a microcrystal oriented at the Bragg angle is encountered. The x-ray scatters by angle $2\theta_B$ with about 40% efficiency.

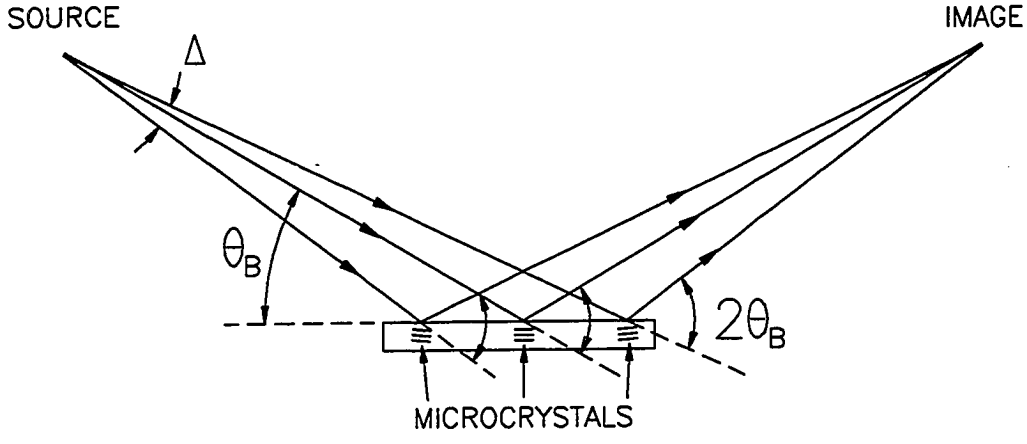

Figure 11.4: The scattering of monoenergetic x-rays by a graphite mosaic crystal. The mosaic spread Δ of microcrystal orientations results in a focusing geometry with angular acceptance Δ.

Now consider an x-ray making an angle $\Delta/2$ to the central ray. If the graphite were in the form of a single perfect crystal the x-ray would not strike the crystal planes at

[4]Available from the Advanced Ceramics Division of Union Carbide, Cleveland, OH.

the Bragg angle and would not be scattered. But in the polycrystalline graphite the x-ray finds a plane at the appropriate orientation to Bragg scatter. The scattered ray crosses the central ray at the image point, located at the same distance from the crystal center as the source. In other words the mosaic crystal duplicates the focusing effect of a bent perfect crystal. X-rays with a slightly different energy $E + \delta E$ have a different Bragg angle $\theta_B - \delta\theta_B$ and are imaged to a different point below the image point shown in Fig. 11.4.

In graphite the crystal-plane spacing d is 3.355 Å. We may then rewrite the Bragg condition in the more convenient form

$$\sin\theta_B = \frac{1.85}{E[\text{keV}]},$$

where $E = \hbar\omega$ is the x-ray energy. The dispersion of the crystal may be found by taking the derivative of the Bragg relation:

$$\cot\theta_B \delta\theta_B = \frac{\delta E}{E}.$$

To analyze the mass-shift effect we need 1% energy bins in the region of E = 4-5 keV, which corresponds to a Bragg angle of 400 mrad (23°) and an angular region of $\delta\theta_B$ = 4 mrad, well within the mosaic spread of $\Delta/2$ = 7 mrad. To analyze up to the third harmonic, which has a cutoff energy of around 13 keV, the Bragg angle decreases to 140 mrad with a 1% energy bin in $\delta\theta_B$ = 1.4 mrad.

Note also that the mosaic spread is larger than the angular spread of 1.5 mrad due to the electron-beam divergence. It is rather well matched to the limiting acceptance of 10 mrad imposed by the hole in the $f2$ mirror.

The distance from the interaction region to the crystal will be around L = 1 m, equal to the distance from the crystal to the x-ray detector. A lead slit of variable width placed in front of the detector will define the energy bin. A 1% bin at the first-harmonic endpoint corresponds to a slit opening of 4 mm.

In order to fully utilize the angular acceptance in the scattering plane of the mosaic spread the crystal must have length

$$l = \frac{L \cdot \Delta}{\sin\theta_B} = \frac{L \cdot \Delta \cdot E[\text{keV}]}{1.85}.$$

To analyze the third harmonic would involve a maximum photon energy of 13 keV, for which the crystal should have l = 10 cm. Pyrolitic graphite is available in up to 8-cm disks, so we could utilize the full mosaic-spread angular acceptance over most of the energy spectrum. The collection efficiency decreases for production angles between 7 and 10 mrad and will be determined experimentally from a calibration run with the laser intensity reduced sufficiently to yield the well-known Compton spectrum.

The 10-mrad acceptance limit set by the mirror hole restricts the energy region we can analyze. This is graphically illustrated in Fig. 11.5, which shows the x-ray production angle as a function of x-ray energy for the first three harmonics, assuming a head-on collision. Bands are shown corresponding to the continuous variation of η from 0 to 0.32,

which results in a range of x-ray energies being produced at a given angle. Most of the x-rays will in fact be produced near the $\eta = 0.32$ edge. We will only have access to the upper half of the energy spectrum of each harmonic. This will be sufficient to analyze the mass-shift effect and demonstrate the existence of the higher harmonics.

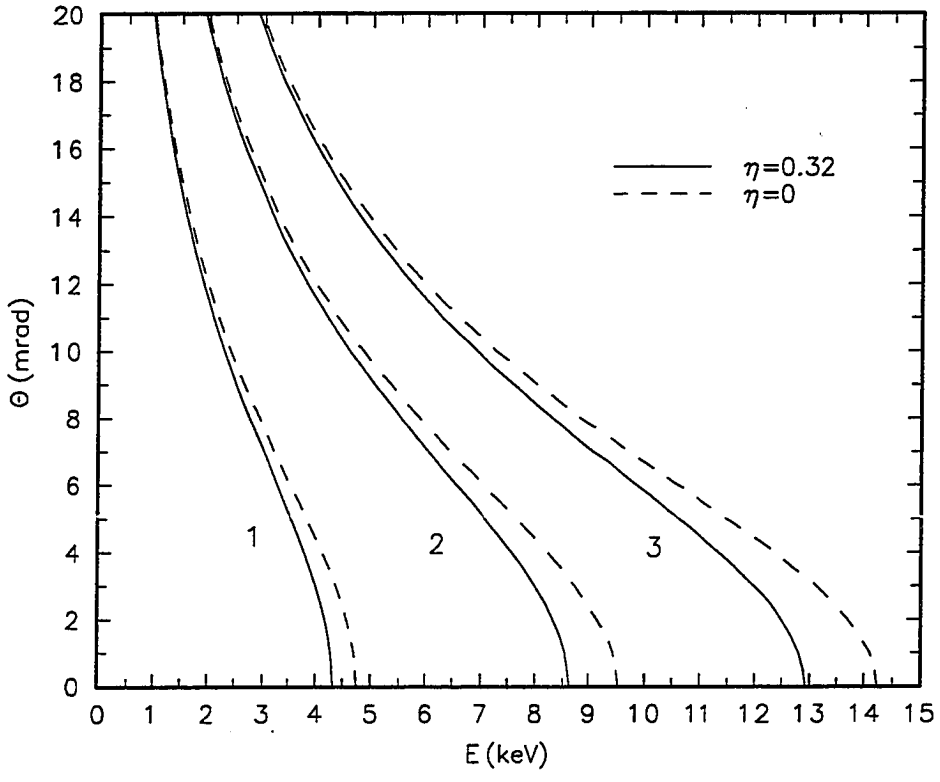

Figure 11.5: The relation between x-ray-production angle and energy for the first three harmonics.

The flat geometry of the crystal provides no focusing transverse to the scattering plane. With source and detector equidistant to the crystal, the transverse size of the image on the detector is twice that of the intercept of the x-rays at the crystal. We would like the angular acceptance in the transverse plane to match that of the scattering plane. Hence the transverse extent of the crystal should be at least $L \cdot \Delta = 14$ mm and the x-ray detector twice this size.

In addition, the mosaic spread Δ of the crystal introduces an azimuthal spread of 2Δ in the scattering angles from a given point. The x-rays then describe an arc of length $L \cdot 2\Delta \cdot \sin\theta_B$ on the face of the detector. To maintain good acceptance the detector should have a transverse size of $2L \cdot \Delta \cdot (1 + \sin\theta_B)$. With a maximum Bragg angle of 38° for 3-keV x-rays, the detector should be 45 mm wide. Since partial acceptance is maintained out to the limit of $\theta = \pm 10$ mrad, it would be optimal to have the crystal

$L \cdot 2\theta = 20$ mm wide and the detector $2L \cdot 2\theta \cdot (1 + \sin\theta_B) = 65$ mm. The Ge detector that will be used for the experiment has an active area 50 mm in diameter.

We have seen that the angular acceptance of the spectrometer will be 100% out to a production angle of 7 mrad and somewhat less out the maximum angle of 10 mrad. The crystal Bragg scatters with about 40% efficiency. So a pulse of 10^7 electrons will yield 7×10^5 x-rays, of which about 3000 would Bragg scatter out of a 1% energy bin of the first harmonic. Each higher harmonic yields about a factor of 30 fewer x-rays in the same size bin.

The x-rays are partially attenuated by any matter they must pass through to reach detector. There is a 0.5-mm-thick beryllium window in front of the Ge detector. Another vacuum window will be required to separate the vacuum of the beamline from the detector, which is in air. The larger this window is the thicker it must be to support one atmosphere. The optimal location is at the entrance to the Bragg-crystal chamber, before the x-rays are dispersed. There it would only need to be about 1″ in diameter (the same as the inner diameter of the beam pipe, which is well matched to our detector acceptance). A Be window would have to be 0.25 mm thick. A better choice might be Kapton, which is much stronger than Be and still has a fairly low x-ray attenuation coefficient since it is made from low-atomic-number hydrocarbons. A 1″-diameter Kapton window would only need to be about 25 μm thick [93], which is equivalent to only about 0.1 mm of Be. Kapton has the additional advantages of being radiation hard, inexpensive, and easier to mount into a window than Be. Be has an x-ray attenuation length of 0.65 mm at 4 keV and 9 mm at 10 keV, so the combined window thickness of 0.6-0.75 mm noticeably attenuates only the low-energy x-rays. Four-keV x-rays are attenuated by a factor of 30-40%.

If the window is placed at the scattering-chamber entrance, it would be a good idea to fill the chamber and spectrometer arm with helium gas at one atmosphere. This has several advantages. Helium gas at one atmosphere has an x-ray attenuation length of 28 m at 3 keV and hence has negligible effect. A He flow system (assuming a slow leak in the rotary seal of the spectrometer arm) would be cheaper to construct than a vacuum system that would maintain sub-torr pressures in the Bragg chamber and x-ray path. A 1″ air gap between the end of the He volume and the detector would introduce another attenuation factor of 78% at 4 keV.

The total efficiency for Bragg-scattered x-ray detection is thus about 25% at 4 keV and essentially 100% at 10 keV. It is fortunate that the attenuation is most severe at low energies, where the production rate is considerably higher. Each pulse of 10^7 electrons yields around 750 detected 4-keV x-rays in a 1% energy bin, 100 second-harmonic x-rays, and three third-harmonic x-rays.

As these x-rays will not be resolved in time, the signal for each beam pulse will be the total x-ray energy absorbed. The number of detected x-rays is determined by dividing the pulse energy by the spectrometer energy setting. It will be important to reduce the backgrounds discussed in Sec. 10.2 to less than one x-ray per pulse, particularly for detection of the third harmonic.

Data collection would consist of 30-50 spectrometer settings at each harmonic, corresponding to the 1% energy bins in the upper portion of each spectrum allowed by the finite angular acceptance. A scan at the first harmonic would proceed rapidly, requiring

only three beam pulses per bin to achieve 2% statistical accuracy. At a repetition rate of 1 Hertz this would require only a couple of minutes. The second harmonic would require 25 beam pulses per point, and the third harmonic 800 pulses, which would take about seven hours to acquire 30 energy settings at 1 Hz. The fourth harmonic could possibly be explored by raising the electron-beam intensity by an order of magnitude and confining the data to only a few energy bins, each of which would require around an hour of beam time.

To calibrate the spectrometer system a first-harmonic scan would be taken with the laser intensity reduced by a factor of ten. The reduced η of 0.1 lowers the mass-shift effect to the 1% level so that the spectrum is that of ordinary Compton scattering. This provides an energy calibration using the well-known endpoint as well as an x-ray spectrum that includes all acceptance and attenuation effects for comparison with the high η spectrum. With the intensity reduced by a factor of ten, the calibration run would take around half an hour of beam time. Calibration at higher x-ray energies could be accomplished either by increasing the beam energy (if the ATF maximum beam energy has been upgraded to 100 MeV), which raises the Compton endpoint as the square of the beam energy, or by placing a radioactive calibration source near the detector. Data collection would be temporally gated to minimize the contribution from constant backgrounds such as cosmic rays and ambient radioactivity.

The possibility exists that the CO_2 laser will not perform at the stated specifications. It may be limited to a repetition rate of a tenth of a Hertz, which would multiply the data-collection times stated above by ten. Such times would still be compatible with the beam time approved for this experiment by the ATF program committee.

As the laser peak intensity decreases, the experiment rapidly becomes less feasible. At 3 GW the mass shift effect has decreased to the 3% level, and there are around 250 detected first-harmonic x-rays per pulse and two second-harmonic x-rays. It is doubtful that a smaller mass shift could be detected due to the smearing of the endpoint discussed above. Detection of a signal with less than one x-ray per pulse is also a questionable endeavor owing to the backgrounds, which will likely mask such a weak signal.

Chapter 12

Conclusions

In closing, we review what has been accomplished during the commissioning of the Accelerator Test Facility low-energy-beamline and what we have learned from the experience. We also briefly discuss the present status of the ATF and the contribution of our efforts to other accelerator programs.

12.1 Overview of Accomplishments

Starting from computer simulations and an empty floor space four years ago we have constructed the world's highest-brightness electron-beam user facility. An electron-source technology developed within the past decade, the rf photocathode gun, has been successfully utilized in a multi-user beamline for the first time. This beamline was designed to provide experimental beam at 4.5 MeV and 50 MeV while maintaining the diagnostic capability to study the properties of the electron beam in detail (the design of the ATF is presented in Chapter 2).

We have commissioned the rf gun and 4.5-MeV injection beamline, during the course of which we have demonstrated the required operational characteristics, as discussed in Chapter 8. Among these are momentum selection, achromatic injection into the linac, and beamline acceptance permitting the high-brightness beam to be transported under a variety of beam tunes.

We have measured the properties of the photoelectron beam in this beamline (Chapter 9):

- peak momentum of 4.5 MeV/c.
- peak normalized brightness of 1×10^{11} A/m^2.
- normalized transverse emittance of 4.0 mm-mrad.
- pulse length of 5-6 psec.
- peak current of 133 A.
- peak current density of 10 kA/cm^2.

All of these parameters meet or exceed design specifications with the exception of the pulse length, which is a factor of two longer. Some of them, such as the brightness

and peak current density, represent new benchmarks in the ongoing efforts to improve electron-beam quality for future experiments; they have only been exceeded in dedicated source-testing experiments. For example, the peak current density is a factor of ten higher than had previously been attained in particle-accelerator sources. The beam brightness appears to be limited at present by the acceptance of the beamline. In general, gun and beamline performance have been in accordance with our theoretical understanding of electron-beam production and dynamics (outlined in Chapters 4 and 5).

We have identified a previously unobserved excitation mode in the rf gun in which a sufficiently intense laser pulse creates a plasma at the photocathode surface. This results in a train of micropulses over many rf cycles, yielding a total charge of more than 100 times that of the normal photoelectron mode. Due to the observed temporal properties of this enhanced emission and its destructive effect on the photocathode, it is not of immediate interest in the context of the ATF experimental program. It does however, represent an interesting process for further study and might provide a useful high-charge source for such applications as high-power free-electron lasers.

The elements of the ATF design and physical construction that were not optimal for producing a stable electron beam were diagnosed. The result was a shutdown beginning in July, 1991 and extending into 1992 during which many of the needed improvements are being made. These include a more precise survey of the low-energy electron-beam optical elements and extensive improvements in the Nd:YAG-laser system. A major lesson of the commissioning period was that a reliable YAG laser with versatile optics is absolutely essential.

After the 1991-2 shutdown, operation of the low-energy beamline will be reestablished, at which point the beam will be injected into the linac and commissioning of the high-energy beamline will begin. Experimental beam at 50 MeV is expected by summer, 1992. Hopefully the CO_2-laser beam will also be available in 1992. The x-ray-backscattering diagnostic we have constructed can then be used to establish the synchronized interaction of the two beams. Other recommended studies are presented in Chapter 10.

Once the experimental program is under way, the x-ray diagnostic will be augmented by an x-ray spectrometer. This will serve as the apparatus of an experiment to study nonlinear Compton scattering in the strong fields present at the CO_2-laser focus (Chapter 11).

12.2 Other High-Brightness Sources

The success of the ATF gun has prompted several other groups to adopt the same design. Among these are [94]:

- The Rocketdyne Division of Rockwell International has chosen the ATF design for use in a program to develop the technology needed for high-power FEL's.
- A group in the UCLA physics department is developing an infrared FEL.

- CERN has initiated a research and development program with the stated aim of building a 1 TeV × 1 TeV electron-positron collider, the CERN Linear Collider (CLIC). A stepping stone on this path is the CLIC Test Facility (CTF), a testbed for some of the technologies required. This facility makes use of the design of the ATF gun and low-energy beamline [95].

- A joint Brookhaven-Grumman research-and-development effort is developing the second-generation gun for the ATF. The goal of this $3\frac{1}{2}$-cell gun is to achieve a brightness ten times higher than has been achieved with the present gun.

Over 20 rf-gun projects can be found in laboratories in the U.S., Europe, Japan, and the "Soviet Union."

High-brightness particle sources are an active area of research at present, and several novel approaches are being explored. Two of these will be briefly sampled here to convey the flavor of this field. A group at the University of Maryland is exploring the concept of the "pseudospark" source. A discharge occurs between a planar anode and a hollow cathode in the presence of low-pressure argon gas. Recent studies have indicated the production of an electron beam with a current of 3 kA and a brightness approaching 10^{12} A/m^2 [17]. This would presumably represent the highest brightness attained in an electron source to date. In addition to electron sources, ion sources are also the subject of much effort. For example, an innovation called the liquid-metal ion source was recently featured in an article in *Scientific American* [96].

The photocathode rf gun, though only in its infancy, has already resulted in notable advances in electron-source technology. Given the rapidly-expanding interest in rf guns and improvements in laser technology, the rf-gun should prove to be an area of tremendous activity and progress. The resulting high-quality electron-beam facilities will in turn make possible the construction of free-electron lasers of higher power and shorter wavelength, the exploration of new particle-acceleration ideas, and other opportunities as yet unseen. In pioneering the use of a new electron source in a user facility, the Brookhaven Accelerator Test Facility represents one step on this interesting journey.

References

[1] J.S. Fraser *et al.*, "Photocathodes in Accelerator Applications," *Proceedings of the 1987 IEEE Particle Accelerator Conference*, edited by Eric R. Lindstrom and Louise S. Miller (Washington, D.C., 1987), 1705.

[2] K.T. McDonald, "Design of the Laser-Driven RF Electron Gun for the Brookhaven Accelerator Test Facility," IEEE Trans. Electron Dev. **ED-35**, 2052 (1988).

[3] K. Batchelor *et al.*, "Design and Modelling of a 5-MeV RF Electron Gun," Brookhaven National Lab publication BNL-41766, 1988.

[4] Richard B. Neal, *The Stanford Two-Mile Accelerator* (W.A. Benjamin, New York, 1968).

[5] J.T. Rogers *et al.*, "Stripline Beam Position Monitor for the Accelerator Test Facility," Brookhaven National Lab report, unpublished, 1991.

[6] Harold Kirk, Brookhaven National Lab, Upton, NY (private communication).

[7] D.F. Voss and L.S. Goldberg, "Simultaneous Amplification and Compression of Continuous-Wave Mode-Locked Nd:YAG Laser Pulses," Opt. Lett. **11**, 210 (1986).

[8] T. Shimada *et al.*, "Generation of High-Brightness 1.06 μm Pulses by Compression of a Chirped Seed in a Nd:YAG Regenerative Amplifier," presented at CLEO '89, Baltimore, MD, 1989.

[9] T. Shimada *et al.*, "Large-Volume High-Pressure CO_2 Laser for Ultrashort Pulse Amplification," Los Alamos publication LAUR-87-3766, contributed to the Conference on Lasers and Electro-Optics '88, Anaheim, California, 1988.

[10] P.B. Corkum, "Amplification of Picosecond 10 μm Pulses in Multiatmosphere CO_2 Lasers," IEEE J. Quantum Electron. **21**, 216 (1985).

[11] S.A. Jamison and A.V. Nurmikko, "Generation of Picosecond Pulses of Variable Duration at 10.6 μm," Appl. Phys. Lett. **33**, 598 (1978).

[12] I. Pogorelsky *et al.*, "Spatial Dynamics of Picosecond CO_2 Laser Pulses Produced by Optical Switching in Ge," in *Short-Pulse High-Intensity Lasers and Applications*, SPIE Proceedings, vol. 1413, edited by Hector A. Baldis, p. 21 (1991).

[13] M.J.W. Rodwell, D.M. Bloom, and K.J. Weingarten, "Subpicosecond Laser Timing Stabilization," IEEE J. Quantum Electron. **25**, 817 (1989).

[14] Robert Malone of Brookhaven National Lab designed and implemented the ATF control system.

[15] C. LeJeune and J. Aubert, "Emittance and Brightness: Definitions and Measurements," in *Applied Charged Particle Optics*, edited by A. Septier, Advances in Electronics and Electron Physics, Supp. 13A (Academic Press, New York, 1980), pp. 159-259.

[16] P.M. Lapostolle, "Possible Emittance Increase Through Filamentation Due to Space Charge," IEEE Trans. Nucl. Sci. **NS-18**, 1101 (1971).

[17] M. Reiser, University of Maryland, College Park (private communication).

[18] M.B. James *et al.*, "Update on the High-Current Injector for the Stanford Linear Collider," IEEE Trans. Nucl. Sci. **NS-30**, 2992 (1983).

[19] E. Munro, "Electron-Beam Lithography," in *Applied Charged Particle Optics*, edited by A. Septier, Advances in Electronics and Electron Physics, Supp. **13B** (Academic Press, New York, 1980), pp. 73-131.

[20] Stephen V. Benson *et al.*, "The Stanford Mark III Infrared Free Electron Laser," Nucl. Instrum. Methods **A250**, 39 (1986); for more details see G.A. Westenskow *et al.*, *Owner's Manual for the Microwave Electron Gun* (HEPL TN-86-1, 1986).

[21] M.T. Wilson and P.J. Tallerico, U.S. Patent No. 4,313,072 (26 January 1982).

[22] D.T. Pierce *et al.*, "GaAs Spin Polarized Electron Source, Rev. Sci. Instr. **51**, 478 (1980).

[23] J.S. Fraser *et al.*, "High-Brightness Photoemitter Injector for Electron Accelerators," IEEE Trans. Nucl. Sci. **32**, 1791 (1985).

[24] R.L. Sheffield, E.R. Gray, and J.S. Fraser, "The Los Alamos Photoinjector Program," Nucl. Instrum. Methods **A272**, 222 (1988).

[25] C.H. Lee *et al.*, "Electron Emission of Over 200 A/cm^2 from a Pulsed-Laser Irradiated Photocathode," IEEE Trans. Nucl. Sci. **32**, 3045 (1985).

[26] P.E. Oettinger *et al.*, "Pulse-Laser-Irradiated High-Brightness Photoelectron Source," Appl. Phys. Lett. **50**, 1867 (1987).

[27] A.H. Sommer, *Photoemissive Materials* (Wiley, New York, 1968), pp. 4-8.

[28] O.S. Heavens, *Thin Film Physics* (Methuen, London, 1970), p. 84.

[29] Neil W. Ashcroft and N. David Mermin, *Solid State Physics* (Saunders College, Philadelphia, 1976), p. 363.

[30] J.R. Oppenheimer, "Three Notes on the Quantum Theory of Aperiodic Effects," Phys. Rev. **31**, 66 (1928).

[31] L.W. Nordheim, "The Effect of the Image Force on the Emission and Reflexion of Electrons by Metals," Proc. R. Soc. London **A121**, 626 (1928).

[32] T. Srinivasan-Rao, J. Fischer, and T. Tsang, "Picosecond Field-Assisted Photoemission from Yttrium Microstructures," J. Opt. Soc. Am. **B8**, 294 (1991).

[33] A. Einstein, Ann. Phys. (Leipzig) **17**, 132 (1905).

[34] M. Cordona and L. Ley, "Introduction," in *Photoemission in Solids I*, edited by M. Cordona and L. Ley (Springer-Verlag, New York, 1978), Topics in Applied Physics, Vol. 26, p. 23.

[35] T. Tsang, T. Srinivasan-Rao, and J. Fischer, "Surface-Plasmon-Enhanced Multiphoton Photoelectric Emission from Thin Silver Films," Opt. Lett. **15**, 866 (1990).

[36] T. Srinivasan-Rao, Brookhaven National Lab (private communication).

[37] A.C. Paul and V.K. Neil, "High-Current Relativistic Electron Guns," in *Applied Charged Particle Optics*, edited by A. Septier, Advances in Electronics and Electron Physics, Supp. **13C** (Academic Press, New York, 1983), pp. 141-170.

[38] W.D. Kilpatrick, "Criterion for Vacuum Sparking Designed to Include Both RF and DC," Rev. Sci. Instr. **28**, 824 (1957).

[39] Gregory A. Loew and J.W. Wang, "RF Breakdown Studies in Room Temperature Electron Linac Structures," SLAC memo SLAC-PUB-4647, presented at the XIIIth International Symposium on Discharges and Electrical Insulation in Vacuum, Paris, 1988.

[40] T. Srinivasan-Rao, J. Fischer, and T. Tsang, "Photoemission Studies on Metals Using Picosecond Ultraviolet Laser Pulses," J. Appl. Phys. **69**, 3292 (1991).

[41] P.B. Corkum *et al.*, "Thermal Response of Metals to Ultrashort-Pulse Laser Excitation," Phys. Rev. Lett. **61**, 2886 (1988).

[42] T. Tsang, T. Srinivasan-Rao, and J. Fischer, "Photoemission Using Femtosecond Laser Pulses," presented at the Thirteenth International Free-Electron Laser Conference, Sante Fe, NM, 1991.

[43] Kwang-Je Kim, "RF and Space-Charge Effects in Laser-Driven RF Electron Guns," Nucl. Instrum. Methods A**275**, 201 (1989).

[44] M. Reiser, "Physics of High Brightness Sources," in *Advanced Accelerator Concepts*, edited by C. Joshi, AIP Conference Proceedings Volume 193, pp. 311-323 (1989).

[45] Juan C. Gallardo and Robert B. Palmer, "Preliminary Study of Gun Emittance Correction," IEEE J. Quantum Electron. **26**, 1328 (1990).

[46] Lloyd Young, "PARMELA – A Particle Dynamics Code for Electron Linacs," Los Alamos National Laboratory, unpublished.

[47] G.D. Warren *et al.*, "MAGIC Users' Group Software, in *Proceedings of the Conference on Computer Codes and the Linear Accelerator Community*, edited by Richard K. Cooper (Los Alamos National Laboratory, 1990), Los Alamos publication LA-11857-C, p. 57.

[48] G.D. Warren, Mission Research Corporation, Los Alamos, NM (private communication).

[49] K.L. Brown *et al.*"TRANSPORT: A Computer Program for Designing Charged Particle Beam Transport Systems," SLAC publication SLAC-91, Rev. 2, UC-28, 1977.

[50] David C. Carey, "TURTLE (Trace Unlimited Rays Through Lumped Elements)," Fermilab publication NAL-64, May, 1978.

[51] K.L. Brown, "A First- and Second-Order Matrix Theory for the Design of Beam Transport Systems and Charged Particle Spectrometers," Stanford Linear Accelerator Center Report-75, 1982.

[52] D.C. Carey, *The Optics of Charged Particle Beams* (Harwood, New York, 1987).

[53] K.D. Jacobs, J.B. Flanz, and T. Russ, "Emittance Measurements at the Bates LINAC," *Proceedings of the 1989 IEEE Particle Accelerator Conference*, edited by F. Bennett and J. Kopta (Chicago, 1989), p. 1526.

[54] See for example S.L. Shapiro, ed., *Ultrashort Light Pulses*, Topics in Appl. Phys. **18** (Springer, Berlin, 1977).

[55] D.J. Bradley, B. Liddy, and W.E. Sleat, "Direct Linear Measurement of Ultrashort Light Pulses with a Picosecond Streak Camera," Opt. Commun. **2**, 391 (1971).

[56] J. Haimson, "Microwave and Beam Optics Design of the Chopper-Prebuncher Injection System and Accelerator Waveguides for the Frascati 450-MeV Electron and 50-MeV Proton Linac," Varian Document RDR-5, 1965.

[57] J. Haimson, "Microwave and Beam Optics Design of Standing Wave Transverse Magnetic Deflection Systems," Varian Technical Memo TMO-90, 1966.

[58] "Optical Characteristics of Cathode Ray Tubes," TEPAC Publication No. 116-B (Electronic Industries Association, 1987).

[59] GTE/Sylvania Technical Information Bulletin CM-9087 (Chemical and Metallurgical Division, Towanda, PA 18848, Nov., 1983).

[60] J.T. Seeman *et al.*, "Beam Tests of Phosphorescent Screens," SLAC Single Pass Collider Memo CN-290, 1985; and J.T. Seeman (private communication).

[61] GTE/Sylvania Technical Information Bulletin CM-9045 (March, 1982).

[62] William H. Press *et al.*, *Numerical Recipes in C* (Cambridge University Press, Cambridge, 1988).

[63] Sol Gruner, computer code DRAW.ASM (Princeton University Physics Department, 1988); modified for ATF use.

[64] Computer code ITEX OFG, Version 2.0 (Imaging Technology Incorporated, 55 Middlesex Turnpike, Bedford, Mass. 01730-1421, 1990); with some undocumented features. A revised library was requested by the author in which several bugs discovered during software development were fixed.

[65] Particle Data Group, "Review of Particle Properties," Phys. Lett. **B239** (1990).

[66] See for example V.K. Zworykin and G.A. Morton, *Television*, 2nd ed. (Wiley, New York, 1954); and N.A. Diakides, "Phosphors," SPIE Proceedings **42**, 83 (1973).

[67] F.-J. Decker, "Beam Size Measurement at High Radiation Levels," Stanford Linear Accelerator Center publication SLAC-PUB-5481, 1991.

[68] Mehran Ardebili and K.T. McDonald, "Third-Order-Transport Studies of the ATF Beam Line," 1988 (unpublished).

[69] X.J. Wang, Ph.D. thesis, ULCA, in progress.

[70] King Leung, Brookhaven National Lab (private communication).

[71] R.W. Schoenlein *et al.*, "Femtosecond Studies of Nonequilibrium Electronic Processes in Metals," Phys. Rev. Lett. **58**, 1680 (1987).

[72] E. Matthias and R.W. Dreyfus, "From Laser-Induced Desorption to Surface Damage," in *Photoacoustic, Photothermal and Photochemical Processes at Surfaces and in Thin Films*, edited by P. Hess, Topics in Current Physics (Springer-Verlag, Berlin, 1989), pp. 89-128.

[73] Yong Jee, Michael F. Becker, and Rodger M. Walser, "Laser-Induced Damage on Single-Crystal Metal Surfaces," J. Opt. Soc. Am. B5, 648 (1988).

[74] O.L. Landen, D.G. Stearns, and E.M. Campbell, "Measurement of the Expansion of Picosecond Laser-Produced Plasmas Using Resonance Absorption Profile Spectroscopy," Phys. Rev. Lett. **63**, 1475 (1989).

[75] T. Tsang *et al.*, "Intense Electron Emission due to Picosecond Laser-Produced Plasmas in High Gradient Electric Field" (unpublished).

[76] Alex H. Lumpkin and Donald W. Feldman, "Diagnostics of the Los Alamos Free Electron Laser Using Streak Systems," Nucl. Instrum. Methods A**259**, 13 (1987).

[77] Anthony E. Siegman, *Lasers* (University Science Books, Mill Valley, CA, 1986), pp. 663-676. The intensity formula given in the text is based on the "1/e criterion" for aperture transmission, namely than the focusing lens has diameter $D = 2\sqrt{2}\sigma$, where σ is the standard-deviation width of the laser-intensity profile at the lens.

[78] R.H. Milburn, "Electron Scattering by an Intense Polarized Photon Field," Phys. Rev. Lett. **10**, 75 (1963).

[79] J.H. Hubbell, "Photon Mass Attenuation and Energy-Absorption Coefficients from 1 keV to 20 MeV," Int. J. Appl. Radiat. Isot. **33**, 1269 (1982).

[80] Andrew Sessler has written several excellent review articles on this subject, including: "New Concepts in Particle Acceleration," *Proceedings of the 12th International Conference on High-Energy Accelerators*, edited by Francis T. Cole and Rene Donaldson (Fermilab, 1983), p. 445; "The Quest for Ultrahigh Energies," Am. J. Phys. **54**, 505 (1986); and "New Particle Acceleration Techniques," Phys. Today **41** (1), 26 (1988).

[81] All experiments described were proposed and approved at the ATF Users' Meeting, Brookhaven National Laboratory, Upton, New York, Nov. 29-30, 1989, Brookhaven publication BNL-43702, CAP #53, ATF-89R.

[82] R.B. Palmer, "A Laser Driven Grating Accelerator," Particle Accelerators **11**, 81 (1980).

[83] S. Smith and E. Purcell, "Visible Light from Localized Surface Charges Moving across a Grating," Phys. Rev. **92**, 1069 (1953).

[84] W.B. Colson, "Classical Free-Electron Laser Theory," in *Free-Electron Laser Handbook*, edited by C. Pellegrini and A. Renieri, Laser Handbook Series (North-Holland, New York, 1989).

[85] J.A. Edighoffer *et al.*, "Observation of Inverse Čerenkov Interaction Between Free Electrons and Laser Light," Phys. Rev. A**23**, 1848 (1981).

[86] J.R. Fontana and R.H. Pantell, "A High-Energy Laser Accelerator for Electrons Using the Inverse Čerenkov Effect," J. Appl. Phys. **54**, 4285 (1983).

[87] L.D. Landau and E.M. Lifshitz, *The Classical Theory of Fields* (Pergamon Press, New York, 1975), p. 118.

[88] A.A. Sokolov and I.M. Ternov, *Radiation from Relativistic Electrons* (American Institute of Physics, New York, 1986), pp. 52-55.

[89] N.B. Narozhny, A.I. Nikishov, and V.I. Ritus, "Quantum Processes in the Field of a Circularly Polarized Electromagnetic Wave," Sov. Phys. JETP **20**, 622 (1965); for a textbook treatment see V.B. Berestetskii, E.M. Lifshitz, and L.P. Pitaevskii, *Quantum Electrodynamics* (Pergamon Press, New York, 1982).

[90] G.A. Schott, *Electromagnetic Radiation* (Cambridge University Press, 1912).

[91] T.J. Englert and E.A. Rinehart, "Second-Harmonic Photons from the Interaction of Free Electrons with Intense Laser Radiation," Phys. Rev. A**28**, 1539 (1983).

[92] C.J. Sparks, "Mosaic Crystals for Obtaining Larger Energy Bands and High Intensities from Synchrotron Radiation Sources," in *Workshop on X-Ray Instrumentation for Synchrotron Research*, edited by H. Winick and G. Brown (SSRL Report 78/04, Stanford, 1978), p. III-35.

[93] Frank Shoemaker, Princeton University (private communication).

[94] In "Captions: Newsletter for the Center for Accelerator Physics," No. 1, edited by Juan Gallardo, Brookhaven National Lab, 1991.

[95] H. Kugler *et al.*, "Beam Dynamics Simulations of the RF-Gun, Particle Source of the CLIC Test Facility," CERN publication CERN/PS 90-23, CLIC Note 117, presented at the European Particle Accelerator Conference, Nice, France, 1990.

[96] Jon Orloff, "Focused Ion Beams," Sci. Am. **265** (4), 96 (October, 1991).